

CHARACTERIZING A REINFORCED CONCRETE BEAM-COLUMN-SLAB  
SUBASSEMBLAGE CONNECTION FOR PROGRESSIVE COLLAPSE  
ASSESSMENT

By

YONG HONG KOH

A THESIS PRESENTED TO THE GRADUATE SCHOOL  
OF THE UNIVERSITY OF FLORIDA IN PARTIAL FULFILLMENT  
OF THE REQUIREMENTS FOR THE DEGREE OF  
MASTER OF SCIENCE

UNIVERSITY OF FLORIDA

2011

© 2011 Yong Hong Koh

To my lovely wife for her love and support

## ACKNOWLEDGMENTS

I would like to express my heartfelt gratitude to my thesis advisor, Professor Theodor Krauthammer for his time, guidance and advice throughout the whole period of time. I would also like to thank my thesis committee member, Dr Serdar Astarlioglu for his time and assistance. Next, I would like to thank both Dr Long Hoang Bui and Mr Loo Yong Tan for their advice and teaching on the finite element software. Furthermore I am honored and grateful for Defence Science and Technology Agency (DSTA), Singapore, for the postgraduate scholarship granted to me. In addition, I thank all my fellow colleagues at the Center for Infrastructure Protection and Physical Security (CIPPS), classmates at University of Florida (UF) and my Singaporean friends in Gainesville for their love and support which made my stay in United State of America (USA) a wonderful experience. Lastly, I would like to express my gratitude to my wife who made a huge sacrifice to quit her job back home and accompany me here for study.

## TABLE OF CONTENTS

	<u>page</u>
ACKNOWLEDGMENTS.....	4
LIST OF TABLES.....	8
LIST OF FIGURES.....	9
LIST OF ABBREVIATIONS.....	16
ABSTRACT.....	23
CHAPTER	
1 PROBLEM STATEMENT.....	25
Introduction.....	25
Objectives and Scope.....	26
Research Significance.....	27
2 BACKGROUND AND LITERATURE REVIEW.....	28
Overview.....	28
Beam-Column Connections.....	28
Two-Member Connection/ Knee Connection.....	29
Three-Member Connection/ T-Connection.....	30
Four-Member Connection/ Interior Connection.....	31
Connection Behavior.....	31
Compressive Strut and Truss Mechanism Model.....	31
Strut and Tie Model.....	32
Beam-Column-Slab Subassemblage.....	33
Effect of Slab on Flexural Strength.....	34
Effect of Transverse Beam.....	35
Force Transfer Mechanism.....	36
Interior connection.....	36
Exterior connection.....	38
Continuous frame.....	38
Slab Contribution to Flexural Strength of Longitudinal Beam.....	39
Type of connections.....	39
Lateral deformation.....	41
Load history.....	41
Shear deformation.....	42
Rotation of the slab.....	43
Boundary condition and continuity.....	44
Joint Shear Behavior.....	46
Formulation of Effective Flange Width/ Effective Slab Width.....	47

Modeling of Beam-Column-Slab Subassemblages .....	50
Experiments and Test Results .....	53
Plastic Hinge .....	55
Moment-Rotation Formulation for Connections .....	57
Material Models .....	58
Concrete .....	58
Compression stress-strain curve .....	58
Tensile strength .....	60
Reinforcement .....	62
Finite Element Analysis .....	64
Verification and Validation Processes .....	65
The Finite Element (FE) Code Abaqus .....	66
Concrete damaged plasticity model (CDP) .....	67
Defining the plasticity parameters for CDP .....	70
Classical metal plasticity .....	72
Elements .....	73
Connectors .....	76
Convergence and iteration control .....	76
Progressive Collapse .....	79
Summary .....	83
<b>3 RESEARCH APPROACH .....</b>	<b>122</b>
Overview .....	122
Beam-Column-Slab Interior Connection Characterization .....	123
Simplified Finite Element Model .....	125
Summary .....	126
<b>4 RESULTS AND DISCUSSION .....</b>	<b>131</b>
Overview .....	131
Verification of the Finite Element Code .....	131
Validation of the Finite Element Code .....	132
Cantilever Rectangular Beam .....	133
Exterior Connection Beam-Column-Slab Subassemblages .....	136
Interior Connection Beam-Column-Slab Subassemblages .....	137
Reinforced Concrete Beam-Column-Slab Connection in This Study .....	139
Resistance Function of the Beam-Column-Slab Connection in this Study .....	140
Moment-Rotation Resistance .....	141
Simplified Structural Elements Based FE Models .....	145
<b>5 CONCLUSION AND DISCUSSION .....</b>	<b>175</b>
Summary .....	175
Conclusion .....	176
Validations .....	176
Characterizations of the Moment-Rotation of Interior Connection .....	176

Structural Element Based Simplified FE Model .....	176
Limitations.....	177
Recommendations for Future Research .....	178

APPENDIX

A PARAMETRIC STUDIES FOR SPECIMEN R4.....	180
B MOMENT CAPACITY CALCULATION OF UPWARD LOADED T-BEAM.....	193
C SIMPLIFIED STRUCTURAL ELEMENTS BASED FINITE ELEMENT MODEL....	197
LIST OF REFERENCES .....	203
BIOGRAPHICAL SKETCH.....	209

## LIST OF TABLES

<u>Table</u>		<u>page</u>
2-1	Various effective flange widths for interior connection.....	117
2-2	Beam and slab reinforcement details for various test series.....	118
2-3	Reinforcement properties for various test series .....	119
2-4	Approximate range of tensile strengths of plain concrete .....	119
2-5	Spurious modes resulted from reduced integration .....	120
2-6	Default values for convergence and iteration controls in Abaqus/Standard....	120
2-7	Occupancy categories.....	121
2-8	Design requirements based on occupancy categories .....	121
4-1	Parameters of concrete damage plasticity material model .....	173
4-2	Summarized material models, parameters and method to be used for finite element (FE) modeling from Appendix A.....	173
4-3	Changes in dilation angle on the modeled tip load in specimen R4.....	174
4-4	Mesh density variation for specimen R4.....	174
4-5	Moment capacity of the FE models for the interior connection with T-Beam..	174
4-6	Comparison of simulation time for FE models .....	174
A-1	Comparison of analysis time between embedded and tie nodes technique for modeling reinforcement for specimen R4 .....	192
A-2	Summary of material models and parameters .....	192

## LIST OF FIGURES

<u>Figure</u>		<u>page</u>
2-1	Reinforced concrete (RC) beam-column connections .....	84
2-2	Knee-connection subjected to opening loads .....	84
2-3	Efficiency of connections .....	85
2-4	Details of connection under opening loads .....	85
2-5	Flow of forces and reinforcement details of T-connections.....	86
2-6	Connection efficiency against steel reinforcement ratio.....	86
2-7	Connection forces .....	87
2-8	Suggested forces within the interior connection .....	87
2-9	Idealized connection behavior .....	88
2-10	Strut-and-tie model .....	88
2-11	Forces that act on the primary members of a connection.....	89
2-12	Variation of slab reinforcement strains along both transverse and longitudinal beam directions .....	90
2-13	Force transfer from longitudinal beam to the slab.....	90
2-14	Forces at slab boundary .....	91
2-15	Force transfer mechanism.....	91
2-16	Force transfer for an exterior connection.....	92
2-17	Proposed force transfer mechanism in an external edge panel.....	92
2-18	Proposed strut and tie model for continuous frame structure .....	93
2-19	Plan view of exterior connection subjected to weak axis bending of the spandrel beam under the slab tension force.....	93
2-20	Sectional view of exterior connection subjected to torsional moments.....	94
2-21	Failure in specimen with slab due to torsional failure in spandrel beam.....	94

2-22	Typical deformation behavior of an interior connection subjected to lateral load.....	94
2-23	Measured stirrup strain for interior and exterior transverse beams.....	95
2-24	Deformation behavior under seismic load .....	95
2-25	Plot of slab effective width ratio versus drift angle .....	96
2-26	Comparison of negative bending moment of longitudinal beam for uni-directional and bi-directional loading .....	96
2-27	Shear deformation of a slab.....	97
2-28	Transverse slab reinforcement strain distribution for isolated subassembly .....	97
2-29	Stress states in slab for S-T case .....	97
2-30	Cracks patterns under uni-axial lateral load .....	98
2-31	Effects of continuity (end beam) on slab curvature due to flexural deformation.....	98
2-32	Longitudinal slab reinforcement strain distribution for continual structure .....	99
2-33	Transverse slab reinforcement strain distribution for continual structure .....	99
2-34	Variation of joint shear stress with different structural configurations .....	100
2-35	Joint mechanism hypothesized to resist the additional force from the tension slab reinforcement .....	100
2-36	Design horizontal shear force for Type 2 connection.....	101
2-37	Notation and definition for a typical effective flange width .....	101
2-38	Idealization for the effective flange width.....	102
2-39	Effective flange width for T-beam .....	102
2-40	Test specimens for interior subassemblages.....	103
2-41	Comparison of measured moments with calculated moments for different effective flange widths .....	103
2-42	Effective tensile flange widths for cast-in-place floor system .....	104
2-43	Simple connection model .....	104

2-44	Improved kinematic formulation for rigid links.....	105
2-45	Suggested strut and tie model for spandrel beam after torsional cracking .....	105
2-46	Typical layout plans and sectional details for various test series.....	106
2-47	Comparison plot of normalized moment and torsional stiffness for interior subassemblages from various test series.....	106
2-48	Cantilever beam at ultimate moment .....	107
2-49	Typical concrete compressive stress-strain curve for different concrete strengths.....	107
2-50	Modified Hognestad stress-strain curve for concrete in compression .....	108
2-51	Typical tensile stress strength curve of reinforced concrete .....	108
2-52	Typical stress-strain curve for steel reinforcement .....	109
2-53	Different idealized steel reinforcement stress-strain curve .....	109
2-54	Proposed bilinear stress-strain curve for steel reinforcement in reinforced concrete.....	110
2-55	Different idealization of steel reinforcement stress-strain curve.....	110
2-56	Proposed steel stress-strain curve modified from Hsu's model .....	111
2-57	Flow process of finite element (FE) analysis for a physical problem .....	111
2-58	FE verification process .....	112
2-59	FE validation process .....	112
2-60	Uniaxial compressive stress-strain curve in concrete damaged plasticity (CDP) material model .....	113
2-61	Tension stiffening stress-strain curve in CDP material model for post failure behavior .....	113
2-62	Drucker-Prager plastic flow potential .....	114
2-63	Friction angles for different concrete compressive strength .....	114
2-64	Parameter study of the dilation angles .....	115
2-65	Typical 8 nodes linear brick element .....	115

2-66	Integration points for 8 node element .....	115
2-67	Typical 2 nodes linear beam element .....	116
2-68	Typical 4 nodes linear shell element.....	116
2-69	Non-linear response in a single increment .....	116
2-70	Components of the simplified structural element based FE building frame model .....	117
3-1	Various types of connections in a typical building frame .....	127
3-2	Proposed three dimensional model for interior connection.....	127
3-3	Global rotation for longitudinal beam .....	128
3-4	Plastic hinge formation .....	128
3-5	Proposed plastic rotation angle which includes the plastic hinge length $l_p$ .....	128
3-6	Simplified model using structural elements .....	129
3-7	Connector type JOIN - only translational dofs .....	129
3-8	Connection type CARDAN -only rotational dofs .....	129
3-9	Flow charts of research approach .....	130
4-1	Comparison of deflection time history of dynamically loaded RC beam with modeled results from Abaqus/Explicit.....	151
4-2	Comparison of load and deflection curve for corner connection (U25) subjected to monotonic load with modeled results from Abaqus/Standard.....	151
4-3	Comparison of load and deflection curve for T-connection (T16) subjected to monotonic load with modeled results from Abaqus/Standard .....	152
4-4	Comparison of load and deflection curve for interior-connection (U69) subjected to monotonic load with modeled results from Abaqus/Standard.....	152
4-5	Elevation and sectional details for rectangular beam specimen R4.....	153
4-6	Stress-strain curves of steel reinforcement for test series .....	153
4-7	Test setup for test series - Plan View .....	154
4-8	Loading history for specimen R4 .....	154

4-9	Measured tip load and tip deflection curve for specimen R4 up till load point (Lp) 13.....	155
4-10	FE model for specimen R4 .....	155
4-11	Comparison plot of modeled and experimental result for specimen R4.....	156
4-12	Comparison plots for variation of dilation angles for specimen R4 .....	156
4-13	Comparison plots for the variation of mesh density for specimen R4 .....	157
4-14	Elevation, plan and sectional details for specimen T2.....	157
4-15	Loading history for specimen T2 till Lp 9 .....	158
4-16	Measured tip load and tip deflection curve for specimen T2 .....	158
4-17	Comparison plot of modeled and experimental result for specimen T2.....	159
4-18	Test setup and elevation view of test specimens.....	159
4-19	Sectional details for specimen S2.....	159
4-20	Load deflection envelope curve for specimen S2 .....	160
4-21	Comparison plot of modeled and experimental results for Specimen S2 .....	160
4-22	Idealized boundary conditions for the FE model for specimen S2.....	161
4-23	Plan layout of the test structure .....	161
4-24	Elevation view of the test structure .....	162
4-25	Elevation view of longitudinal beams.....	162
4-26	Elevation view of transverse beams .....	163
4-27	Elevation view of spandrel beams .....	163
4-28	Cross-sectional details of the beams.....	164
4-29	Top slab reinforcement details near column Grid C-3 .....	164
4-30	Bottom slab reinforcement details near column Grid C-3 .....	165
4-31	Typical T-Beam sectional details for longitudinal beam.....	165
4-32	Concrete stress-strain curve from Hognestad (1951) for compression and Hsu (1993) stiffening model for tension .....	166

4-33	Steel reinforcement stress-strain curve modified from Hsu (1993) with $C_f = 0.80$ and $C_s = 0.50$ .....	166
4-34	Progressive modeling of interior connection .....	167
4-35	FE symmetry half model for interior connection with T-beam (Predominantly continuum based model) .....	168
4-36	Moment-rotation curves of the FE models for the interior connection (T-beam) .....	168
4-37	Finite element symmetry half model for interior connection (Predominantly continuum based model) .....	169
4-38	Load-rotation curve between interior connections (full connection versus idealized T-beam connection only) .....	169
4-39	Schematic view of a structural element based FE model (Interior connection with rectangle beam only).....	170
4-40	Comparison plot between the continuum and structural element based FE models (Interior connection with rectangle beam only).....	170
4-41	Schematic view of structural element based FE model (Full connection including longitudinal, transverse, spandrel beams and slabs).....	171
4-42	Comparison plot of the load-rotation curve for the full interior connection of this study .....	171
4-43	Biaxial moment interaction curve.....	172
4-44	Comparison of moment-rotation behaviors from Power Model and the continuum based FE model .....	172
A-1	Modified Hognestad compression stress-strain curve for concrete .....	186
A-2	Comparison plots between various tension stiffening models with constant dilation angle and cracking stress for specimen R4.....	187
A-3	Comparison plots of different cracking stress $f_{cr}$ based on Hsu tension stiffening model for specimen R4 .....	187
A-4	Different idealization for steel stress-strain curve .....	188
A-5	Comparison plots of different steel stress-strain curve idealization for specimen R4.....	188
A-6	Comparison plot of load-displacement curve with variation of equivalent yield stress correction factors $C_f$ for specimen R4 .....	189

A-7	Comparison plots of load-displacement curve with variation of initial stiffness correction factors $C_s$ for specimen R4 .....	189
A-8	Comparison plot for displacement and force controlled loading for specimen R4 .....	190
A-9	Comparison of embedded and tie nodes technique for modeling reinforcement for specimen R4.....	190
A-10	Comparison of interaction points between reinforcement and concrete .....	191
B-1	Cross-section, strain and force distribution of a T-beam loaded upwardly (slab in compression) .....	196
C-1	Continuum FE model for beam-column connection for longitudinal beam (rectangle cross-section only).....	201
C-2	Moment-rotation relationship of beam-column connection for beams with rectangle cross-sectional subjected to downward loads .....	201
C-3	Geometric for transformed stiffness calculation for uncracked section (Not to scale).....	202
C-4	Geometric for effective moment of inertia calculation for cracked section based on American Concrete Institute (ACI) 318-08 (Not to scale).....	202

## LIST OF ABBREVIATIONS

$A_0$	Initial area of metal
$A_c$	Current area of metal
$A_s^*$	Area of slab reinforcement within a spacing of $S_s$
$A_{s1}$	Area of bottom beam steel which is assumed to limit the magnitude of the moment applied to a connection
$A_{s1}$ to $A_{s5}$	Area of steel reinforcement layers 1 to 5
$A_{sl}$	Area of transverse beam longitudinal reinforcement
$a$	Depth for concrete compressive stress block
$a_{sj}$	Area of one radial hoop
$b$	Beam width
$b_e$	Effective flange width
$b_f$	Protruding effective flange
$b_w$	Beam web width
$c$	Neutral axis depth
$c$	Column dimension
$C_a$	Displacement correction parameter
$C_f$	Equivalent steel stress correction factor
$C_s$	Initial steel young modulus correction factor
$C_x$	Beam concrete compression zone
$C_\alpha^n$	Tolerance value for $C_a$
$D$	Resultant diagonal compressive slab force
$d$	Section effective depth
$d_1$ to $d_5$	Effective depth to steel reinforcement layers 1 to 5
$d_b$	Beam effective depth

$d_c$	Compression damage parameter for Abaqus concrete damage plasticity model
$d_{lb}$	Diameter of the longitudinal reinforcement
$d_s$	Slab effective depth
$d_t$	Tension damage parameter for Abaqus concrete damage plasticity model
$E_0$	Concrete initial elastic young modulus
$E_c$	Elastic modulus of concrete
$E_{cd}$	Descending elastic modulus
$E_p$	Modulus for strain hardening
$E_p'$	Ascending slope of strain hardening curve for Hsu (1993) steel model
$E_s$	Steel reinforcement initial elastic young modulus
$E_s'$	Reduced initial steel young modulus
$F_1$ to $F_5$	Forces for reinforcement layers 1 to 5
$F_c$	Concrete compressive force
$F_s$	Tension force
$f_c$	Concrete stress
$f'_c$	Uniaxial concrete compressive strength under standard test cylinder
$f_c''$	Maximum compressive stress
$f_{cr}$	Concrete cracking stress
$f_{ct}$	Split tensile strength
$f_{max}$	Maximum steel stress
$f_r$	Modulus of rupture
$f_s$	Steel reinforcement stress

$f_{s1}$ to $f_{s5}$	Stresses of steel reinforcement layers 1 to 5
$f_t'$	Direct tensile strength
$f_y$	Yield strength of steel reinforcement
$f_y^*$	Apparent yield stress of steel reinforcement
$f'_y$	Equivalent yield stress for the bilinear steel stress-strain curve
$f_{yj}$	Yield strength of radial steel bars
$f_{ys}$	Yield strength of slab steel reinforcement
$f_{yt}$	Yield strength of transverse beam longitudinal steel reinforcement
$f_{bo}/f_{co}$	Ratio of the initial equibiaxial compressive yield stress to the initial uniaxial compressive yield stress
$G$	Plastic potential function
$h$	Overall beam depth
$h$	Section depth
$h_1$	Column depth
$h_2$	Beam depth
$h_b$	Beam deflection
$I$	Internal forces
$I_0$	Number of iterations prior to the commencement of divergence check in Abaqus/Standard
$l_1$ to $l_5$	Lever arm to neutral axis for reinforcement layers 1 to 5
$l_a$	Next internal
$l_c$	Lever arm of concrete compressive force to neutral axis
$I_R$	Number of iterations prior to the commencement of the logarithmic rate of convergence check in Abaqus/Standard
$K$	Ratio of the second stress invariant on the tensile meridian to that of the compressive meridian

$K_0$	Initial tangent stiffness
$k_i$	Initial connection stiffness
$L$	Beam span length
$l$	Length of the cantilever
$l_p$	Length of the plastic hinge
$M$	Moment
$M_r$	Flexural strength ratio
$M_u$	Ultimate moment of a cross-section
$N^{ls}$	Abaqus/Standard line search value
$n$	Numbers of the legs of the radial steel bars provided
$n_s$	Shape factor
$P$	External forces
$P_L$	Axial load
$\bar{p}$	Hydrostatic pressure stress
$\bar{q}$	Mises equivalent effective stress
$R_a$	Residual forces or error
$R_\alpha^n$	Tolerance value for $R_a$
$S_1, S_2$	Clear spacing between adjacent beams
$S_s$	Spacing of slab reinforcement
$T_2$	Tension force in horizontal direction
$T_x$	Longitudinal slab reinforcement tension force
$T_y$	Transverse slab reinforcement tension force
$t$	Slab thickness
$t_i$	Current time step
$t_{i+1}$	Next time step

$u_0$	Initial displacement
$u_1$	Horizontal displacement of the inner edge of the plastic
$u_2$	Horizontal displacement of the outer edge of the plastic
$u_a$	Next displacement
$V_1$	Shear force in vertical direction
$V_2$	Shear force in horizontal direction
$v_1$	Vertical displacement of the inner edge of the plastic hinge
$v_2$	Vertical displacement of the outer edge of the plastic hinge
$v_c$	Joint shear resistance provided by diagonal compressive strut
$v_j$	Total joint shear resistance
$v_s$	Joint shear resistance provided by lateral reinforcement due to truss action
$v_u$	Design joint shear
$w_c$	Density of concrete
$x$	Protruding flange width
$z$	Clear distance from the critical section to the point of contra flexure
$\alpha$	Orientation of cracks in degree
$\sigma_c$	Concrete compressive stress
$\sigma_{co}$	Initial yield stress of concrete
$\sigma_{cu}$	Ultimate stress of concrete
$\sigma_{nom}$	Nominal stress
$\sigma_t$	Concrete tensile stress
$\sigma_{to}$	Tensile failure stress of concrete
$\sigma_{true}$	True stress
$\varepsilon$	Flow potential eccentricity

$\epsilon^p$	Plastic strain increment
$\epsilon_o$	Concrete strain at maximum compressive stress
$\epsilon_c$	Concrete strain or total compressive strain
$\epsilon_c^{in}$	Concrete Inelastic strain
$\epsilon_c^{pl}$	Concrete compressive plastic strain
$\epsilon_{cm}$	Concrete nominal strain
$\epsilon_{cr}$	Concrete cracking strain
$\epsilon_{ln}^{pl}$	Logarithmic plastic strain
$\epsilon_{nom}$	Nominal strain
$\epsilon_{oc}^{el}$	Concrete elastic compressive strain
$\epsilon_{ot}^{el}$	Concrete elastic tensile strain
$\epsilon_s$	Steel strain
$\epsilon_{s1}$ to $\epsilon_{s5}$	Steel strains for reinforcement layers 1 to 5
$\epsilon_{sc}$	Maximum strain where Hsu (1993) steel model is valid
$\epsilon_t$	Total tensile strain in concrete
$\epsilon_t^{ck}$	Concrete cracking strain
$\epsilon_t^{pl}$	Concrete tensile plastic strain
$\epsilon'_y$	Equivalent yield strain for the bilinear steel stress-strain curve
$\rho$	Reinforcement ratio
$\delta_i^s$	Displacement of slab reinforcement due to bond slip
$\delta_i^T$	Elongation of transverse beam
$\delta_i^t$	Transverse beam in plane deflection
$\Delta C'_c$	Column vertical compression zone force
$\Delta_e$	Inter-story drift

$\Delta p$	Longitudinal beam deformation
$\phi$	Friction angle
$\phi_u$	Curvature at ultimate moment
$\phi_y$	Curvature at yield moment
$\varphi$	Dilation angle
$\theta$	Rotation
$\theta_g$	Global rotation
$\theta_0, \theta_p$	Plastic rotation
$\mu$	Viscosity parameter

Abstract of Thesis Presented to the Graduate School  
of the University of Florida in Partial Fulfillment of the  
Requirements for the Degree of Master of Science

CHARACTERIZING A REINFORCED CONCRETE BEAM-COLUMN-SLAB  
SUBASSEMBLAGE CONNECTION FOR PROGRESSIVE COLLAPSE  
ASSESSMENT

By

Yong Hong Koh

May 2011

Chair: Theodor Krauthammer  
Major: Civil Engineering

Finite element (FE) codes; an advance numerical tool can be used in the fast and accurate assessment of progressive collapse of building structures. Past research on moment resisting steel frames have proved the feasibility of the usage of FE codes for the analysis of progressive collapse. In the same research, it was shown that the accuracy of the overall building structure simulation is highly dependent on the accuracy of the modeling of the steel connections. Similarly, FE codes have also been used successfully to derive the resistance function of reinforced concrete (RC) interior connection (with rectangle beam cross-section only).

The objective of this study is to better understand the behavior of reinforced concrete beam-column connection under monotonic loading. The interior beam-column-slab subassembly connection of a 4-story full scale reinforced concrete building frame that was tested for progressive collapse under blast loads was selected as the prototype connection to be studied. A predominantly continuum based FE model using Abaqus was developed for this interior connection subassembly. This FE model considered the effect of the longitudinal, transverse, spandrel beams and slab on load

resistance of the connection. The load resistance function of this interior connection subassembly under monotonic loading was then derived.

A fast running simplified structural elements based FE model was also developed to attempt to simulate the behavior of this interior connection. This simplified FE model was able to produce reasonably good estimates of the load-rotation function of the interior connection at a much reduced computational time. This reduction in computation time could result in significance time and cost saving in the progressive collapse assessment of building structure.

## CHAPTER 1 PROBLEM STATEMENT

### **Introduction**

*Bad connections prevent the structure from mobilizing its full resistance*

(Krauthammer, 2008). The connections must be properly designed and constructed to ensure that the adjacent connecting structural elements (beam, slab, column and wall etc) fully mobilize their strength.

Extensive research had been done during the past forty years on beam-column connections subjected to lateral loads due to seismic activities. The knowledge gained from these past research studies had been documented and implemented in code provision such as that of the American Concrete Institute (ACI).

However, the behaviors of reinforced concrete (RC) beam-column connections are still not well understood under the effects of abnormal loadings. Beam-column connections have complex stress distribution due to load and geometric discontinuities and cannot be described by the classical Bernoulli-Euler beam theory (Krauthammer, 2008). This complexity is compounded in the event of abnormal loadings (such as blast, impact load; etc) and few models are available in the literature to describe its behavior.

Watson and Inkester (1982) noticed that in the event of abnormal loadings such as blast, the beam-column connections often sustain more damage than the structural components subjected directly to the blast loading. The beam-column connections may become the point of weakness of the whole structure and potentially resulting in catastrophic consequences from progressive collapse of parts or the whole structure.

Currently, the designs of buildings against progressive collapse are subject to guidelines set forth by authorities such as Unified Facilities Criteria (UFC, 2009) and

General Services Administration (GSA, 2003). Different design approaches are given and common structural analysis software products are used to aid in the design of the structure to minimize the possibility of progressive collapse. Advance numerical tools, such as finite element (FE), are seldom used as it is computationally expensive and time consuming to model the entire structure for progressive collapse.

Tan (2010) characterized an isolated reinforced concrete beam-column connection without slab and transverse beams under monotonic loading via advanced nonlinear FE analysis using continuum and structural base elements. The mechanical behavior of the beam-column connection as a whole is expressed in term of its moment versus (vs) rotation relationship, and a simplified connector model had been developed to represent the behavior of the beam-column connection.

### **Objectives and Scope**

The objective of this research is to study the behavior of reinforced concrete beam-column connection under monotonic loading. The focuses of the research will be on the followings:

- Overall load-rotation behavior of the beam-column connection including the contribution from slab, transverse and spandrel beam using a predominantly continuum typed FE model.
- To develop an alternative simplified structural elements based FE model to represent the load-rotation behavior of the interior beam-column connection system.

The scope of this research is limited to the followings:

- Geometric dimension and reinforcement details of an interior connection of a building (test structure) that was tested for progressive collapse under abnormal loadings in October 2010 will be used.
- The effect of the slab on the beam-column connection based on an assumed effective flange/slab width.

- Torsional effects of the slab in both in-plane and out of plane directions are ignored.
- Other types of reinforced concrete connections (external beam-column or wide beam connections, etc.) were not considered.

### **Research Significance**

The simplified structural elements based FE model could be use for the analysis of progressive collapse in buildings. Significant time and cost saving could be achieved as compared to traditional progressive collapse assessment conducted using the predominantly continuum based FE model. The simplified FE model can be used as a fast preliminary tool to check for the potential of progressive collapse of a certain building structure, or as an additional check to complement the building design based on current guidelines.

## CHAPTER 2 BACKGROUND AND LITERATURE REVIEW

### **Overview**

A beam-column joint is defined as that portion of the column within the depth of the deepest beam that frames into the column (ACI Committee 352, 2002). In most structural concrete frames, the joint size is often limited by the size of the adjacent structural members connecting to it. Due to this constraint in dimensions and coupled with poor reinforcement detailing, the strength and ductility of the connection may be significantly reduced as compared to the adjacent primary structural components. The joint might be a point of weakness within the whole structural frame. Thus, it is crucial to understand the complex forces and transfer mechanisms that happen within the joint to enable a proper design or detailing of the reinforcement in joint.

This chapter will touch on the basic beam-column connection types, the force transfer mechanism, the effect of the slab and transverse beam on the connection and various proposed analytical models for the beam-column-slab connections. It will also look into material models, assumed effective flange/slab width of the main longitudinal beam, various experimental tests by other researchers and a review of the advance numerical model used in this research. A review of progressive collapse design guidelines will also be presented.

### **Beam-Column Connections**

Four typical beam-column connections (slabs are not shown for clarity) are shown in Figure 2-1. In accordance to ACI Committee 352 (2002), the connections are classified into two categories. Type 1 connection is composed of those members that are designed to ACI Committee 318 (2008) strength requirements without significant

inelastic deformation. While for Type 2 connection, frame members are designed to be able to sustain their strength under reversal of deformations into the inelastic domain.

### **Two-Member Connection/ Knee Connection**

A two-member connection is commonly found at the corner of a portal frame structure. The connection may be subjected to either opening or closing load in which the connection that is under opening loads will be more severely affected by cracking.

Large tensile stresses developed at the reentrant corner and in the middle of the connection which resulted in diagonal cracks due to the prying action of the opening load are shown in Figure 2-2 by MacGregor and Wight (2005).

Nilsson and Losberg (1976) showed that with proper detailing, the efficiency of a connection can be significantly increased. Efficiency of connection is defined as the ratio between the measured and the theoretical moment capacities. In Figure 2-3 connection detail B, with the additional of hook bars and diagonal bar enclosing the concrete core, the efficiency of the connection increased to 123%. The double hook bars and the diagonal bars helped to resist the tensile stresses that had developed diagonally across the middle of the connection and the reentrant corner respectively. The bars limit the width of the cracks and thus enhanced the strength of the connection. In addition, the diagonal bars assist in the confinement of the concrete core of the connection which further improves its strength and ductility.

For large knee connection, Park and Paulay (1975) suggested to use radial bars to resist all the diagonal tensile stresses in the middle of the connection as shown in Figure 2-4. In addition, diagonal bars equal or larger than half of the limiting flexural longitudinal steel  $A_{s1}$  is provided to serve as an anchor point for the radial bars and to

limit the propagation of the diagonal crack which originated from the reentrant corner.

The area of one radial hoop is given by:

$$a_{sj} = \left[ \frac{f_y}{f_{yj}} \sqrt{1 + \left( \frac{h_1}{h_2} \right)^2} \right] \frac{A_{s1}}{n} \quad (2-1)$$

Where  $f_y$ ,  $f_{yj}$  is the yield strength of the flexural bar and radial bars respectively,

$h_1$ ,  $h_2$  is the column and beam depth respectively,  $A_{s1}$  is the area of the bottom beam steel which is assumed to limit to the magnitude of moment applied to the connection and  $n$  is the number of legs provided.

### **Three-Member Connection/ T-Connection**

A three-member connection or T-connection is usually located at the exterior beam-column connection, at the base of retaining wall and at the roof beam-column connection.

The flow of forces and detailing within the T-connections are illustrated in Figure 2-5 by MacGregor and Wight (2005). Figure 2-6 shows the results from the tests performed by Cook and Mitchell (1988), where the joint efficiency is plotted against the steel reinforcement ratio  $\rho$ . The cross represents the connection detail B and the triangle represents the connection detail C as presented in Figure 2-5. Connection detail C is able to contain the diagonal crack that occurred in the middle of the connection better and thus able to achieve a joint efficiency of 80% to 110% versus that of 24% to 40% for connection detail B.

## **Four-Member Connection/ Interior Connection**

A four-member connection is an interior connection with beams framing into it from all sides of a column. The connection needs to be designed for all the forces that may act on them (e.g., axial load, bending moment, torsion and shear etc.). The forces within a connection would vary as a result of the different type of loadings (such as gravity or lateral load) as represented in Figure 2-7 by Nilson et al. (2004). For lateral loading, Nilsson (1973) suggested that tensile crack will occur across the diagonal if the tensile resultant  $\sqrt{2}F_s$  is greater than the tensile strength of the concrete as shown in Figure 2-8. This lateral load case was not tested by Nilsson.

### **Connection Behavior**

It is critical to understand the behavior and force transfer mechanism within a connection. This is to ensure that the connection will be well designed and adequately detailed to achieve its design performance. Different models that attempt to represent the complex mechanism at play at the connections are available. Two such models would be presented in the following sections.

### **Compressive Strut and Truss Mechanism Model**

Park and Paulay (1975) idealized the behavior of a connection under shear forces as a combination of two separate resisting mechanisms. The two mechanisms are the diagonal concrete compressive strut action and truss action as shown in Figure 2-9. The diagonal concrete compressive strut action is formed by the compression and shear forces that act at the boundary of the connection due to beams and column as represented in Figure 2-9 A. The truss action is formed by the bond stress transfer between beam and column longitudinal reinforcement as shown in Figure 2-9 B. It was

suggested that each bond force components across a small length of the connection needs to maintain equilibrium. The equilibrium is maintained by diagonal compressive struts (via concrete between the diagonal cracks) and vertical/horizontal tensile forces (from the uniformly distributed lateral reinforcement).

The shear resistance effect for each mechanism is assumed to be additive and thus the total shear resistance in the joint is:

$$v_j = v_c + v_s \quad (2-2)$$

Where  $v_j$  is the total joint shear resistance,  $v_c$  is the joint shear resistance provided by the diagonal compressive strut and  $v_s$  is the joint shear resistance provided by the lateral reinforcement due to truss action.

### **Strut and Tie Model**

Strut and tie model has been used successfully as a basis for the design of D-region in beams. Nilson et al. (2004) suggested that the same basis can be applied to describe the behavior of a connection as shown in Fig 2.10. Counterbalancing moments are produced at the column and beam due to lateral load (seismic load) applied to the connection of a frame. The line of action of the vertical forces intersects the line of action of the horizontal forces at two diagonally opposite corners of the joints. This intersection creates a single diagonal compressive strut across the middle of the connection. The tension bars at both the column and the beam members needs to be properly anchored to ensure the adequate development of the bar's yield strength. The tension force assumed is the yield force achieved by the reinforcement bars. The main function of the column ties in the connection is to provide restraints to the outward buckling of the column longitudinal bars. They also help in improving the confinement

effect of the core thus enhancing both ductility and strength of the connection.

Furthermore, the column ties, help to limit the cracking caused by the diagonal tensile stresses perpendicular to the diagonal compressive strut.

### **Beam-Column-Slab Subassemblage**

The different types of connection and the connection behavior had been reviewed in the preceding sections. An important part of a beam-column connection involves the interaction of the slab and the transverse beam on the behavior and performance of the connection. In a ductile frame design, North America design codes adopt a “strong column and weak beam” design philosophy. According to this philosophy, members framing into a connection are designed so that the plastic hinge forms on the beams, thus ensuring that the main load carrying columns don’t yield or fail first. A flexural strength ratio  $M_r$  is used to gauge the relatively flexural strength of the columns versus that of the beams. ACI Committee 352 (2002) provisions, section 4.4.2 states that for Type 2 connections that are part of the primary seismic resistance system, the  $M_r$  calculated using factored axial load, should not be less than 1.2.

$$M_r = \frac{\text{Sum of all the flexural strength of top and bottom columns}}{\text{Sum of the flexural strength of the longitudinal beams}} \quad (2-3)$$

One of the critical aspects that affect the sequence of yielding is the determination of the flexure strength of the beams. According to ACI Committee 318 (2008) provisions, to calculate the flexure strength of the beams under positive moment, an effective slab width is assumed to be part of the flange of the beam contributing to the compression resistance. The compressive contribution from the slab reinforcement is ignored. However, the code does not contain any provision for the effective slab width under negative moment. It ignores the slab’s steel tension contribution to the flexure

capacity of the beam when the slab is in tension and the beam is essentially designed as a rectangle section. The beam negative flexural capacity needs to be reasonably estimated to ensure that it will yield before the column member or else there will be a shift in the sequence of yielding, leading to potential collapse.

The following sections will elaborate on the effects of the presence of slab, transverse beam, the force transfer mechanism of a beam-column-slab connection, factors affecting the slab contribution to flexural strength of the beam, joint shear behavior, suggested effective slab width for negative moment, FE models and presents some test results from past experiments.

### **Effect of Slab on Flexural Strength**

Ma et al. (1976) tested some beam-column subassemblages under cyclic loading. It was observed that the flexural capacities of those specimens that included the slab had 20% to 30% higher negative flexural moment capacities than those specimens with rectangular beam section only. Thus effect of slab significantly enhanced the flexural strength of the specimens.

A seven story reinforced concrete full scale structure was tested under lateral loads (seismic) at the Building Research Institute in Japan (ACI, 1984). It was found that the measured base strength was around 70% higher than the calculated value. It was concluded that the major contribution of the differences between the measured and calculated base shear is due to the contribution of slab reinforcement in tension under negative moment.

Durrani and Zerbe (1987) tested six exterior beam-column-slab subassemblages under cyclic loading. They were investigating on the effects of transverse beam and slab width on the performance of the connection. It was observed that considerably

higher negative flexural capacities in the range of 70% were achieved for those specimens with slab.

In summary, the presence of the slab reinforcement in tension under negative bending moment contributes to higher flexural strength of the longitudinal beam.

### **Effect of Transverse Beam**

Ehsani and Wight (1985) observed from exterior beam- column-slab subassemblage tests that the joint transverse reinforcement strains in specimens with transverse beam and slabs were lower than those without. This observation suggested that the effective volume of the joint resisting the joint shear is enlarged by the presence of the transverse beam, thus reducing the shear stress demand of the hoops. In addition, the shear cracks width in the joint is limited due to the improved confinement effect.

Similarly, Durrani and Zerbe (1987) subjected 6 exterior connection subassemblages to lateral load and observed that the spandrel beams are only effective in providing the confinement effect to the joint core before the spandrel beam reached its torsional capacity. The confinement effect decreases rapidly once the torsional capacity of the spandrel beams were exceeded which was collaborated by the swift increase in the strain of the joint reinforcement measured.

Kitayama et al. (1991) subjected five interior connections with different configurations to lateral loads. It was observed that the specimen with transverse beams and no slab had achieved higher joint shear strength of approximately 20% more than that of specimen without both the transverse beams and slab. The enhancement in joint shear strength is attributed to the confinement effect presented by the additional transverse beams to the joint core.

## **Force Transfer Mechanism**

A beam-column-slab subassembly connection is subjected to internal forces that arise due to the various loads that act on the primary members that frame into its connection. Figure 2-11 (slab is not shown for clarity) by Wang et al. (2007); portray some of the forces such as axial loads, moments, shears and torsion that can act on the primary members.

A beam-column-slab subassembly when subjected to lateral loads (seismic load), generally developed tensile strains in the slab reinforcements bent under negative moment. The slab reinforcement tensile strain varies along both the transverse and longitudinal beam directions as shown in Figure 2-12 by Durrani and Zerbe (1987). The strain decreased as the distance increased from the longitudinal beam along the transverse beam direction. Vice versa, the strain decreased as the distance increased from the transverse beam along the longitudinal beam direction.

## **Interior connection**

Flexural deformation of the longitudinal beam initiates the tension contribution of the slab reinforcement when it is subjected to a negative bending moment. As the top surface of the beam lengthens along the beam length, plane shear stress is generated at the side interface between the beam web and slab. The shear stress transfers the longitudinal beam strain to the slab and thus engages the slab steel reinforcement in tension along the transverse beam as shown in Fig 2.13 by French and Moehle (1991).

Due to moment equilibrium of the isolated subassembly slab panel which is bounded by both the longitudinal and transverse beam, similar orthogonal tension forces are required that varies along the longitudinal beam as shown in Figure 2-14 B by French and Moehle (1991).

Ammerman and French (1989) summarized the results of the four test series on RC beam-column-slab connections and discussed the method of force distribution for the interior connection subjected to lateral load (seismic load). It was observed from the tests that, a state of slab-in-tension (S-T) and slab-in-compression (S-C) exists on opposite sides of the column due to the lateral load.

French and Moehle (1991) provided a clearer representation of the force transfer as discussed by Ammerman and French (1989) above. For S-T case, the top of the beam web and the slab reinforcement will be subjected to tensile forces while the bottom of the beam will be under compression as shown in Figure 2-15 C. Due to the need for equilibrium, a large amount of the tensile forces produced on the side of the S-T are resisted by the tensile forces provided by the slab reinforcement on the S-C side as shown in Figure 2-15 B. The remaining unbalanced forces are carried by the column. Although the slab in the S-C side is theoretically compression in nature, it is subjected to tensile forces instead as a result of the force transfer nonetheless. The tensile forces on the slab on the S-C side are then passed onto the longitudinal beam by shear. These shear forces which occurred at the interface between the beam web and slab are resisted by the flexural beam compressive force, which in term equilibrates the flexure tension force at the bottom of the beam web as presented in Figure 2-15 C.

Suzuki et al. (1983) suggested that the tensile forces that have developed at the S-C side of the slab reinforcement have a tendency to lessen the torsional moments imposed on the transverse beam. This may be due to the reduction of the net slab reinforcement tension force as a result of the counteracting tensile forces that occurred in the slabs on both sides of the transverse beam. Joglekar (1984) confirmed this in

tests where lower levels of twist were measured on the transverse beam of interior connections as compared to that of exterior connections for the same lateral load. He also observed that none of the transverse beam from the interior connection specimens failed in torsion.

### **Exterior connection**

Figure 2-16 shows the flow of forces at the exterior connection (Paultre et al., 1989). Similar to the interior connection, the flexural deformation of the beam caused tension forces in the slab reinforcement when subjected to negative moment. The slab reinforcement tension force would act about the shear center of the transverse beam and induced a torsional moment. The torsional moment in turn produced torsional shear at the interface of the connection and would interact with the net joint shear force (from longitudinal beam bars, slab bars tension force and column shears etc).

As the torsional moments at the external transverse beam were not mitigated by the tensile forces that were present in the slab of the S-C side of an interior connection, the transverse beam might be susceptible to torsional failure. This was observed for most of the exterior beam-column-slab specimens tested by Zerbe and Durrani (1985).

### **Continuous frame**

Cheung et al. (1991) proposed a force transfer mechanism for cracked concrete slab at both external edge and interior panels of a continuous frame structure subjected to lateral loads (seismic). For external edge panels as shown in Figure 2-17, extensive diagonal crack occurred in the slab panel. The shear resistance of the transverse beam is assumed to be negligible. In order to maintain equilibrium of forces, a diagonal concrete compression force ( $D$ ) and also tension forces ( $T_x$  and  $T_y$ ) in both the

longitudinal and transverse slab steel reinforcement needs to be developed in the slab. These forces can be simplified into a strut and tie model.

This mechanism is further explored to explain the force transfer within the internal panels of the frame structure where it was observed that the cracks formed were in the transverse direction (vertical up) as presented in Figure 2-18. The vertical transverse crack suggested that no shear deformation occurred within the internal panels. The longitudinal slab steel reinforcement act as tension ties, while the beam concrete web act as compression strut to form a strut and tie mechanism.

### **Slab Contribution to Flexural Strength of Longitudinal Beam**

In structures where the longitudinal beams are subjected to negative moments due to lateral loading, the slab reinforcement acting in tension has been found to increase the beam negative flexural capacity substantially. The slab contribution to this increase of beam flexural strength is dependent of several variables. This section will highlight some key variables such as the type of connections, lateral deformation level, load history, boundary conditions and continuity, shear deformation and slab rotation that influence the amount of slab participation.

#### **Type of connections**

The type of connection (interior or exterior) affects the slab contribution to the flexural strength of the longitudinal beam. As shown in the preceding section, tensile strains developed in the slab reinforcement under negative moment will generate tension force in the slab. In the case of the exterior connection, the spandrel/transverse beam is the only structural element available to resist the slab reinforcement tension force. The spandrel beam will bend in the weak axis of the beam cross-section and twist about the vertical axis of the beam due to torsion as shown in Figure 2-19 and Figure 2-

20 respectively by Franco et al. (1995). Thus the stiffness of the transverse beam plays a vital part on the effect of slab participation in the exterior connection.

It has been observed by Durrani and Zerbe (1987) that large torsional crack was formed at the side of the spandrel beam as loading increased. The crack spiraled around the top surface of the beam and connects with the flexural crack in the longitudinal beam at the front face of the column, causing the specimen to split into two parts, as shown in Figure 2-21. It was suggested thus that only a certain width of the slab (effective slab width) contributes to the flexural strength of the longitudinal beam.

The effective slab width is limited by the torsional capacity of the spandrel beam. For connections where the spandrel beams have reached their torsional capacity, the effective slab width is equal to the column width plus twice the depth of the spandrel beam.

For an interior connection subjected to lateral load, the typical deformation behavior is shown in Figure 2-22 (Shahrooz et al., 1992). Slab on each side of the transverse beam will alternate between tension and compression. Qi and Pantazopoulou (1991) reported that the cracking patterns observed in the interior transverse beam is less severe, even when the extent of the slab participation is more than that of the exterior connection. This suggests that the internal transverse beam experienced lower stresses as compared to those of the spandrel beam. This suggestion is supported by lower stirrup strain measurements for the interior beams as compared to the external beams, as reflected in Figure 2-23.

The differences in the stirrup strain experienced by the interior and exterior transverse beams can be attributed to the transfer mechanism as previously described

by Figure 2-15. For the interior transverse beam, the slab tension forces that developed on the S-T side of the transverse beam are partly balanced by the slab tension forces developed in the S-C side and the column shear force. Thus, the net tensile forces from the slab reinforcement acting on the interior transverse beam would be greatly reduced as compared to that experienced by the spandrel beam. In addition, due to the presence of slabs on both sides of the beam, the torsional stiffness of the interior transverse beam is enhanced and the shear center is raised significantly closer to the slab. This results in a lower overall torsional moment experienced by the transverse beam in the interior connection.

### **Lateral deformation**

The slab tensile strain generally increased with increasing load or connection deformation. For seismic loading, the magnitude of deformation is measured as a function of the inter-story drift, which is the relatively displacement  $\Delta_e$ , between two floors when subjected to lateral load as shown in Figure 2-24 (Cheung et al., 1991). The inter-storey drift generally increased with increasing lateral load applied.

Kurose et al. (1991) indicated that the slab contribution to the negative bending moment resistance generally increased with increased drift. The increased in the slab effective width, with increasing drift angle is evident as shown in Figure 2-25 for all the three specimens tested.

### **Load history**

French and Boroojerdi (1989) tested an interior beam-column-slab connection laterally loaded first to a moderate level in one direction and then loaded the same connection in the orthogonally direction. The previous damage due to loading in the first

direction reduced the flexural strength and stiffness of the connection at first; however, with increasing deformation in the orthogonal direction, no reduction in flexural strength and stiffness were observed. It appears that the initial damage to the connection due to the first loading direction has no lasting reduction effect on the flexural strength and stiffness of the connection when loaded in the orthogonal direction.

Cheung et al. (1991) subjected interior connections to both uni-directional and simultaneous bi-directional lateral load via displacement controlled loading. It was observed that for the same imposed displacement ductility, the flexural strength developed during the bi-directional displacement was always lesser than that achieved during the uni-directional displacement as presented in Figure 2-26. The two values within one column represent the range of moments that was observed when the top reinforcement was yielding.

### **Shear deformation**

As presented in Figure 2-27 B, an infinitesimal slab element A is subjected to both shear and tensile force in the case of S-T (Ammerman and French, 1989). The tensile force was produced by the top slab reinforcement as the longitudinal beam undergone deformation. Due to the difference in flexural moments, a net tensile force is produced in the direction of  $T_2$  and is equilibrated by shear forces  $V_1$  and  $V_2$ . The shear forces caused shear deformation to element A as shown in Figure 2-27 C. The shear deformation produced non-uniform strain across the length of the transverse beam, where the longitudinal slab reinforcement strains decreased with increased distance from the longitudinal beam. The normal elastic assumption of plane remaining plane is no longer valid.

Ammerman and French (1989) described on several parameters that affect the amount of shear deformation. Parameters such as i) the slab longitudinal reinforcement ratio, ii) distribution of slab reinforcement and iii) aspect ratio of the slab panel needs to be considered. In general, increasing the amount of slab longitudinal reinforcement ratio, concentration of slab reinforcement at a further distance from the column and increasing the slab width to length aspect ratio will lead to larger shear stresses and more shear deformation. The increase in the shear deformation would enhance the degree of non-uniformity of strain distribution across the slab and result in the reduction of the slab effective width's participation to the flexural strength of the longitudinal beam.

### **Rotation of the slab**

Suzuki et al. (1983), French and Boroojerdi (1989) have all observed that the transverse slab reinforcement strains generally have the opposite trend to that of the longitudinal slab reinforcement strains. The longitudinal slab reinforcement strains decreased as the transverse distance increased from the longitudinal beam, previously shown in Figure 2-12. On the contrary, the transverse slab reinforcement strains increased as the longitudinal distance increased from the transverse beam, as shown in Figure 2-28 (French and Boroojerdi, 1989). The presence of this opposite trend of the strain distribution for the steel reinforcement suggested that the slab rotates about the vertical axis.

Figure 2-29 shows the forces and stresses experienced in the slab on the S-T side (Ammerman and French, 1989). Tensile forces that developed in the slab along both the transverse beam and longitudinal beam generated a net slab rotation about point K. This slab rotation act to further reduce the magnitude of the longitudinal slab

reinforcement strain, thus also reducing the slab width's participation to the longitudinal beam flexural strength.

### **Boundary condition and continuity**

The previous sections dealt primarily with the effect of the slab contribution based on isolated subassemblages. It has been shown that there are significant differences in the behavior between an isolated subassemblages and a continual structure. The continual structure is a better representation of an actual building. Crack patterns between these two systems shows the apparent differences, as presented in Figure 2-30 (French and Moehle, 1991). Diagonal crack originated near the column and propagated diagonally across the slab for the isolated subassemblages as compared to the uniform vertical crack in the transverse direction for a continual structure.

French and Moehle (1991) summarized the difference in the general behavior of the isolated and continual beam-column-slab connections. It was suggested that the effect from the free slab boundaries was most significant in creating the differences in behavior between the two tested systems. The free slab boundaries affect slab shear deformation, slab rotation and flexural deformation which ultimately influence the flexural strength of the longitudinal beam.

Shear deformation and rigid body rotation of the slab for isolated subassemblages had been dealt with in the preceding sections. In a continuous structure, like in an actual building, shear distortion and rigid slab rotation are unlikely or greatly minimized, as they are restrained by adjacent slabs to ensure compatibility with the surrounding structural components.

Ammerman and French (1989) have shown the differences in the slab curvature due to slab flexural deformation between the two systems. For the isolated

subassemblages where two edges of the slab were not restrained when lateral loads were applied, the free ends of the slab have the tendency to uplift. The unrestrained edges of the slab will move upward relative to the longitudinal beam to produce non-uniform curvature across the slab, as shown in Figure 2-31A. For the tested continual structure, slab edge continuity for one side was achieved with an additional end beam. The additional restraint provided by the end beam produced a more uniform curvature along the length of the main beam, as presented in Figure 2-31B.

Qi and Pantazopoulou (1991) tested the response of a reinforced concrete frame under lateral load and observed that the longitudinal slab reinforcement strain is more uniform for a continual structure (See Figure 2-32), as compared to that of the isolated subassemblages that were presented in Figure 2-12. The general trend where the slab reinforcement strain decreased as the transverse distance from the longitudinal beam increased is still the same for both the systems.

However, this is not the case for the transverse slab reinforcement strain. For continuous structure, the transverse slab reinforcement strains were at maximum near the column but reduced toward the midspan of the longitudinal beam, as observed from test conducted by Yoshimura and Kurose (1985). This is presented in Figure 2-33, and it is contrary to that of the isolated subassemblages where the maximum slab bars strain is located furthest away from the column, as shown in Figure 2-28.

The overall effect of the increased restraints posed by the continual structure suggests that the slab contribution may be larger in this type of structure than that of an isolated subassemblage system. The larger slab contribution is due to the more

uniform longitudinal slab reinforcement strain produced and would thus increase the longitudinal beam flexural strength as a result.

### **Joint Shear Behavior**

Qi and Pantazopoulou (1991) evaluated the average joint shear stresses in the beam-column-slab joints of a reinforced concrete structure subjected to lateral load. They found out that the joint stresses were well below the limits recommended by ACI-ASCE committee 352 (1985). The joint stresses were similarly lower than the limits as spelt out by ACI-ASCE committee 352 (2002). It was estimated that a substantial amount of the total joint shear stress were due to the torsional shear stresses generated from the transverse beam when subjected to the longitudinal slab reinforcement tension force. The torsional shear stresses are approximately 32.5% and 55% of the total joint shear stresses for interior and exterior connections respectively.

From Figure 2-34 presented by Kitayama et al. (1991), by comparing the different combination of structural elements, it was evident that the joint shear strength increased with each additional structural element added to specimen A. The maximum joint shear strength was achieved with specimen D with the inclusion of both the slab and the transverse beam into the connection.

As presented in Figure 2-35, Cheung et al. (1991) hypothesized that the tensile forces generated from the slab reinforcement are resisted by the beam concrete compression zone force  $C_x$ . The force  $C_x$ , when combined with the corresponding vertical compression force from the column  $\Delta C'_c$  formed a diagonal compressive strut within the joint core. The diagonal compressive strut would be capable of resisting the additional horizontal and vertical shear forces that developed due to the inclusion of the

slab without the needs of any additional joint lateral reinforcement. Although the joint seems to be of no danger of failure through the increase in joint shear due to the inclusion of the slab, there is still a possibility that the joint might fail instead due to the shear compression failure of the diagonal compressive strut.

ACI committee 352 (2002) recognized the increased contribution of joint shear from the slab and revised the design joint shear,  $v_u$  requirements. The design horizontal joint shear is calculated at a mid-height plane of the joint. It accounts for all the shear forces, tension and compression forces from the beam and slab reinforcement at the boundaries of the joint as presented in Figure 2-36.

### **Formulation of Effective Flange Width/ Effective Slab Width**

It had been reviewed earlier that the flexural strength of the beam-column-slab connection is dependent on the contribution of the slab reinforcement in negative flexural moment. Different researchers used different reference points and definitions for the effective flange/ slab width. Figure 2-37 shows the notation used in this study to describe the effective flange width.

Due to the non-uniform longitudinal slab reinforcement strain distribution, the useful assumption that plane remains plane is not longer valid. In order to simplify the calculation of the flexural strength of the longitudinal beam including the slab reinforcement contribution, it is more convenient to define an effective flange width. Pantazopoulou et al. (1988) defined the effective flange width as the length for which the plane remains plane assumption can be assumed for both the beam and slab cross-section. The effective flange width assumption results in the same resisting moment for the same curvature, as shown in Figure 2-38.

The effective flange width influences a number of key parameters as summarized by Franco et al. (1995).

- The flexural strength ratio  $M_r$  may be underestimated if the effective flange width is underestimated during the design stage.
- The desired sequence of yielding based on the “strong column and weak beam” design philosophy may be affected if the slab contribution is underestimated. The column might yield instead of the beam.
- The increased in the negative flexural strength of the longitudinal beam may significantly reduce the ductility and energy dissipation capabilities of the beams.
- An increased in the effective flange width would result in larger shears in the joint and the beam, could result in premature shear failures.

ACI Committee 352 (2002) section 3.32 states that for Type 2 connection where the slab is monotonically casted with the beam, the effective flange width  $b_e$  for all connections (except exterior and corner connection without transverse beams) should adhere to that prescribed by ACI Committee 318. As per ACI Committee 318 (2008), section 8.12.2 for T-beam, the effective flange width  $b_e$  and the protruding effective flange width,  $b_f$ , are limited by the followings:

- $b_e \leq L/4$
- $b_f \leq 8t$  and
- $b_f \leq 0.5 S_1$  or  $S_2$

French and Boroojerdi (1989) measured the moments achieved for the interior subassemblages at 2% inter-storey drift and ultimate load for three specimens, shown in Figure 2-40. They compared the measured moments with the estimated moment capacity calculated from three different effective flange widths as shown in Figure 2-41. For the beam width case, the calculated longitudinal beam flexural strength is based on the beam web only. In the case of the ACI width, it is based on the superposition of two

components. The first component consists of the effective width prescribed for the slab in compression as mentioned in ACI Committee 318 (2002) section 8.10. The second component consists of the remainder of the slab (not considered to be effective flange of the beam) which acts independently and contributes to the longitudinal beam flexural strength. The approach in the second component was used simply as an empirical method to account for the non-linear strain distribution across the slab reinforcement. Lastly, the flexural strength from the available full slab width is computed.

The ultimate flexural strength measured under negative moments ranges between the moment capacities calculated for the ACI width and the full slab width. It corresponded approximately to 80% of the full slab width. In addition, the measured moments at 2% inter-storey drift were also evaluated. It was observed that the measured moments correlated well and is within 10% of the moments calculated from the ACI width for interior connections with reasonably torsional stiff transverse beam (Specimen 2 and 3).

Pantazopoulou and Moehle (1990) observed from the results of quarter scale frame structure test conducted by Qi (1986) that the effective flange width varies for interior and exterior connection. For interior connection, the protruding flange width from each side of the beam web is 1.6 times the beam effective depth at yield moment and 3 times the beam effective depth at ultimate moment. As for the exterior connection, the protruding flange width at yield moment is similar to that of the interior connection. However the flange width did not increase with increasing connection deformation.

Cheung et al. (1991) suggested that the effective flange width  $b_e$  in tension may be taken as the lesser of the following, as shown in Figure 2-42:

- One quarter of the span of the beam in the affected direction, extending from each side of the beam center.
- One half of the transverse span of the affected beam, extending from each side of the beam center.
- For exterior connection, one quarter span of the transverse span of the affected beam, extending from each side of the beam center.
- For exterior connection without transverse beam, one half of the column width, extending from each side of the beam center.

The effective flange widths suggested from different experiments for interior connection are summarized below in Table 2-1. An arbitrary beam and slab length dimension is assumed for the computation of the effective flange width. Longitudinal and transverse beam span length: 354", width of beam web: 12", height of beam: 21.75", slab thickness: 10" and beam effective depth: 19.25".

Exterior connections are excluded as their effective flange width is highly dependent on the torsional stiffness of the spandrel beams and thus varies significantly from case to case.

### **Modeling of Beam-Column-Slab Subassemblages**

Various analytical models have been proposed by researchers to model the behavior of the slab contributions for the enhancement to the flexural strength of the longitudinal beam.

Pantazopoulou et al. (1988) proposed a simple closed-form model to account for the effect of slab on the negative flexural moment capacity of the longitudinal beam. The model is valid for interior connection with assumed rigid transverse beams (both in torsion and weak axis bending). The model assumed all the inelastic flexural deformation in the beam and the slab occurred within a length equal to the effective beam depth  $d_b$ , along the length of the main longitudinal beam. The beam and slab are

assumed to deform in the same magnitude to ensure strain compatibility. In addition, to simplify the computation effort, the non-linear longitudinal slab reinforcement strain distribution across the transverse beam is replaced with an idealized effective flange width (see Figure 2-38). The idealized effective flange width is used so that the plane remain plane assumption can be used. The model consists of rigid links connecting the longitudinal beam bars to the slab reinforcements at the transverse beam, as presented in Figure 2-43.

The diagonal rigid links approximate the relatively stiff in plane action of the concrete and slab reinforcement interaction. As the beam deformed, the rigid link will also deform by a certain length in the direction of the link generating tension force that is transmitted to the longitudinal slab rebar. Comparing the moment-deformation relations with experimental results, the model showed good correlation throughout the deformation range.

Shahrooz et al. (1992) improved on the preceding model by Pantazopoulou et al. (1988). The previous model overestimated the extent of slab contribution in connection, for flexible transverse beam and was unable to simulate the longitudinal slab steel strain distribution under excessive bond slip. This proposed new model, as shown in Figure 2-44, relied on better kinematic formulation which enhanced the compatibility conditions at the connection. It accounts for the transverse beam displacement from both flexural and torsional deformations such as in plane deflection  $\delta_i^t$ , (due to weak axis bending), displacement of slab reinforcement due to bond slip  $\delta_i^s$ , elongation of the transverse beam  $\delta_i^T$  and the longitudinal beam deformation  $\Delta p$ . This proposed new model works well for both interior and exterior connections.

Franco et al. (1995) suggested a strut-and-tie model to estimate the effective flange width of an exterior connection after torsional cracking of the spandrel beam. The effective flange width is essential to estimate the flexural moment capacity of the longitudinal beam under negative bending moment. As the torsional stiffness of the spandrel beam decrease significantly after cracking, a different mechanism is present to resist the additional load. The strut-and-tie model, as presented in Figure 2-45, is formed with the outer most longitudinal transverse beam reinforcement acting as the tension chord. The slab concrete acts as compressive strut (dashed lines), while the longitudinal slab reinforcement acts as vertical tension ties.

The protruding flange width from each side of the beam can be calculated from Equation 2-4. It is determine by equating the moments about a nodal point at the column, while limiting the forces of both the slab reinforcement and the longitudinal transverse beam bars to their respectively yield forces. Comparison with experimental results produced good estimates of the amount of the effective slab reinforcement.

$$\frac{A_s^* f_{ys}}{S_s} (x) \left( \frac{x}{2} \right) = A_{sl} f_{yt} (0.8 c) \quad (2-4)$$

Where  $A_s^*$  is the area of slab reinforcement within a spacing of  $S_s$  ;  $f_{ys}$  and  $f_{yt}$  is the yield stress of slab and transverse beam longitudinal reinforcement respectively;  $x$  is the protruding flange width;  $A_{sl}$  is the area of the transverse beam longitudinal reinforcement and lastly  $c$  is the column dimension.

## Experiments and Test Results

Ammerman and French (1989) summarized the results of four test series conducted on reinforced concrete beam-column-slab subassemblages. The four test series are, as follows (see Figure 2-46).

- Suzuki et al. (1983) - where one half scale subassemblage (UTo) with nipped corner slab which represented interior connection was tested. UTo have lower slab reinforcement (around 50% lower) than specimens from other test series (See Figure 2-46A).
- Jogkekar (1984) - four full scale subassemblages which represented both interior (TIP and TIM) and exterior connections (TEP and TEM) were tested. TIM and TEM are modified models with higher longitudinal beam and column reinforcement ratio than their respective control model TIP and TEP. These specimens come with end beams at the far end of the longitudinal beam to account for the effect of boundary conditions on moment capacity of the main beam (See Figure 2-46B).
- Zerbe and Durrani (1985) - four subassemblages (J4-J7) which represented exterior connections were tested (See Figure 2-46C).
- Ammerman and French (1988) - three half scale subassemblages (EW1-EW3) which represented interior connections were tested. The torsional stiffness of the transverse beams is varied to study its effect on the moment capacity of the longitudinal beam (See Figure 2-46D).

The beam and the slab configuration used in the various test series are reflected in Table 2-2. Beam bars size varies from United State (US) Number (No.) 2 to US No. 7 while the slab reinforcement varies from US No. 2 to US No. 4. Similarly, Table 2-3 presents the properties of the reinforcement used with the yield strength of the reinforcement varying from 48 ksi to 77 ksi.

Figure 2-47 presents a comparison plot of normalized moment and normalized torsional stiffness of interior subassemblages from the various test series. The moment presented is based on the sum of the measured moment and the moment due to the self weight of the beams and slab. There is a need to normalize both the moment and torsional stiffness due to the differences in geometric and material properties of the

specimens from the various test series. The moment is normalized by dividing the combined moments (measured and self weight's contribution) with the calculated ultimate moment capacities. Full slab width is assumed in the negative flexure capacities calculation and ultimate concrete compression strain of 0.003 is used. Similarly, the torsional stiffness is normalized by dividing the torsional stiffness (assumed elastic behavior) of the transverse beam with the flexural stiffness (assumed cracked section) of the main longitudinal beam. This ratio give an indication of the relatively distribution of the column moment between the transverse and longitudinal beams.

It appears that there is a general trend for the moment capacities to increase when the torsional stiffness increases. This result suggests that the torsional rigidity of the transverse beam plays a significant part in the moment capacities as it increases the slab participation. However, the enhancement in moment capacity is more pronounced in the lower torsional stiffness zone (for specimens EW1 to EW2) than the specimens (EW2 to EW3) within the higher torsional stiffness zone. It appears that specimens EW2 and EW3 have relatively uniform moment capacity.

It was stated by Ammerman and French (1989) that it was uncertain if the higher moment capacities developed by the TIP and UTo specimens can be attributed to a higher torsional stiffness or results of other parameters. This is because both tests did not have an equivalent control specimen to compare the results with, unlike that presented in the EW1 to EW3 test series. The higher moment capacity obtained for TIP specimen was suggested to be as a result of the boundary condition. The interior connection of the TIP specimen come with end beams at the far end of the longitudinal

beam, which helps to produce a more uniform tensile strain across the longitudinal slab reinforcement. For the UTo specimen, it achieved the highest moment capacity with the least amount of slab reinforcement (around 50% less) as compared to other specimens. It was suggested by Ammerman and French (1989) that the presence of lower slab reinforcement, which reduced the amount of shear deformation in the slab, produced a more uniform slab reinforcement strain distribution. The uniform slab reinforcement strain distribution thus leads to more slab participation and enhanced the flexural strength of the beam. Furthermore, the reduction in shear deformation in specimen UTo seems to have a more significant effect on the slab strain distribution, than that from the stiffer boundary condition (with end beams) in the TIP specimen. This is suggested as the moment capacity achieved by UTo is higher than that of TIP.

From the above mentioned test series, it could be observed that the flexural moment capacity of the main longitudinal beam is affected by torsional stiffness of the transverse beams, the boundary condition, and the shear deformation of the slab.

### **Plastic Hinge**

Based on the “Strong Columns and Weak Beams” design philosophy, plastic hinging on the beam is encouraged and designed for. Uma and Prasad (2006) stated that through proper detailing, the inelastic deformation of the beam at the plastic hinge location can be catered, however the same inelastic demand cannot be sufficiently provided for with column detailing.

A plastic hinge is formed when the RC member has reached the ultimate moment and curvature at the critical section of the RC member. The region where the bending moment exceeds the yield moment of the section is the inelastic region and this region spread along the beam length as the beam deformed. As presented in Figure 2-48

(Park and Paulay, 1975), the shaded area represented the inelastic rotation/curvature that occurred at the plastic hinge location. As the inelastic rotation/curvature was not uniform, it is idealized into a uniform region over a plastic hinge length of  $l_p$  as shown.

With the formation of the plastic hinge, the rotation (elastic and inelastic) of the beam is concentrated at the plastic hinge location. The beam would continue to rotate until it fails and thus the moment resistance of the beam- column- slab connection could be represented by an equivalent moment-rotation curve. In order to compute the rotation of the beam, it is essential to estimate the length of the plastic hinge.

Several empirical equations have been proposed to estimate the length of the plastic hinges. They are presented, as follow:

Sawyer (1964) proposed this expression for the equivalent length of the plastic hinge as:

$$l_p = 0.25d_b + 0.075z \quad (2-5)$$

Corely (1966) suggested the following expression, based on results gathered from simply supported beams that were tested.

$$l_p = 0.5d_b + 0.2\sqrt{d_b}\left(\frac{z}{d_b}\right) \quad (2-6)$$

For both Sawyer (1964) and Corely (1966),

$d_b$  is the effective depth of beam in inches.

$z$  is the clear distance from the critical section to the point of contra flexure.

Paulay and Priestley (1992) provided a good estimate of the equivalent plastic hinge length for cantilever beam, which results in  $l_p \approx 0.5 h$  for typical beam and column properties.

$$l_p = 0.08l + 0.022d_{lb}f_y (MPa) \quad (2-7)$$

$$l_p = 0.08l + 0.15d_{lb}f_y (ksi) \quad (2-8)$$

Where  $l$  is the length of the cantilever.

$h$  is the section depth.

$d_{lb}$  is the diameter of the longitudinal reinforcement.

$f_y$  is the yield strength of the reinforcement.

Conrath et al. (1999) stated that the plastic hinge length due to flexure is about equal to the member's section effective depth  $d$ .

### **Moment-Rotation Formulation for Connections**

The moment-rotation resistance function is generally used to characterize the behavior of connections when subjected to loadings. FE models can be used to simulate this connection behavior and generate the required moment-rotation curve. There exist mathematical formulas that can describe the moment-rotation curve for steel connections. Yim (2007) used Abaqus/Standard (Simulia, 2010) to simulate the resistance function for steel connection and it correlated reasonably well, with that calculated from the Power Model or the Richard-Abbot equation (Richard and Abbott, 1975). Tan (2010) had simulated the behavior of reinforced concrete connection in Abaqus/Standard and suggested that the Power Model might overestimate the moment capacity for the RC connection. A variation of the Power Model could be developed to be used to represent the moment-rotation of RC connections. The modified Power Model could include parameters that reflect the influence of reinforcement details on the moment-rotation of the RC connections and then be utilized to define the spring behaviors in FE models to simulate RC connection behaviors.

$$M = \frac{k_i \theta}{\left\{ 1 + \left( \frac{\theta}{\theta_0} \right)^{n_s} \right\}^{\frac{1}{n_s}}} \quad (2-9)$$

Where  $k_i$  is the initial connection stiffness.

$\theta$  is the rotation.

$\theta_0$  is the plastic rotation.

$n_s$  is the shape factor.

$M$  is the moment.

## Material Models

### Concrete

Concrete is a non-homogenous material which composes of cement, aggregates (sand and gravel) and chemically mixed with water. Cement paste and aggregates individually have linear and brittle stress-strain relationship in compression. However, the mixed product concrete exhibits non-linear and somewhat ductile stress-strain relationship when compressed. This is as a result of the gradual development of micro cracking and redistribution of stresses within the concrete matrix. Concrete is generally much stronger in compression than in tension. The tensile strength of concrete is approximately in the range of 8% to 15% of the compressive strength depending on the types of tensile test adopted.

### Compression stress-strain curve

The typical test for evaluating the strength of concrete involves short-time uniaxial compression tests on plain concrete cylinders (6 inches diameter by 12 inches high).

The typical results are presented in a stress-strain curve, as shown in Figure 2-49 (Macgregor and Wight, 2005).

The modified Hognestad stress-strain curve, as shown in Figure 2-50, is commonly used to represent concrete under compression of up to 6000 pounds per square inches (psi). It consists of a second degree parabola till the apex of the curve at  $f_c''$  followed by a linear descending branch till a limiting strain of 0.0038.

Ascending branch, for  $\varepsilon_c \leq \varepsilon_0$

$$f_c = f_c'' \left[ \frac{2 \varepsilon_c}{\varepsilon_0} - \left( \frac{\varepsilon_c}{\varepsilon_0} \right)^2 \right] \quad (2-10)$$

Descending branch, for  $\varepsilon_c > \varepsilon_0$  and less than 0.0038

$$f_c = f_c'' - E_{cd} (\varepsilon_c - \varepsilon_0) \quad (2-11)$$

Where  $f_c$  is the concrete compressive stress.

$$f_c'' = 0.9 f_c' \quad \text{is the maximum concrete compressive stress.} \quad (2-12)$$

$f_c'$  is the uniaxial concrete compressive strength under standard test cylinder.

$\varepsilon_c$  is the concrete strain.

$$\varepsilon_0 = \frac{1.8 f_c''}{E_c} \quad \text{is the concrete strain at maximum compressive stress.} \quad (2-13)$$

Elastic modulus  $E_c$  is given in ACI Committee 318 (2008) as:

$$E_c = w_c^{1.5} 33 \sqrt{f_c'} \quad \text{for} \quad 90 \text{ lb / ft}^3 \leq w_c \leq 160 \text{ lb / ft}^3$$

$$E_c = 57000 \sqrt{f_c'} \quad \text{for normal weighted concrete with } f_c' \text{ in psi.} \quad (2-14)$$

Descending elastic modulus,  $E_{cd}$  can be taken as

$$E_{cd} = \frac{0.15 f_c''}{0.0038 - \varepsilon_0} \text{ or } 500 \text{ ksi} \quad (2-15)$$

## Tensile strength

Plain concrete can be tested in tension in three main ways and the tensile strength obtained from these three tests varies as shown in Table 2-4 by Nilson et al. (2004).

ACI Committee 318 (2008) Section 8.6.1, recommends that the average splitting tensile strength  $f_{ct} = 6.7\sqrt{f'_c}$  for normal weight concrete. Similarly, in Section 9.5.2.3, the modulus of rupture for normal weight concrete is  $f_r = 7.5\sqrt{f'_c}$  with  $f'_c$  in psi for both cases.

Although the tensile strength in concrete is low as compared to the compressive strength, it does not drop to zero immediately after concrete had cracked, as shown in Figure 2-51. Before cracking, the stress-strain curve is basically linear and upon cracking a significant drop in tensile strength occurs and the stress-strain curve becomes curved. Three tension stiffening models to represent the tension behavior of RC are presented below.

Vecchio and Collins (1981) suggested the following tensile stress-strain curve, based on their panel tests at the University of Toronto.

Ascending branch, for  $\varepsilon_c \leq \varepsilon_{cr}$

$$f_c = E_c \varepsilon_c \quad (2-16)$$

Descending branch, for  $\varepsilon_c \geq \varepsilon_{cr}$

$$f_c = \frac{f_{cr}}{1 + \sqrt{\frac{\varepsilon_c - \varepsilon_{cr}}{0.005}}} \quad (2-17)$$

Where  $E_c$  is the same elastic modulus as the compression stress-strain curve.

$$\varepsilon_{cr} = \frac{f_{cr}}{E_c} \text{ is the cracking strain.} \quad (2-18)$$

$$f_{cr} = 4 \sqrt{f'_c} \text{ is the concrete cracking stress of plain concrete with } f'_c \text{ in psi.} \quad (2-19)$$

Similarly, Mitchell and Collins (1991) proposed the following expression for the concrete tensile stress-strain curve.

Ascending branch, for  $\varepsilon_c \leq \varepsilon_{cr}$

$$f_c = E_c \varepsilon_c \quad (2-20)$$

Descending branch, for  $\varepsilon_c \geq \varepsilon_{cr}$

$$f_c = \frac{f_{cr}}{1 + \sqrt{\frac{\varepsilon_c - \varepsilon_{cr}}{0.002}}} \quad (2-21)$$

Where  $E_c$  is the same elastic modulus as the compression stress-strain curve.

$$\varepsilon_{cr} = \frac{f_{cr}}{E_c} \text{ is the cracking strain.} \quad (2-22)$$

$$f_{cr} = 4 \sqrt{f'_c} \text{ is the concrete cracking stress of plain concrete with } f'_c \text{ in psi.} \quad (2-23)$$

Hsu (1993) described the tensile stress- strain curve of concrete as follows:

Ascending branch, for  $\varepsilon_c \leq \varepsilon_{cr}$

$$f_c = E_c \varepsilon_c \quad (2-24)$$

$$E_c = 47000 \sqrt{f'_c} \quad (2-25)$$

Descending branch, for  $\varepsilon_c \geq \varepsilon_{cr}$

$$f_c = f_{cr} \left( \frac{\varepsilon_{cr}}{\varepsilon_c} \right)^{0.4} \quad (2-26)$$

$$f_{cr} = 3.75 \sqrt{f'_c} \quad (2-27)$$

Where,  $f'_c$  is the uniaxial concrete cylinder compressive strength with  $f'_c$  in psi.

$f_{cr}$  is the concrete cracking stress of plain concrete in psi.

$\varepsilon_{cr}$  is the cracking strain.

## Reinforcement

As mentioned above, concrete is strong in compression but weak in tension, thus steel reinforcement are added to concrete to resist the tensile forces generated during loadings. Figure 2-52 shows the typical stress- strain curve of steel reinforcement (Hassoun and Manasser, 2005).

Different idealizations of one-dimensional stress-strain curves for steel were proposed by Chen (1982), as shown in Figure 2-53.

However, as shown in Figure 2-54, Hsu (1993) observed from experiments that the stress-strain curve for steel in reinforced concrete differs from the idealized curve. The presence of cracks alters the stress distribution of both the concrete and steel across the cracks. The apparent yield stress,  $f_y^*$  of reinforced concrete is much less than the yield stress,  $f_y$  of bare steel. A plot of average stress and average strain across the cracks yield good fit with the experimental data and thus Hsu proposed the use of a bilinear stress-strain curve (dashed line) with an equivalent yield stress  $f'_y$ , to describe the behavior of steel embedded in concrete.

### Hsu's Bilinear Stress-Strain Curve for Steel

$$f_s = E_s \varepsilon_s \text{ for } f_s \leq f'_y \quad (2-28)$$

$$f_s = f'_y = \left(1 - \frac{2 - \alpha / 45}{1000 \rho}\right) \left[0.43 + 0.5 \frac{f^*_y}{f_y}\right] f_y \quad \text{When } f_s \geq f'_y \quad (2-29)$$

$$E_p' = \left[3.3 - 2.5 \frac{f^*_y}{f_y}\right] E_p \quad \text{is the strain hardening slope for the bilinear curve.} \quad (2-30)$$

$$E_p = 0.025 E_s \text{ or } 10 f_y \quad (2-31)$$

Where  $\alpha$  is the orientation of the cracks. 90 degree is for vertical cracks (pure flexural) and 45 degree is for diagonal cracks (with shear).

$$f^*_y = \left[1 - \frac{4}{\rho} \left(\frac{f_{cr}}{f_y}\right)^{1.5}\right] f_y \quad \text{is the apparent yield stress.} \quad (2-32)$$

$$f_{cr} = 3.75 \sqrt{f'_c} \quad \text{is the cracking stress.} \quad (2-33)$$

$f'_y$  is the equivalent yield stress for the bilinear stress-strain curve.

$\rho$  is the tension steel ratio.

$E_s$  is the steel reinforcement initial elastic young modulus.

Hsu's steel model seems to be able to match the experiment data well. However, for larger steel strain range, the prediction by the model is not realistic or overestimates the actual stress. The stress estimated by Hsu's expression will keep on increasing with strain without bound as shown in Figure 2-55. Thus, a new stress-strain curve for steel is proposed in this study, which capped the usage of Hsu's model to the steel strain,  $\varepsilon_{sc}$ , as shown in Figure 2-56.

#### Modified Hsu's Steel Stress-Strain Model

$$f_s = E_s \varepsilon_s \quad \text{for } f_s \leq f'_y \quad (2-34)$$

$$f_s = f'_y = \left(1 - \frac{2 - \alpha / 45}{1000 \rho}\right) \left[0.43 + 0.5 \frac{f^*_y}{f_y}\right] f_y \quad \text{When } f_s \geq f'_y \quad (2-35)$$

$$E_p' = \left[3.3 - 2.5 \frac{f^*_y}{f_y}\right] E_p \quad (2-36)$$

$$E_p = 0.025 E_s \text{ or } 10 f_y \quad (2-37)$$

$$f_s = f_{\max} \quad \text{When } f_s \geq f_{\max} \text{ which occurred at } \varepsilon_{sc} \quad (2-38)$$

$$\varepsilon_{sc} = \frac{f_{\max} - f'_y}{E_p'} + \varepsilon'_y \quad (2-39)$$

$$\varepsilon'_y = \frac{f'_y}{E_s} \quad (2-40)$$

Where  $\varepsilon_{sc}$  is the maximum strain where Hsu's steel model will be used.

$\varepsilon'_y$  is the equivalent yield strain for the bilinear stress-strain curve.

### Finite Element Analysis

Finite Element Analysis (FEA) is essentially the establishment and the solving of a set of governing algebra equations for a stated problem. Cook et al. (2003) described the FEA as a method for numerical solution of field problems (physical problems). FEA is applicable to any type of field problems (heat transfer, stress analysis etc) and is thus widely used in civil and structural engineering to solve complex problems.

To solve a field problem, the determination of the spatial distribution of one or more dependent variables is required. These variables can be classified as primary variables (e.g., displacements or temperature) or as secondary variables that are derived from the primary variables (e.g., forces or stresses). The field problems are often described by mathematical expression (differential or integral expression). The

flow process for the usage of FEA to solve a problem is summarized by Bathe (1996), as presented in Figure 2-57.

The first step to solve a problem is to identify the problem and to determine the more critical physical phenomena or behavior involved in the problem. Once the physical nature of the problem has been understood, a mathematical model can thus be created. The mathematical model is an idealization based on the various assumptions to attempt to solve the physical problem. It is important to realize that FEA is only an approximation. Even the most accurate FEA model may not represent the physical behavior observed if the mathematical model assumed is inappropriate. Thus it is critical that the results from the FEA be validated against experimental results to ensure the validity of the modeled result and to enhance the confidence in usage of the model to simulate physical problems.

### **Verification and Validation Processes**

Verification and validation of computational simulations are the primary methods for quantifying and building confidence in the modeled results.

The processes of verification and validation are shown in Figure 2-58 and 2-59, respectively (Oberkampf et al., 2004). Verification deals with the assessment of the accuracy of the computational model (programmed mathematic algorithms) with known solutions. Relationship of the simulation with the actual physical condition is not a concern here. On the other hand, validation is the assessment of the accuracy of the computational model by comparing with experimental data. Relationship of the simulation with the actual physical condition is the key focus here.

## The Finite Element (FE) Code Abaqus

The following review of FE code Abaqus is based on the Abaqus Version 6.10 documentation (Simulia, 2010). Abaqus is a FE method based simulation program which can be use for both linear and non-linear simulations. It has an extensive library of both material models and elements which can be used to model virtually any geometry and most typical engineering materials. It is designed to be of general purpose and thus can be used in a wide variety of application such as structural problems, heat transfer, acoustic, and soil mechanics etc. It has three main analysis products - Abaqus/Standard, Abaqus/Explicit and Abaqus/CFD, with the first two products mainly used in structural applications.

In reference to structural applications, Abaqus/Standard can be used to solve both static and dynamic problems (quasi-static). It is implicit in nature where it solves a series of equations at each solution “increment” for static problem or equations of motion at the each time step for dynamic problems. Global stiffness matrix is formed and the solutions are obtained via the inversion of the stiffness matrix. Abaqus/ Explicit on the other hand uses an explicit integration analysis method, where the equations of motion are satisfied at current time step  $t_i$  and extrapolated to determine the solution of the next time step at  $t_{i+1}$ . Due to the extrapolation of results, the time steps increments provided needs to be small to ensure accuracy of the solutions. Abaqus/Explicit is suited to model extremely fast and transient dynamic events such as blast, impact and even contact problems.

The disadvantages of using implicit integration analysis method is that a full stiffness matrix inversion is required to obtain the solution and is computationally

expensive since equilibrium is satisfied at each time step. For explicit integration analysis, no matrix inversion is required to obtain the solution and although small time steps are required to ensure accuracy of the result due to extrapolation. As such each time step is computationally much cheaper than that of the implicit method. Moreover, explicit analysis method is more suitable for non-linear analysis, as the small time step provisioned will help to capture the transition point between linear to non linear region.

Yim (2007) used a combination of Abaqus/Standard and Abaqus/Explicit to model the behavior of steel moment connections for building subjected to blast and collapse loads. The moment resistance function of the steel connections was determined using Abaqus/Standard. Abaqus/Explicit was used in the analysis of a three dimensional (3D) simplified building model subjected to progressive collapse under abnormal loads.

Similarly, Tan (2010) used Abaqus/Standard to establish the moment- rotation resistance functions for RC beam- column connections (rectangle beam section only) under monotonic loads.

### **Concrete damaged plasticity model (CDP)**

There are three material models available in Abaqus, to model the behavior of concrete. They are the concrete smeared cracking, cracking model for concrete, and the concrete damaged plasticity (CDP) model. The concrete smeared cracking model is only available in Abaqus/Standard, and is primarily used to model concrete that is subjected to monotonic loading under low confining pressure. It uses the concept of “smeared cracking” where individual macro cracking are not tracked but the average stress-strain relationship representing the equivalent cracked concrete behavior is used instead and accounted for in the integration points of the element. The cracking model is only available in Abaqus/Explicit, and is used primarily for applications where the

behavior is governed by brittle failure or tension cracking. It can also be use to model brittle rocks or ceramics. Lastly, the concrete damaged plasticity model is available in both Abaqus/Standard and Abaqus/Explicit and designed to model concrete subjected to monotonic, cyclic and/or dynamic loading.

CDP is selected for use in this study as it is more versatile and available in both Abaqus/Standard and Abaqus/Explicit. The CDP material model is a continuum, plasticity-based model which accounts for concrete damage. The basic assumptions are that concrete fails in both tensile cracking and compressive crushing. Thus, to describe the material behavior of concrete, two stress-strain curves depicting both the tensile and compression failure mechanism are used.

The uniaxial compression stress-strain curve is presented in Figure 2-60. It consists of a linear response governed by initial (undamaged) elastic young modulus,  $E_o$ , until the initial yield stress,  $\sigma_{co}$ . After which, it follows a curve path in the plastic region and peaked at the ultimate stress,  $\sigma_{cu}$ , where the strength reduces beyond the ultimate stress. Similarly, the behavior of concrete in tension is presented in Figure 2-61. It consists of a linear response governed by initial (undamaged) elastic young modulus,  $E_o$ , until the tensile failure stress,  $\sigma_{to}$ . Thereafter, the post failure behavior is reflected by the tension stiffening effect where the strength is reduced. Tension stiffening simplifies the interaction and load transfers between concrete and steel reinforcement over cracks by representing the combined behavior in term of average stress and average strain across the cracked region. Tension stiffening must be specified for the CDP material model. Abaqus suggested that a linear degradation of

strength from the maximum at the cracking stress to zero at the ultimate strain. A reasonable estimate of the ultimate strain is given as ten times the initial cracking strain.

The CDP material model is also applicable to cyclic load and the behavior of concrete needs to account for damage due to reversal of load. The load reversals might lead to strength and/or stiffness degradation. Concrete damaged during the unloading phase is characterized by two damage parameters,  $d_c$  and  $d_t$ , for compression and tension damage respectively. They range from zero (no damage) to one (total loss of strength).

The stress-strain curve outside the elastic range in the compression field can be specified by stress and the inelastic (crushing) strain,  $\varepsilon_c^{in}$ . The inelastic strain is defined as the total compressive strain ( $\varepsilon_c$ ) minus the elastic compressive strain ( $\varepsilon_{oc}^{el}$ ), as shown below.

$$\varepsilon_c^{in} = \varepsilon_c - \varepsilon_{oc}^{el} \quad (2-41)$$

Where,  $\varepsilon_{oc}^{el} = \frac{\sigma_c}{E_0}$  and  $\sigma_c$  is the concrete compressive stress.

Abaqus converts the inelastic strain values into plastic strain values,  $\varepsilon_c^{pl}$  automatically. The plastic strain values are calculated by Equation 2-42 and always need to be positive.

$$\varepsilon_c^{pl} = \varepsilon_c^{in} - \left( \frac{d_c}{1-d_c} \right) \left( \frac{\sigma_c}{E_0} \right) \quad (2-42)$$

In the tension regime, the failure behavior is defined by specifying the post failure stress and the cracking strain,  $\varepsilon_t^{ck}$ . The cracking strain is defined as the total strain ( $\varepsilon_t$ )

minus the elastic strain ( $\varepsilon_{ot}^{el}$ ), as shown below. A lower limit of post failure stress of

$\sigma_t \geq \frac{\sigma_{to}}{100}$  is specified in Abaqus to minimize potential numerical problems.

$$\tilde{\varepsilon}_t^{ck} = \varepsilon_t - \varepsilon_{ot}^{el} \quad (2-43)$$

Where,  $\varepsilon_{ot}^{el} = \frac{\sigma_t}{E_0}$  and  $\sigma_t$  is the concrete tensile stress and  $\sigma_{to}$  is the tensile

failure/cracking stress.

Similarly, the cracking strain values are converted into plastic strain values,  $\varepsilon_t^{pl}$  automatically. The plastic strain values are calculated by Equation 2-44 and always need to be always positive.

$$\varepsilon_t^{pl} = \tilde{\varepsilon}_t^{ck} - \left( \frac{d_t}{1-d_t} \right) \left( \frac{\sigma_t}{E_o} \right) \quad (2-44)$$

### Defining the plasticity parameters for CDP

Various plasticity parameters are required to define the CDP material model properly. The parameters are the dilation angle ( $\varphi$ ), the flow potential eccentricity ( $\varepsilon$ ), the compressive stresses ratio ( $f_{bo} / f_{co}$ ), the stress invariant ratio ( $K$ ) and the viscosity parameter ( $\mu$ ).

Concrete can exhibit significant volume change (dilation) when subjected to large inelastic strain. This dilation is caused by the plastic distortion and the distortion can be adequately represented by a suitable plastic potential function  $G$ . In Abaqus, the Drucker-Prager hyperbolic plastic potential function, as shown in Figure 2-62, is used. This plastic potential function is dependent on both the dilation angle ( $\varphi$ ) and flow potential eccentricity ( $\varepsilon$ ).

The dilation angle is measured in the  $\bar{p} - \bar{q}$  plane at high confining pressure, where  $\bar{p}$  is the hydrostatic pressure stress, and  $\bar{q}$  is the Mises equivalent effective stress, while  $\dot{\varepsilon}^p$  is the plastic strain increment vector. In the verification of a material model developed by Lee and Fenves (1998), the dilation angle is specified as 31 degrees. Nielsen (1999) correlated the relationship between the friction angle ( $\phi$ ) and dilation angle ( $\varphi$ ) of concrete as  $\sin(\phi) = \tan(\varphi)$ . The relationship between the friction angle and compressive strength of concrete is presented in Figure 2-63. Jankowiak and Lodygowski (2005) conducted a parametric study on a three points and a four points bending RC beam to establish the dilation angles. The least square method is used to minimize the error between the computed plastic potential,  $G$ , and the experimental results. The dilation angle  $\varphi$  was determined to be 38 degrees. Similarly, Malm (2006) conducted a parametric study on a RC beam subjected to four points bending load, and the results are presented in Figure 2-64. The best fit with the experimental results lied between 30 and 40 degrees.

Malm (2009) summarized the studies done on the dilation angles and suggested that the dilation angle to be used in the CDP material model should be in the range of 25 to 40 degrees for the normal grade concrete. The suggested range of dilation angles is applicable for both the tension and compression biaxial stress states.

$\varepsilon$ , which is the flow potential eccentricity, defines the rate at which the plastic potential, as shown in Figure 2-62, approaches the asymptote. The plastic potential is a straight line when  $\varepsilon$  is zero. The default value in Abaqus is 0.1.

$f_{bo} / f_{co}$  is the ratio of the initial equibiaxial compressive yield stress to the initial uniaxial compressive yield stress. The default value in Abaqus is 1.16, while Jankowiak and Lodygowski (2005) suggested 1.12 in their parameter study conducted.

$K$  is the ratio of the second stress invariant on the tensile meridian to that of the compressive meridian. The default value in Abaqus is 0.667.

$\mu$ , is the viscosity parameter used in the viscoplastic regularization of the constitutive equations. It is used to resolve convergence difficulties in implicit analysis programs especially in material models that possess softening behavior or stiffness degradation. The default value in Abaqus/Standard is 0.0 while this parameter is ignored in Abaqus/ Explicit.

### **Classical metal plasticity**

The behavior of the reinforcement can be modeled with a combination of linear elastic and classical metal plasticity material model. The elastic material model is required to define the recoverable part of the strain. As for the plastic material model, it uses the Mises yield surface with an associated plastic flow rule to describe the inelastic behavior. Choices of hardening rule included perfect plastic material (No hardening), isotropic hardening including Johnson-Cook hardening (for high rate deformation) and kinematic hardening (for cyclic loads).

Material data definition or data input in Abaqus is in terms of “true” stress or Cauchy stress and logarithmic plastic strain. Thus, nominal stress-strain data needs to be converted prior to the input into the material model in Abaqus. The equations required for the conversion are specified, as shown below.

$$\sigma_{true} = \sigma_{nom} (1 + \varepsilon_{nom}) = \frac{P_L}{A_c} \quad (2-45)$$

$$\sigma_{nom} = \frac{P_L}{A_0} \quad (2-46)$$

$$\sigma_{true} = \sigma_{nom} \frac{A_0}{A_c} \quad (2-47)$$

$$\varepsilon_{ln}^{pl} = \ln(1 + \varepsilon_{nom}) - \frac{\sigma_{true}}{E} \quad (2-48)$$

Where,  $\sigma_{true}$  &  $\sigma_{nom}$  are the true and nominal stresses, respectively.  $P_L$  is the axial load onto the metal,  $A_0$  &  $A_c$  are the initial and current area of the metal, respectively. While,  $\varepsilon_{ln}^{pl}$  &  $\varepsilon_{nom}$  are the logarithmic plastic and nominal strain, respectively.

## Elements

First order elements are elements that have nodes only at the corners and uses linear interpolation in each direction to calculate the required field variables. Second order elements are elements that have middle node within the element and used quadratic interpolation instead. Abaqus states that second order isoparametric elements with reduced integration provide the most cost-effective elements in problems in which a smooth solution are expected. However, in cases where large strain gradients, limit load analysis and/or plasticity analysis undergo large strains, the first order elements with reduced integration are preferred.

Consequently, 8 nodes linear (first order) brick element C3D8R with reduced integration and hourglass control were used to model the concrete in space, as shown in Figure 2-65. This element has four integration points available at each face, as shown in Figure 2-66. Each face or plane of the brick element is essentially a linear plane stress element, which would suffer from parasite shear locking. Shear locking occurs as the linear edge of the plane cannot exhibit pure bending behavior, thus, generating

additional shear resistance resulting in stiffer element. In order to minimize shear locking, it is common to use reduced integration with only one gauss integration point, as presented in Figure 2-66. Cook et al. (2004) stated that reduced integration reduces computational times and might improve the accuracy of computed FE results by overcoming the problem of over-stiffness due to the choice of element types (linear, quadratic etc). However, reduced integration introduces a defect called spurious modes, or hourglass effect, which contributed instability into the model. Furthermore, spurious modes produced deformation without strain at the integration points and thus lead to element deformation without any strain energy. Analysis results are questionable if spurious modes are presence. Different element types are susceptible to different degree of spurious modes when reduced integration is used, as shown in Table 2-5.

In Abaqus, the hourglass control method of Flanagan and Belytschko (1981) which provides artificial stiffness and damping is used. This method is generally successful for linear and mildly non-linear problem but may cause problems in strong non-linear problem. Although, there are potential that hourglassing might occurred due to the use of the reduced integration, despite the use of the hourglass control, it could be successfully managed by avoiding point concentrated load. Thus, the benefit of faster computation speed for reduced integration could be harvested without sacrificing reliability in the results.

Linear (first order) 2 nodes beam element B31, with one gauss integration point is used to model the reinforcement, as shown in Figure 2-67. B31 utilizes the Timoshenko beam theory, which accounts for the transverse shear strain, and thus, allows for shear flexibility. The conventional elastic assumptions that plane section remains plane does

not hold true. January and Krauthammer (2003) found that beam elements are more suitable than truss elements for the modeling of the reinforcement. Beam elements allow both the shear and bending behavior while truss elements only resist axial forces. Their study established that both the shear and bending behavior are necessary when refined meshes are used to achieve convergence of modeled result to test data.

Linear (first order) 4 nodes shell elements S4R, with reduced integration, hourglass control and finite membrane strain were used to model the slab, as shown in Figure 2-68. S4R belongs to the conventional shell elements type which discretizes a body by defining the geometry at a reference surface (usually, the mid surface is chosen). The shell elements have both the displacement and rotational degree of freedoms (dofs). S4R is suitable for both thin and thick shell problems.

Different methods are available to connect the beam elements and solid elements together to simulate the reinforced concrete behavior. Tan (2010) used the embedded element technique to connect the host elements (Solid brick elements- concrete) with the embedded elements (beam elements – reinforcement). The embedded elements are allowed to retain their rotational degree of freedoms (dofs) while constrained to the translational dofs of their host elements.

A tie constraint, or tie node method, could also be utilized to connect the brick and beam elements together. A tie constraint connects two separate surfaces/nodes together so that there is no relative movement between the two ties surfaces or nodes. Both translational and rotational dofs are equal for both the master and the slave surfaces/nodes. The surface with the less refined mesh is often chosen as the master surface to improve on the computational speed.

## Connectors

Connectors in Abaqus allow the modeling of the mechanical relationship between two points (discrete geometry, i.e. node to node) in an assembly. Complex kinematic and kinetic relationships between the nodes can be modeled effectively as the connector elements do not eliminate the dofs of the connected nodes. The types of connections available are presented as follow:

- Translational basic – translational dofs at both the connector element nodes and rotational dofs at one or both nodes are affected.
- Rotational basic - only rotational dofs at both nodes on the connector element are affected.
- Specialized rotational basic – affects other dofs available at the nodes on the connector element in addition to the rotational dofs.
- Assembled connections – predefined combinations of the above mentioned connection types (e.g., Translation basic and rotational basic , translational basic or specialized rotational basic etc)
- Complex connections – affects a combination of dofs at the nodes on the connector elements which cannot be combined with any other connection components.

## Convergence and iteration control

Abaqus/Standard uses implicit integration method as mentioned earlier. Thus, in non-linear problems, the solution process involves a combination of incremental and iterative procedures to achieve equilibrium with an acceptable degree of error. The loading/prescribed conditions are broken into a series of time increments which can correspond to physical or arbitrary time. At each time increment, the equilibrium solution is attempted. In equilibrium, the external forces  $P$  must balance with the internal forces  $I$ .

$$P - I = 0 \quad (2-49)$$

The non-linear response of a structure to a small external load increment,  $\Delta P$ , based on the time increment is illustrated in Figure 2-69. Abaqus/Standard uses the initial conditions/configuration/geometry of the structure to generate the initial tangent stiffness,  $K_0$ , and initial displacement,  $u_0$ . With these two parameters, the displacement correction ( $C_a$ ) is calculated and the next displacement ( $u_a$ ) and internal force ( $I_a$ ) are generated based on the structure's constitutive model.

The residual force or error ( $R_a$ ) is the difference between the applied load and the internal force (Equation 2-50), and equilibrium is achieved if  $R_a$  is zero. However, in non-linear problems,  $R_a$  will never be zero. In order to determine equilibrium, Abaqus/Standard compares the  $R_a$  to a tolerance value  $R_\alpha^n$ . By default  $R_\alpha^n$  is set to 0.5% of an average force in the structure averaged over time. Abaqus commended that this tolerance value produced a close approximation to the exact solution that is rather strict in term of engineering standard.

$$R_a = P - I_a \quad (2-50)$$

In addition, Abaqus/Standard will only accept the calculated solution if another criterion is satisfied. The displacement correction for the last time step  $C_a$  must be small, relative to the total incremental displacement. The default value for  $C_\alpha^n$  is 1% of the incremental displacement. In summary, both  $R_\alpha^n$  and  $C_\alpha^n$  must be satisfied before a solution is deemed converged.

Abaqus/Standard has a feature that allows the automatic adjustment of the size of the time increments to solve the non-linear problem efficiently. Only the size of the initial increment needs to be specified in the simulation. The suggested values for the initial

increment range from 5% to 10% of the total time. At each time increment, Abaqus/Standard will perform iterations, where it tries to find equilibrium. The default is sixteen iterations for each attempt on a single time increment. In the instance where 16 iterations have been performed, but the solution has yet to converge or if the solution is deemed to be diverging, the attempt to achieve equilibrium will be abandoned. A new attempt with a reduced time increment will be tried to achieve equilibrium. For each unsuccessful attempt, the time increment is reduced to 25% of the previous one. By default, five attempts will be tried before the whole analysis is terminated.

For highly non-linear problems, the direct solver (Newton method) used in Abaqus/Standard may diverge during the iteration process. Abaqus/Standard has a line search feature that automatically detects the divergence situation. It helps to minimize divergence occurrences by applying a scale factor to the calculated solution correction/displacement correction. The feature is only available when the quasi-Newton method is chosen as the solver. However, this feature can be activated for the Newton Method by specifying  $N^{ls} = 5$ .

Two parameters are used to control the time increment; they are  $I_0$  and  $I_R$ .  $I_0$  is used to control the divergence check. Divergence is deemed to occur when the residual force  $R_a$ , for two consecutive iterations does not decrease. The default value for  $I_0$  is 4, and after 4 iterations Abaqus/Standard will proceed to check the iteration process for divergence. If divergence seems apparent, the current attempt will be cancelled and a new attempt with a reduced time increment as mentioned above will be carried out.  $I_R$  is the number of equilibrium iterations after which the logarithmic rate of convergence check commence. The default value for  $I_R$  is 8. Abaqus/Standard suggests that

increasing  $I_0$  and  $I_R$  to 8 and 10, respectively, will minimize the premature cutbacks of the time increment and speed up the analysis.

Malm (2009) suggested several general ways to avoid convergence difficulties in finite element analysis. One of the methods is to define the model properly (mesh, boundary conditions, load, etc) to reduce the potential numerical singularities that might occur in the global stiffness matrix. Another possibility is to amend the convergence criteria to allow for more iterations prior to checking for convergence. Alternatively, the problem can be possibly converted to a quasi-static analysis where explicit integration method is used. This can be achieved by giving the loads a small velocity, hence ensuring that the kinematic energy generated is minute, relatively to the internal strain energy. Lastly, artificial damping can be introduced into the model which reduces the rate of the energy dissipation from the crack elements to its surroundings. It was also recommended for Abaqus/Standard to reduce the tolerances and increase the number of iterations, before convergence check is done to improve on the convergence.

In summary, the few important solutions and time control parameters for Abaqus/Standard are reviewed. The default values are summarized in Table 2-6.

### **Progressive Collapse**

The partial collapse of the 22 story Ronan Point apartment in East London in 1968 due to an internal gas explosion marked a new page in the history of progressive collapse. Other significant occurrence of progressive collapses in recent history includes the Murrah Federal Building in 1995 and World Trade Center 2001 due to bomb and airplane attack respectively, resulted in huge loss of life and property.

Mohamed (2006) described progressive collapse of structures as being initiated by the loss of one or more primary load carrying structural components. It can be caused by any extreme events such as gas explosion, blast, fire, earthquake, foundation failure, vehicular impact, etc. Thus, leading to the redistribution of loads to other structural components that may not be able to withstand the extra load, and resulting in further failure. This recurring process will continue until a stable equilibrium is reached, upon which a significant portion of the building might have already been destroyed.

Krauthammer (2008) described that progressive collapse occurs when the loading pattern or boundary conditions of the structure changes such that the structural members fail as they are loaded beyond their capacity.

Sasani and Sagioglu (2010) characterized both analytically and experimentally the dynamic load redistribution of a 20 storey RC structure that had an interior ground floor column removed suddenly. No progressive collapse occurred from the sudden removal of the column, only a small vertical deformation of approximately 0.35 inches measured on the second floor remained. It was observed that the columns above the removed ground floor column lost their axial compressive forces/strains significantly much faster than the vertical displacement. It seems that the gravity loads were redistributed away from the damage location at every floor levels. Thus, it was concluded that the whole structure on the floors above the ground floor contributed to the redistribution of gravity load that was carried previously by the removed column.

Building provision or codes described below have some guidelines to aid in the design of structures against progressive collapse. In general, to resist progressive

collapse, buildings should be designed to have adequate ductility, strength and redundancy.

ASCE 7 (2002) defines two general approaches that would help in the reduction of the possibilities of progressive collapse.

- Indirect design approach – resistance to progressive collapse is implicitly provisioned by prescribing minimum requirements such as resistance, ductility and continuity.
- Direct design approach – resistance to progressive collapse is considered explicitly. Two design methods are available. 1) Alternate path (AP) – which requires that the structure be capable of bridging over the removed structural element and to confine the damage area locally. 2) Specific local resistance (SLR) – which requires that the chosen structural components in the building be locally enhanced to be able to resist a specific threat or load.

It should be noted that no quantitative requirements are provided for both the direct and indirect design approaches in the ASCE 7 (2002).

Federal buildings are generally designed according to the guidelines of the General Services Administration (GSA). GSA (2003) provides a threat independent methodology for minimizing the potential for progressive collapse in new and existing buildings. It should be noted that the guidelines are not a part of blast design or blast analysis. A flow-chart methodology is provided for the determination if the facility under consideration might be exempted from detailed consideration for progressive collapse. For those facilities, that required detailed progressive collapse considerations, two analysis approaches are available.

- Linear procedure - Typically applicable to buildings less than 10 stories and with typical structural configuration. A linear procedure implies the use of either a static or dynamic linear-elastic FEA.
- Non-linear procedure – For high rise or buildings that contain atypical structural configurations. It implies the use of static or dynamic FEA that capture both the material and geometric nonlinearity.

Unified Facilities Criteria (UFC, 2009) is the design guidelines for progressive collapse which applies to military departments, Department of Defense (DoD) agencies and DoD field activities. Progressive collapse protection is required for facilities that are higher than three stories. The level of progressive collapse design is dependent on the Occupancy Category (OC) as shown in Table 2-7 and affects the design requirements as presented in Table 2-8.

The design requirements in general, utilize a combination of design methods:

- Tie forces – specify a tensile force capacity (tie forces) in the floor and roof system and requires that the ties be interconnected in both horizontal and vertical directions. The tie forces enhanced continuity, ductility and redundancies by transferring load from damaged area to undamaged zone.
- Alternate path – requires that the building must be able to bridge over the missing structural components via another load transfer path.
- Enhanced local resistance – increase protection to the external wall and columns by enhancing the shear and flexural capacity, which aims to reduce the possibility and extent of damage.

Dusenberry (2002) presented some of the guidelines provided by The Interagency Security Committee (ISC) for new buildings. The relevant ones include that structural components should be designed and detailed with reinforcement patterns to support loadings in other directions beside the primary loading direction (providing both top and bottom reinforcement in slab and beam to account for load reversal etc). Lap splices should develop the full capacity of reinforcement. Lastly, transfer girders should be avoided.

In order to understand or design for progressive collapse well, attention should not only be focused on the design of the primary structural members, it is equally critical to understand how connections behave under this extreme event. Yim (2007) utilized Abaqus/Standard to derive the moment resistance function of a steel connection

subjected to static loading using a continuum based FE model. He also developed a simplified structural element based FE building frame model for the fast running progressive collapse analysis. The simplified FE model, as shown in Figure 2-70 consists of beams and connector elements which are used to represent the behavior of the actual beam-column connections. The connector elements are defined with the moment resistance function derived from the continuum based FE model to simulate the actual connections behavior. Abaqus/Explicit is utilized for the progressive collapse analysis, using the simplified structural element based FE building frame model.

A four story full scale RC structure was tested for progressive collapse under abnormal loading in October 2010. The test structure will be presented in more details in Chapter four.

### **Summary**

Various beam column connection types, connection behavior, and load transfer mechanisms have been presented and discussed. Different models have been proposed by various researchers to attempt to describe these connection behaviors. FEA is useful to aid researchers in understanding the complex behavior and mechanism in a beam-column-slab connection, it can, however, be time consuming. Various progressive collapse design guidelines and requirements are also available. A fast running simplified structural element based FE model for steel building frame has been shown to be feasible for the progressive collapse analysis under abnormal loads.

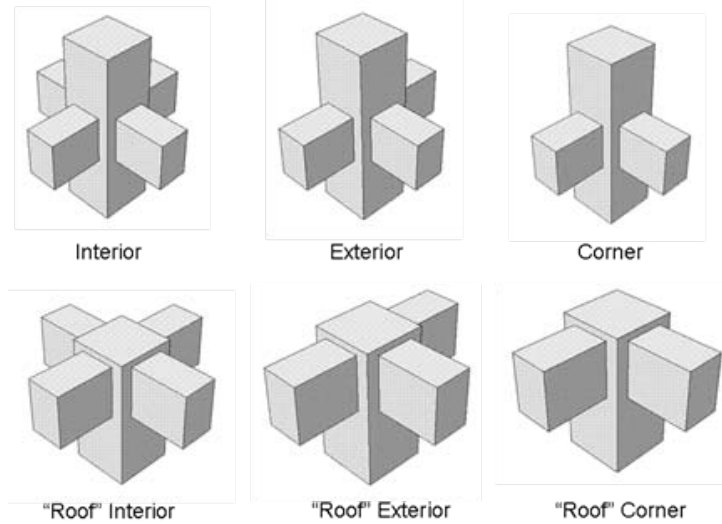


Figure 2-1. Reinforced concrete (RC) beam-column connections (Adapted from ACI Committee 352, 2002).

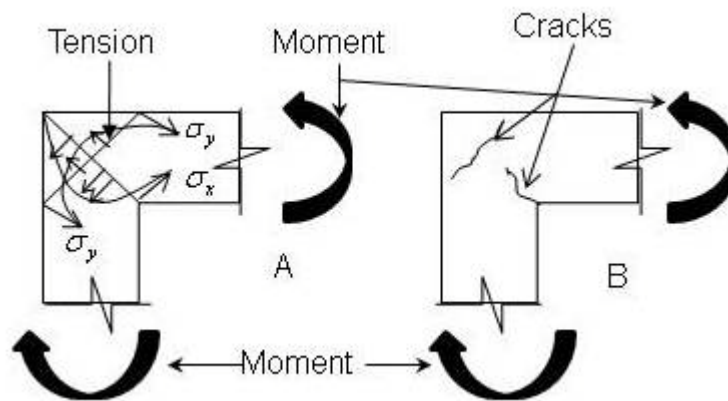


Figure 2-2. Knee-connection subjected to opening loads (Adapted from MacGregor and Wight, 2005). A) stresses on joint area and B) cracks.

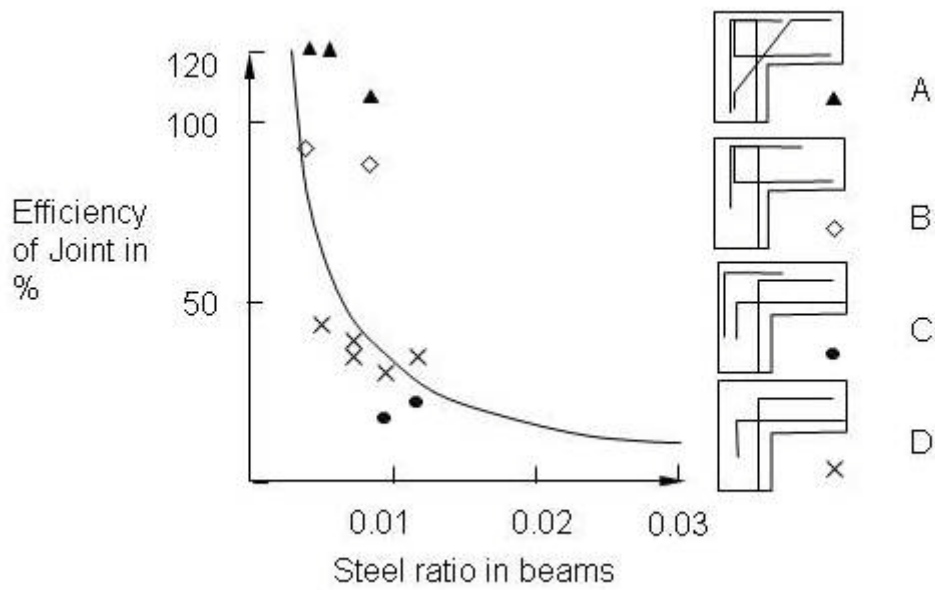


Figure 2-3. Efficiency of connections (Adapted from MacGregor and Wight, 2005).

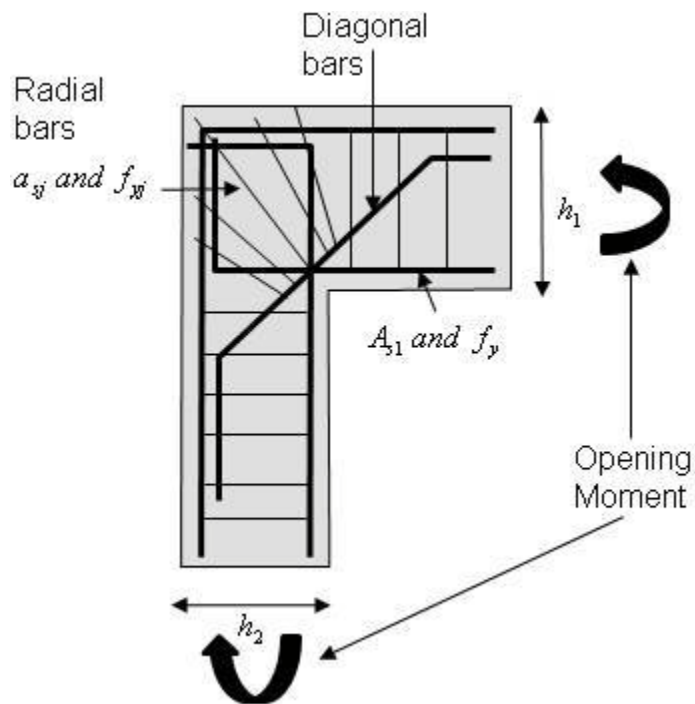


Figure 2-4. Details of connection under opening loads (Adapted from Park and Paulay, 1975).

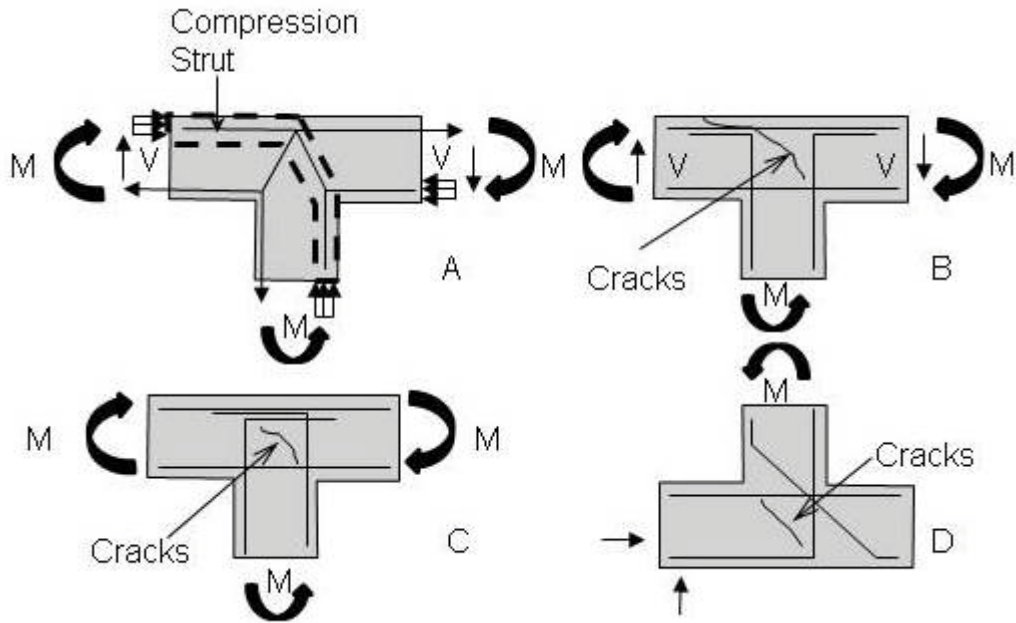


Figure 2-5. Flow of forces and reinforcement details of T-connections (Adapted from MacGregor and Wight, 2005). A) strut and tie model of joint, B) unsatisfactory detail, C) satisfactory detail and D) base of retaining wall.

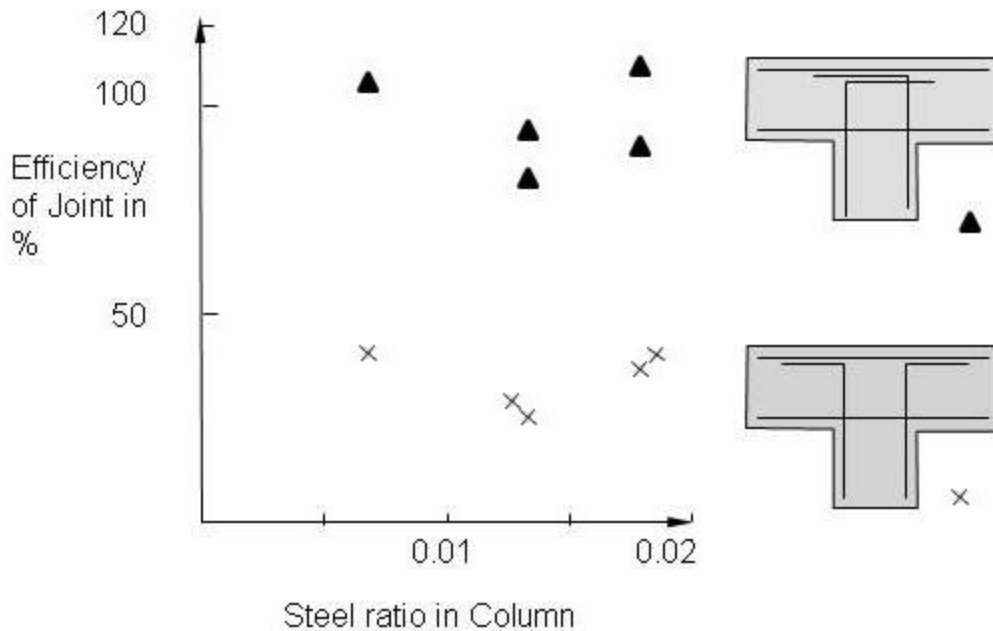


Figure 2-6. Connection efficiency against steel reinforcement ratio (Adapted from MacGregor and Wight, 2005).

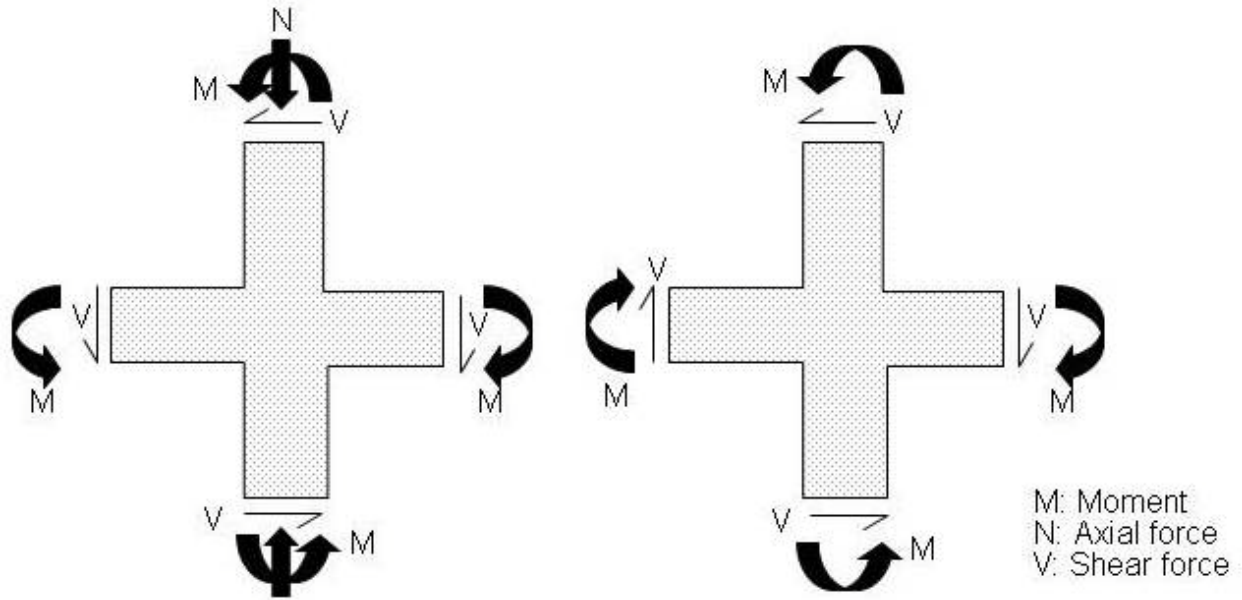


Figure 2-7. Connection forces (Adapted from Nilson et al., 2004). A) gravity loads and B) lateral loads.

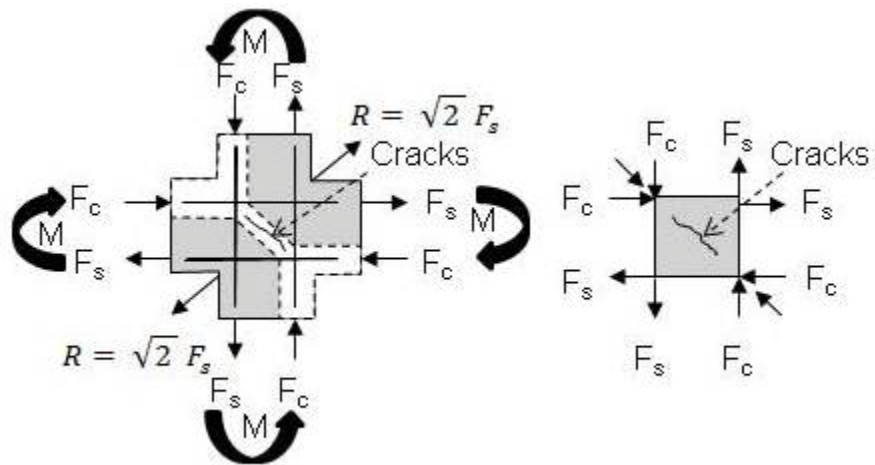


Figure 2-8. Suggested forces within the interior connection (Adapted from Nilsson, 1973).

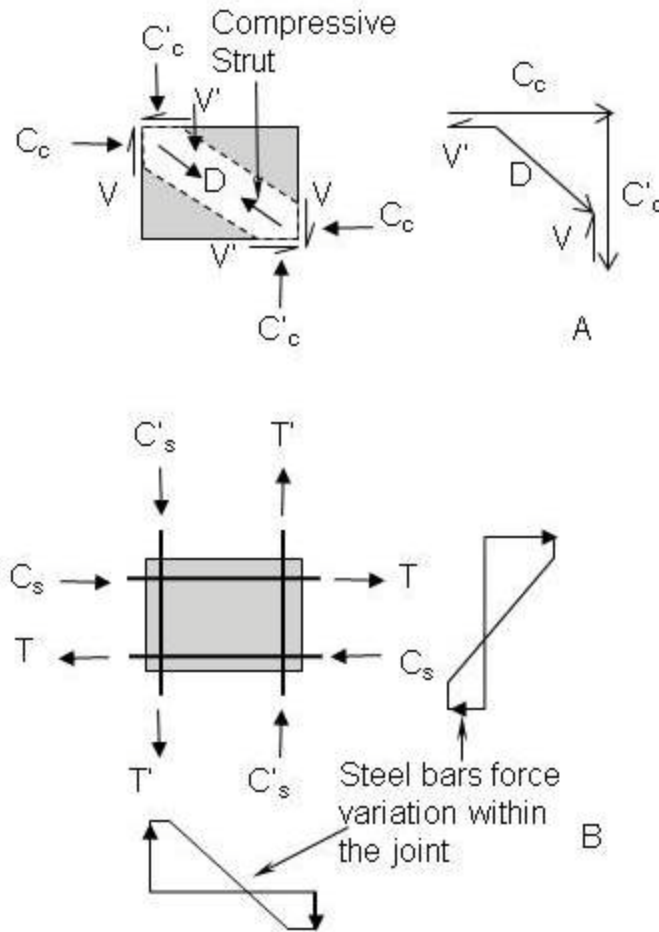


Figure 2-9. Idealized connection behavior (Adapted from Park and Paulay, 1975). A) strut mechanism and B) truss mechanism

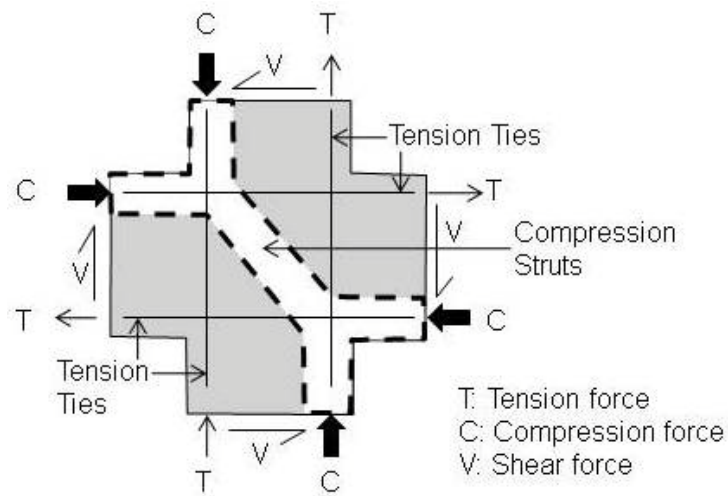


Figure 2-10. Strut-and-tie model (Adapted from Nilson et al., 2004).

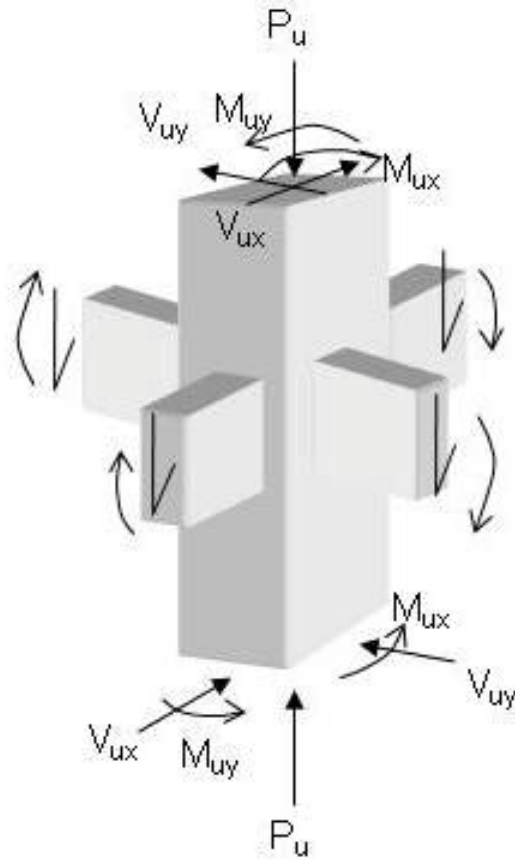


Figure 2-11. Forces that act on the primary members of a connection (Adapted from Wang et al., 2007).

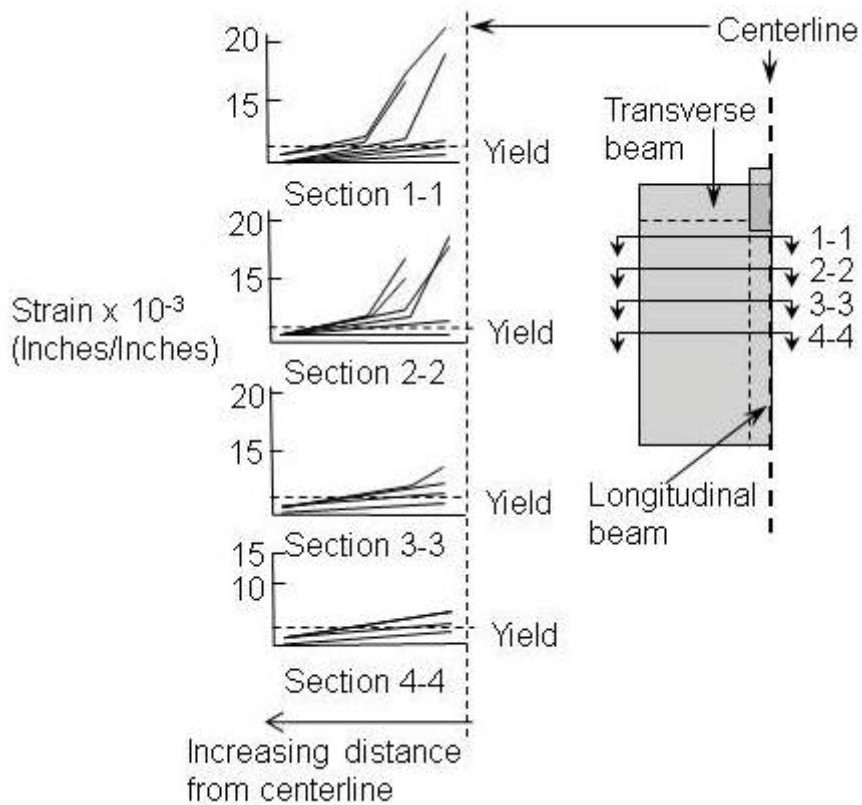


Figure 2-12. Variation of slab reinforcement strains along both transverse and longitudinal beam directions (Adapted from Durrani and Zerbe, 1987).

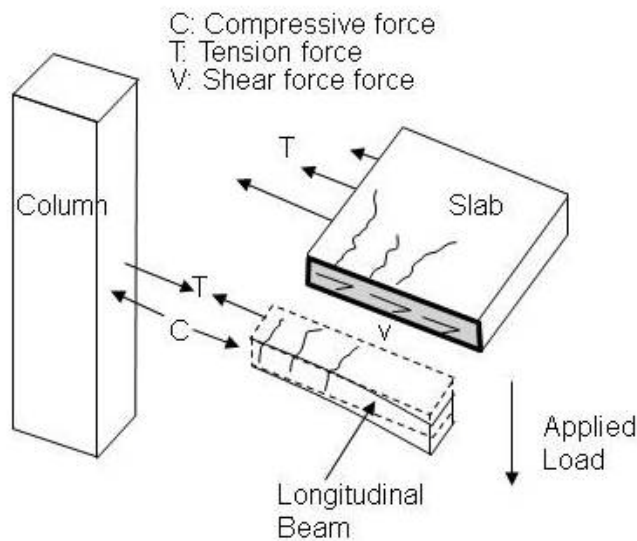


Figure 2-13. Force transfer from longitudinal beam to the slab (Adapted from French and Moehle, 1991).

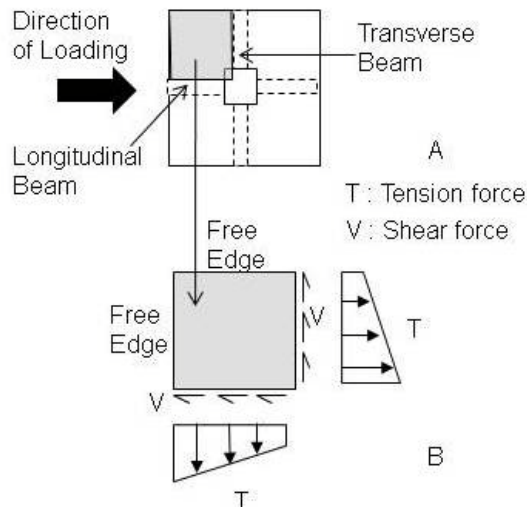


Figure 2-14. Forces at slab boundary (Adapted from French and Moehle, 1991). A) plan view and B) possible forces generated at slab panel boundaries.

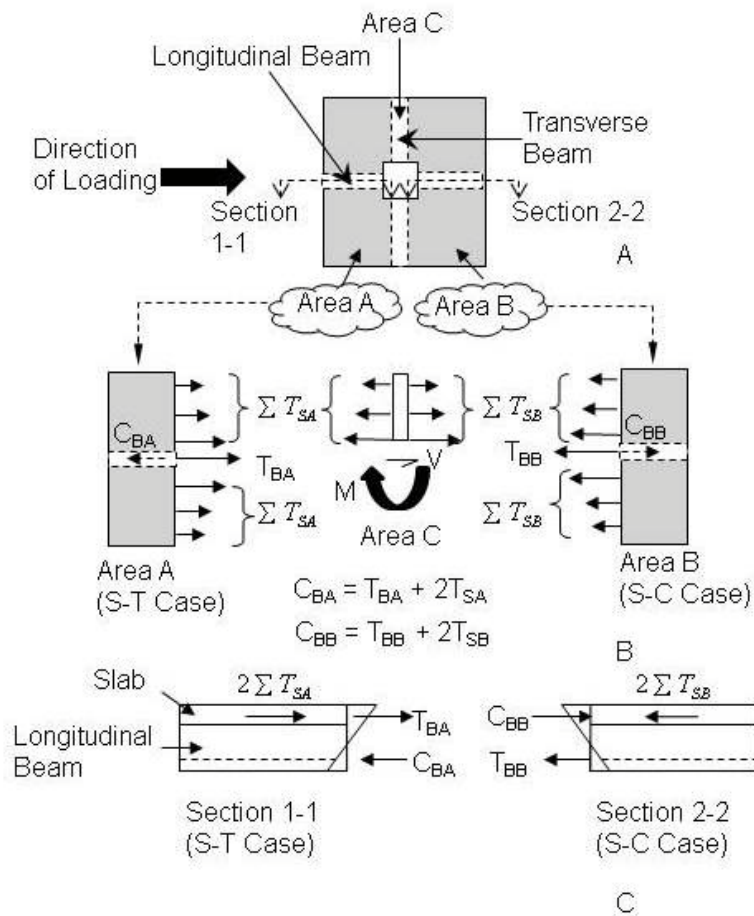


Figure 2-15. Force transfer mechanism (Adapted from French and Moehle, 1991). A) plan view, B) force transfer from S-T to S-C and C) forces at interface.

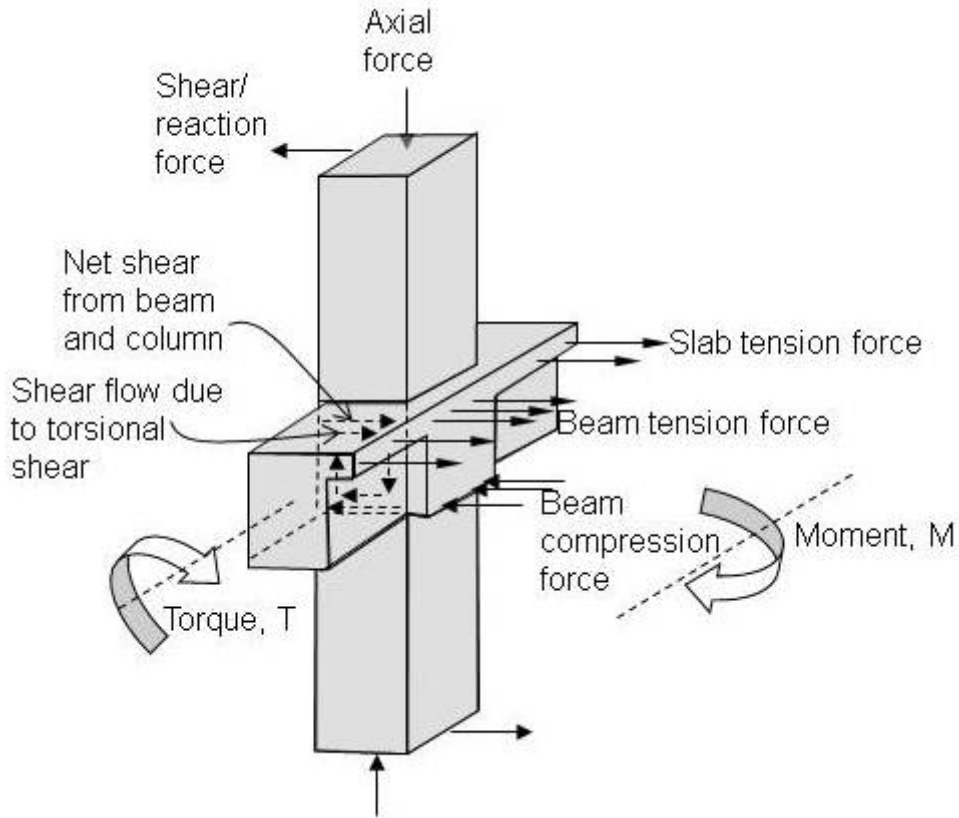


Figure 2-16. Force transfer for an exterior connection (Adapted from Paultre et al., 1989).

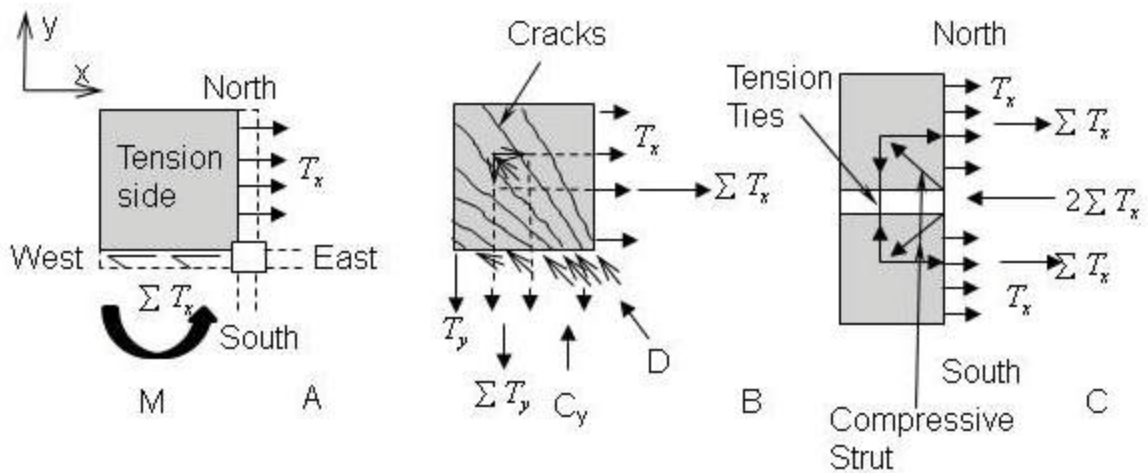


Figure 2-17. Proposed force transfer mechanism in an external edge panel (Adapted from Cheung et al., 1991). A) equilibrium of forces in x direction only, B) equilibrium of forces in both x and y directions and C) idealized strut and tie model.

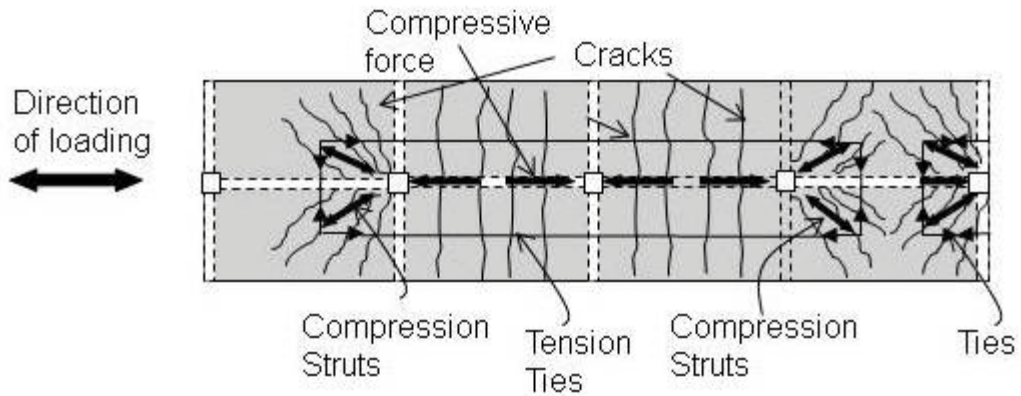


Figure 2-18. Proposed strut and tie model for continuous frame structure (Adapted from Cheung et al., 1991).

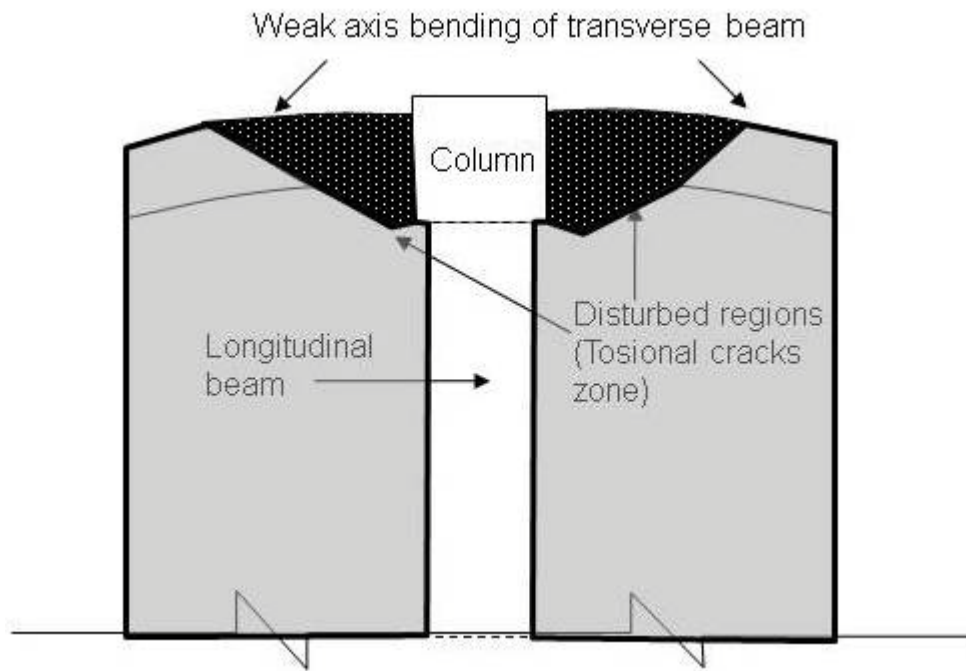


Figure 2-19. Plan view of exterior connection subjected to weak axis bending of the spandrel beam under the slab tension force (Adapted from Franco et al., 1995).

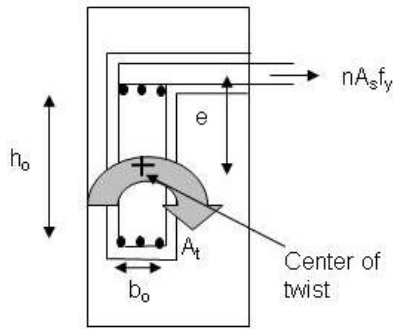


Figure 2-20. Sectional view of exterior connection subjected to torsional moments (Adapted from Franco et al., 1995).

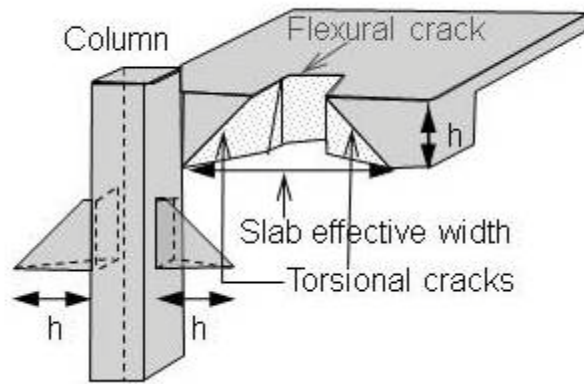


Figure 2-21. Failure in specimen with slab due to torsional failure in spandrel beam (Adapted from Durrani and Zerbe, 1987).

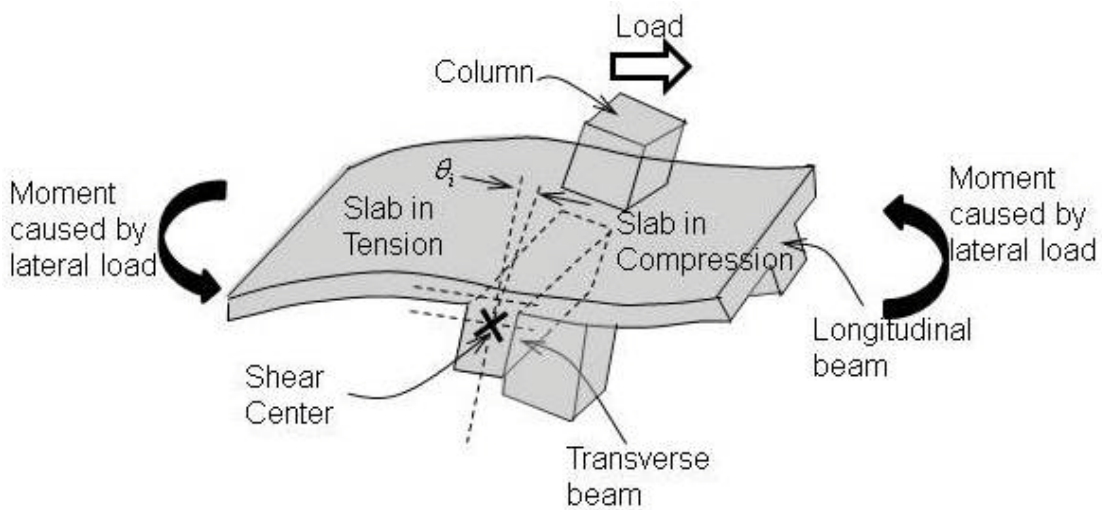


Figure 2-22. Typical deformation behavior of an interior connection subjected to lateral load (Adapted from Shahrooz et al., 1992).

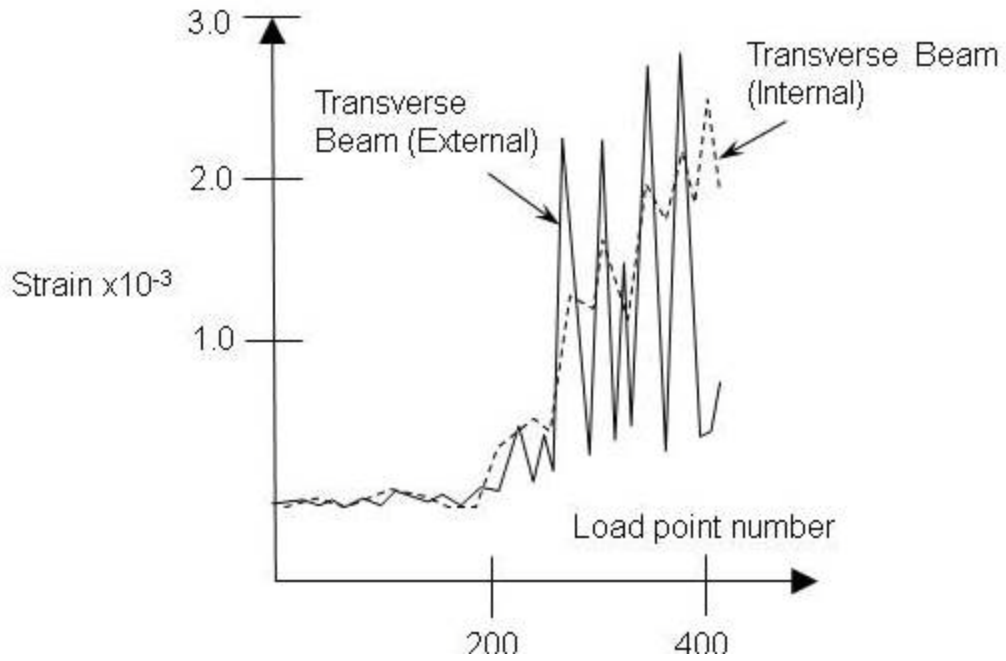


Figure 2-23. Measured stirrup strain for interior and exterior transverse beams (Adapted from Qi and Pantazopoulou, 1991).

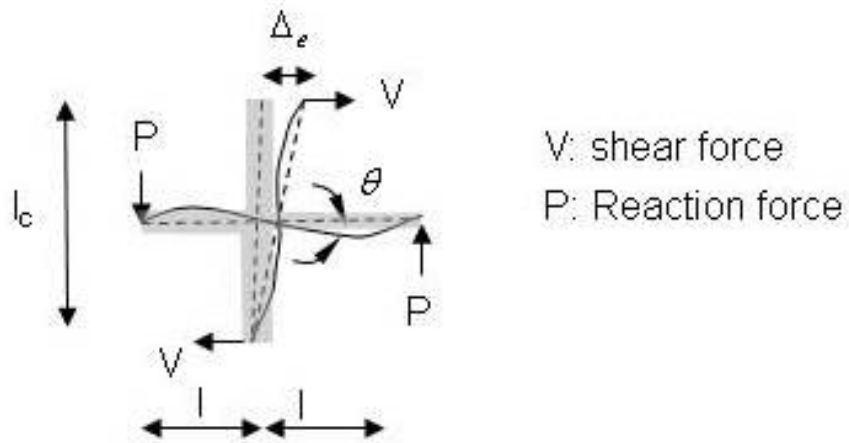


Figure 2-24. Deformation behavior under seismic load (Adapted from Cheung et al., 1991).

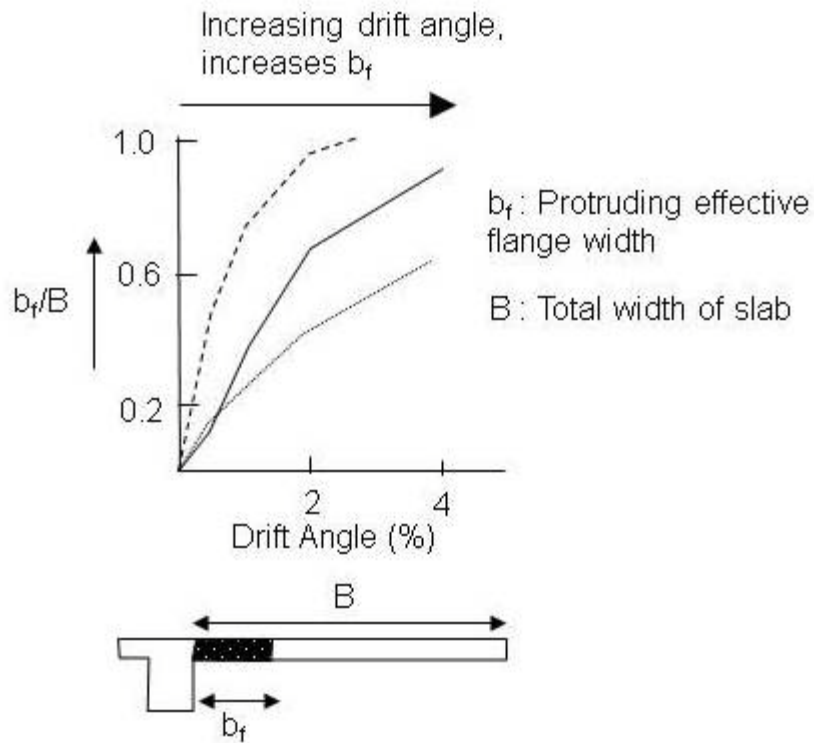


Figure 2-25. Plot of slab effective width ratio versus drift angle (Adapted from Kurose et al., 1991).

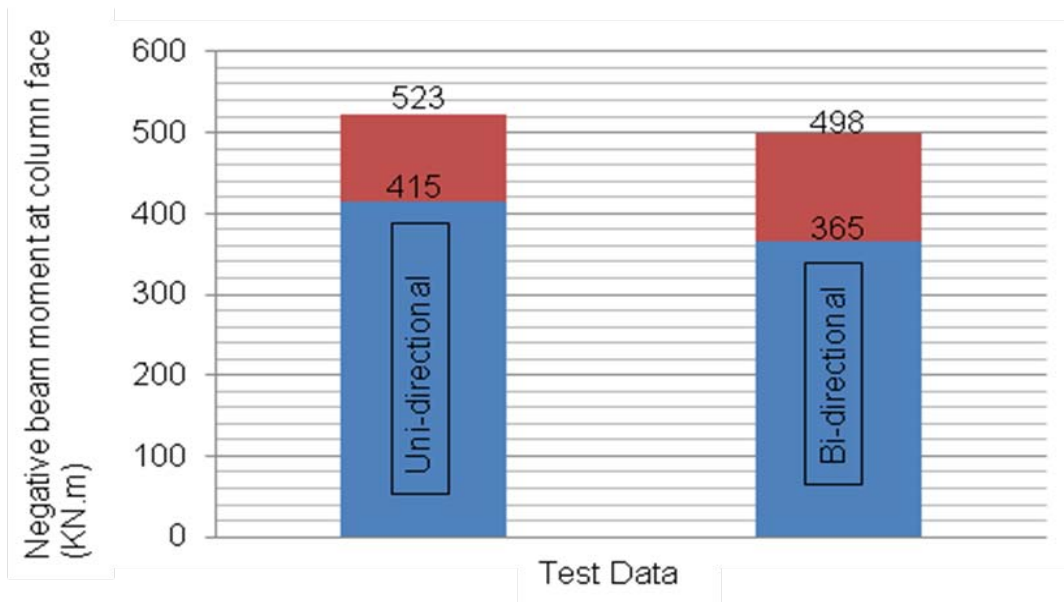


Figure 2-26. Comparison of negative bending moment of longitudinal beam for uni-directional and bi-directional loading (Adapted from Cheung et al., 1991).

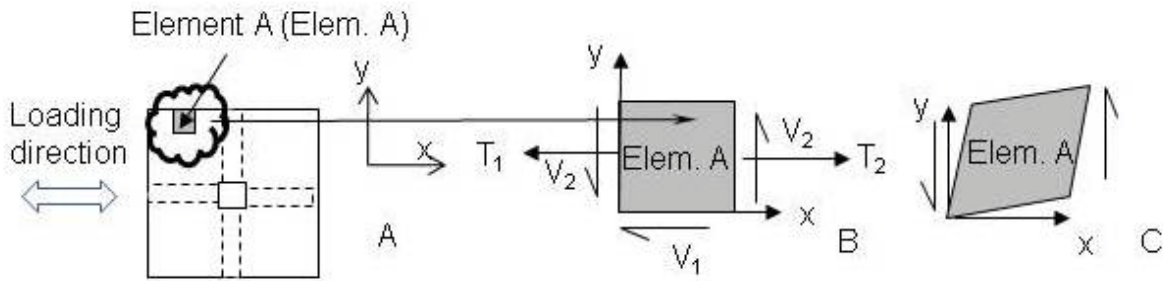


Figure 2-27. Shear deformation of a slab (Adapted from Ammerman and French, 1989). A) plan view, B) forces at element A and C) shear deformation.

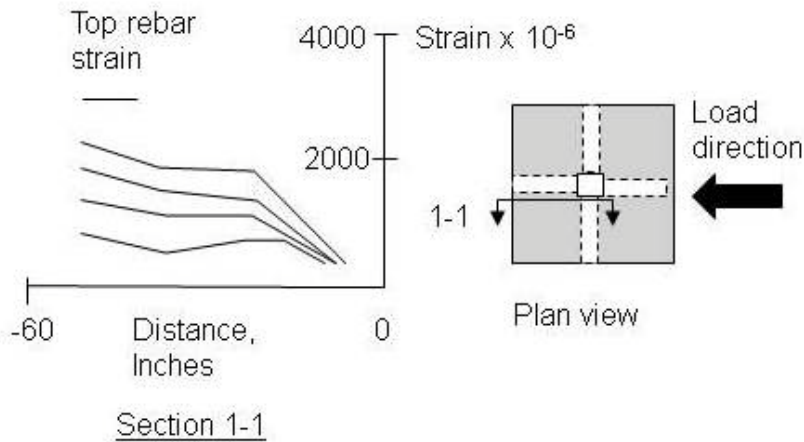


Figure 2-28. Transverse slab reinforcement strain distribution for isolated subassembly (Adapted from French and Boroojerdi, 1989).

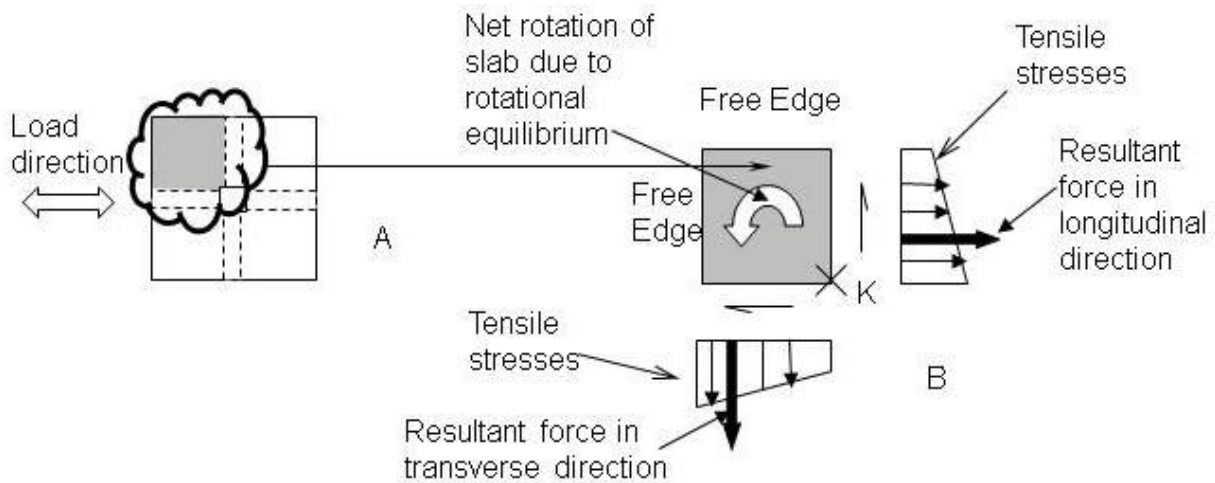


Figure 2-29. Stress states in slab for S-T case (Adapted from Ammerman and French, 1989). A) plan view and B) stresses acting on the slab (S-T case).

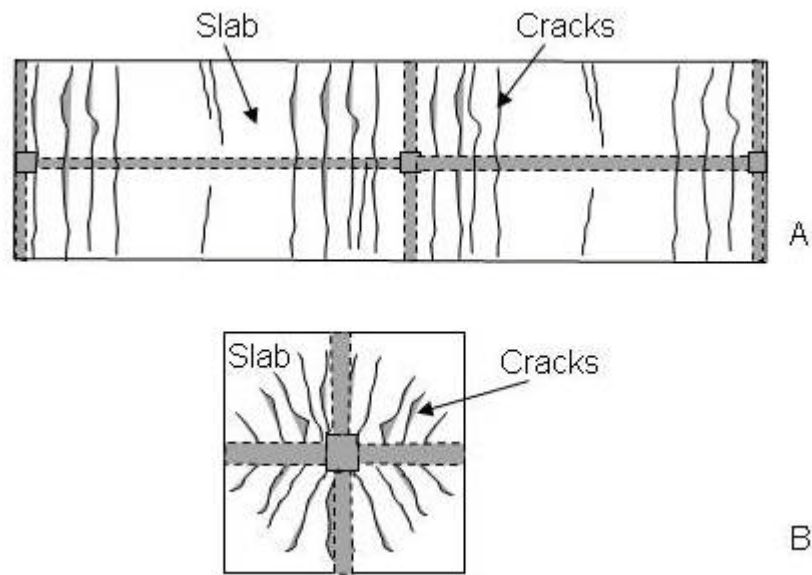


Figure 2-30. Cracks patterns under uni-axial lateral load (Adapted from French and Moehle, 1991). A) continuous panels and B) isolated panels.

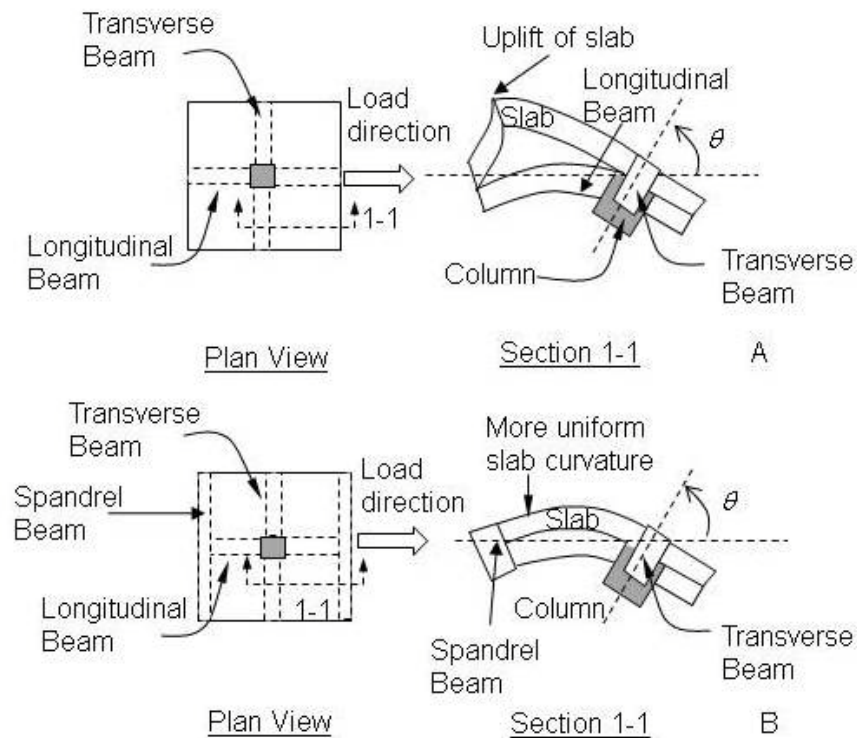


Figure 2-31. Effects of continuity (end beam) on slab curvature due to flexural deformation (Adapted from Ammerman and French, 1989). A) with no end beam and B) with end beam.

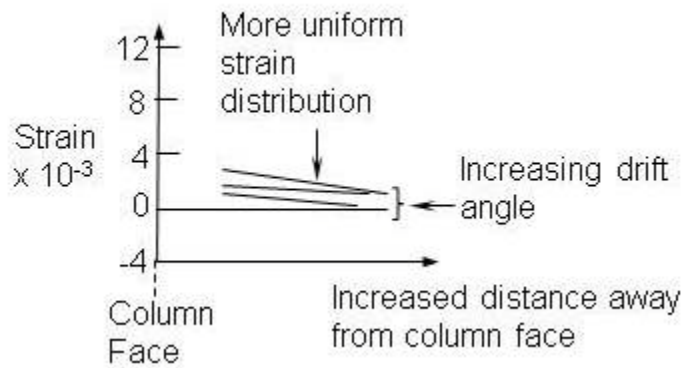


Figure 2-32. Longitudinal slab reinforcement strain distribution for continual structure (Adapted from Qi and Pantazopoulou, 1991).

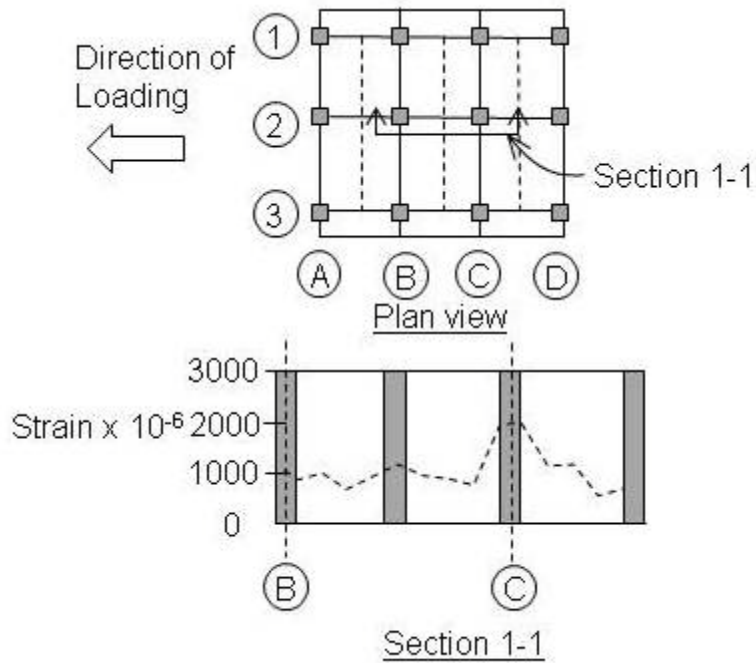


Figure 2-33. Transverse slab reinforcement strain distribution for continual structure (Adapted from French and Moehle, 1991).

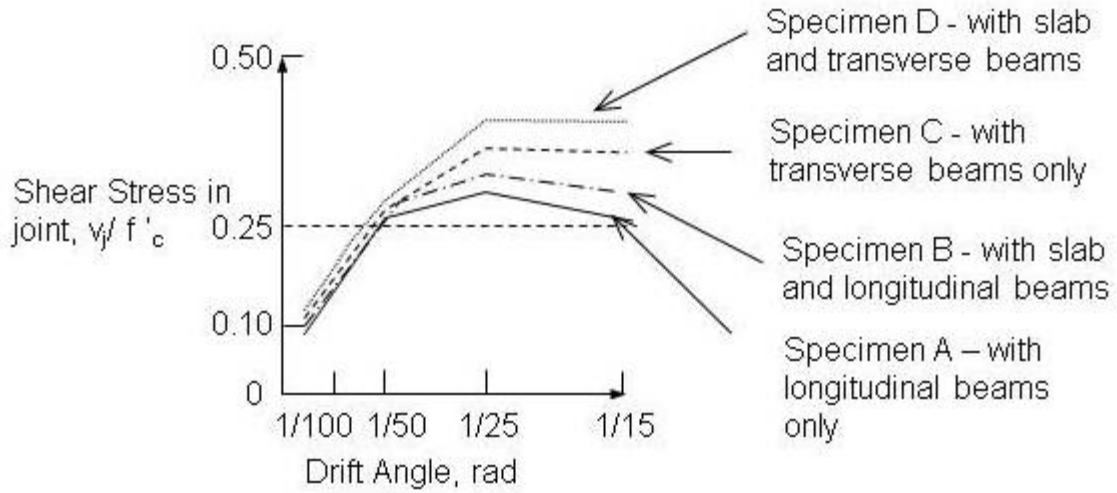


Figure 2-34. Variation of joint shear stress with different structural configurations (Adapted from Kitayama et al., 1991).

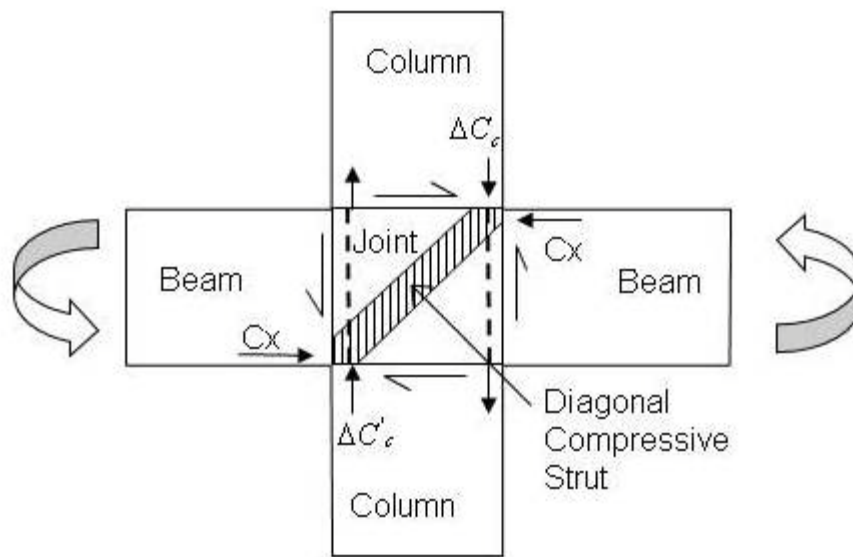


Figure 2-35. Joint mechanism hypothesized to resist the additional force from the tension slab reinforcement (Adapted from Cheung et al., 1991).

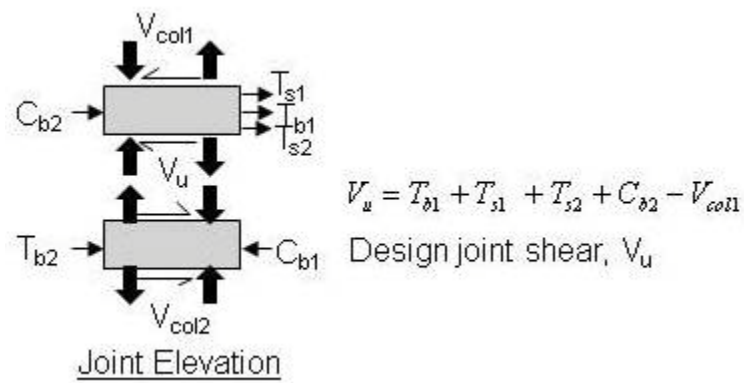


Figure 2-36. Design horizontal shear force for Type 2 connection (Adapted from ACI committee 352, 2002).

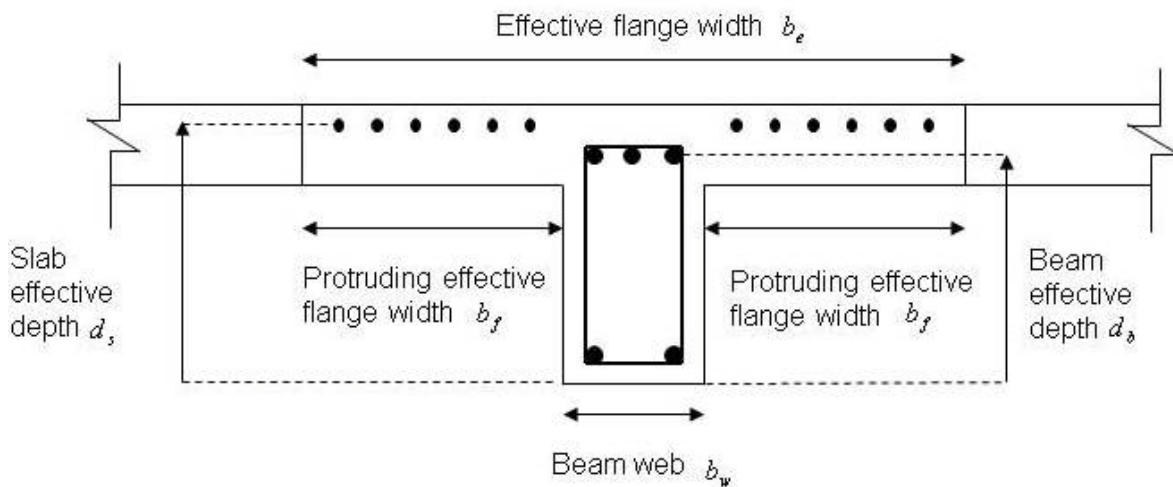


Figure 2-37. Notation and definition for a typical effective flange width.

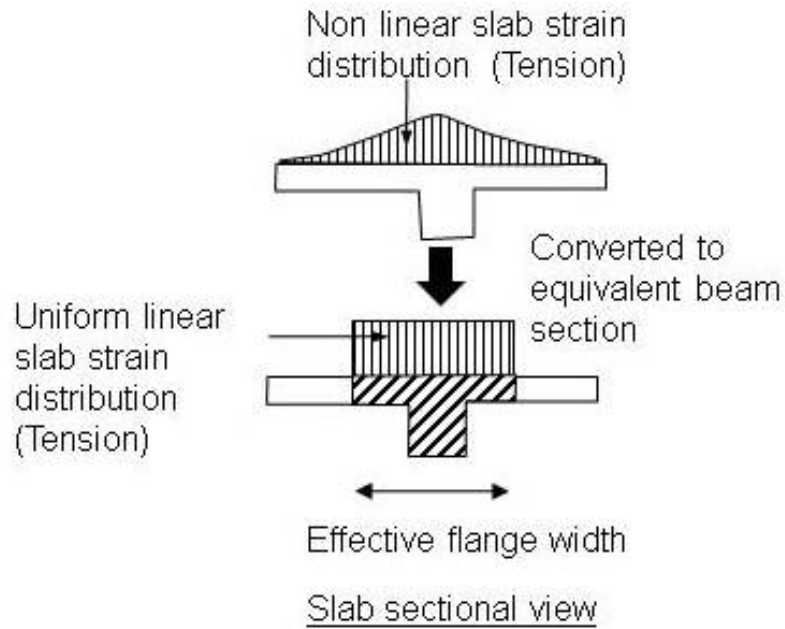


Figure 2-38. Idealization for the effective flange width (Adapted from Pantazopoulou et al., 1988).

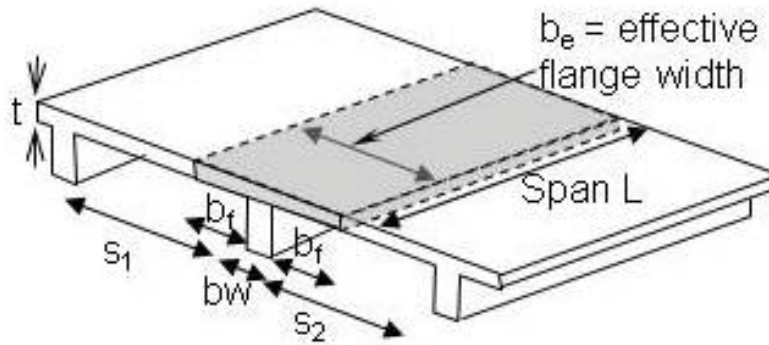


Figure 2-39. Effective flange width for T-beam (Adapted from ACI Committee 318, 2008).

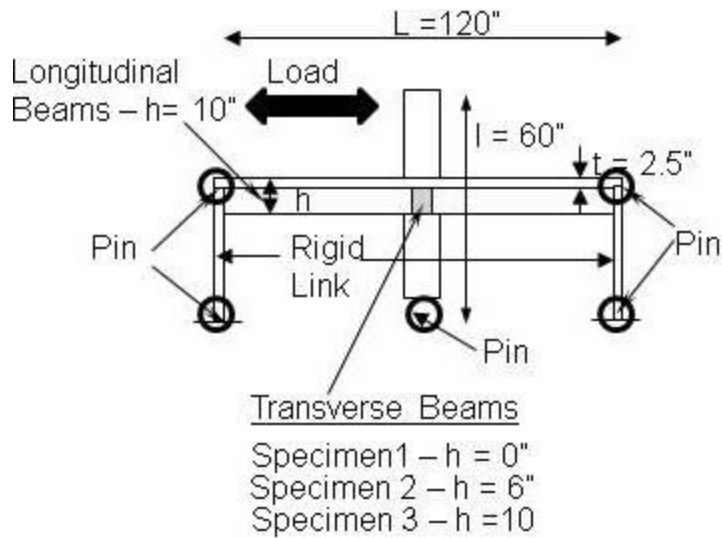


Figure 2-40. Test specimens for interior subassemblages (Adapted from French and Boroojerdi, 1989).

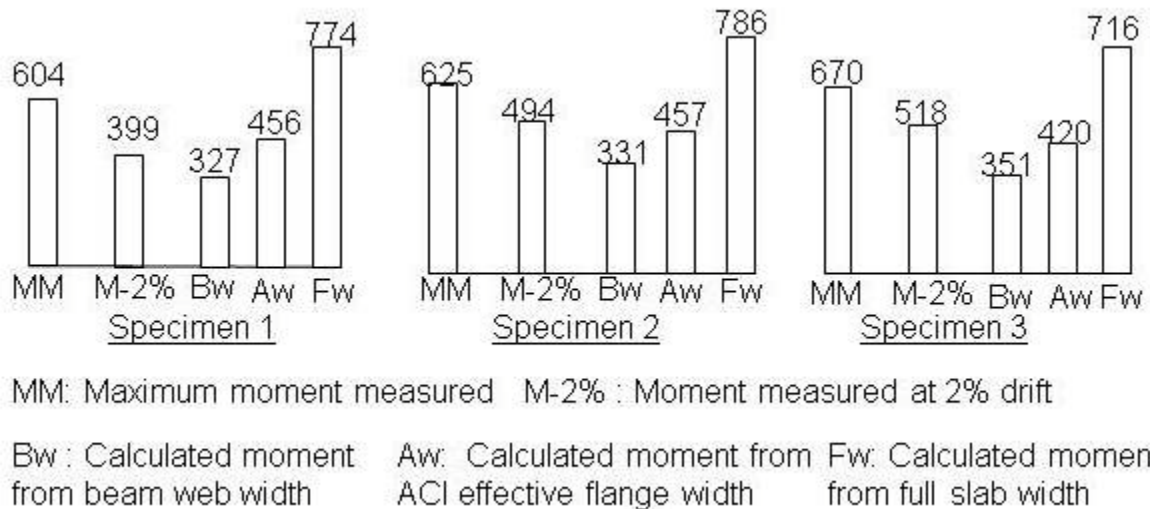


Figure 2-41. Comparison of measured moments with calculated moments for different effective flange widths (Adapted from French and Boroojerdi, 1989).

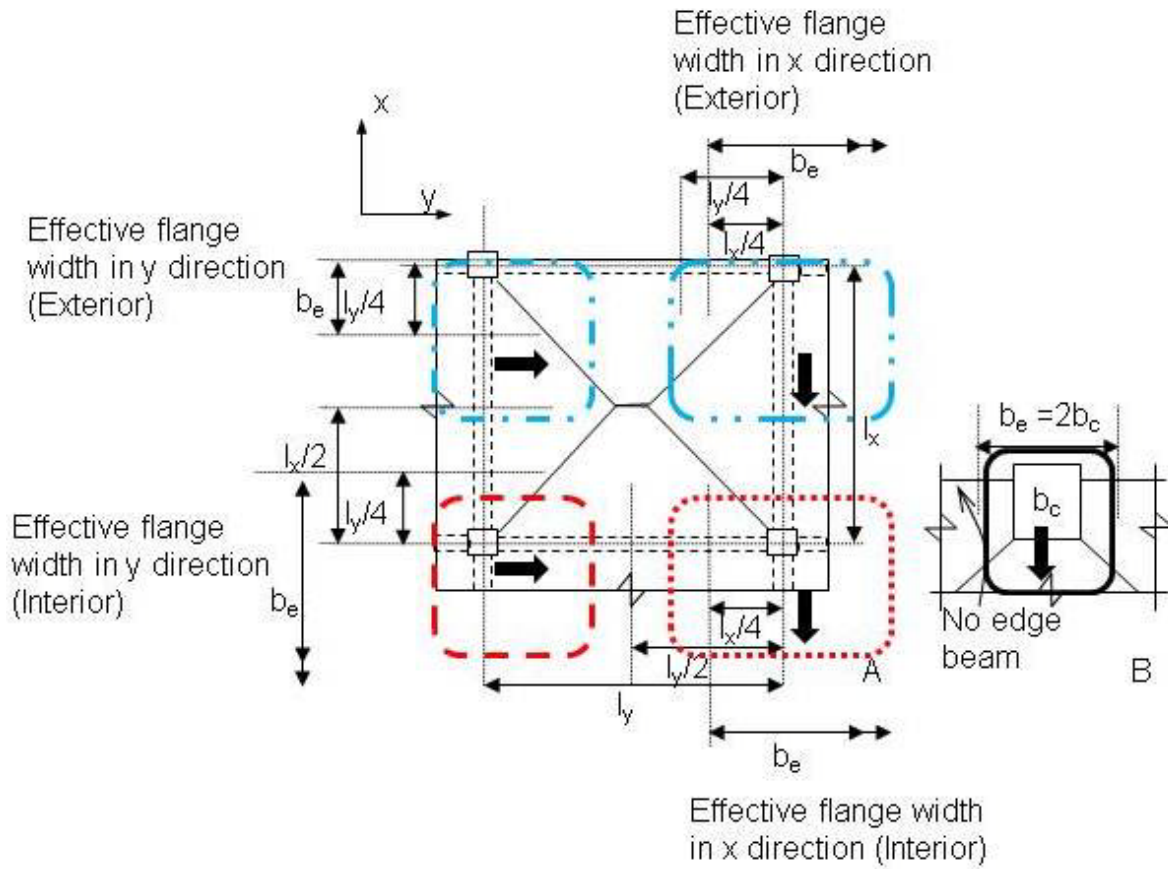


Figure 2-42. Effective tensile flange widths for cast-in-place floor system (Adapted from Cheung et al., 1991). A) interior connection and B) exterior connection without transverse beam.

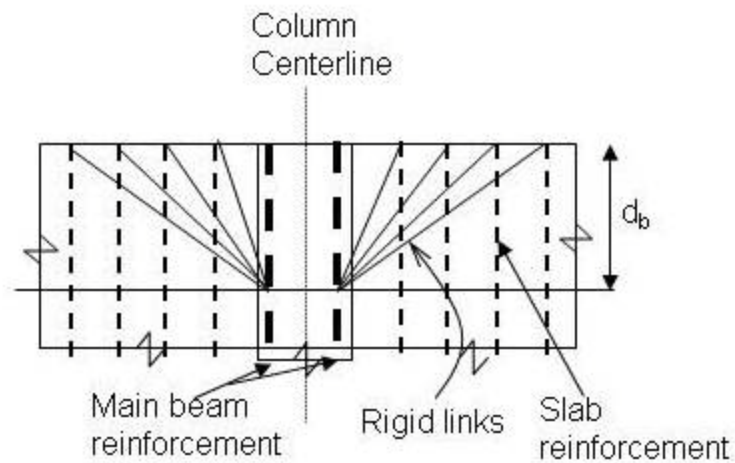


Figure 2-43. Simple connection model (Adapted from Pantazopoulou et al., 1988).

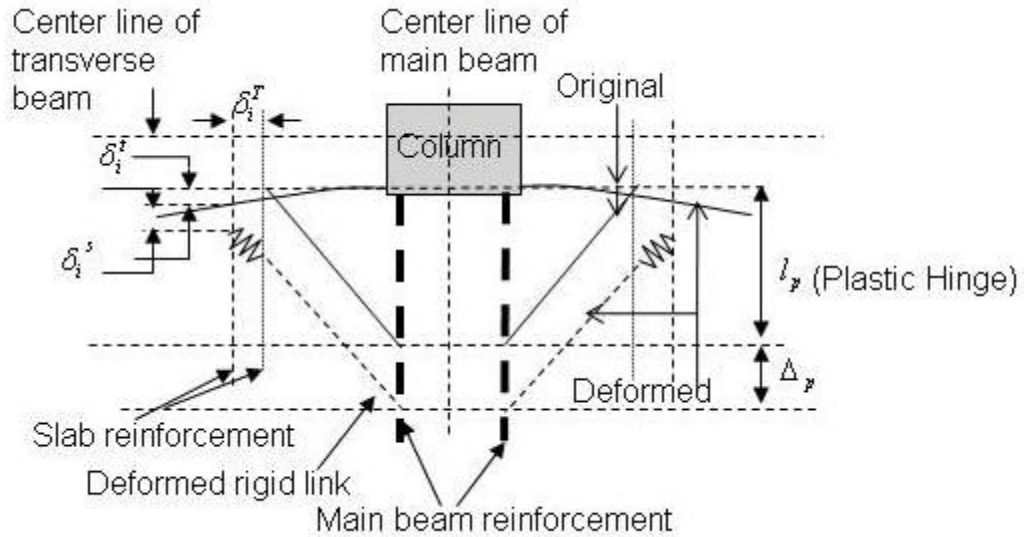


Figure 2-44. Improved kinematic formulation for rigid links (Adapted from Shahrooz et al., 1992).

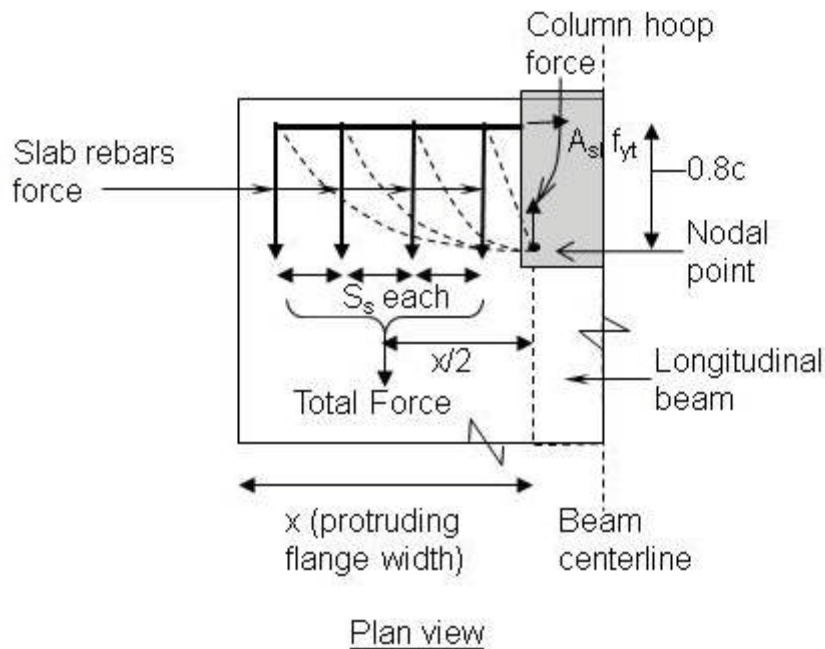


Figure 2-45. Suggested strut and tie model for spandrel beam after torsional cracking (Adapted from Franco et al., 1995).

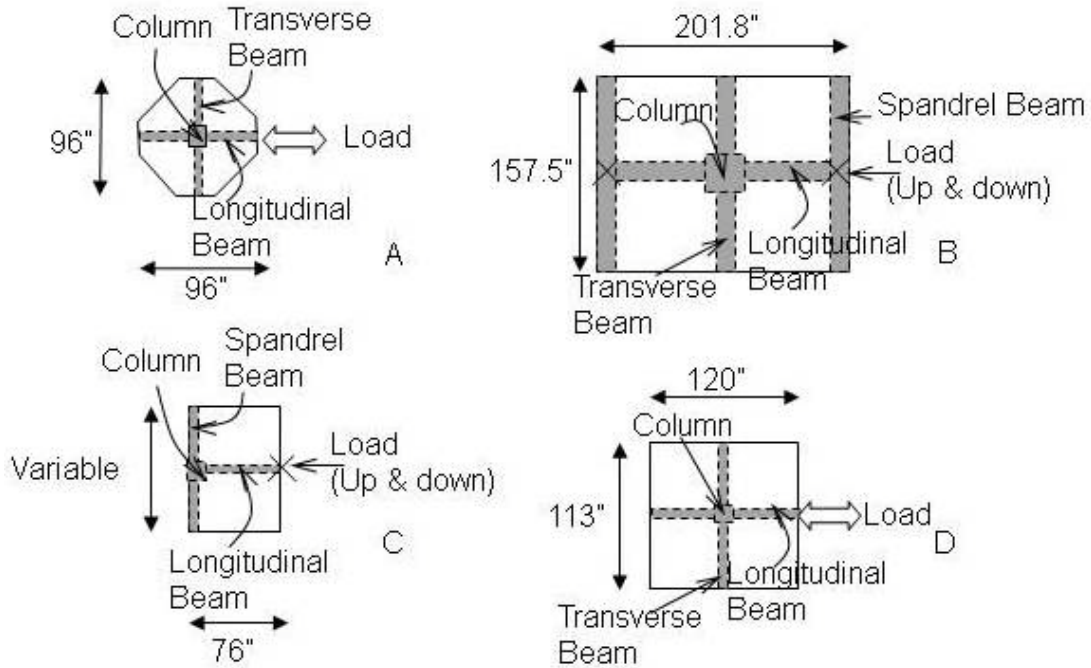


Figure 2-46. Typical layout plans and sectional details for various test series (Adapted from Ammerman and French, 1989). A) Uto, B) TIP, TEP, TIM and TEM, C) J4 to J7 and D) EW1 to EW3.

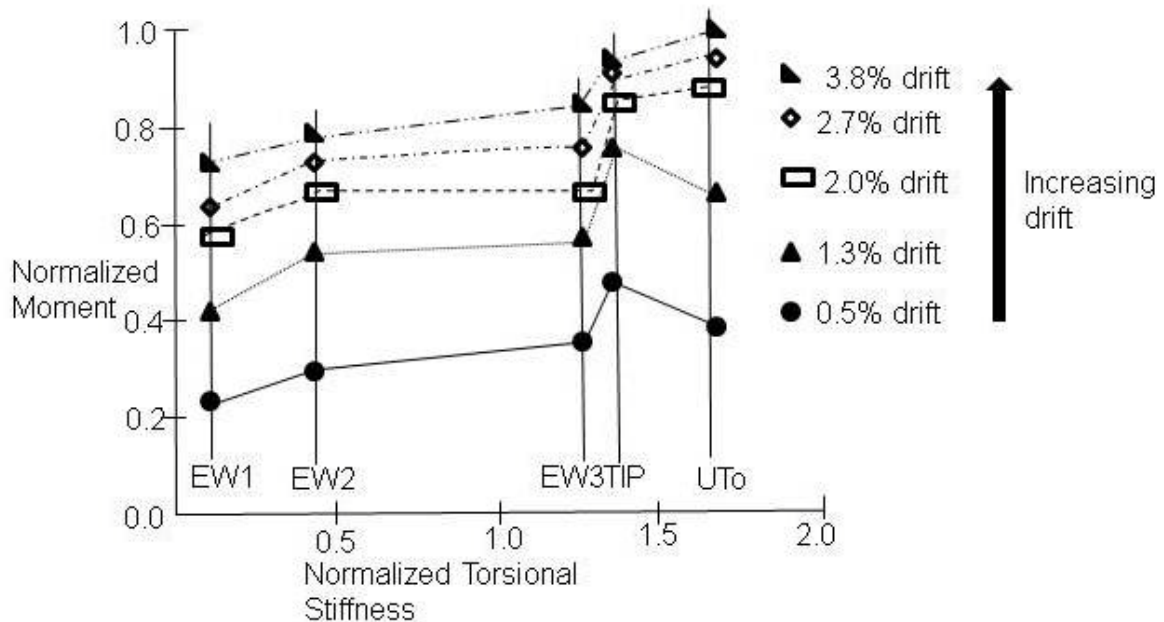


Figure 2-47. Comparison plot of normalized moment and torsional stiffness for interior subassemblages from various test series (Adapted from Ammerman and French, 1989).

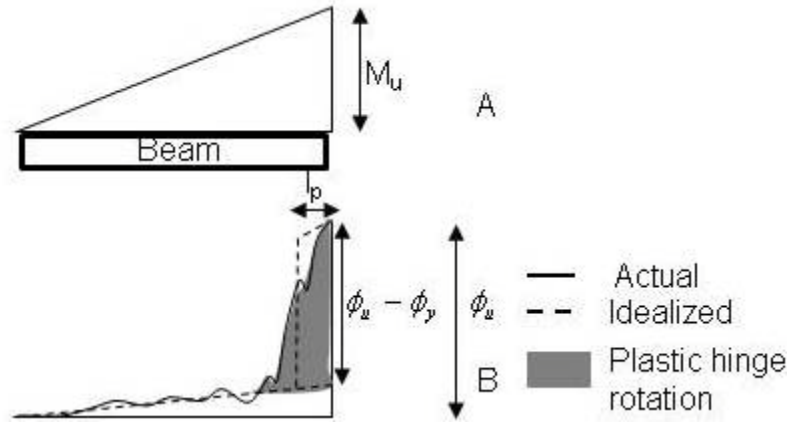


Figure 2-48. Cantilever beam at ultimate moment (Adapted from Park and Paulay, 1975). A) bending moment diagram and B) curvature diagram.

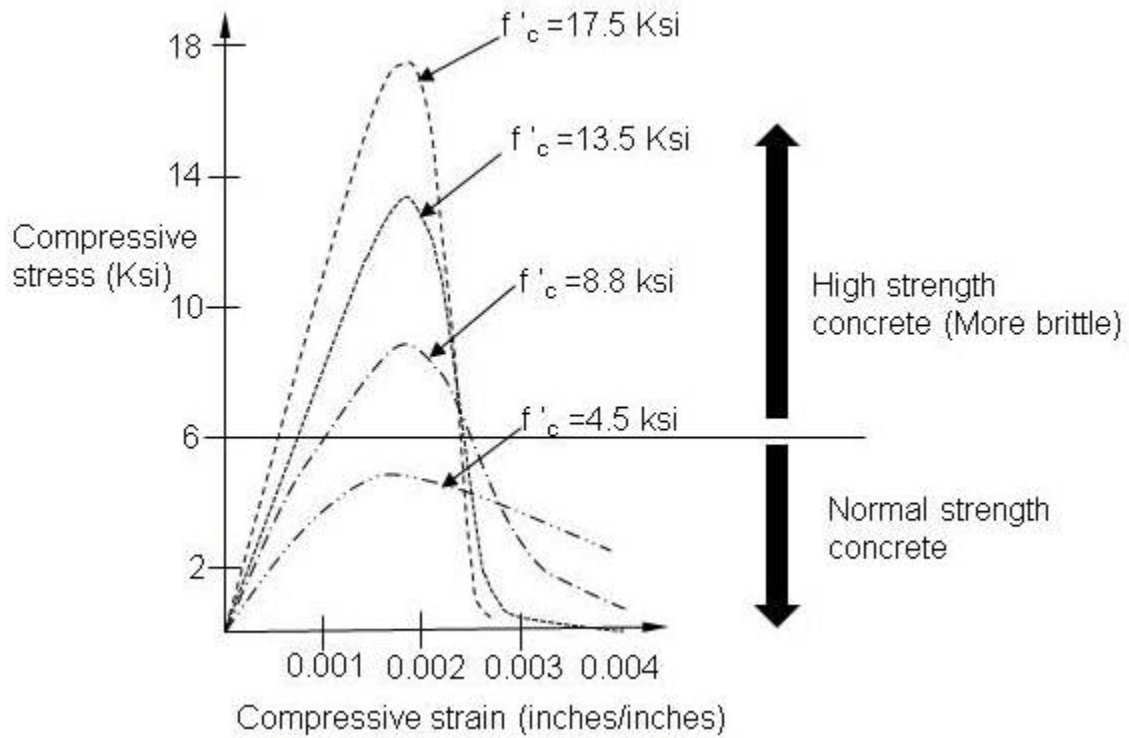


Figure 2-49. Typical concrete compressive stress-strain curve for different concrete strengths (Adapted from Macgregor and Wight, 2005).

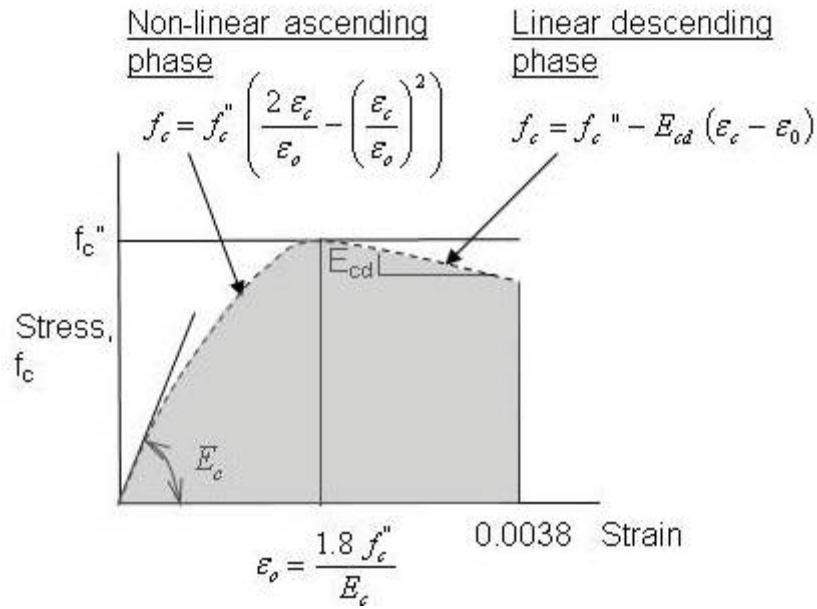


Figure 2-50. Modified Hognestad stress-strain curve for concrete in compression (Adapted from Macgregor and Wight, 2005).

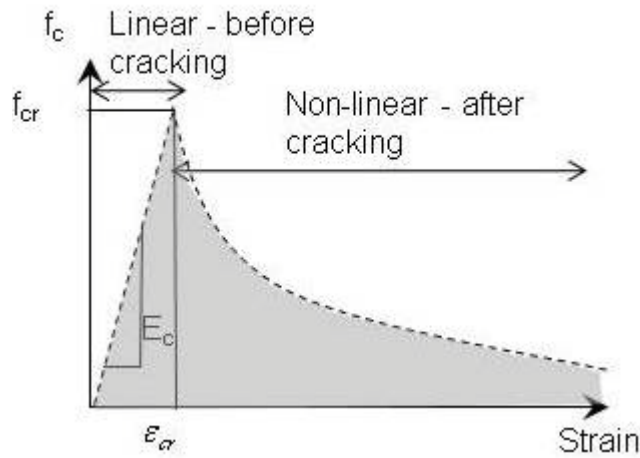


Figure 2-51. Typical tensile stress strength curve of reinforced concrete (Adapted from Hsu, 1993).

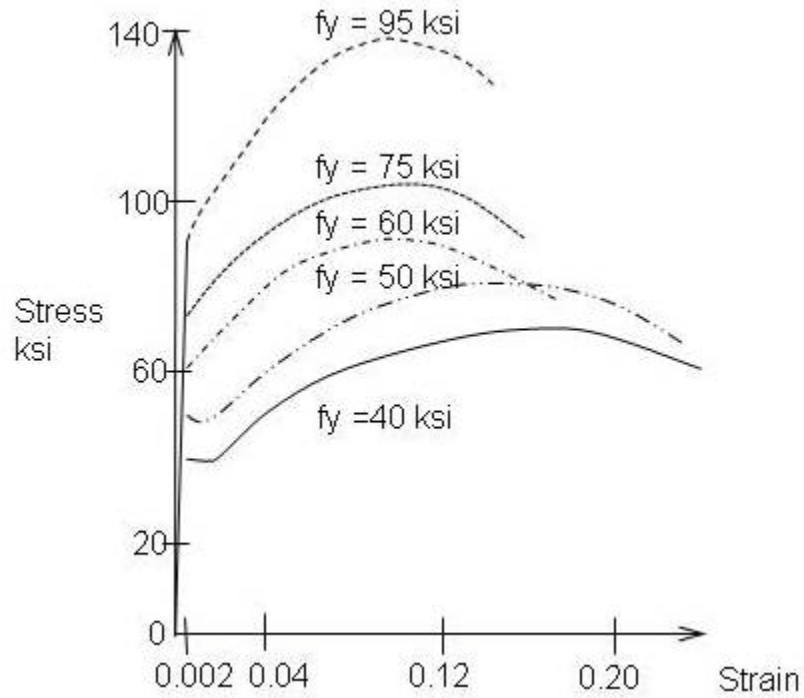


Figure 2-52. Typical stress-strain curve for steel reinforcement (Adapted from Hassoun and Manasser, 2005).

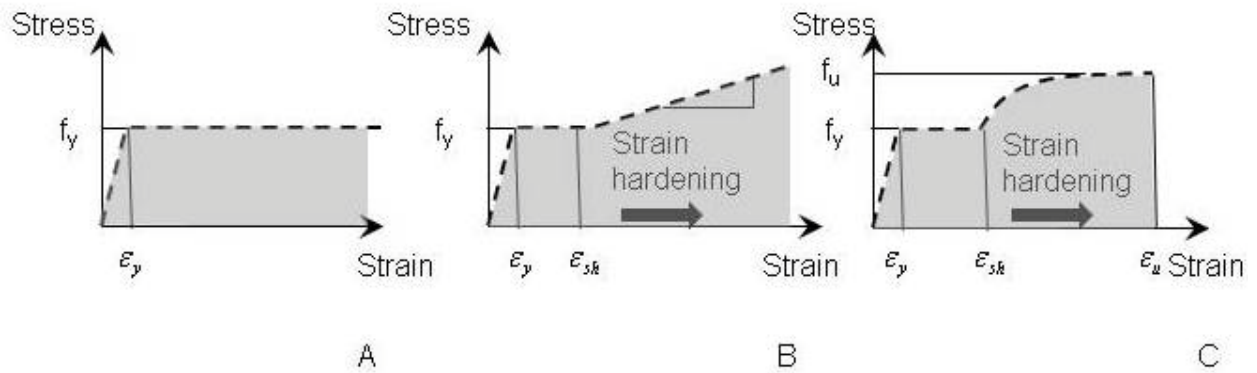


Figure 2-53. Different idealized steel reinforcement stress-strain curve (Adapted from Chen, 1982). A) elastic- perfect plastic, B) bi-linear and C) non-linear.

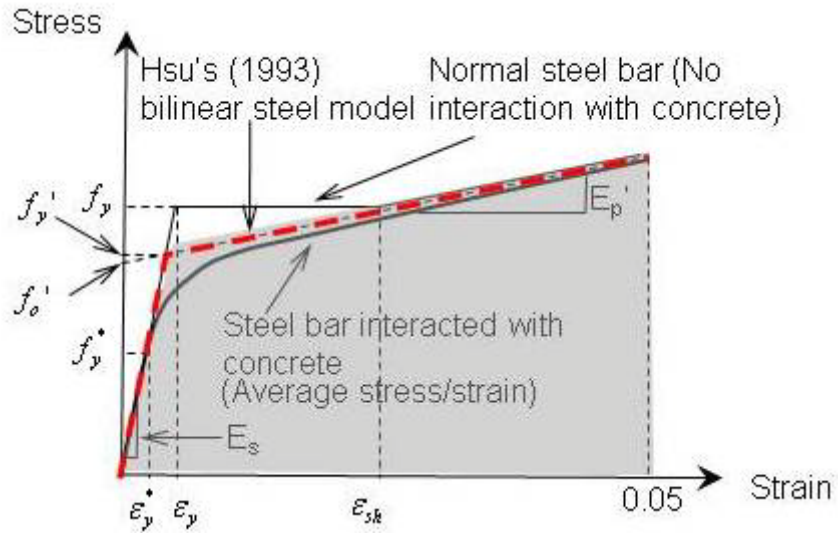


Figure 2-54. Proposed bilinear stress-strain curve for steel reinforcement in reinforced concrete (Adapted from Hsu, 1993).

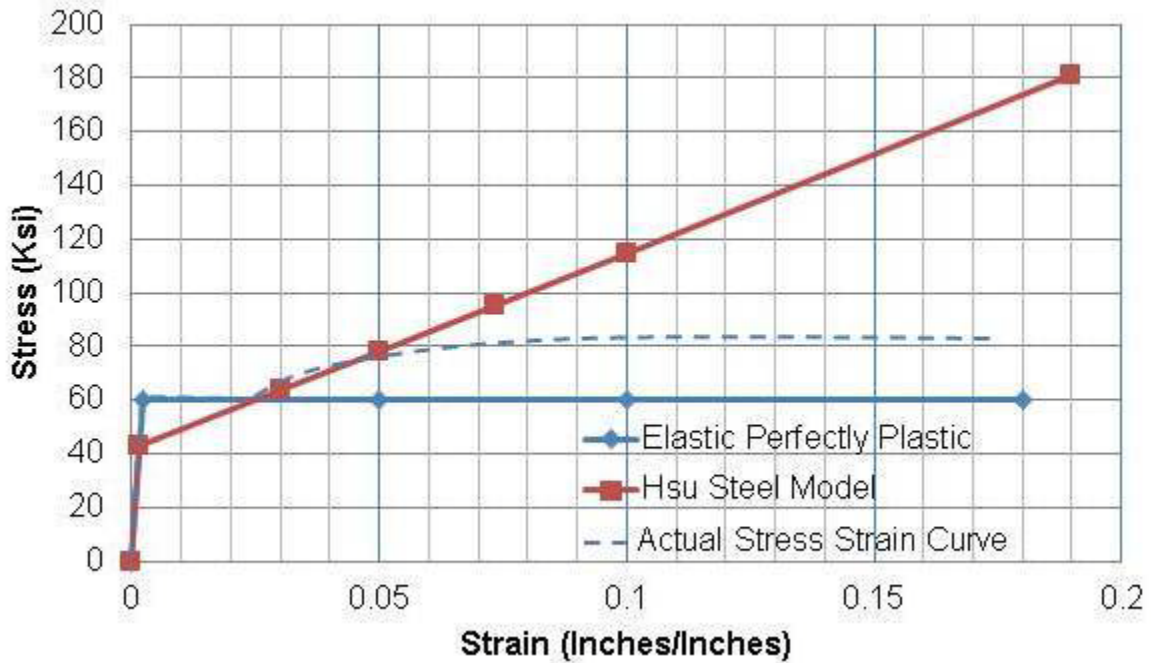


Figure 2-55. Different idealization of steel reinforcement stress-strain curve.

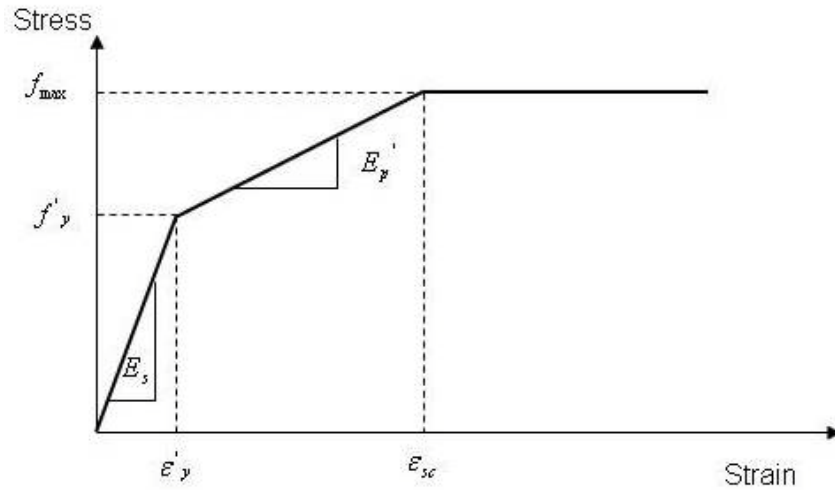


Figure 2-56. Proposed steel stress-strain curve modified from Hsu's model.

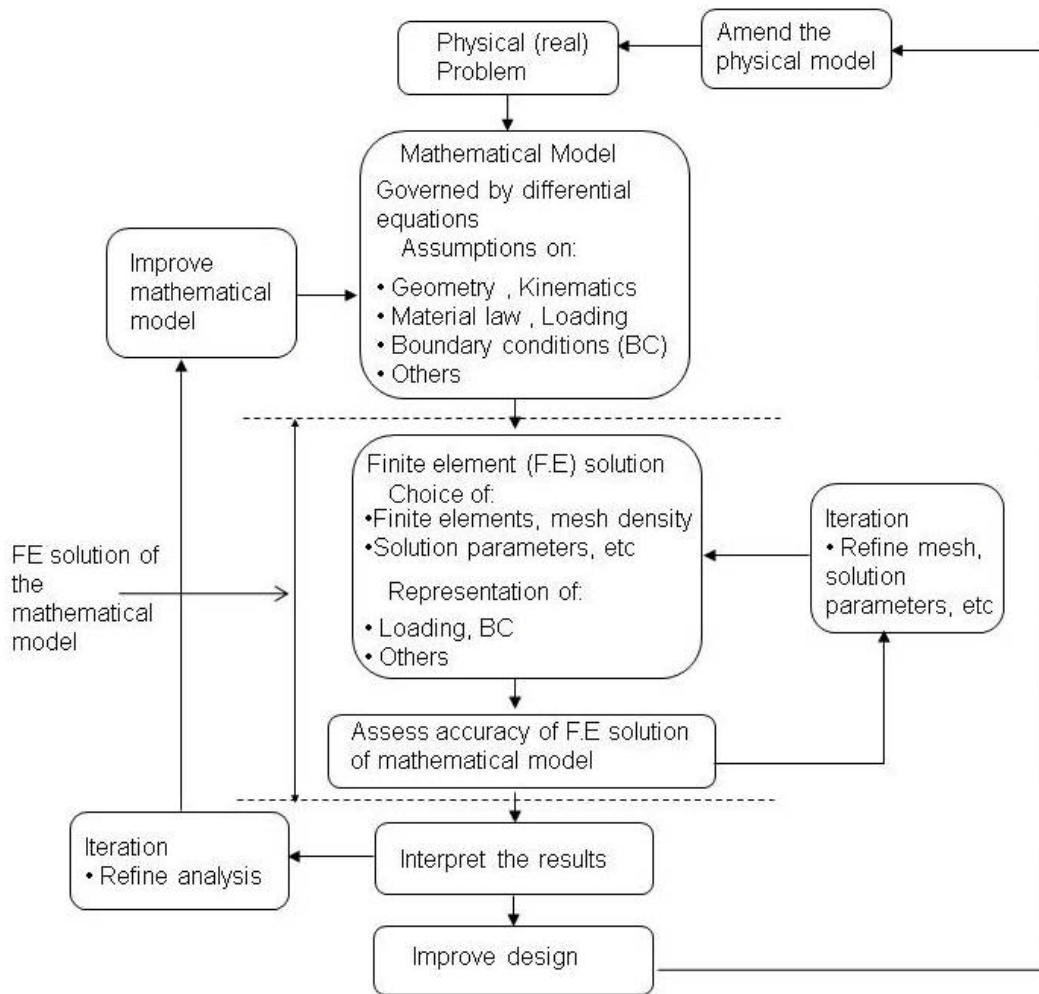


Figure 2-57. Flow process of finite element (FE) analysis for a physical problem (Adapted from Bathe, 1996).

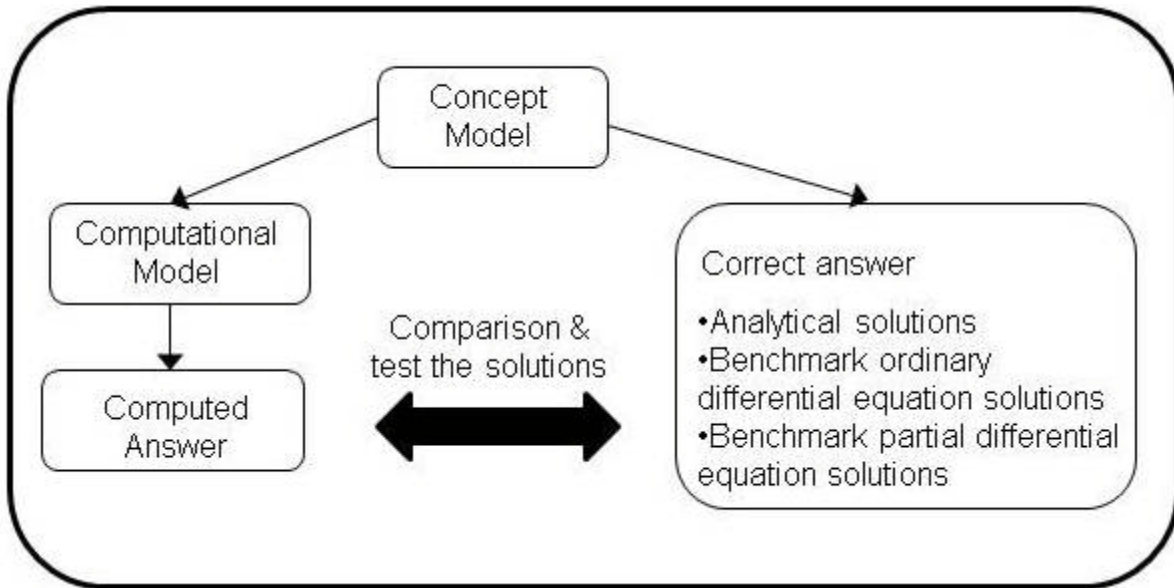


Figure 2-58. FE verification process (Adapted from Oberkampf et al., 2004).

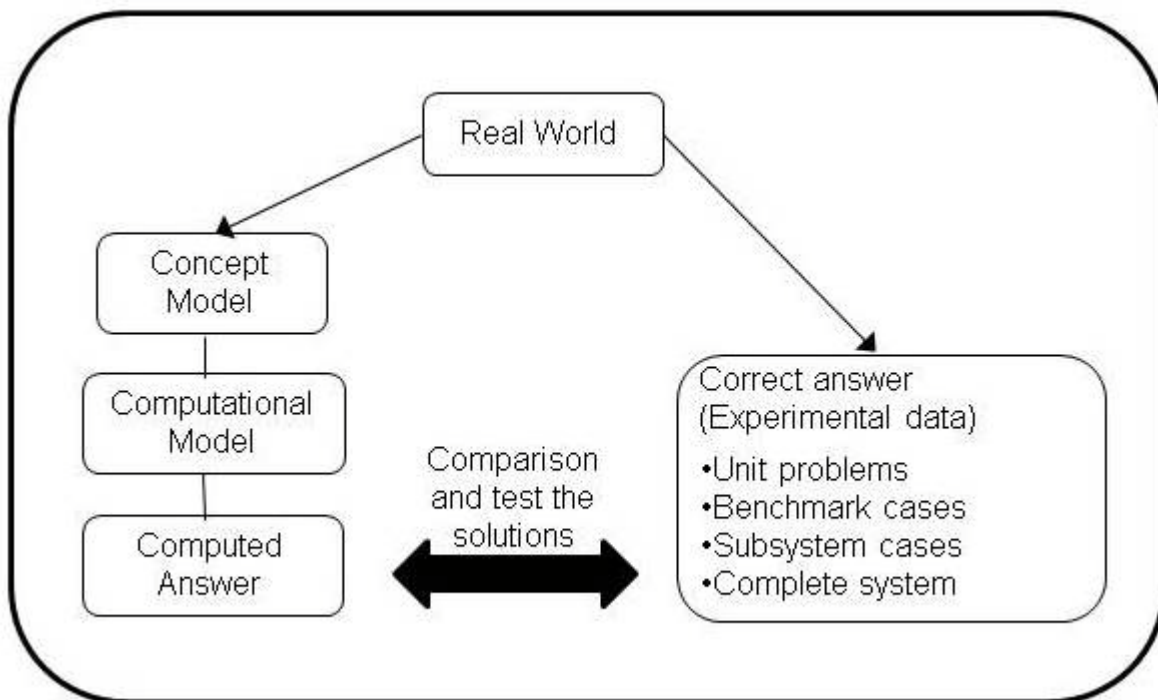


Figure 2-59. FE validation process (Adapted from Oberkampf et al., 2004).

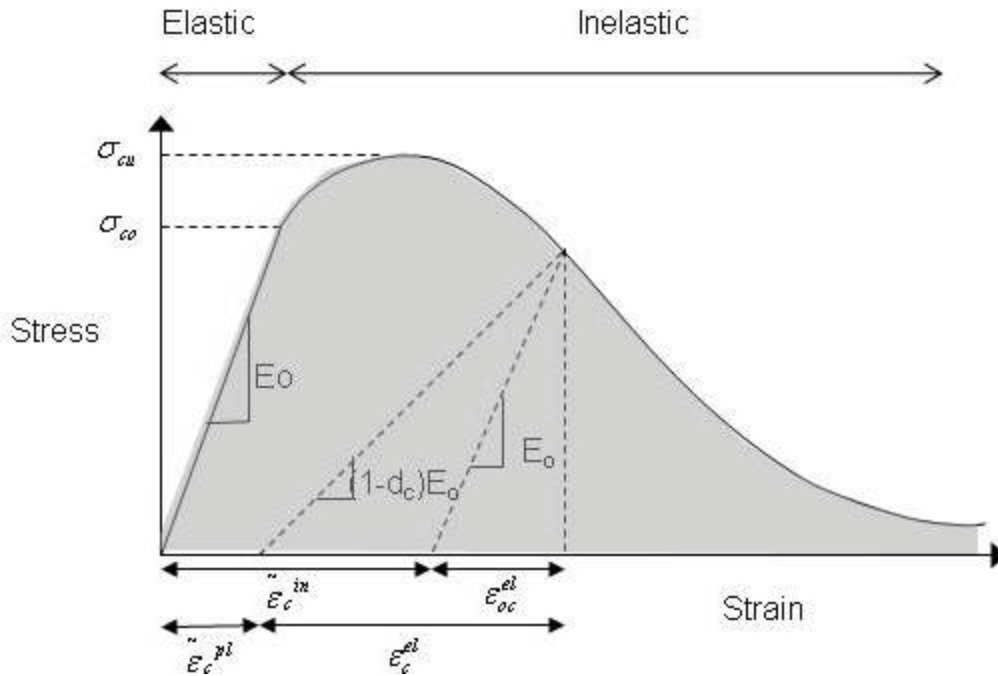


Figure 2-60. Uniaxial compressive stress-strain curve in concrete damaged plasticity (CDP) material model (Adapted from Simulia, 2010).

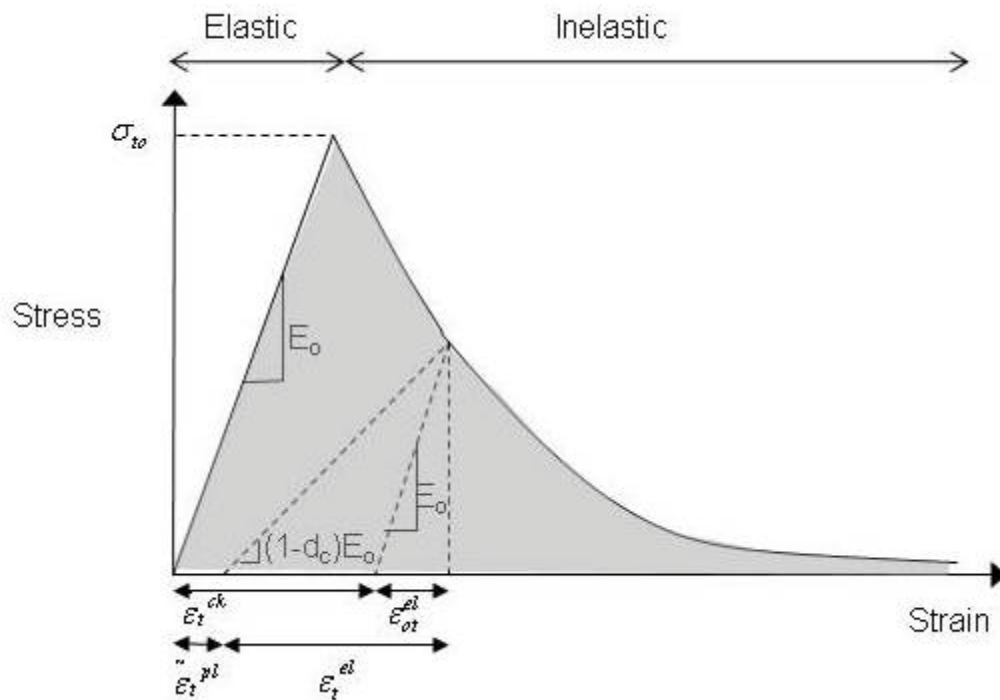


Figure 2-61. Tension stiffening stress-strain curve in CDP material model for post failure behavior (Adapted from Simulia, 2010).

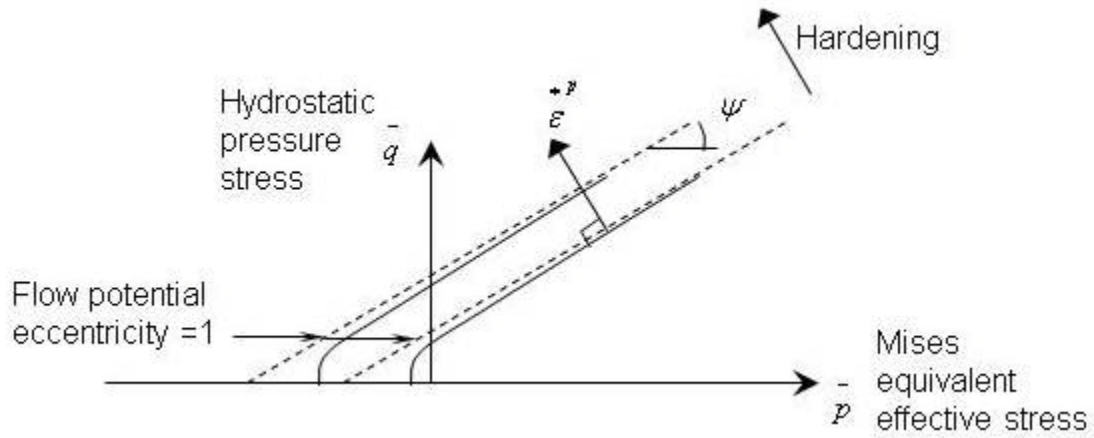


Figure 2-62. Drucker-Prager plastic flow potential (Adapted from Simulia, 2010).

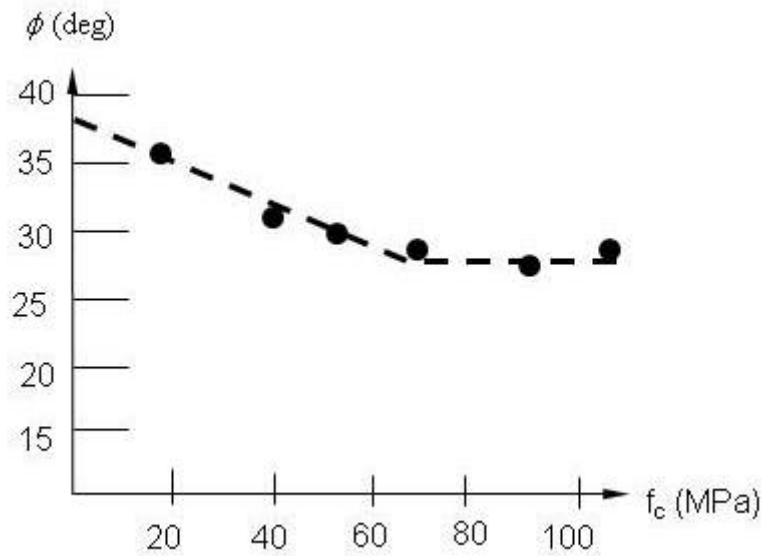


Figure 2-63. Friction angles for different concrete compressive strength (Adapted from Nielsen, 1999).

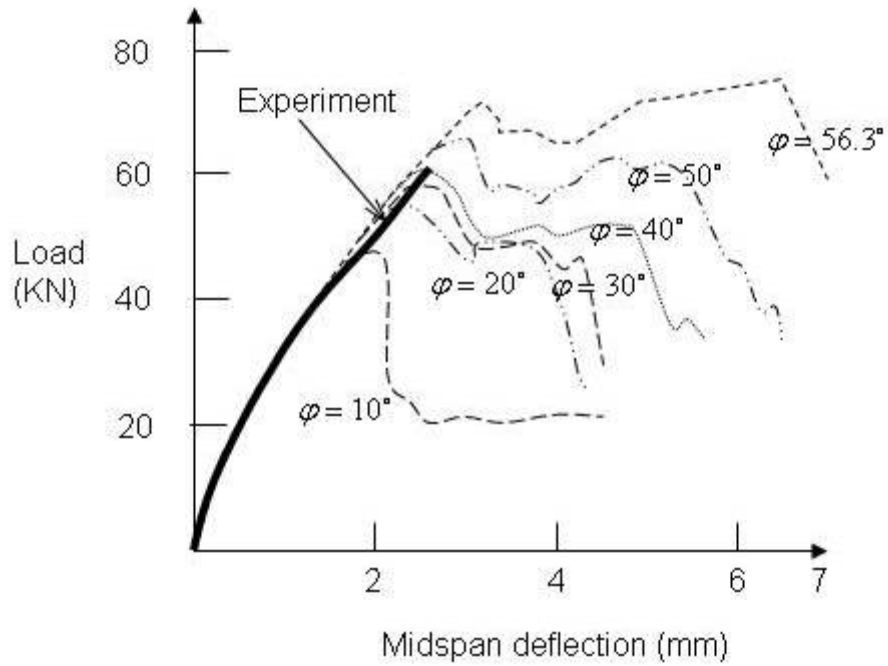


Figure 2-64. Parameter study of the dilation angles (Adapted from Malm, 2006)

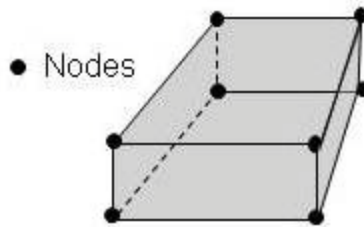


Figure 2-65. Typical 8 nodes linear brick element (Adapted from Simulia, 2010).

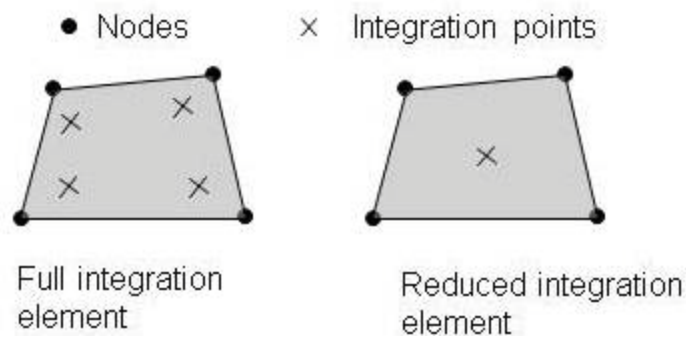


Figure 2-66. Integration points for 8 node element (Adapted from Simulia, 2010).

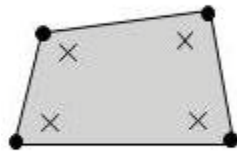
• Nodes    × Integration point



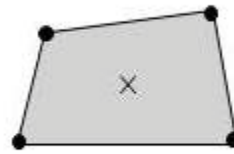
2 node element

Figure 2-67. Typical 2 nodes linear beam element (Adapted from Simulia, 2010).

• Nodes    × Integration points



Full integration element



Reduced integration element

Figure 2-68. Typical 4 nodes linear shell element (Adapted from Simulia, 2010).

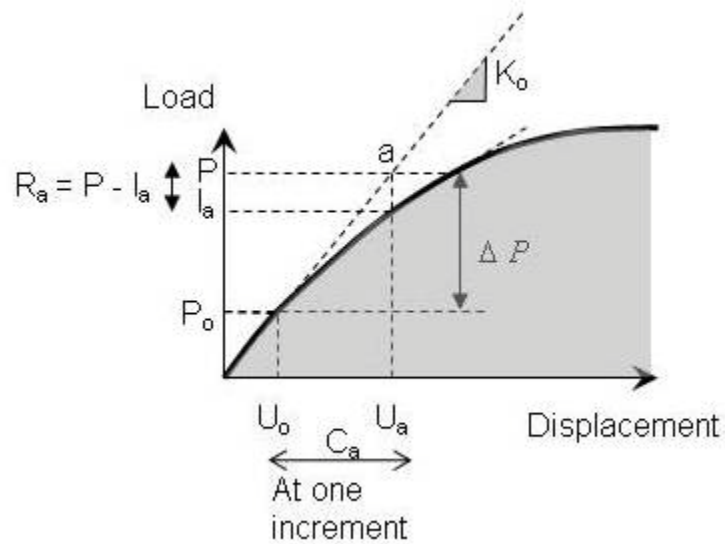


Figure 2-69. Non-linear response in a single increment (Adapted from Simulia, 2010).

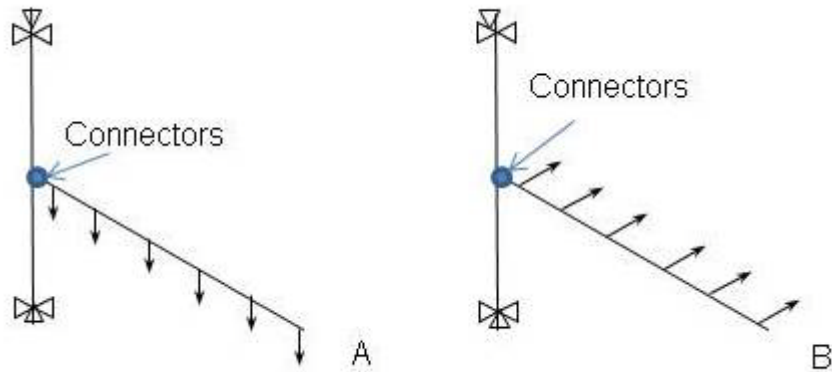


Figure 2-70. Components of the simplified structural element based FE building frame model (Adapted from Yim, 2007).

Table 2-1. Various effective flange widths for interior connection

S/N	References	Protruding Effective Flange Width, $b_f / d_s$	Remarks
1	ACI Committee 352 (2002), section 3.32	1.99	ACI Committee 352 (2002), section 3.32 further reference to provision in ACI Committee 318 (2008), section 8.12.2 for T-beam. Computed from the provision assuming an arbitrary beam and slab dimensions.
2	French and Boroojerdi (1989) – For Seismic	4.50	Computed based on 80% of the full slab width that corresponds to the ultimate moment at ~ 4% to 5% inter-storey drift
3	Pantazopoulou and Moehle (1990) - For Seismic	3.00	Observed from experiments from Qi(1986) for ultimate moment
4	Cheung et al.(1991) - For Seismic	4.29	Computed from Figure 2-42

Table 2-2. Beam and slab reinforcement details for various test series (Adapted from Ammerman and French, 1989).

Element	Subassemblage				
	EW1-3	TIP, TEP	TIM, TEM	UTo	Rice
Longitudinal beam					
Top	3 US. No.3	3 US. No.6	5 US. No.7	4 No. D13 <sup>a</sup>	4 US. No.6
Bottom	2 US. No.3	2 US. No.6	3 US. No.7	4 No. D13	4 US. No.6
Transverse Beam					
Top	3 US. No.3	3 US. No.6	4 No.7	4 No. D13	2 US. No.8
Bottom	2 US. No.3	2 US. No.6	3 No.7	4 No. D13	2 US. No.8
Transverse reinforcement	US. No.2 @ 4" c.c. <sup>c</sup>	US. No.3 @ 4" c.c	US. No.3 @ 4" c.c	D6 <sup>b</sup> @ 3" c.c	US. No.4 @ 6" c.c
Slab					
Longitudinal direction	US. No. 2 <sup>d</sup> @7.5" c.c	US. No. 3 <sup>d</sup> US. 6 Nos @ 7.9" c.c 4 US. Nos @ 11.8" c.c 6 US. Nos @ 7.9" c.c	US. No. 3 <sup>d</sup> 6 US. Nos @ 7.9" c.c 4 US. Nos @ 11.8" c.c 6 US. Nos @ 7.9" c.c	D6 @7.9" c.c	US. No.4 @ 6" c.c
Slab					
Transverse direction	US. No. 2 <sup>d</sup> @7.5" c.c	US. No. 3 <sup>d</sup> @11.8" c.c	US. No. 3 <sup>d</sup> @11.8" c.c	D6 @7.9" c.c	US. No.4 @ 9" c.c

<sup>a</sup>D13 similar to US. No.4

<sup>b</sup>D6 similar to US. No.2

<sup>c</sup>c.c = center to center spacing

<sup>d</sup>Slab reinforcement in top and bottom (two layers).

Table 2-3. Reinforcement properties for various test series (Adapted from Ammerman and French, 1989).

Bar Size (1)	Diameter (in) (2)	Area (in <sup>2</sup> ) (3)	Yield Strength (Ksi) (4)	Ultimate Strength (Ksi) (5)	$\epsilon_{sh}^a$ (6)
EW1-3					
US. No. 2	0.25	0.05	61.1	85.1	0.024
US. No. 3	0.375	0.11	73.1	114.5	0.012
TIP, TEP					
US. No. 3	0.375	0.11	60	b	b
US. No. 6	0.75	0.44	58	b	b
TIM, TEM					
US. No. 3	0.375	0.11	75	b	b
US. No. 7	0.875	0.6	75	b	b
UTo					
D6	0.24	0.04	48	60	b
D13	0.51	0.21	51	76	b
Rice					
US. No. 4	0.5	0.2	77	109	0.015
US. No. 6	0.75	0.44	60	92	0.012
US. No. 8	1	0.79	70	104	0.012

<sup>a</sup> onset of strain hardening

<sup>b</sup> Information is not available in this reference

Table 2-4. Approximate range of tensile strengths of plain concrete (Adapted from Nilson et al., 2004)

	Normal weight concrete, (psi)	Light weight concrete, (psi)
$f_t'$	3 to $5\sqrt{f_c'}$	2 to $3\sqrt{f_c'}$
$f_{ct}$	6 to $8\sqrt{f_c'}$	4 to $6\sqrt{f_c'}$
$f_r$	8 to $12\sqrt{f_c'}$	6 to $8\sqrt{f_c'}$

Table 2-5. Spurious modes resulted from reduced integration (Adapted from Cook et al., 2004)

Element Type	Gauss Quadrature Rule		Spurious modes from reduced integration
	Full Integration	Reduced Integration	Number
4 node <sup>1</sup>	2 x 2	1	2
8 node <sup>1</sup>	3 x 3	2 x 2	1
9 node <sup>1</sup>	3 x 3	2 x 2	3
8 node <sup>2</sup>	2 x 2 x 2	1	12
20 node <sup>2</sup>	3 x 3 x 3	2 x 2 x 2	6

<sup>1</sup> Plane

<sup>2</sup> Solid

Table 2-6. Default values for convergence and iteration controls in Abaqus/Standard.

Description	Symbol	Value
Tolerance value for residual forces	$R_{\alpha}^n$	0.005
Tolerance value for displacement correction	$C_{\alpha}^n$	0.01
Line search attempts (For Newton Method)	$N^{ls}$	0
No of iterations for divergence check	$I_0$	4
No of iterations for logarithmic convergence check	$I_R$	8

Table 2-7. Occupancy categories (Adapted from UFC, 2009).

Occupancy Type	Occupancy Category (OC)
: Buildings in OC I in Table 1 of UFC 3-310-01, : Low Occupancy Buildings <sup>1</sup>	I
: Buildings in OC II in Table 1 of UFC 3-310-01, : Inhabited buildings with less than 50 personnel, primary gathering buildings, billeting and high occupancy family housing <sup>1,2</sup>	II
: Buildings in OC III in Table 1 of UFC 3-310-01	III
: Buildings in OC IV in Table 1 of UFC 3-310-01 : Buildings in OC V in Table 1 of UFC 3-310-01	IV

<sup>1</sup> As defined by UFC 4-010-01 Minimum Antiterrorism Standards for Buildings

<sup>2</sup> OC II is the minimum occupancy category for these buildings, as their population or function may require designation as OC III, IV or V.

Table 2-8. Design requirements based on occupancy categories (Adapted from UFC, 2009).

Occupancy Category	Design Requirements
I	No specific requirements
II	Option 1: TF for the entire structure and ELR for the corner and penultimate columns or walls at the first story.  Option 2: AP for specified column and wall removal locations.
III	AP for specified column and wall removal locations; ELR for all perimeter first story columns or walls.
IV	TF; AP for specified column and wall removal locations; ELR for all perimeter first and second story columns or walls.

TF - Tie Forces

AP - Alternate Path

ELR - Enhanced Local Resistance

## CHAPTER 3 RESEARCH APPROACH

### **Overview**

The emphasis of this study is to use a predominantly continuum based FE model to simulate the load-rotation behavior of a RC beam-column-slab subassemblage (interior connection). In addition, this study would develop a simplified structural elements based FE model to replace the predominantly continuum based FE model for the interior connection subassemblage. This simplified structural elements based FE model for the interior connection could eventually be used for the fast assessment of a building frame when subjected to progressive collapse.

Abaqus version 6.10 that is used in numerical simulations must first be validated to ensure that the model can produce reasonably accurate and trustworthy results. Upon validation of the code, it could then be used to model the interior connection of this study and predict its behavior under loading with increased confidence.

Verification process is required to ensure that the code executes the programmed mathematical algorithms for the specified problems correctly. It does not attempt to relate the conceptual model with the actual real life situation or solution. Thus the process of validation is critical to complete the picture. The validation process attempts to relate the conceptual model with the real world behavior. It also attempts to test if the chosen material models, structural mesh or model parameters are adequate to simulate the physical problem.

There are extensive verification tests for elements and materials in Abaqus. They are based on problems with well established solutions provided for, in the verification

manual of the code (Simulia, 2010). Some of the verification tests would be briefly reviewed in Chapter 4. The focus would be instead placed on the validation process.

Tan (2010) showed that Abaqus/Standard could be used to model the behavior of reinforced concrete frame connections (corner, T and interior connections) under monotonic loads reasonably well, as shown in Figure 3-1. The connections that were validated did not include the contribution of both the slab, transverse and spandrel beams. In addition, he had also validated the usage of Abaqus/Explicit on simply-supported reinforced concrete beam subjected to dynamic load.

To further expand on the cases that Tan (2010) had validated using Abaqus, three additional cases would be modeled and compared with experimental results. All cases include the contribution of slab and transverse beam except for the case of the cantilever rectangle beam.

A cantilever rectangle beam and a cantilever T-beam (exterior connection) by Ma et al. (1976) subjected to monotonic load would be modeled using Abaqus/Standard. Specimen S2 which is an interior connection tested by Durrani and Wight (1982) would be the third validation case. The details of the validation would be presented later in Chapter 4.

### **Beam-Column-Slab Interior Connection Characterization**

The interior connection would be characterized to consist of the following main structural components and subjected to monotonic load as shown in Figure 3-2.

- Longitudinal beams
- Transverse beams
- Spandrel beams
- Assume effective flange width for the longitudinal beam
- Slabs (To provide boundary constraints)

A predominantly continuum based FE model of the above interior connection in Figure 3-2 will be constructed. The shaded region consists of a column height of  $d_b$  (each on top and bottom of the connection), longitudinal beam length  $d_b$  (on both sides) and effective flange width is modeled with continuum elements for concrete and beam elements for the steel reinforcement. This shaded region is modeled with a finer mesh density. The length  $d_b$  is chosen to represent the plastic hinge region, as mentioned in Chapter 2. For those structural components outside of this shaded region, they are modeled with coarser mesh of continuum and beam elements for the concrete and steel reinforcement respectively. The rest of the hatched areas are slabs that would be modeled with shell elements.

The rationale behind the focus on the shaded region of the above proposed predominantly continuum based FE model is driven by the computational needs. It is much faster to run the analysis for an isolated area than that of an entire FE model with the same dense level of mesh. Furthermore, as majority of the deformation or action of the connection occurred within the plastic hinge region, it is critical to focus the computation efforts to this region so that reasonable estimate of the connection load resistance could be obtained.

For the structural components outside this shaded area, its primary role is to transfer the force and moments to the connection area. Thus, its load-deformation relationship is not a major concern and the accuracy of the results within the plastic hinge region (shaded area) would not be greatly sacrificed if coarser meshes are used for these structural components.

The global rotation,  $\theta_g$ , of the longitudinal beam is defined as the angle between the un-deformed and the deformed beam, as shown in Figure 3-3, where,  $L$  is the beam span length and  $h_b$ , is the beam deflection.

$$\theta_g = \tan^{-1} \frac{h_b}{L} \quad (3-1)$$

However, the global rotation angle is not an accurate representation of the rotation that occurs at the plastic hinge region, since the length of the plastic hinge formed is not taken into account. Figure 3-4 shows a better representation of the rotation at the connection when the length of the plastic hinge is accounted for.

Yim (2007) has proposed that the rotation at connection should account for the length of the plastic hinge,  $l_p$ . Thus, the proposed plastic rotation angle  $\theta_p$  is, as presented in Figure 3-5.

$$\tan \theta_p = \frac{v_2 - v_1}{u_2 - u_1 + l_p} \quad (3-2)$$

### **Simplified Finite Element Model**

The predominantly continuum based finite element model could be simplified to a structural elements based FE model which consists of a series of beam and connector elements, as shown in Figure 3-6. The beam elements will be used to model the beam and column structural components. The connector elements (JOIN and CARDAN) would be used to represent the moment resistance of the interior connection (rectangle cross-section) obtained from the predominantly continuum based FE model similar to that conducted by Tan (2010). The simplified structural element based FE model would be subjected to the same loading and boundaries conditions, as that experienced by the

predominantly continuum based FE model. The simplified FE model should be able to produce similar load- rotation behavior as the predominantly continuum based FE model to ensure its validity as an alternative system.

The connector type JOIN, as shown below in Figure 3-7, is a part of the basic connection types that exist in the Abaqus library of connector elements. It has only translational dofs in 3 directions and it makes the position of node a and b permanently fixed at the same location (same coordinate) and translate as one node. Connector type CARDAN is also part of the basic connection types but it has only rotational dofs in 3 directions, as shown in Figure 3-8. It is characterize by three Cardan (Byrant) angles that describe the relative position of node b to node a about their respective local directions.

### **Summary**

The preceding sections described the characterization of the beam-column-slab interior connection. It also touched on the development of a simplified structural element based FE model that would serve as a faster alternative to the predominantly continuum based FE model. The flow chart as shown in Figure 3-9 summarized the approach that needs to be completed for this study to achieve its objectives.

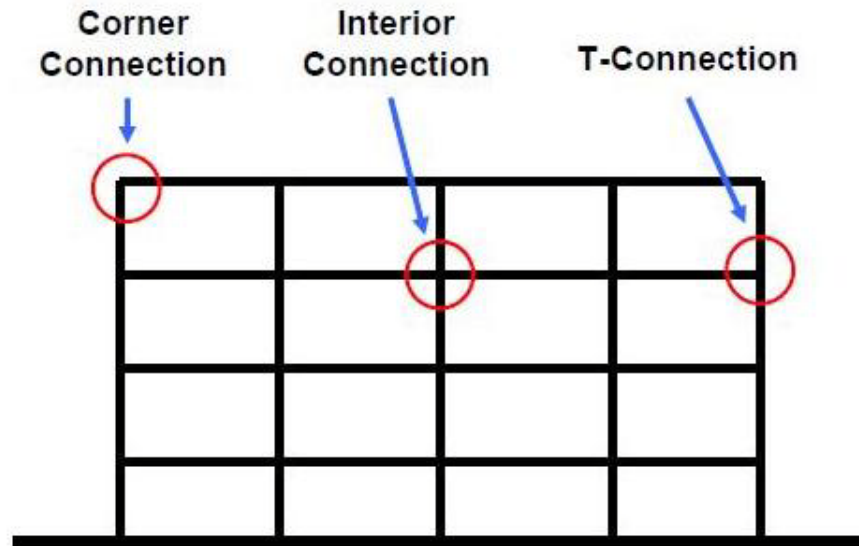


Figure 3-1. Various types of connections in a typical building frame (Tan, 2010).

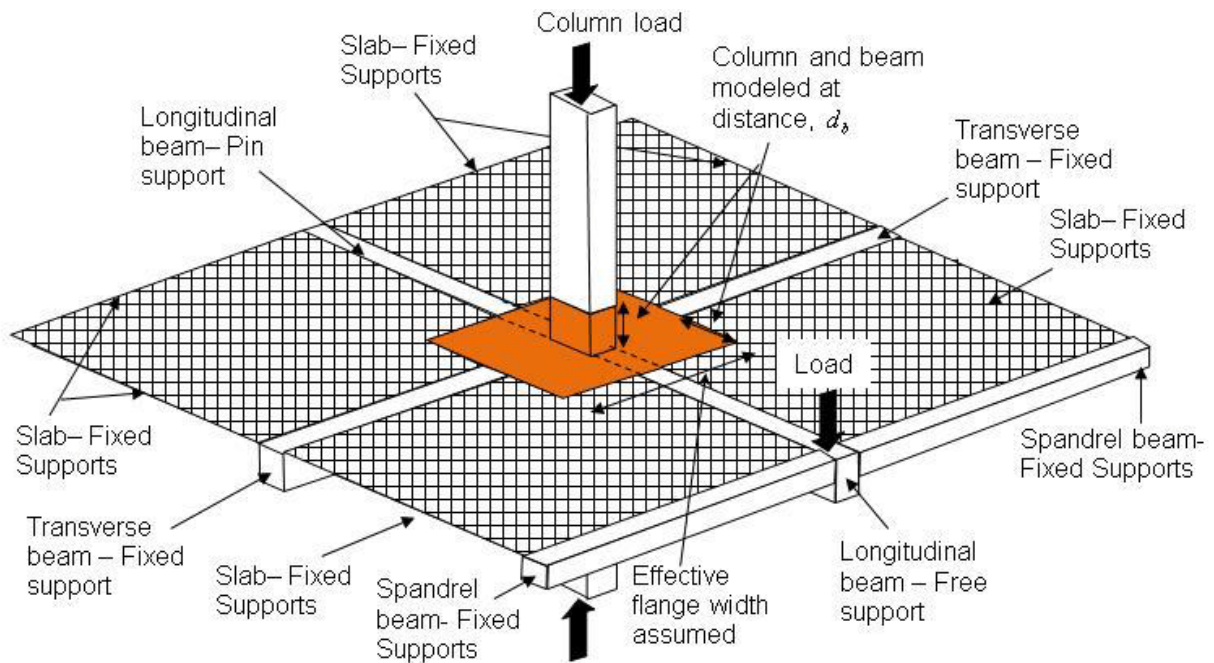


Figure 3-2. Proposed three dimensional model for interior connection.

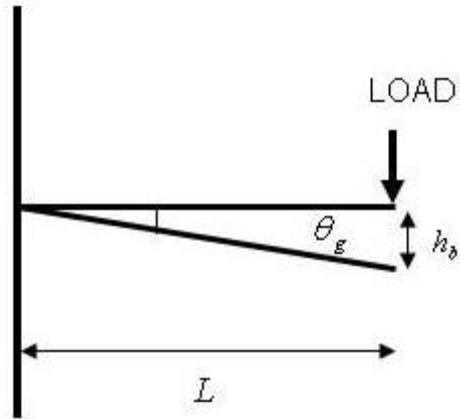


Figure 3-3. Global rotation for longitudinal beam (Tan, 2010).

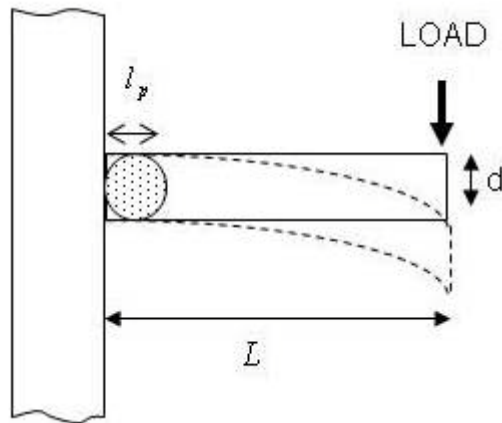


Figure 3-4. Plastic hinge formation (Adapted from Tan, 2010).

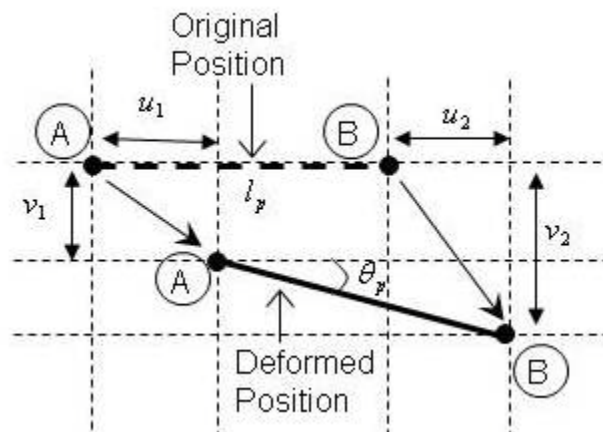


Figure 3-5. Proposed plastic rotation angle which includes the plastic hinge length  $l_p$  (Adapted from Yim, 2007).

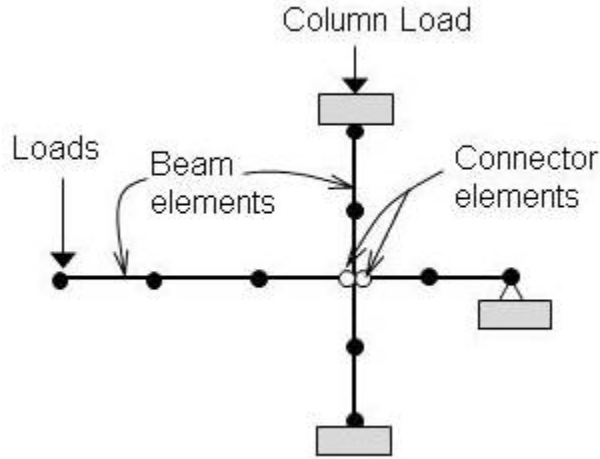


Figure 3-6. Simplified model using structural elements (Adapted from Tan, 2010).

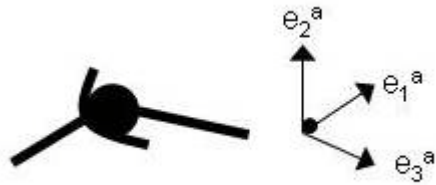


Figure 3-7. Connector type JOIN - only translational dofs (Adapted from Simulia, 2010).

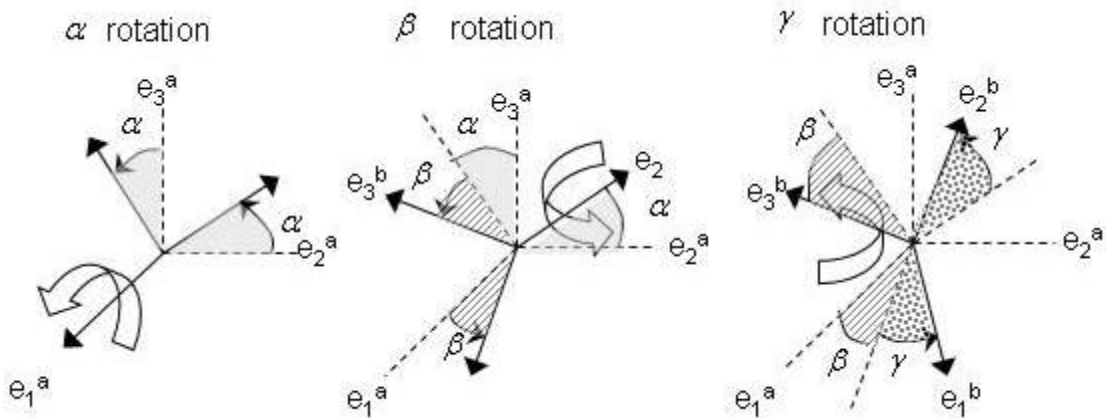


Figure 3-8. Connection type CARDAN - only rotational dofs (Adapted from Simulia, 2010).

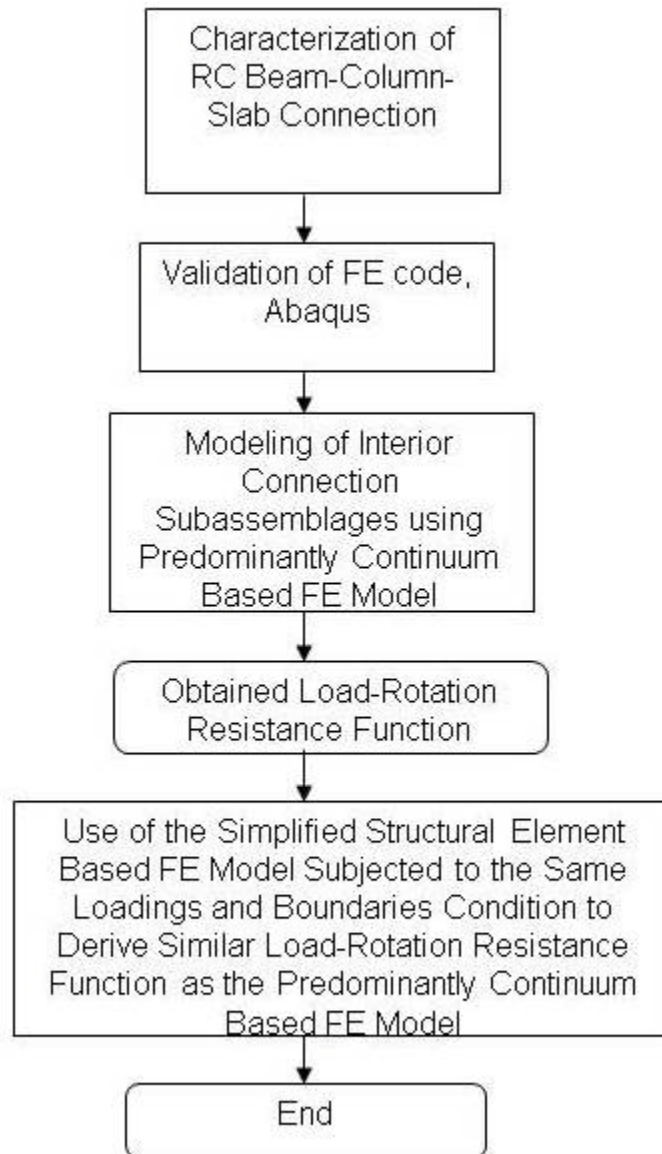


Figure 3-9. Flow charts of research approach.

## CHAPTER 4 RESULTS AND DISCUSSION

### **Overview**

This chapter would first touch on the verification and the proposed additional validation cases for the FE code Abaqus. Next, the details for the 4 story full scale test structure would be presented. Lastly, the simulation results for the FE models for the interior connection of this study would be discussed as well.

### **Verification of the Finite Element Code**

As mentioned in Chapter 3, the purpose of the verification process of the FE code is to ensure that the programmed mathematic algorithms work as per its intended function. Abaqus has done extensive verification as per described in its verification manual (Simulia, 2010). As our focus is on the characterization of the interior connection, the verification process would only be briefly covered for the elements and material used in the FE model.

The continuum C3D8R elements were verified in both Abaqus/Standard and Abaqus/Explicit for the followings:

- Hourglass control
- Kinematic formulation
- Tied contact surfaces
- Multi-point constraints and shear

The B31 elements were tested for small displacements and large rotations when subjected to different loading conditions. The connector type JOIN and CARDAN were verified by testing for the connection behavior in their respective dofs when subjected to a damped free vibration analysis with initial conditions or sinusoidal excitation of a damped spring-mass system. In addition, connection type CARDAN was also verified in

Abaqus/Standard for the perturbation analysis in eigenvalues buckling cases under elastic connector behaviors.

The S4R shell elements were verified for the followings:

- Effect of plane stress, plane strain and membrane load.
- Initial and constant curvature.
- Bending, shear and tensile stresses and section forces within the shell thickness.

Concrete Damage Plasticity which is used to describe the concrete's material properties were verified too using continuum elements for inelastic behavior of concrete in both uni-axial and biaxial stress states.

### **Validation of the Finite Element Code**

Tan (2010) had validated both Abaqus/ Standard and Abaqus/Explicit with the following cases.

- Dynamic loading on rectangular beams using Abaqus /Explicit (Feldman and Seiss, 1956).
- Monotonic loading on corner, T and interior connections using Abaqus/Standard (Nilsson, 1973).

For the case of Feldman and Seiss (1956), the Abaqus/Explicit model produced reasonable match of the deflection time history, as shown in Figure 4-1.

Similarly, the results from the Abaqus/Standard matched reasonably well with the experimental results from Nilsson (1973) for both the corner and T-connection, as presented in Figure 4-2 and 4-3 respectively.

As for the case of the interior connection (U69), the FE model produced a higher load carrying capacity than that measured in the experiment. However, both the maximum load of the model and the test occurred at similar deflection, as presented in Figure 4-4. Tan (2010), attributed the discrepancies in the results to the inability of the Abaqus simulation to model the steel reinforcement stresses variation across cracked

concrete. In cracked concrete, insufficient development length between the cracks might result in the full yield capacity of the steel reinforcement not being fully achieved. The Abaqus model might be inherently stiffer than the actual situation, due to the fact that the steel stress is dependent on its geometric location and not a function of the available development length between the cracks. Furthermore, since only one sample of the interior connection was tested, there might be a presence of variability to the experiment results due to the small sample size. Therefore, Tan (2010) commented that Abaqus/Standard could still be used to model the behavior of interior RC connection reasonably well despite the enhancement in the load carrying capacity of the connection.

Additional tests are proposed in this study for the validation of Abaqus/Standard as the previous cases conducted by Tan (2010) did not include the contribution of the slab and transverse beams to the connection. The cases that are presented include:

- Cantilever beam subjected to monotonic loadings by Ma et al. (1976).
- Exterior connection subjected to monotonic loadings by Ma et al. (1976).
- Interior connection subjected to cyclic loadings by Durrani and Wight (1982). The loading condition was simplified to represent monotonic loading for the validation.

### **Cantilever Rectangular Beam**

Specimen R4 from the test series conducted by Ma et al. (1976) is used as an initial starting point to establish the various parameters that should be used in the FE model. The rectangular cantilever beam was mounted to a huge stump to simulate a rigid/fixed end connection. The elevation and section details of specimen R4 are presented in Figure 4-5. The geometry of the beam is 9 inches wide by 16 inches deep and consists of 4 US No. 6 and 3 US No. 5 as top and bottom steel reinforcement,

respectively. US No. 2 hoops and vertical ties at 3.5 inches spacing were provisioned as transverse reinforcement. The stress-strain curves for the reinforcement are shown in Figure 4-6. The concrete compressive strength  $f'_c$  is 4380 psi.

The test setup is presented in Figure 4-7, where the specimen was laid on its side to minimize the effect of gravity and self weight. It is loaded with a hydraulic actuator connected to the end of the cantilever. Specimen R4 was subjected to cyclic loadings via displacement controlled method, as shown in the load history presented in Figure 4-8. Positive displacement was defined as the direction that produced a negative flexural moment at the top of the beam. Although it was loaded cyclically, the response of the specimen up till load point (Lp) 13 of the load history was essentially due to monotonic loading. The measured load deflection curve (monotonic load) till Lp13 is presented in Figure 4-9.

Specimen R4 was modeled in Abaqus/Standard as a cantilever beam with fixed ends. C3D8R continuum brick elements were used to model the concrete and B31 beam elements were used to model the steel reinforcement, as shown in Figure 4-10. The B31 beam elements were then embedded into the C3D8R elements to connect them together. The FE model was loaded via displacement controlled method where a prescribed displacement was applied at the tip. Reaction forces which represented the tip loads were obtained from the analysis and plotted against the tip displacement.

Concrete damage plasticity model from Abaqus was used to model the concrete behavior. The default parameters for CDP in Abaqus/Standard mentioned in the Chapter 2 and summarized in Table 4-1 was used.

A series of parametric studies were done, as detailed in Appendix A, to establish the material model, appropriate parameters to be used, type of loading, and to test out the modeling technique. The results of the parametric studies were summarized in Table 4-2, which gave the best match between the modeled and experiment results. It was observed that the two correction factors were required to modify the Hsu steel model. They were the equivalent yield stress correction factor  $C_f$  that helped to reduce the modeled yield load to match that of the experimental yield load. In addition, the initial steel young modulus correction factor  $C_s$  was used to simulate the softening effect of the concrete after extensively cracking had occurred, but not accounted for in the original Hsu's steel model.

The comparison plot between the simulated results and the experimental result is shown in Figure 4-11. The FE model is based on the suggestion proposed in Table 4-2, and was subjected to a tip displacement (4.2 inches) at a specified distance away from the support to simulate the displacement controlled loading. The FE model produced good results with the ability to match the experimental results well, both in term of physical load deflection behavior and also the tip and yield load magnitude. The difference in the modeled and measured tip load is 0.5%.

Further parametric studies, based on the materials models and parameters presented in Table 4-2, were done to establish the effects of dilation angle and mesh density changes on the structural response. As presented in Figure 4-12 and Table 4-3, in general, the increased in the dilation angle led to an increased in the modeled tip load. The structure seems to become stiffer as the dilation angle increased and thus required more tip load in order to achieve the same tip displacement.

The accuracy of the modeled results is often controlled by density of the mesh with denser mesh generally producing more accurate results. Three different mesh densities were modeled for both the concrete and the steel reinforcements. They are as follows:

- Cube of 1.5 inches on each side for concrete and 1.5 inches long for steel.
- Cube of 1.25 inches on each side for concrete and 1.25 inches long for steel.
- Cube of 1.0 inches on each side for concrete and 1.0 inches long for steel.

As shown in Figure 4-13 and Table 4-4, the 1.0 inches mesh density is a reasonable mesh size and the achieved difference between the measured and modeled tip load is small (0.5%).

### **Exterior Connection Beam-Column-Slab Subassemblages**

Specimen T2 from the test series conducted by Ma et al. (1976) included the addition of a 2.25 inches thick slab to the beam tested in specimen R4. The elevation, plan and section details of T2 are presented in Figure 4-14. The width of the slab is 36 inches and consists of two layers of longitudinal slab reinforcement (top and bottom) of US No. 2 at 6 inches spacing coupled with one top layer of transverse slab reinforcement of US No. 2 at 10.5 inches spacing. The stress-strain curves for the reinforcement are shown in Figure 4-6, and the test setup is the same, as presented in Figure 4-7. The concrete strength differs at 4610 psi.

The load history is presented below in Figure 4-15, and the response of the structure could be deemed to be under monotonic load up till Lp 9. The load versus tip deflection for specimen T2 till Lp 9 (monotonic load) is shown in Figure 4-16.

The material models, type of elements, modeling technique and mesh density of the elements as utilized in specimen R4 were adopted here as well. The two main changes were the dilation angle and the slope of strain hardening part of steel

reinforcement  $E_p'$ , as presented in Figure 2-56. The dilation angle was increased to 38 degrees, which is a reasonable figure, as it is close to the friction angle of sand. Sand is used as fine aggregate in the concrete. In addition,  $E_p$  was increased by 1.25 times as compared to that of  $10f'_y$ , as proposed by Hsu (1993). This value was calculated from experimental results of Specimen T2.

The result of the simulation is presented in Figure 4-17. The T2 FE model shows a reasonable correlation of the physical behavior as compared to the experimental results. The modeled tip load was approximately 3% lower than that of the measured tip load.

### **Interior Connection Beam-Column-Slab Subassemblages**

Specimen S2 is an interior beam-column-slab connection tested by Durrani and Wight (1982). The test setup and elevation view of the test series are shown in Figure 4-18 A and B respectively. For specimen S2, the longitudinal and transverse beams are both 11 inches wide but with varying depths of 16.5 and 15 inches respectively, while the column is 14.25 inches on both sides. The interior connection was loaded laterally as shown.

The sectional details are shown in Figure 4-19, where the slab is 4 inches thick. The slab consists of one orthogonal layer of top steel reinforcement of US No. 4 at 4 and 6 inches center to center (c/c) spacing for longitudinal and transverse direction, respectively. The main longitudinal beam consists of top reinforcement of 4 US No. 4 and 2 US No. 7 while the bottom reinforcement consists of 4 US No. 6. The transverse beam consists of 4 US No. 6 each for the top and bottom reinforcement. All the beams

are bounded by US No. 3 hoops at 3.5 inches c/c spacing. The column reinforcement consists of 8 US No. 8 and double hoops of US No. 4 spaced at 3.5 inches c/c.

The specimen was loaded cyclically via displacement controlled. The load-deformation for each of the cycle in one direction was extracted and presented in an envelope curve that reflected only the maximum load in each cycle, as shown in Figure 4-20.

The result of the FE model as compared to the experiment is presented in Figure 4-21. There appears to be a reasonable match in the physical behavior between the test and the FE modeled result. However, there is significant difference of approximately 20% in the maximum tip load achieved. The reasons for the discrepancy are possibility due to the following aspects.

- Difference in loading conditions – The actual specimen was loaded cyclically while in the FE model, it was loaded monotonically. Thus, the FE model would not be able to capture the potential reduction in stiffness and load capacity associated with the cyclic loading of a cracked connection. However, it was observed from the load-displacement envelope curve for specimen S2, that there was no loss of load capacity even with stiffness degradation due to the cyclic loading. Thus, similarly, the difference in the loading condition should not be the main contributing reason for the discrepancy between the FE and the experimental tip load results.
- Boundary conditions – The boundary conditions of the FE model were not modeled exactly as that of the actual test specimen. The left and right beam of the specimen S2 were attached to a pin and supported by movable vertical arms, as presented in Figure 4-18. The bottom support was restrained from movement via rollers. In the FE model, the left and right beam supports were simply modeled as a roller at the centerline of the beam while the bottom support was assumed fixed, as shown in Figure 4-22. Differences in the boundary conditions would have a significantly influence in load resistance behavior. For example, in the case of a beam subjected to uniformly distributed loading, the differences of the end moment at the support between a simply supported beam and a fixed end beam is approximately 66%. As, however, the boundary conditions of specimen S2 is closer to the fixed end condition than an pinned support and thus the differences between the experimental result and the derived result would not be close to 66%. The semi-rigid boundary condition of the specimen S2 could thus be estimated to

contribute approximately ranging from 16.5% to 33% of the differences in the modeled and experimental results.

The differences in the boundary conditions between the FE model and the actual test specimen seems to have a bigger contribution to the 20% end tip load discrepancy as shown in Figure 4-21. Overall, the FE model is generally able to simulate the actual behavior of the connection rather well despite the discrepancies in results. The modeled tip load was of the same order of magnitude as the experimental results and the general load deformation profile was similar to the test observation.

In summary, generally all the FE models for the three validation cases (Specimens R4, T2 and S2) have shown good correlations both in term of the physical load deformation behavior and also in term of the maximum load capacity. The validated cases have enhanced the confidence level on the usage of FE to model the interior connection of this study.

### **Reinforced Concrete Beam-Column-Slab Connection in This Study**

The interior connection in this study would be based on the 4 story structure subjected to progressive collapse testing under abnormal load. This interior connection would be modeled using Abaqus/Standard to obtain its load-rotation relationship. The plan layout and the elevation view of the test structure are presented in Figure 4-23 and 4-24, respectively. Only the interior connection framed by grid 3 – C and the shaded area in Figure 4-23 would be modeled.

Figures 4-25, 4-26 and 4-27 shows the elevation views of the longitudinal, transverse and spandrel beams respectively, while the beam sectional details for these beams are presented in Figure 4-28. The thickness of the slab is 10 inches, and the top and bottom slab reinforcement in the longitudinal and transverse direction near column

at grid 3-C consist mostly of US No.3 rebars at 5 inches spacing, as shown in Figures 4-29 and 4-30. The exception to that is at the slab bottom reinforcement from Grid 3 to Grid 2.5 which is US No.3 at 8 inches c/c in both directions.

The longitudinal beam under negative bending moments would be modeled as a T-beam (including slab contribution) and the typical sectional detail is presented in Figure 4-31.

Concrete compressive strength for the structure is set at  $f'_c$  of 4000 psi and Grade 60 steel reinforcement conforming to the latest ASTM specification A616 or A706 would be used. The stress strain curve for concrete is obtained using Hognestad (1951) for compression and Hsu's (1993) tension stiffening model with  $f_{cr} = 3.75 \sqrt{f'_c}$ , as shown in Figure 4-32. For reinforcement, Hsu's (1993) model with correction factors  $C_f = 0.80$  and  $C_s = 0.50$  were used, as presented in Figure 4-33. The Concrete Damaged Plasticity material model from Abaqus/Standard would be used for this simulation as well.

### **Resistance Function of the Beam-Column-Slab Connection in this Study**

The following section described how the connection was modeled in Abaqus using the predominantly continuum based FE model. The FE model did not considered possible damages to the other structural components (beams, slab, other columns etc) from the blast load and account only for the immaculate sudden removal of the ground floor column C-4. This is done so that FE model adhere to the current guidelines proposed by GSA (2003) and UFC (2009), where the entire progressive collapse assessment are conducted based on a single column removal concept.

The interior beam-column-slab connection would be idealized using a combination of continuum elements and shell elements to simplify the model in order to limit the numbers of elements and to improve computation speed. In addition, symmetry was employed to reduce the FE model size by half. The main contributor to the negative flexural strength of the connection was assumed to be provided by the longitudinal beam (T-Beam) with the estimated effective flange width. It would be modeled in this study using a combination of continuum C3D8R elements and beam B31 structural elements. The shell S4R structural elements were added to simulate the remaining non-effective slabs that are assumed to have lesser contribution to the flexural capacity of the longitudinal beam. The shell elements also serve to provide boundary conditions restraint. The FE model will be done in a progressively, as shown in Figure 4-34, so as to ensure that a working model is available prior to attempts to simulate the behavior of the interior connection. The shaded zone represents areas modeled with much finer mesh density. The FE model will be loaded monotonically in two different directions to obtain its moment/load –rotation resistance function.

### **Moment-Rotation Resistance**

The symmetry half FE model of an interior connection with T-beam is shown in Figure 4-35, below. The protruding effective flange width assumed is  $4.5 d_b$  on each side from the beam web, as selected from Table 2-1. Finer mesh densities were assigned to the region near the connection which would experience the most severe stresses.

The moment-rotation curves of the interior connection with T-beam subjected to both downward (negative moment) and upward loading (positive moment) were plotted

on the same side to allow for easy comparison, as presented in Figure 4-36. Local rotations as presented in Figure 3-5 were used.

At downward loading (negative moment), the model displayed a higher moment capacity than that of the upward loading. This is correct, as the top portion of the beam and the slab is under tension and thus more reinforcements are contributing to load resistance. Vice versa, at upward loading (positive moment), more reinforcement from the beam and the slab are under compression. Thus, in order to maintain force equilibrium, the neutral axis depth would decrease which resulted in an increased in curvature. The increased in the curvature thus enhanced the ductility of the model which is reasonably captured by the upwardly loaded FE model.

The moment capacity of the downward loaded interior connection (T-beam) was compared with that obtained from DSAS (Astarlioglu and Krauthammer, 2009). DSAS is a multifunctional structural analysis program capable of modelling the response of wide range of structural components under static or dynamic loads. As DSAS is currently unable to calculate the moment capacity for T-beam, for the case of negative moment capacity, the T-beam was idealized into a rectangle beam instead so that DSAS could be used. The moment capacity for the FE model was approximately 22.3% higher than that as obtained from DSAS. The differences could be due to the simple idealization of the T-beam with the rectangle beam section. Despite the idealization, the moment capacities obtained were within the same order of magnitude and thus were deemed reasonable.

As DSAS is currently unable to calculate the positive moment capacity of a T-beam and no suitable idealization could be adopted, provision from ACI Committee 318

(2008) was used instead. For the upward loaded interior connection (T-beam), the positive moment capacity is approximately 16.7% higher than the nominal moment capacity calculated from ACI Committee 318 (2008). See Appendix B for more details of the calculation.

The predominantly continuum based FE models registered higher moment capacity than that was calculated for example by the ACI 318-08. This could be as a result of the FE model accounting for the spatial effect of the plastic hinge. The yielding of the additional beam cross-sections along the plastic hinge length  $l_p$ , as shown in Figure 2-48 would contribute to an increase in the moment capacity. In the case of the nominal moment capacity calculated by ACI 318-08, failure occurs at only one beam cross-section. In general, the FE models for the interior connection with T-Beam are able to capture both the physical load-deformation behaviour and also provide a reasonable estimate of the moment capacity of the system.

Figure 4-37 presents the symmetry half FE model for the interior connection for this study. The longitudinal, transverse and spandrel beams are modeled with continuum elements while most parts of the slab are modeled using structural based shell elements. The load-rotation behavior between the interior connection with T-beam only and the full connection (Longitudinal, transverse, spandrel beams and slabs) when subjected to downward loading were compared. It was observed that significant differences in the load capacity and ductility existed, as shown in Figure 4-38. The full interior connection had much greater load capacity and this could be attributed to the following various possible factors:

- Additional load transfer paths via the spandrel beams and the slabs.

- Tension membrane effect of the slab when the beams and the slabs undergo large deformation due to the simulated loss of support column.
- Two dimensional (2D) effects of the slab contributions are accounted for. Both the longitudinal and transverse slab steel reinforcements contributed to load resistance. For the interior connection with T-beam, only the longitudinal steel reinforcements contributed to load resistance.

As for the differences in the ductility, the interior connection with T-beam only acted like a cantilever beam, and thus, its ductility is limited as the beam would fail once plastic hinge are formed. However, in the case of the full interior connection, the system was able to further deform and redistribute loads via the slab after plastic hinges formed in both the longitudinal and spandrel beams. This would help in enhancing the ductility of the whole system.

The comparison of the full interior connection when subjected to loadings in two opposite directions produced expected results. At upward loading, the load capacity of the connection was lesser than that of the downward loading. Furthermore, the ductility of the upward loaded connection was larger, as well. These observations are reasonable as more reinforcements were in compression during the upward loading, which contributed to the increased in ductility. Similarly, since less reinforcement was in tension, thus the load capacity would correspondingly be lower, as compared to the downward loading case.

Overall, the simulated results from the full interior connection FE models appear to be realistic as it adheres to the general known physical behavior associated with reinforced concrete. It was able to provide a reasonable estimate of the load resistance function of a full interior connection system. From the FE models, it is evident that the membrane action of the slab plays a critical role in enhancing the load resistance.

## Simplified Structural Elements Based FE Models

A simplified structural elements based FE model would be used to replace the predominantly continuum FE model for the interior connection as described in the preceding section. The load-rotation behavior of the simplified FE model would be compared with that of the predominantly continuum FE model to assess its applicability as a quick accurate alternative FE model.

The simplified structural element based FE model for the interior connection consists of the following components:

- Beam elements – To represent structural components such as columns and beams. Effective moment of inertia as calculated from ACI 318-08 was used for the beam elements to simulate the effect of cracking (See Appendix C for more details).
- Shell elements – To represent the slab.
- Connector elements – To represent the moment resistance function of RC beam – column connection with rectangle cross-section. The connectors consisted of a combination of JOIN and CARDAN connection types which represent the basic translational and rotational dofs, respectively.

Tan (2010) have derived the moment resistance relationship of an interior beam – column connection with rectangle cross-section. Similarly, the moment-rotation relationship of the connection at the longitudinal beam and the spandrel beam, as shown in Grid 3-C and 4-D of Figure 4.23 respectively, were derived using continuum FE models (See Appendix C for details). The derived moment-rotation relationships from the continuum FE models were then used to define the properties of the connector elements that were used in the simplified structural element based FE model. Figure 4-39 presents a schematic view of a part of the structural element based FE model where the connector element was given the moment-rotation relationship of the connection

with the longitudinal beam (rectangle cross-section) derived from the continuum FE model.

From Figure 4-40, it is evident from the close match of the results, that the connector element are capable of representing the mechanical resistance behavior of the connection derived from continuum based FE model.

As presented in Figure 4.41, the full structural element based FE model that attempted to simulate the behavior of the interior connection of this study (as shown in Figure 4-37) was constructed.

The load-rotation behavior of both the predominantly continuum based FE model (full interior connection) and the simplified structural elements based FE model were compared in Figure 4.42. The simplified structural elements based FE model was able to produce a reasonably close match in the load-rotation behavior with maximum differences not exceeding 6%. The discrepancies in the result are due to the inability of the simplified structural elements based FE model to account for the spatial variation of the stiffness along the beams due to cracking. In the simplified structural elements based FE model, the stiffness of the beams are idealized and represented by the effective moment of inertia which was calculated from ACI 318-08. The effective moment of inertia calculated was then applied across the whole beam length and thus was not able to account for the actual spatial variation of the stiffness of the beam due to cracking.

The simplified structural elements based FE model had been shown to be able to produce good match in the load-rotation behavior. Most important of all, the simplified structural element based FE model used only a tiny fraction of the time to complete the

analysis, as tabulated in Table 4-6. This results in a significantly saving in computation time as compared to the predominantly continuum based FE model.

Although, the simplified structural elements based FE model was able to produce reasonably close match to the load-rotation behavior as compared to that derived from the more time consuming predominantly continuum based FE model, it is still not complete or ideal yet. The current simplified model only accounts for the bending resistance about the main axis only. It did not consider the bending resistance about the weak axis and furthermore, the possible combinations of interaction between the various force mechanisms that could be present in the interior connection subassemblage. The possible interactions between various force mechanisms that are not accounted are listed as follow:

- Biaxial moment interaction in both main and weak axis bending.
- Biaxial moment coupled with shear.
- Biaxial moment coupled with axial force (similar to column).
- Biaxial moment coupled with torsion.
- Shear coupled with tensile or compressive forces.
- All the above effects or various combinations of them

An example of the interaction between the bending resistance in both the main and the weak axis is illustrated in Figure 4-43. The presence of moment about one axis would generally reduced the moment capacity in the other direction and thus this reduction effect needs to be accounted for and incorporated into the simplified FE model. Similarly, there exist other established methodology used to describe the effects of the interaction between the various combinations of force mechanisms described above, however, they are often considered independently from one another. Thus there is also a need to look into how to couple the independent contributions from the various

combinations of force mechanism into one cohesive and comprehensive simplified FE model.

Further time saving could be achieved if the mechanical resistance behavior of the beam-column connection described previously that was used to define the connector elements, were estimated using a mathematical model. The mathematical model (Power Model) by Richard and Abbott (1975) was used as a starting point for the RC beam-column connection. As presented in Chapter 2, Power Model was used to estimate the moment-rotation relationship for steel connection. Parametric studies were conducted to derive the moment-rotation behavior for the RC beam-column connections using the Power Model. The parameters (initial rotational stiffness, shape factors etc) required for the Power Model were estimated via the methods as listed below:

- Parameters estimated from ACI 318-08.
- Parameters estimated from the continuum based FE model.

The moment-rotation relationship as calculated from the Power Model was compared with the mechanical resistance relationship obtained from the continuum based FE model as shown in Figure 4-44.

Using the parameters estimated from ACI 318-08, the derived moment-rotation using the Power Model was stiffer and moment capacity was lower. It was observed that the estimation by ACI 318-08 is not able to capture the enhancement in the moment capacity due to plastic hinge formation and thus the end moment capacity estimated was lower. In addition, the initial rotational stiffness estimated was stiffer, which could similarly be due to the code did not considered the effect of cracked stiffness across the plastic hinge length.

Using the parameters obtained from the continuum based FE model, the moment-rotation behavior using the Power model was calculated. The calculated moment-rotation behavior was not able to match the non-linear behavior obtained from the continuum based FE model after the elastic behavior of the connection had been exceeded. The shape factor was then varied to try to curve fit the calculated moment-rotation behavior with that obtained from the continuum based FE model. A good fit was obtained at a shape factor of approximately 2.43.

From the above parametric studies, it was observed that the Power Model has the potential to closely predict the moment-rotation behavior of the RC beam-column connection. The following aspects could be studied upon in the future to adapt the Power Model to estimate the mechanical resistance function of the RC beam-column connection:

- An analytical approach to account for the elastic rotational stiffness and the enhancement of the moment capacity of the RC beam-column connection from the plastic hinge formation.
- An analytical approach to derive the suitable shape factor to be used in the RC beam-column connection. The shape factor could be dependent on various factors such as geometry of the section, material properties, reinforcement detail or cracked stiffness etc. The proposed shape factor could be calibrated using the moment-rotation behaviors generated from continuum based FE models.

It was shown in this chapter that FE modeling is capable of predicting the load – rotation behavior of the RC interior connection subassemblage. Some aspects of the FE modeling are summarized below (Refer to Appendix A for more details):

- Concrete Damaged Plasticity model in Abaqus which account for the damage to concrete was selected in this study. Various plasticity parameters were required to define the CDP concrete model in plastic behavior. The default values as shown in Table 4-1, were adopted in the study with the exception of the dilation angle which was user-specified. A dilation angle of 38 degrees was selected for this study based on literature review (Jankowiak and Lodygowski , 2005).

- In the CDP concrete model, suitable material models to represent the behavior of concrete (compression and tension) and steel reinforcement were selected as well. Parametric studies were conducted to aid in the selection of the material models. For concrete in compression, the modified Hognestad (1951) was used. For the concrete in tension, three tension stiffening models were evaluated and the Hsu's tension stiffening model was selected. Similarly, the choice of the idealization for the steel reinforcement stress-strain relationship would also influence the load response behavior of the FE model. Three different steel stress-strain idealizations were reviewed and it was observed that the steel reinforcement model from Hsu (1993) gave the best fit with respect to the physical load –displacement behavior.
- It was also observed that the tensile cracking stress for concrete,  $f_{cr}$  have significant influence on the load-displacement behavior of RC beams. Thus parametric studies were conducted to choose the right cracking stress. It was observed that  $f_{cr} = 3.75 \sqrt{f'_c}$  as proposed in the tension stiffening model by Hsu (1993) gave the best load-displacement response for the validated case.
- As mentioned above, Hsu's steel model gave the best fit between the modeled and the experimental results; however, some modifications to the steel model were required to further improve the results. The proposed modifications were the inclusion of two correction factors  $C_f$  and  $C_s$  to correct for the overly high yield strength of steel and to account for the softening of concrete's stiffness after cracking respectively. Parametric studies were conducted to determine the right values to be used.  $C_f = 0.8$  and  $C_s = 0.5$  were proposed for this study.
- With reference to the derivation of load-displacement behavior, displacement controlled loading would be more appropriate. Displacement controlled loading is where the loading of the specimens are governed by prescribed displacements at different time intervals. As the behavior of RC structural component in the non-linear region is governed by the load history, it would be easier to use displacement controlled loading as often the load history are unknown. In addition, displacement controlled loading was chosen as it closely emulated that of the actual experiments and thus proper comparison between the results were possible.
- Two different techniques to account for the interaction between the concrete and the steel reinforcement were reviewed as well. They are the embedded and tie node techniques where the derived results from both techniques closely match the experimental result. It was observed that the tie node technique required much less analysis time as compared to the embedded technique; however the tie node method required also significantly more time to model. Thus for large scale FE model, the embedded method might be preferred until better modeling capability is available for the tie node method.

- In addition, there is a need to conduct a mesh size convergence check to determine the suitable mesh size required for optimal analysis. Parametric studies were conducted where the mesh density sizes were varied and the modeled results of the required parameter (displacement) were compared. The suitable mesh density size adopted in this study was 1 inch.

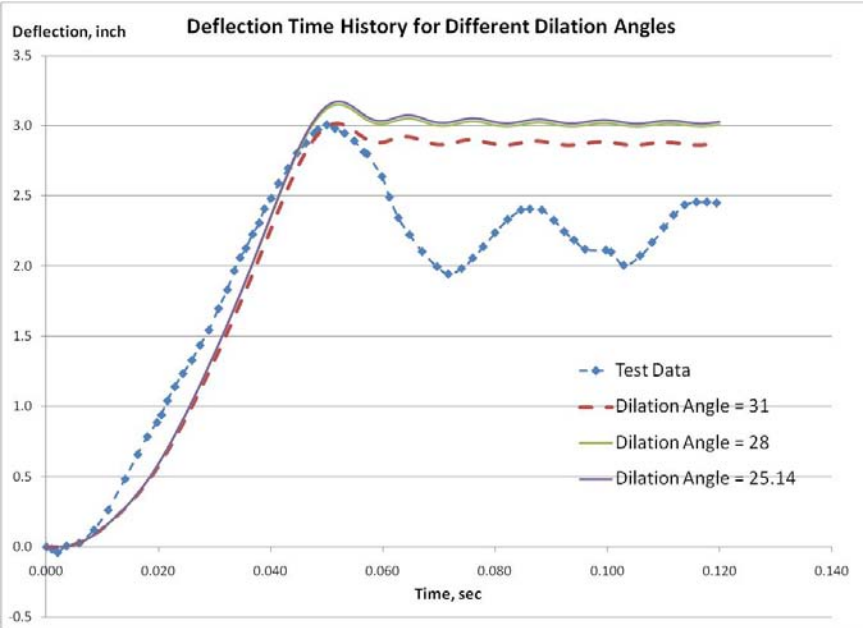


Figure 4-1. Comparison of deflection time history of dynamically loaded RC beam with modeled results from Abaqus/Explicit (Tan, 2010).

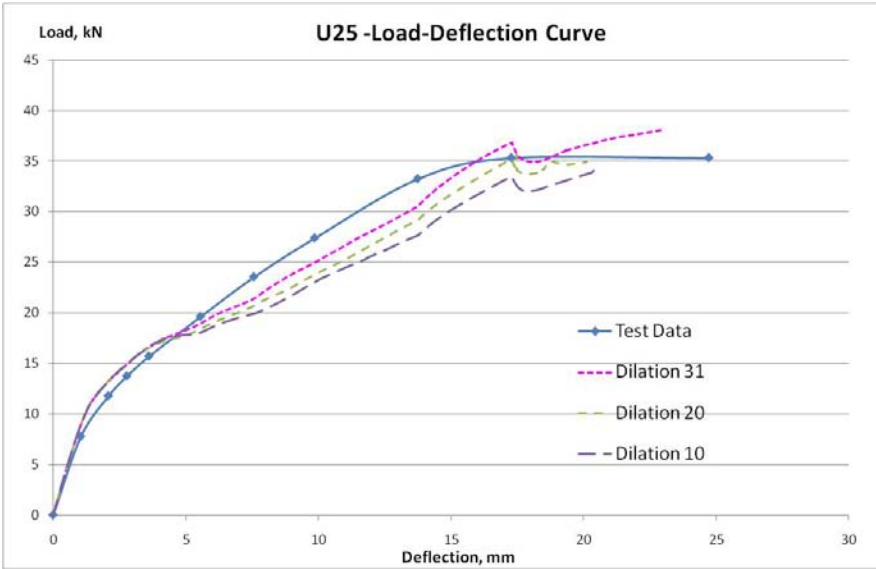


Figure 4-2. Comparison of load and deflection curve for corner connection (U25) subjected to monotonic load with modeled results from Abaqus/Standard (Tan, 2010).

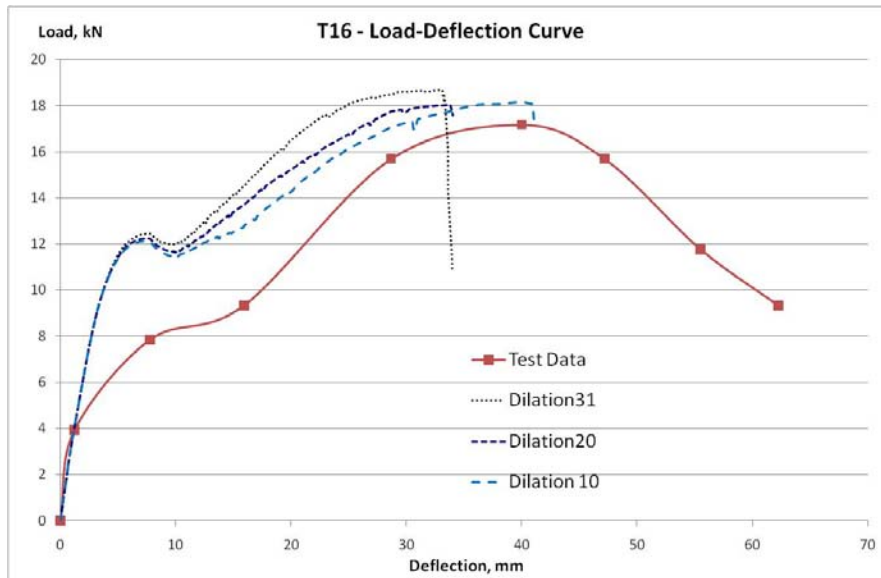


Figure 4-3. Comparison of load and deflection curve for T-connection (T16) subjected to monotonic load with modeled results from Abaqus/Standard (Tan, 2010).

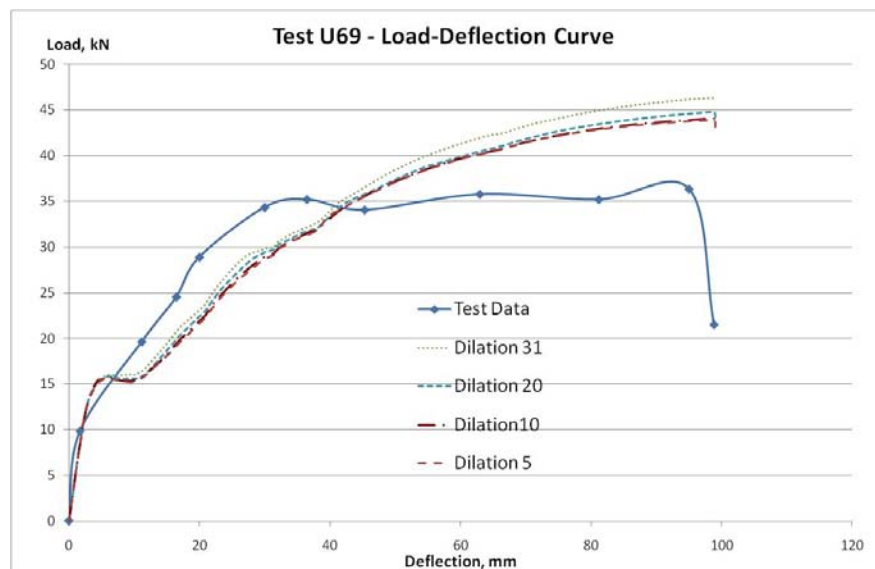


Figure 4-4. Comparison of load and deflection curve for interior-connection (U69) subjected to monotonic load with modeled results from Abaqus/Standard (Tan, 2010).

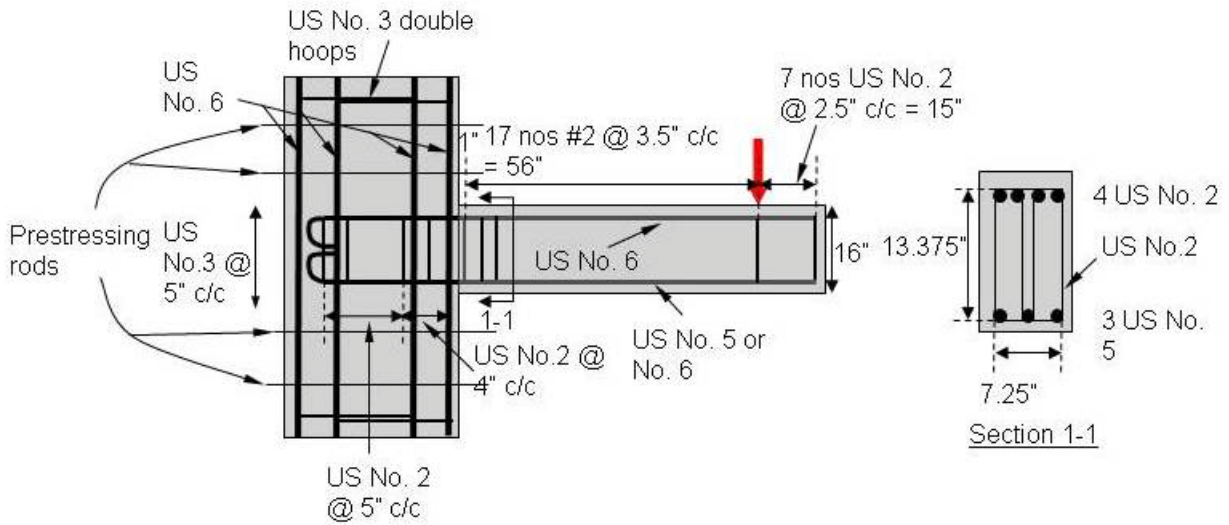


Figure 4-5. Elevation and sectional details for rectangular beam specimen R4 (Adapted from Ma et al., 1976).

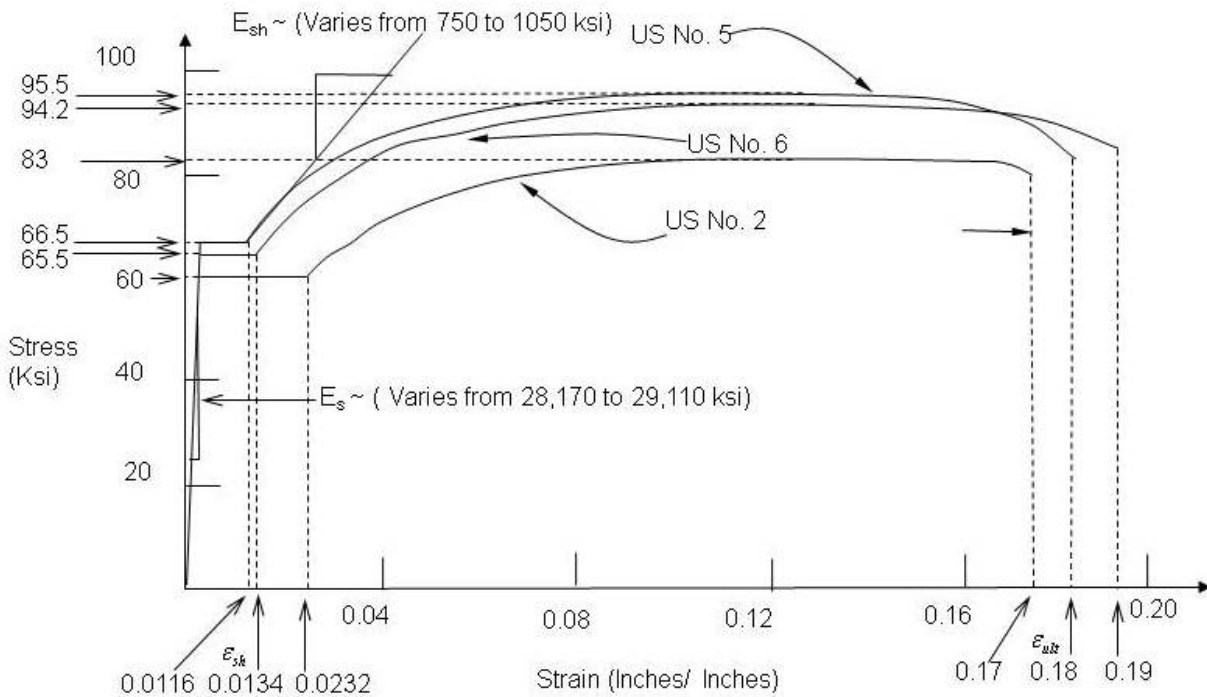


Figure 4-6. Stress-strain curves of steel reinforcement for test series (Adapted from Ma et al., 1976).

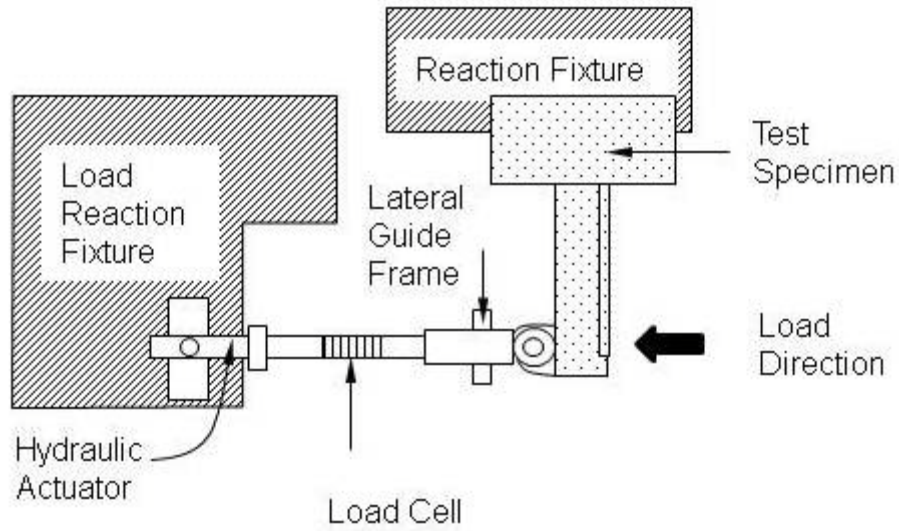


Figure 4-7. Test setup for test series - Plan View (Adapted from Ma et al., 1976).

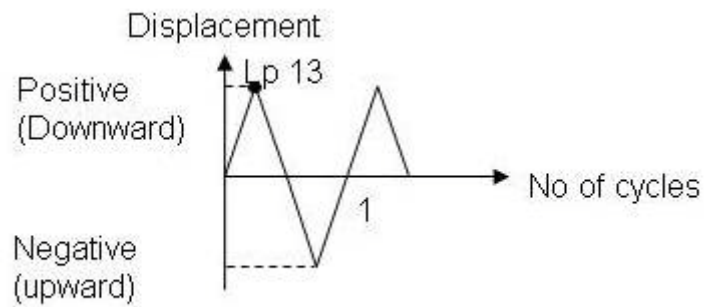


Figure 4-8. Loading history for specimen R4 (Adapted from Ma et al., 1976).

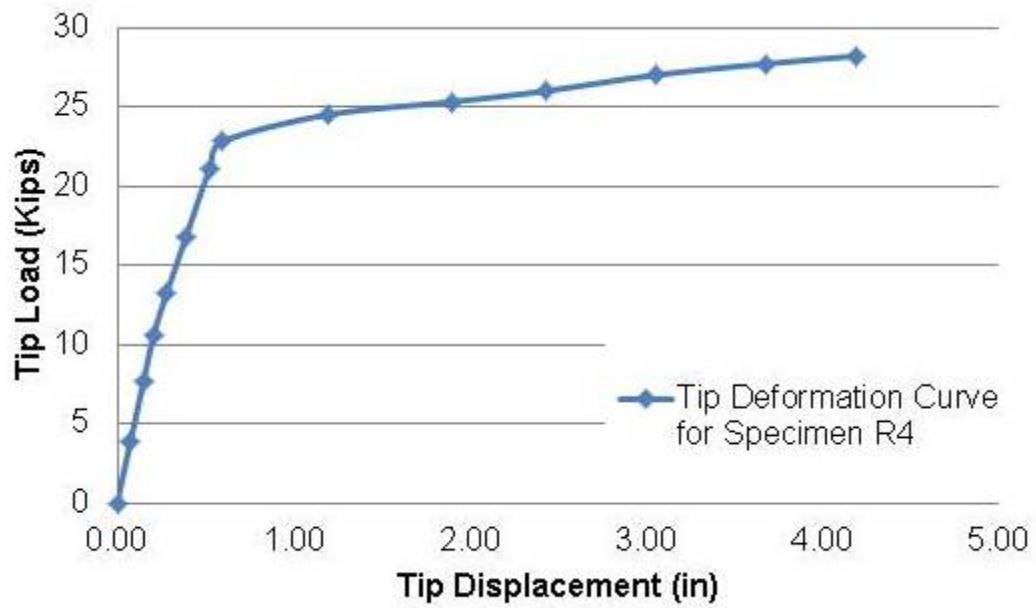


Figure 4-9. Measured tip load and tip deflection curve for specimen R4 up till load point (Lp) 13 (Adapted from Ma et al., 1976).

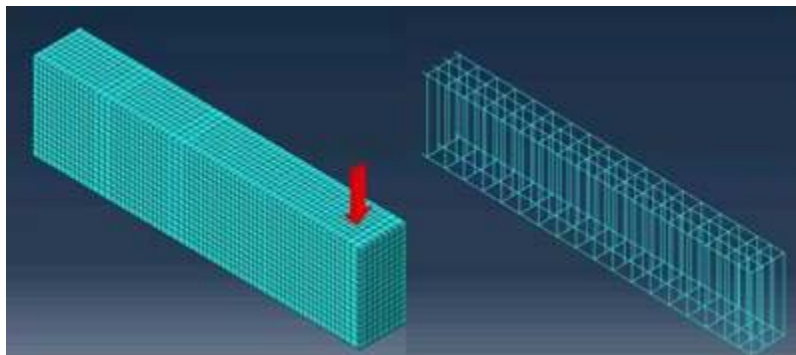


Figure 4-10. FE model for specimen R4.

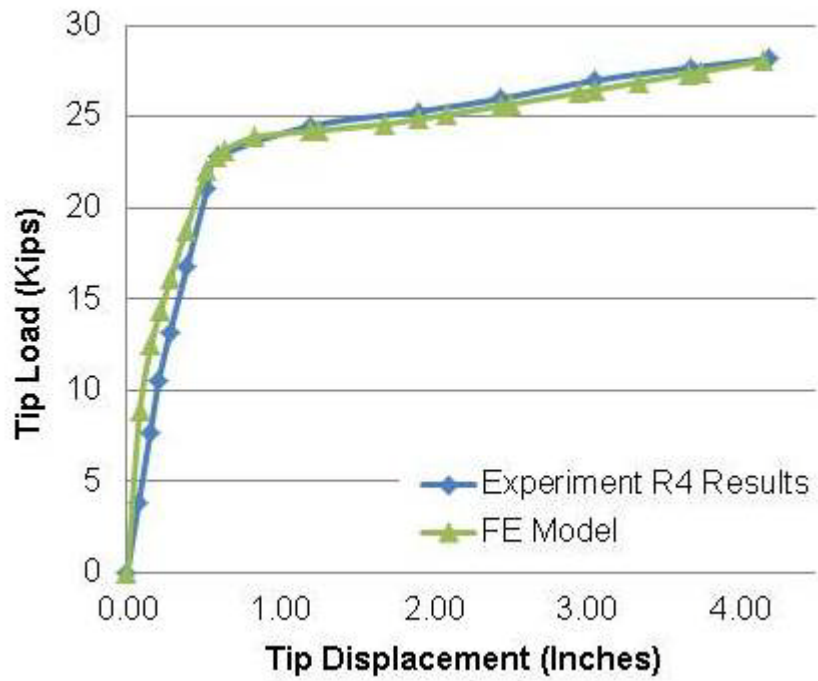


Figure 4-11. Comparison plot of modeled and experimental result for specimen R4.

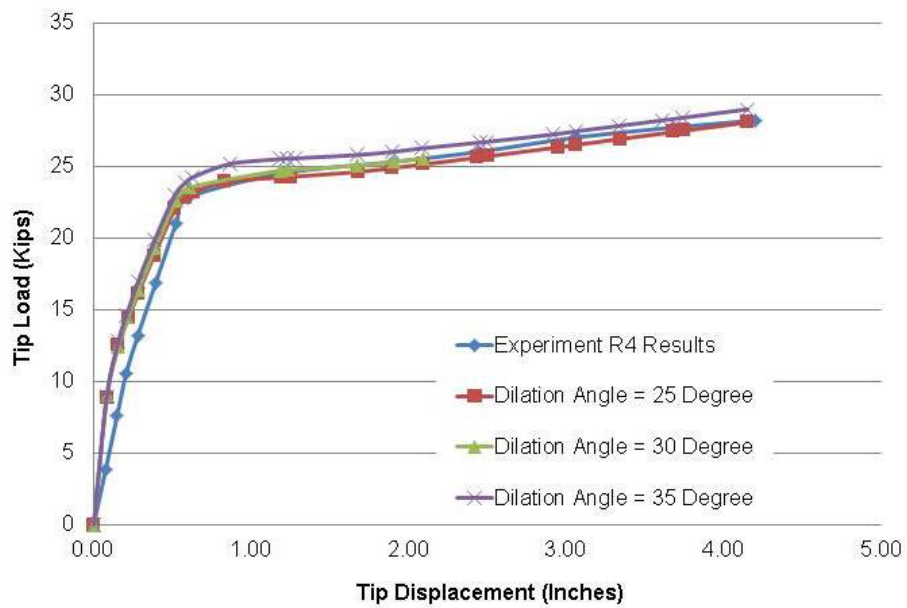


Figure 4-12. Comparison plots for variation of dilation angles for specimen R4.

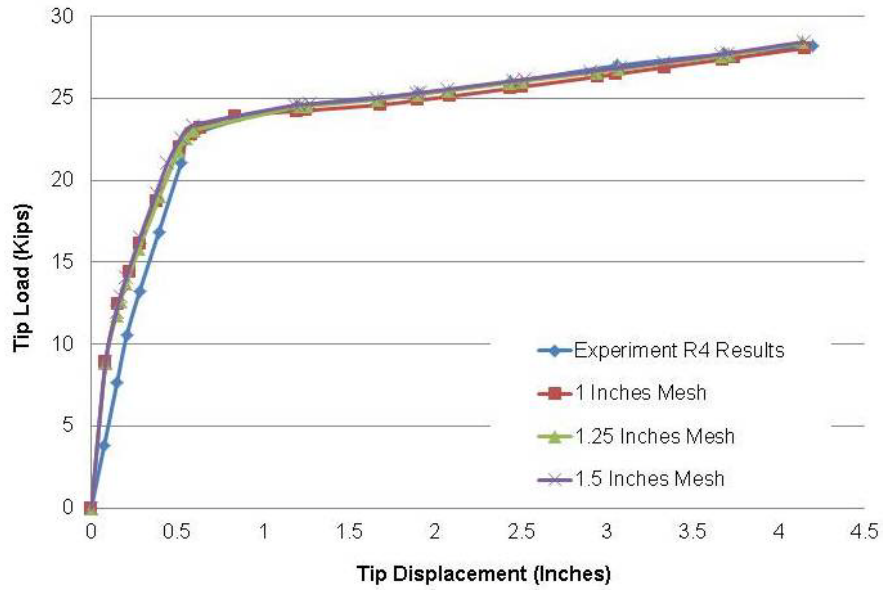


Figure 4-13. Comparison plots for the variation of mesh density for specimen R4.

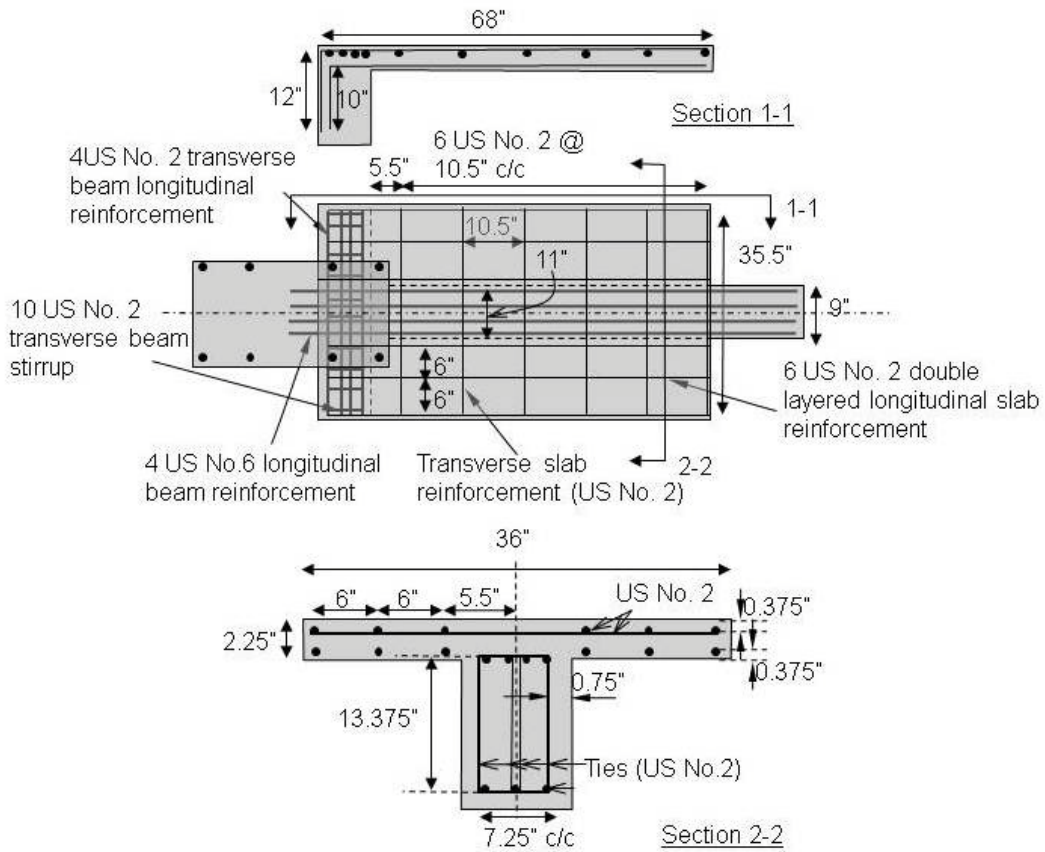


Figure 4-14. Elevation, plan and sectional details for specimen T2 (Adapted from Ma et al., 1976).

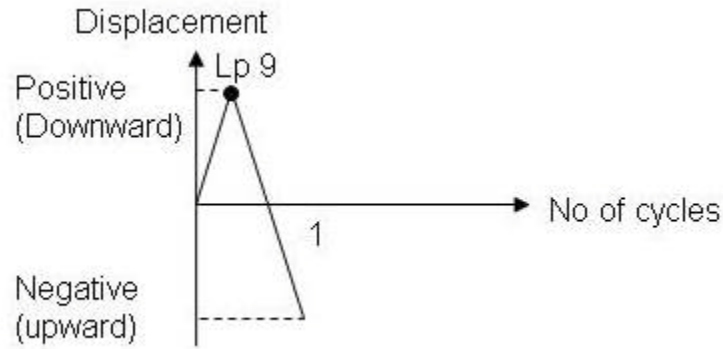


Figure 4-15. Loading history for specimen T2 till Lp 9 (Adapted from Ma et al., 1976).

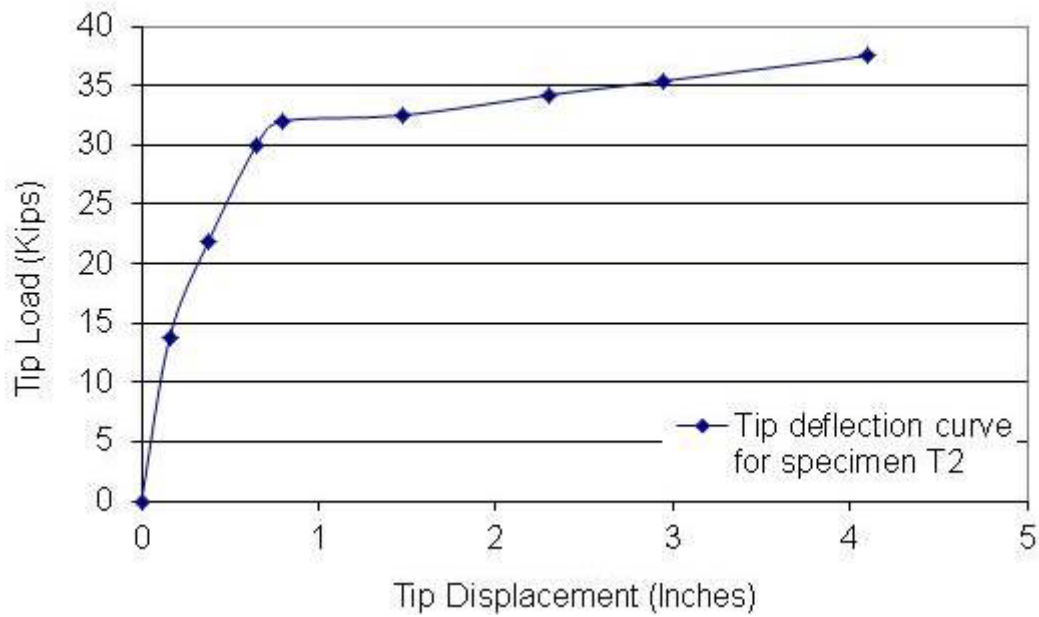


Figure 4-16. Measured tip load and tip deflection curve for specimen T2 (Adapted from Ma et al., 1976).

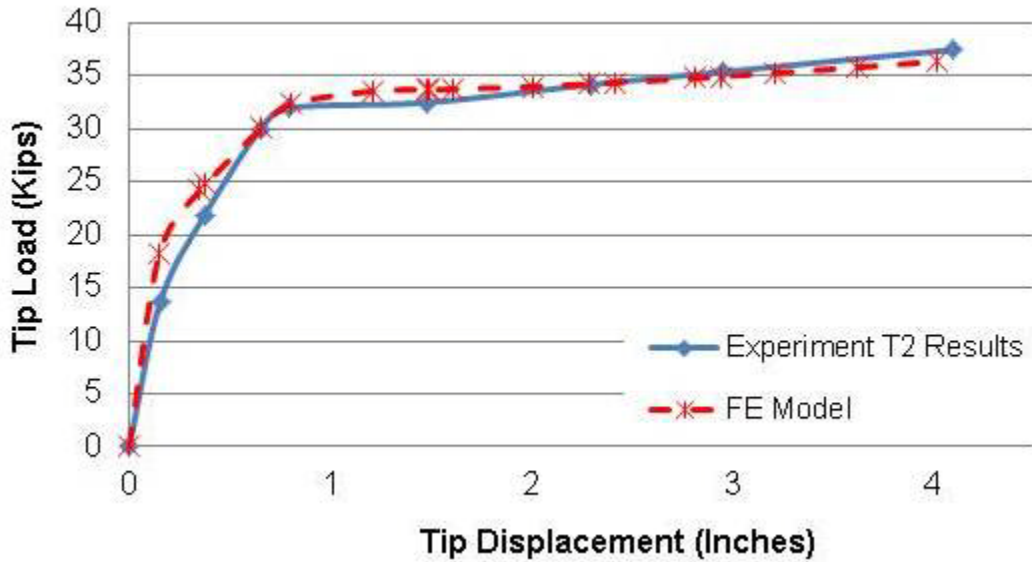


Figure 4-17. Comparison plot of modeled and experimental result for specimen T2.

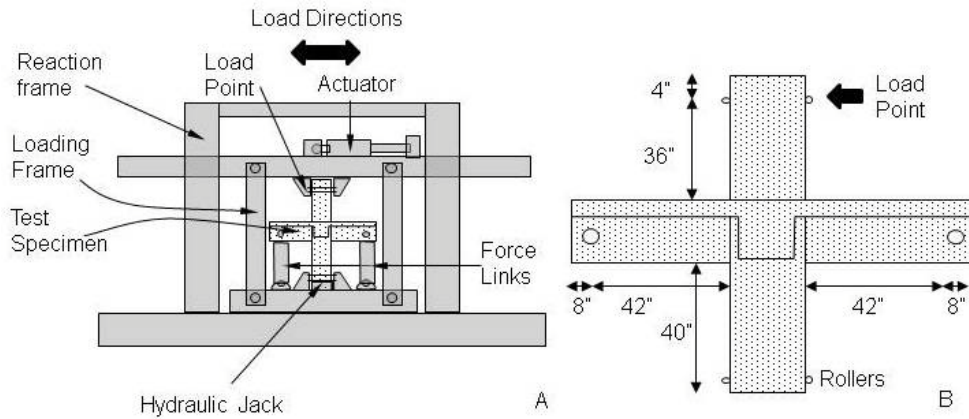


Figure 4-18. Test setup and elevation view of test specimens (Adapted from Durrani and Wight, 1982). A) test setup and B) blown up elevation view.

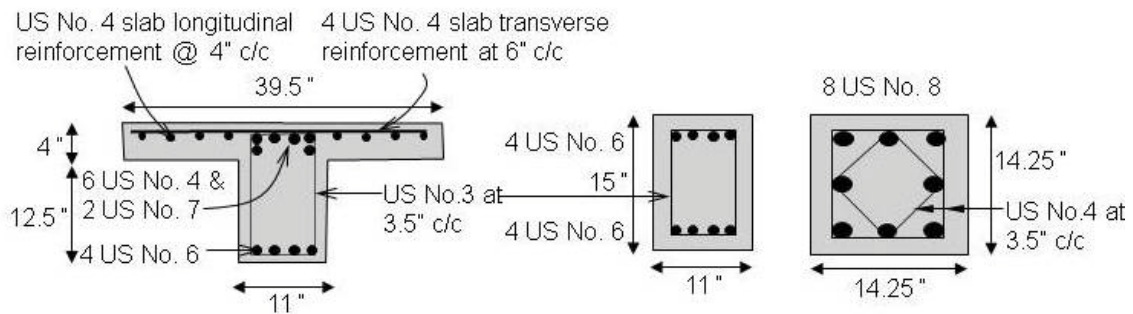


Figure 4-19. Sectional details for specimen S2 (Adapted from Durrani and Wight, 1982).

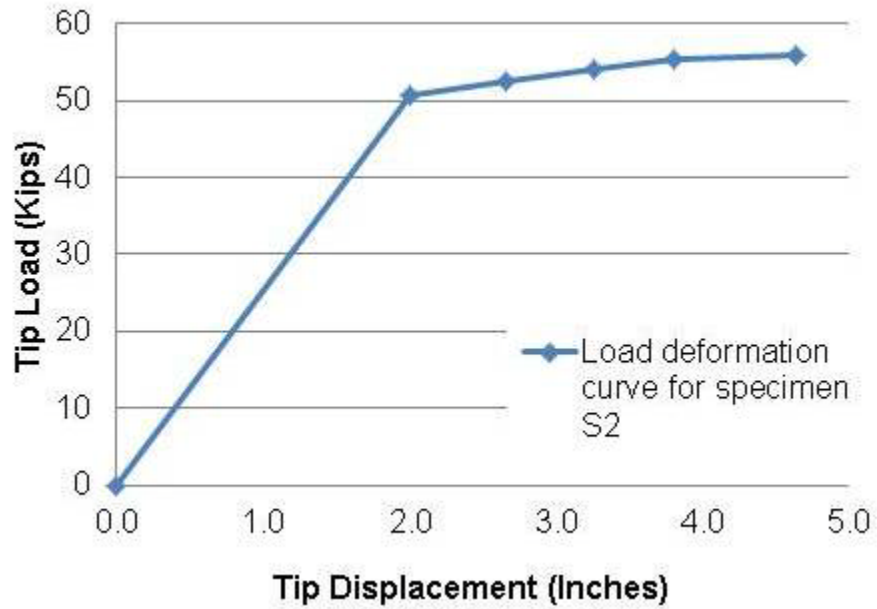


Figure 4-20. Load deflection envelope curve for specimen S2. (Adapted from Durrani and Wight, 1982).

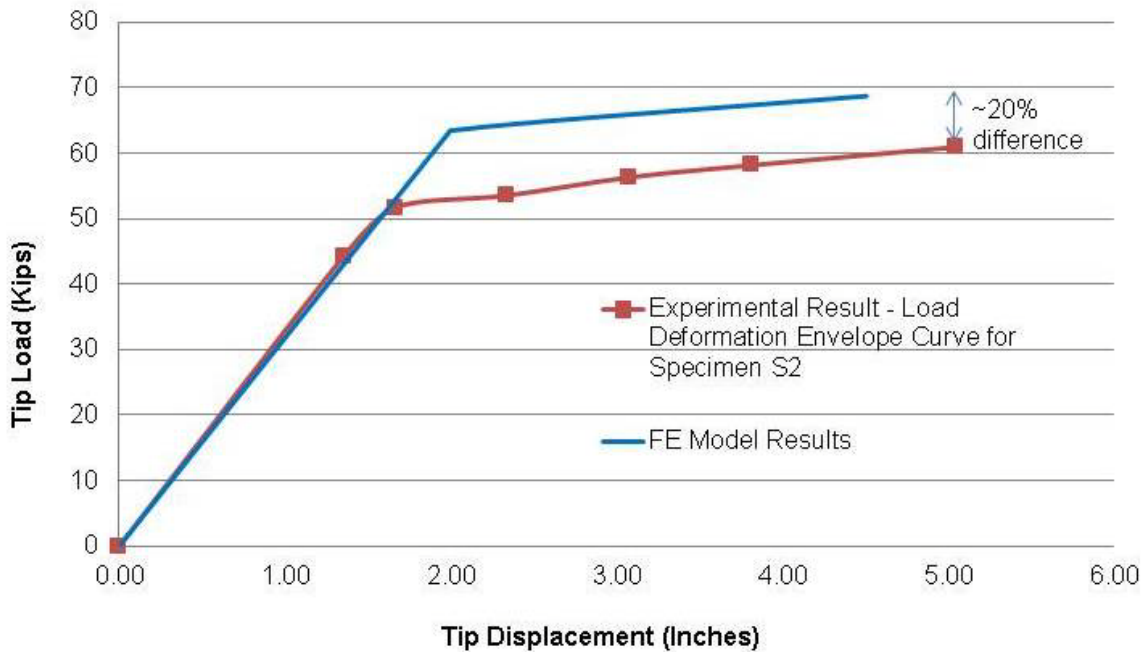


Figure 4-21. Comparison plot of modeled and experimental results for Specimen S2.

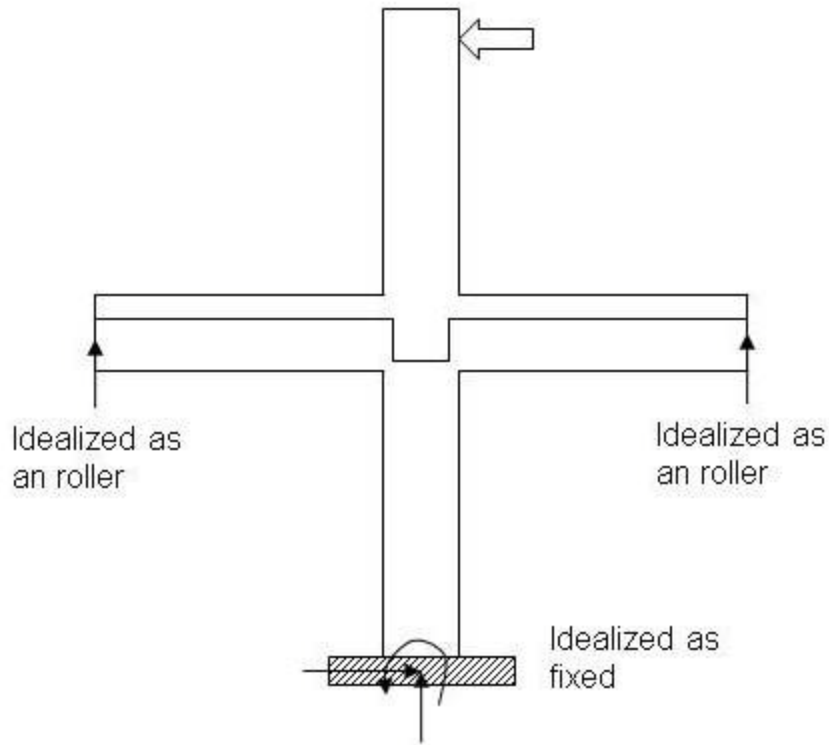


Figure 4-22. Idealized boundary conditions for the FE model for specimen S2.

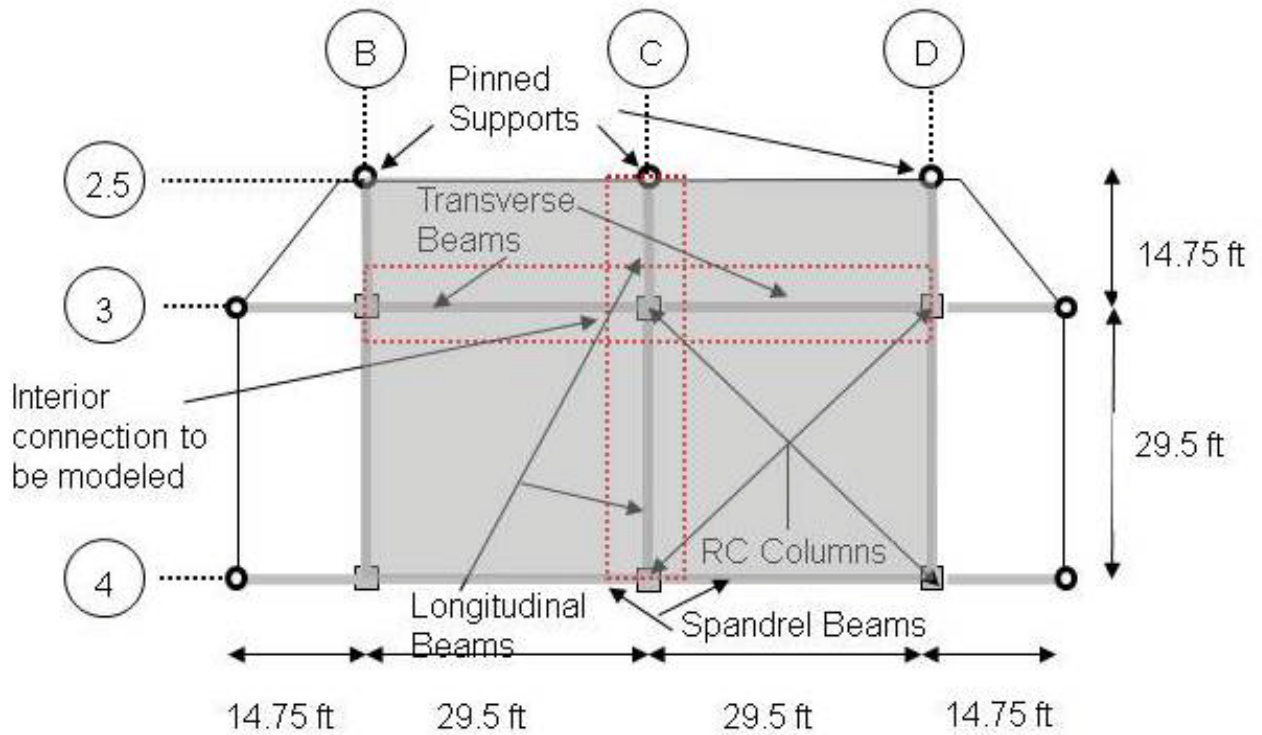


Figure 4-23. Plan layout of the test structure.

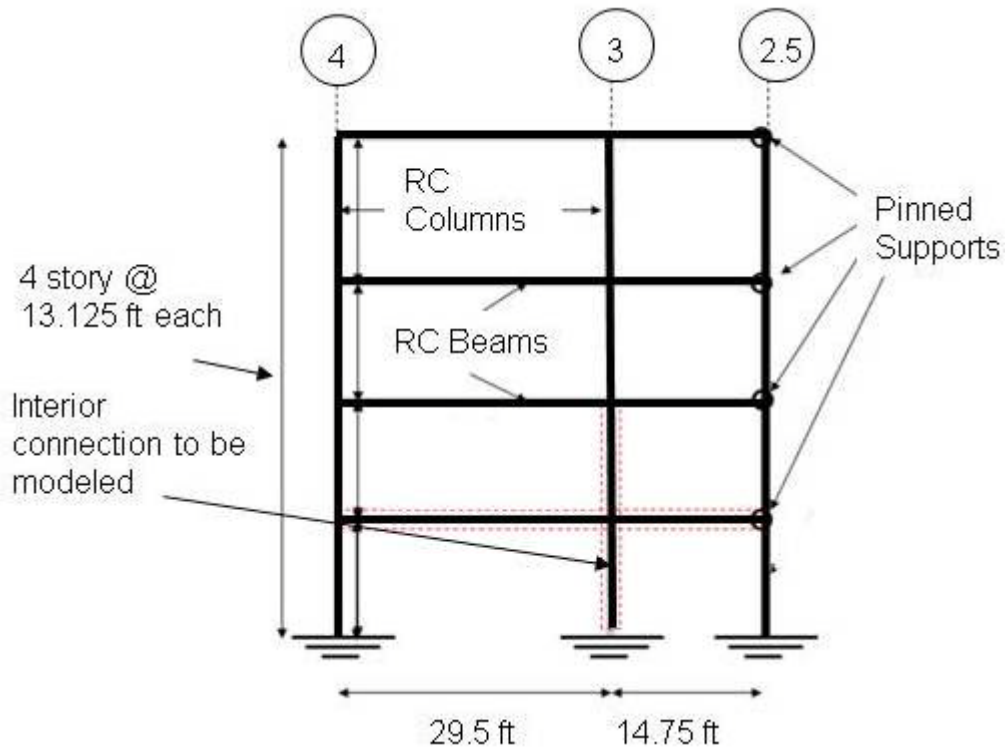


Figure 4-24. Elevation view of the test structure.

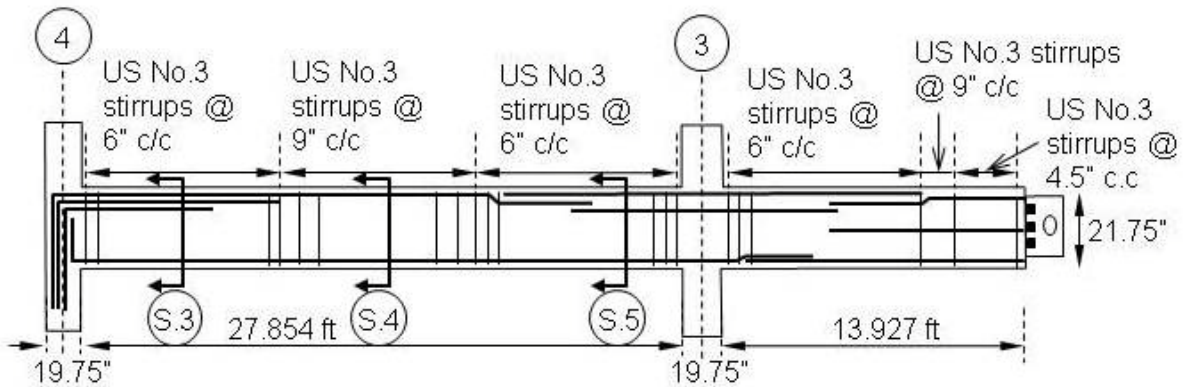


Figure 4-25. Elevation view of longitudinal beams.

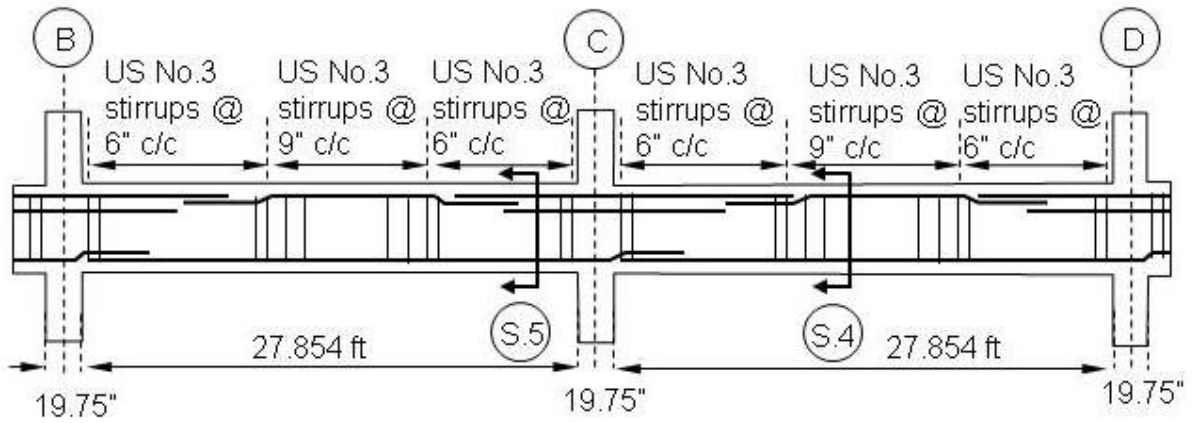


Figure 4-26. Elevation view of transverse beams.

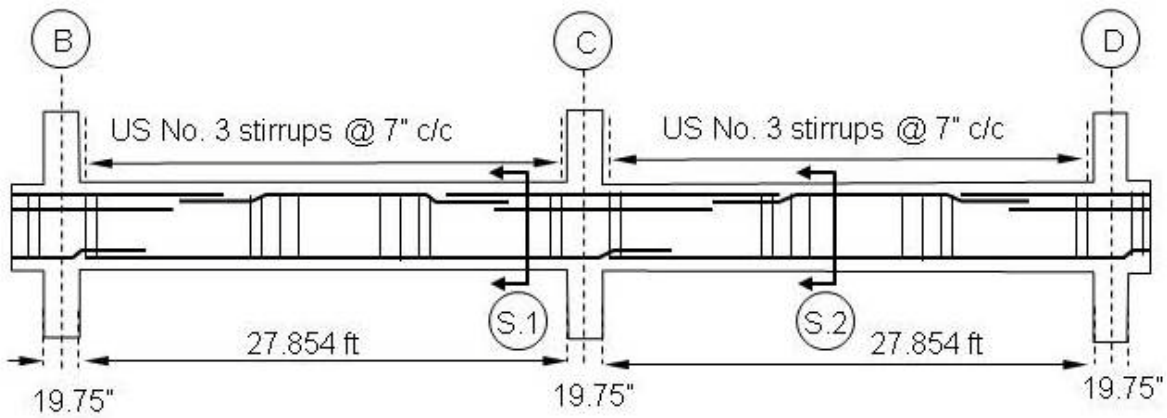


Figure 4-27. Elevation view of spandrel beams.

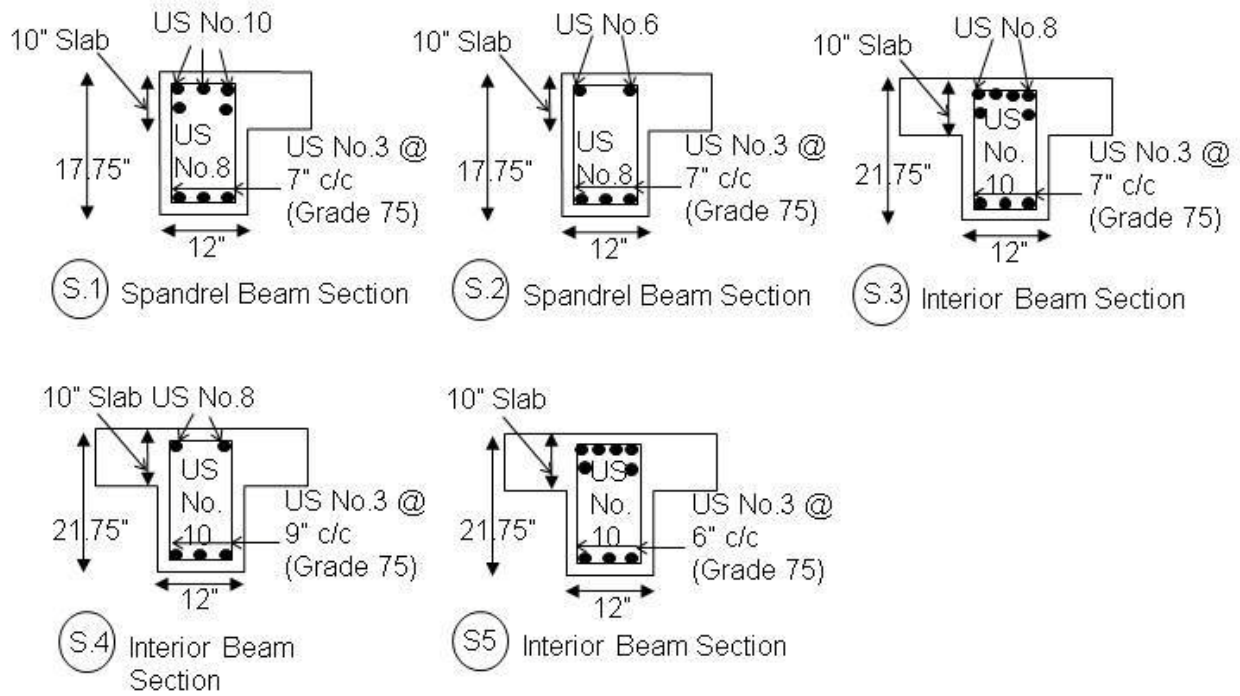


Figure 4-28. Cross-sectional details of the beams.

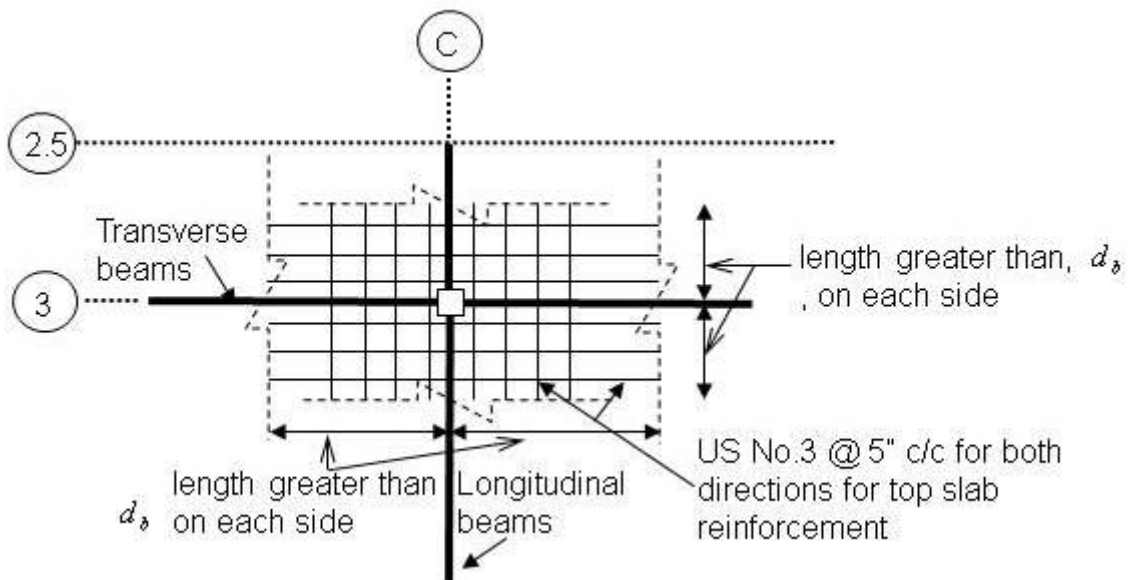


Figure 4-29. Top slab reinforcement details near column Grid C-3.

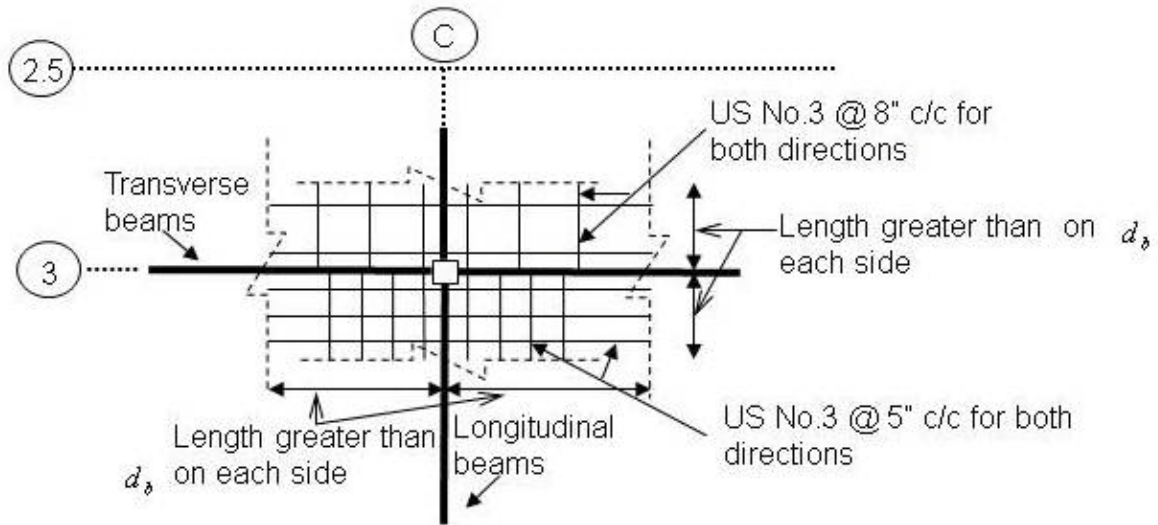


Figure 4-30. Bottom slab reinforcement details near column Grid C-3.

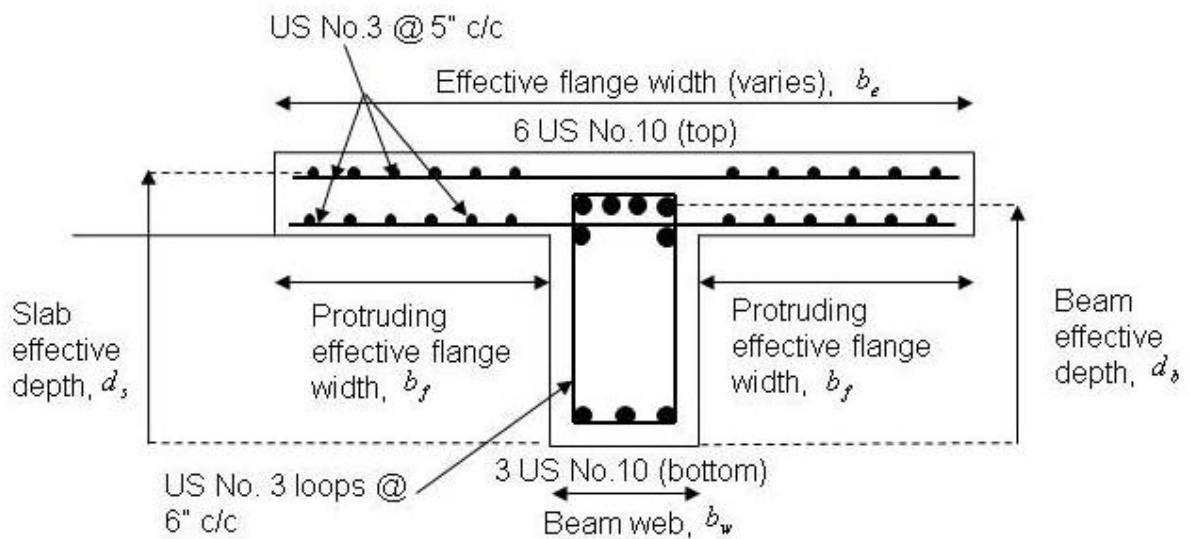


Figure 4-31. Typical T-Beam sectional details for longitudinal beam.

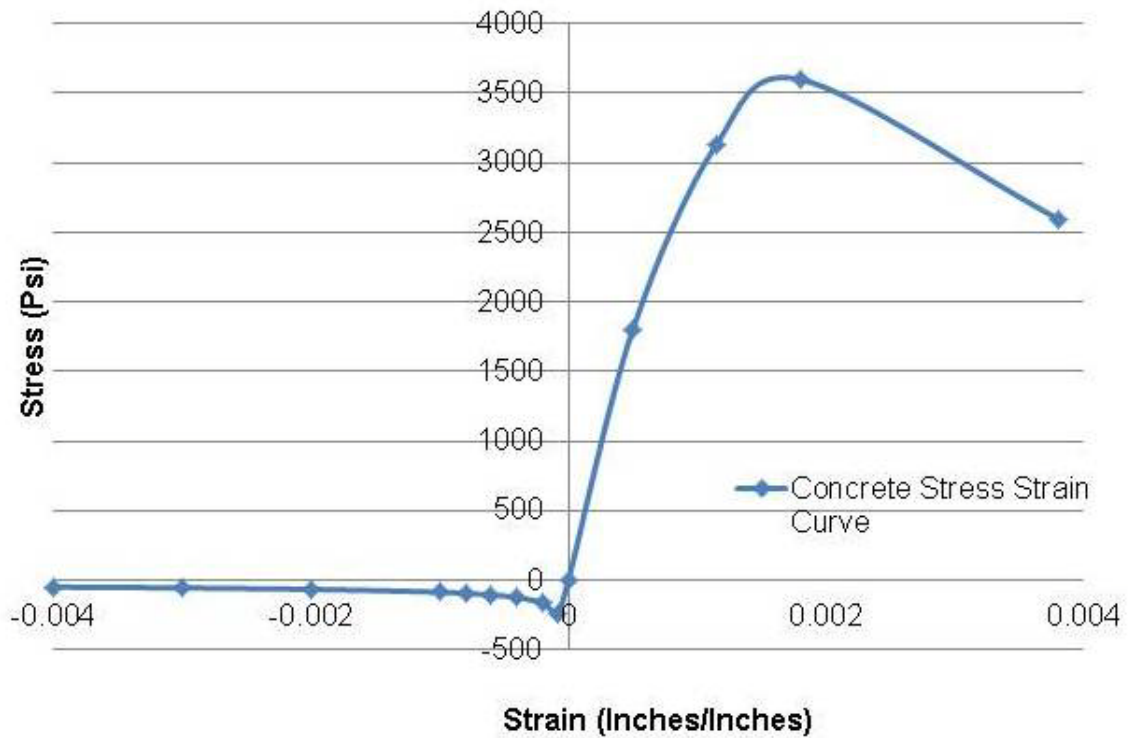


Figure 4-32. Concrete stress-strain curve from Hognestad (1951) for compression and Hsu (1993) stiffening model for tension.

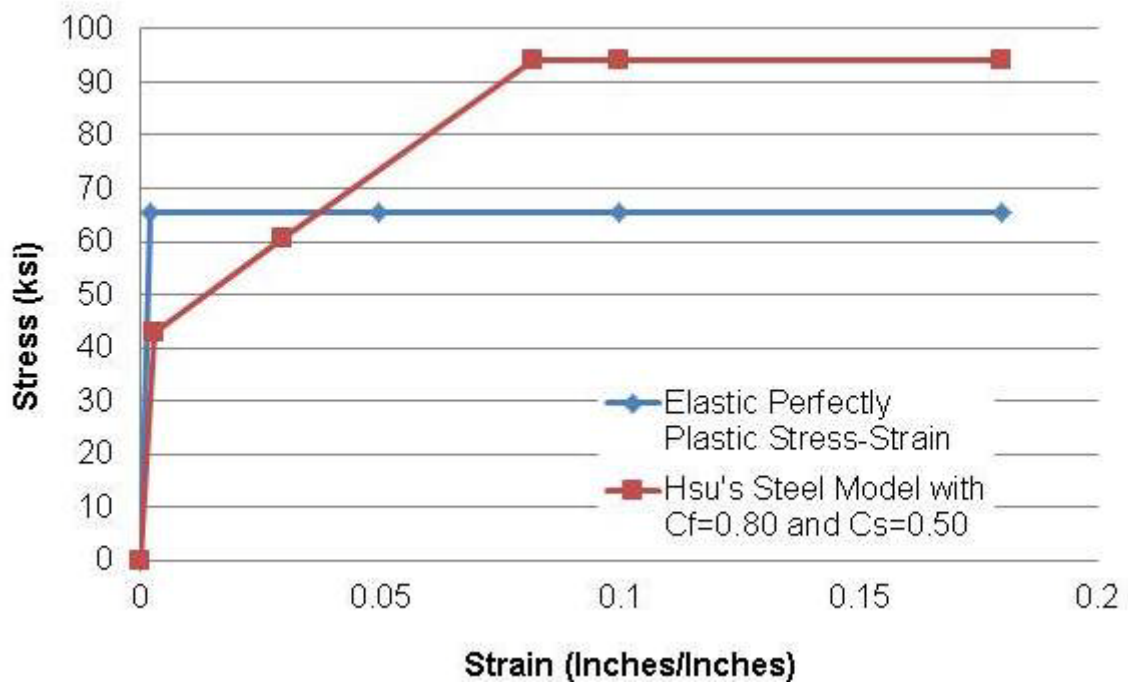


Figure 4-33. Steel reinforcement stress-strain curve modified from Hsu (1993) with  $C_f = 0.80$  and  $C_s = 0.50$ .

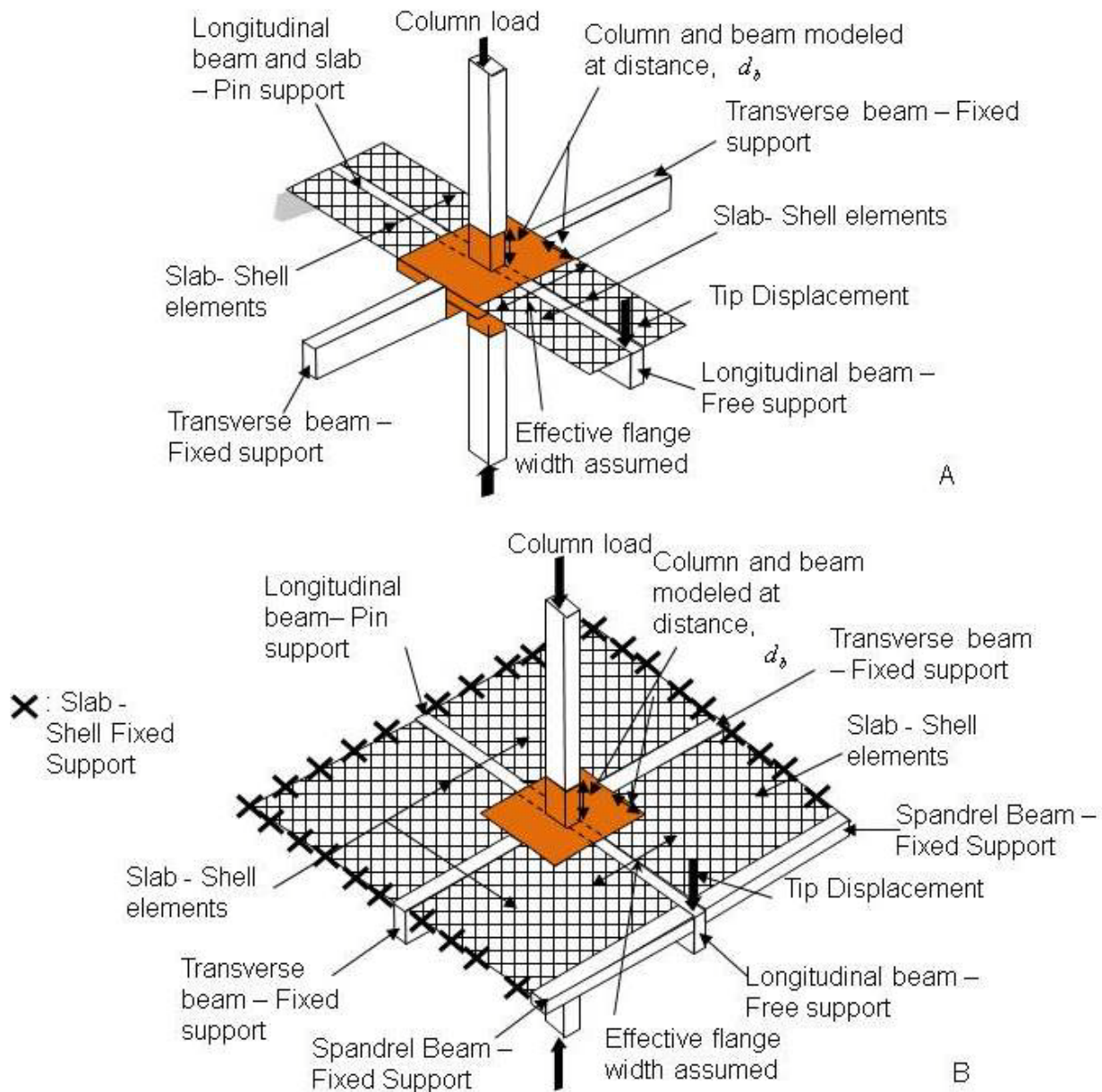


Figure 4-34. Progressive modeling of interior connection. A) detailed shaded zone and T-beam and B) detailed shaded zone and shells (Includes longitudinal, transverse and spandrel beams).

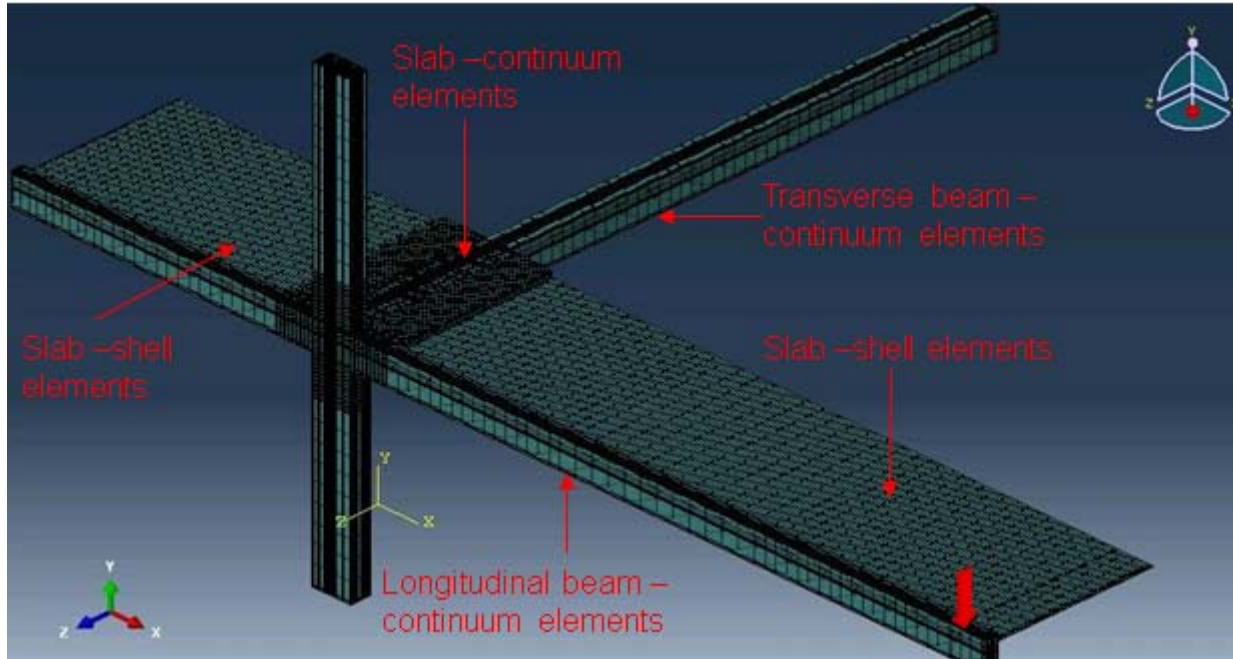


Figure 4-35. FE symmetry half model for interior connection with T-beam (Predominantly continuum based model).

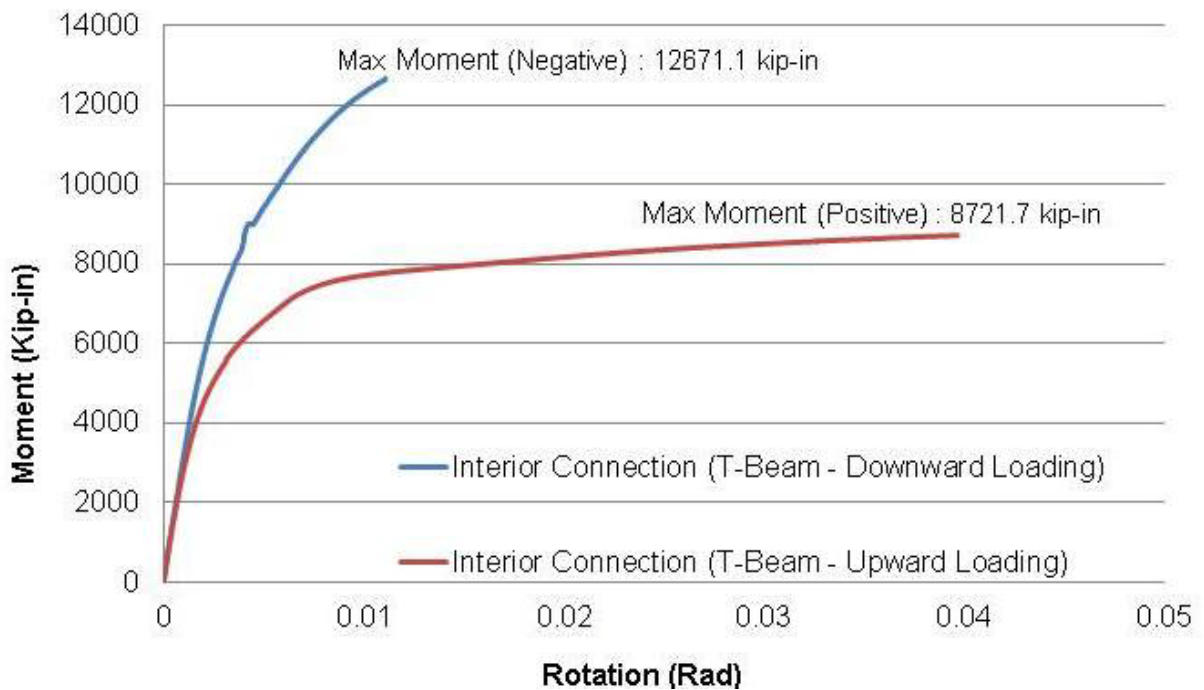


Figure 4-36. Moment-rotation curves of the FE models for the interior connection (T-beam).

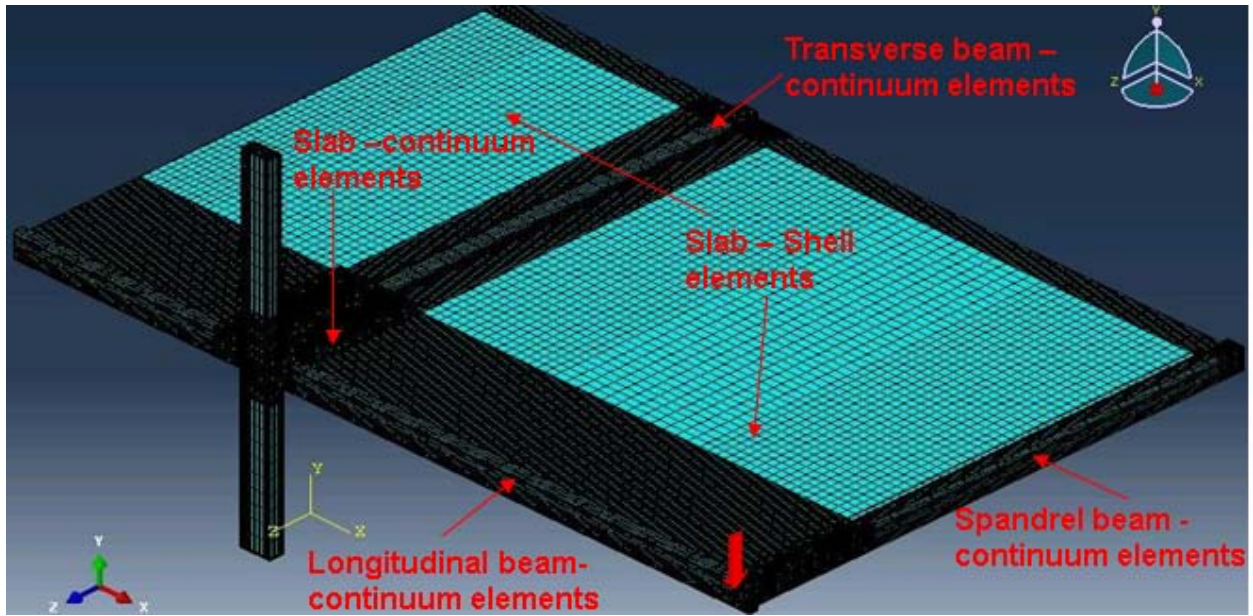


Figure 4-37. Finite element symmetry half model for interior connection (Predominantly continuum based model).

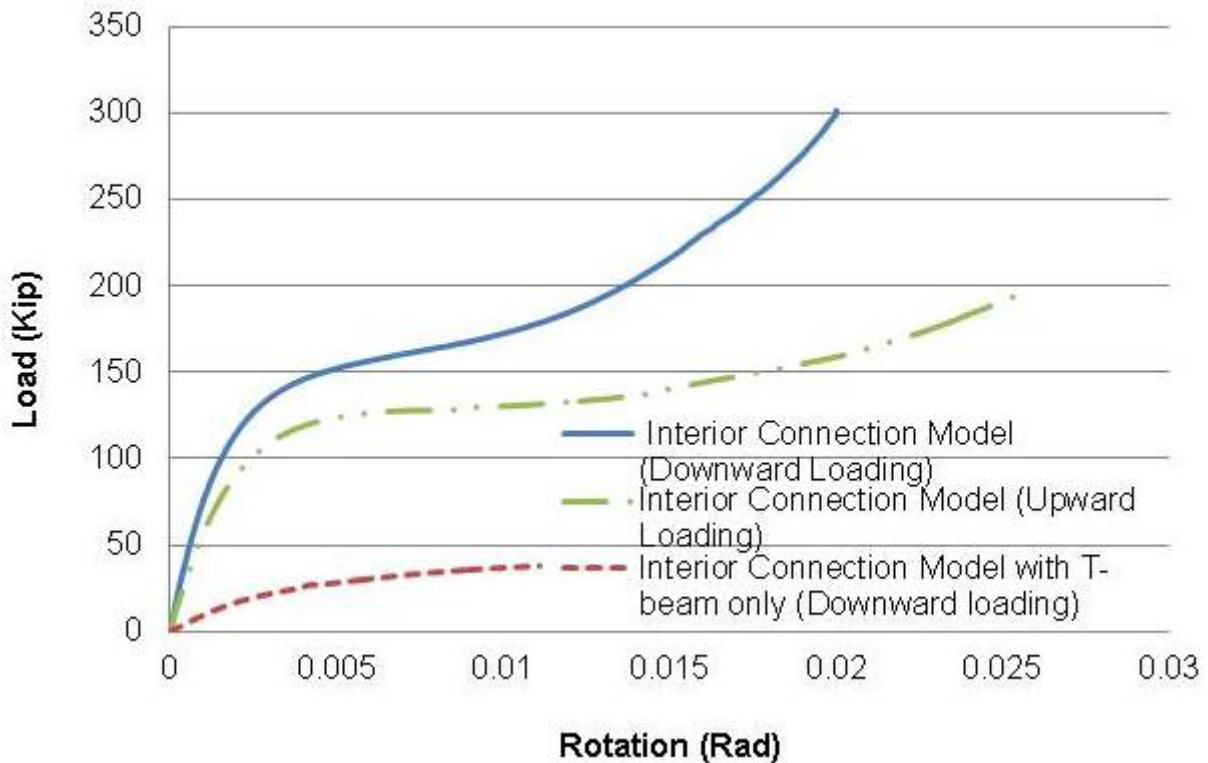


Figure 4-38. Load-rotation curve between interior connections (full connection versus idealized T-beam connection only).

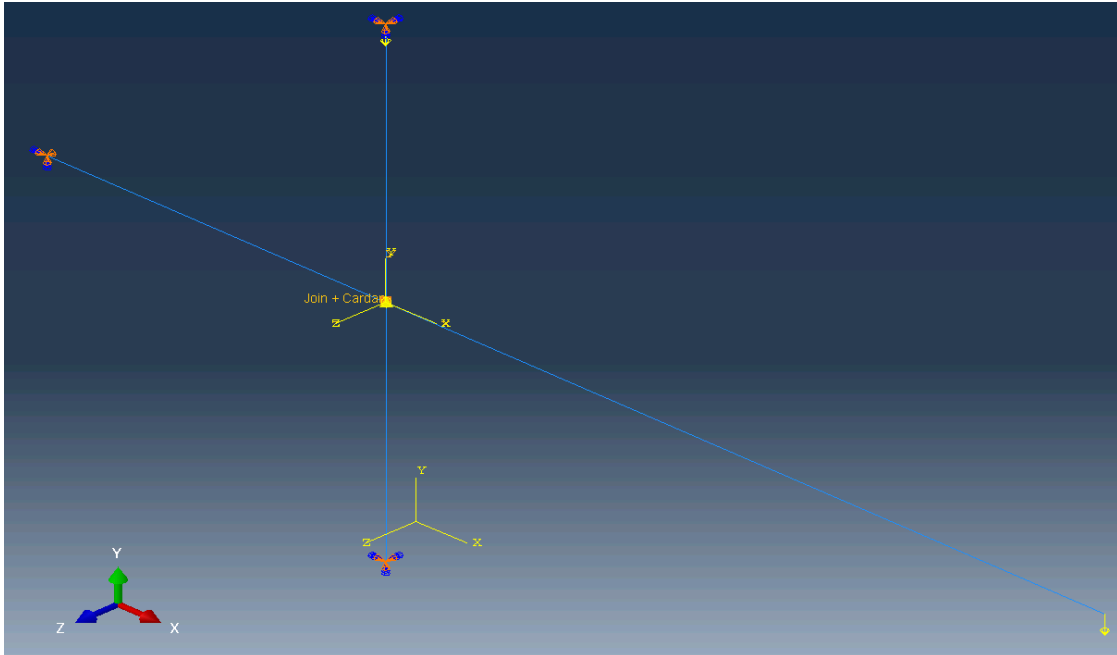


Figure 4-39. Schematic view of a structural element based FE model (Interior connection with rectangle beam only).

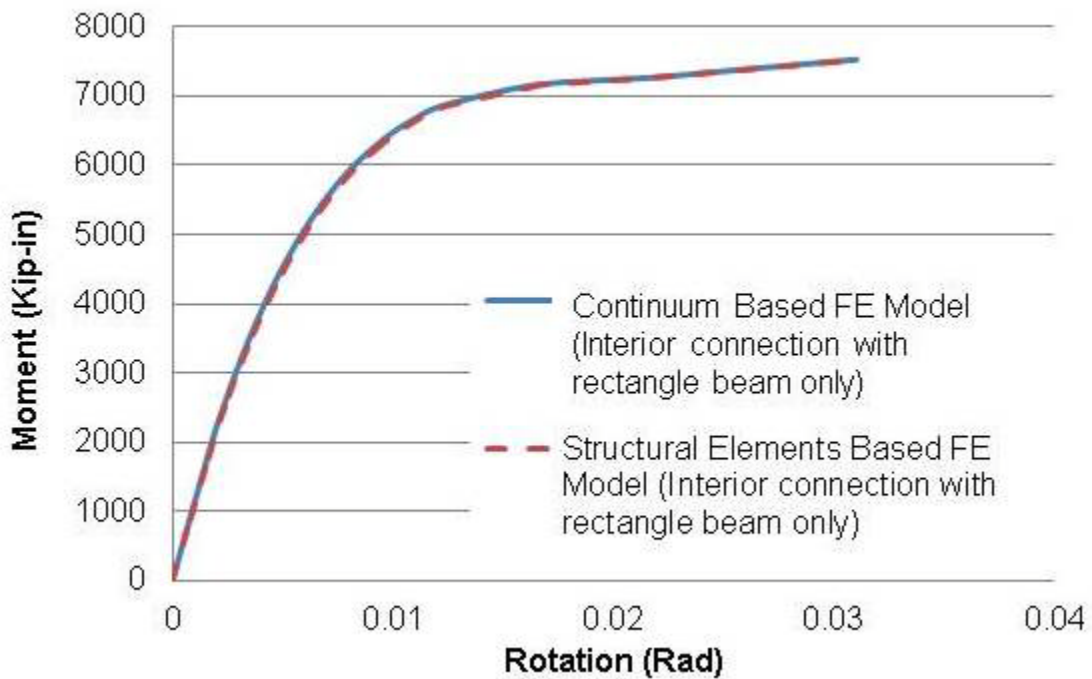


Figure 4-40. Comparison plot between the continuum and structural element based FE models (Interior connection with rectangle beam only).

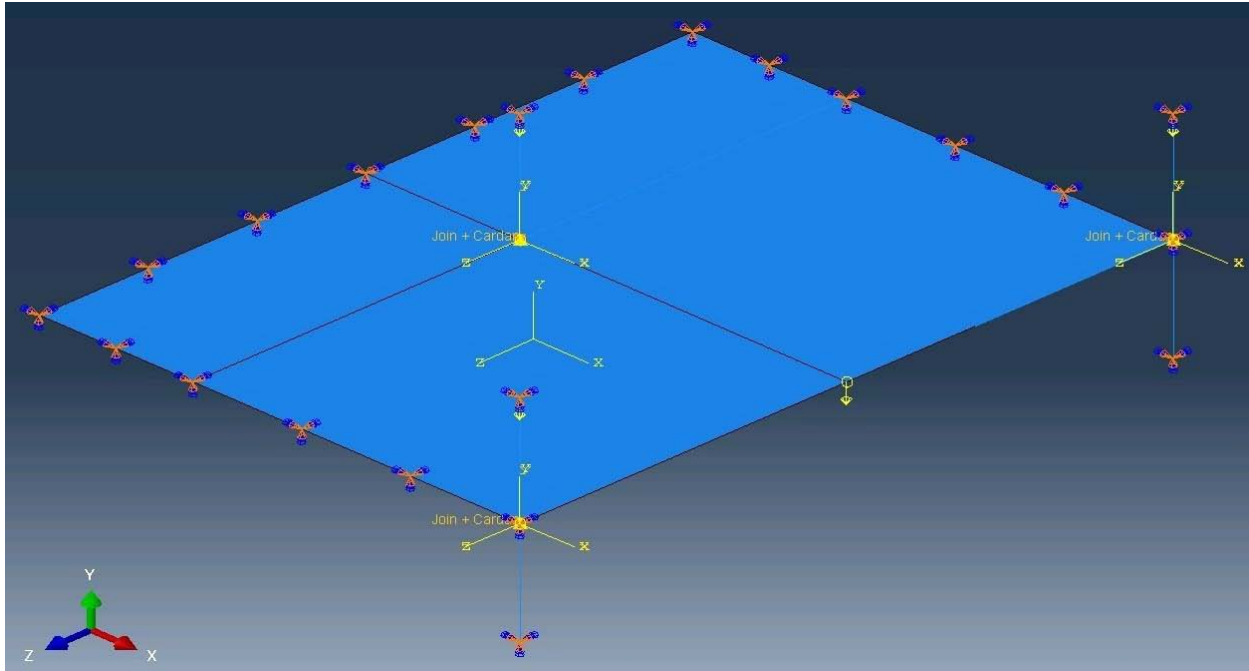


Figure 4-41. Schematic view of structural element based FE model (Full connection including longitudinal, transverse, spandrel beams and slabs).

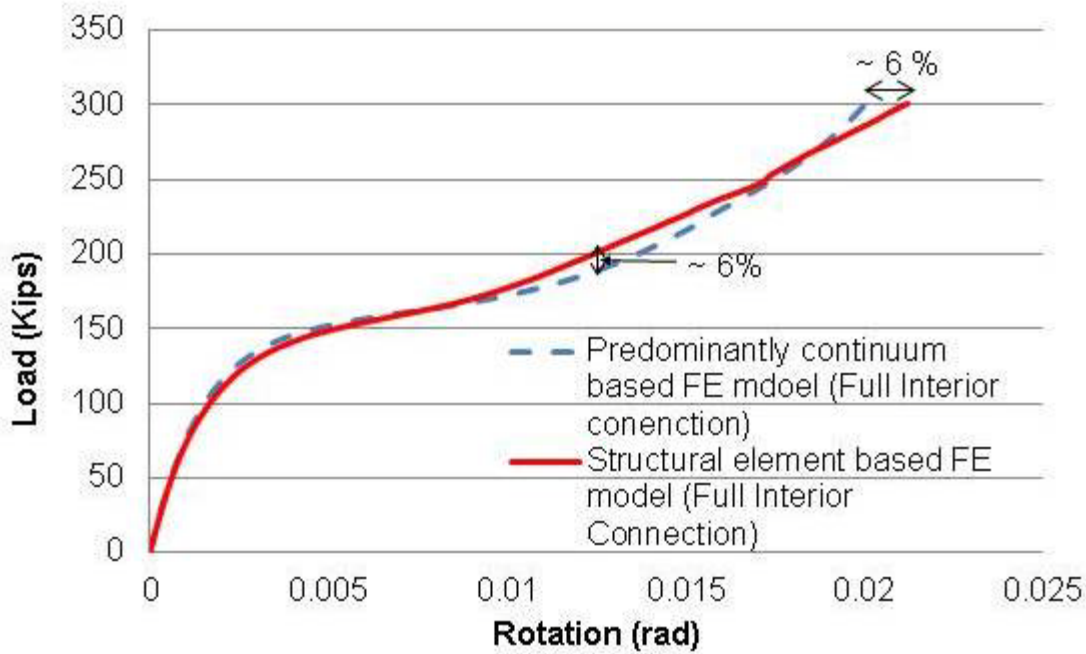


Figure 4-42. Comparison plot of the load-rotation curve for the full interior connection of this study.

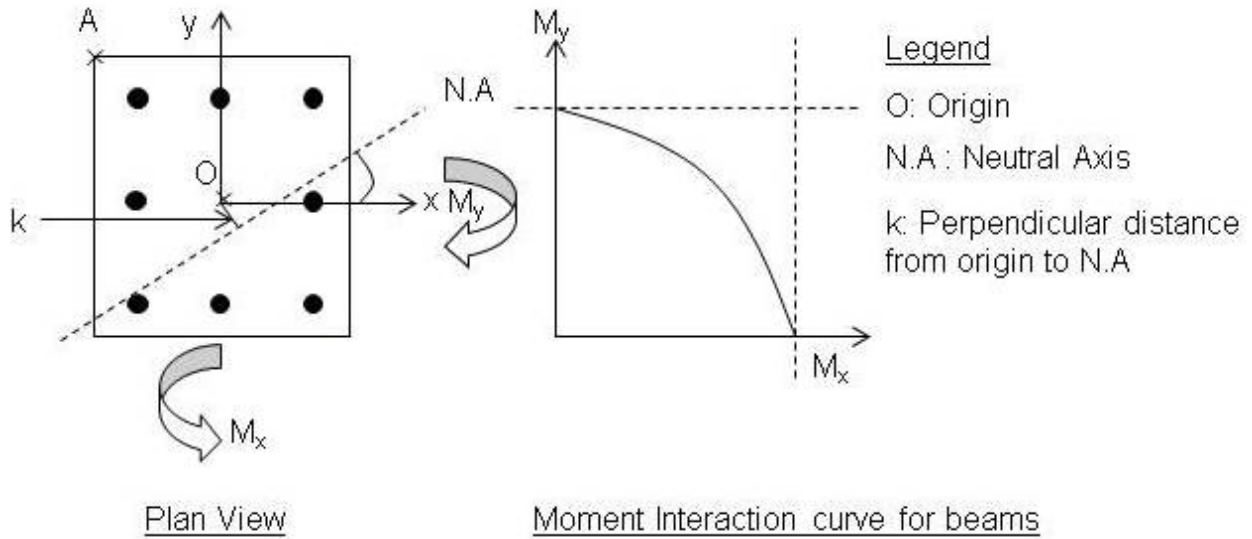


Figure 4-43. Biaxial moment interaction curve.

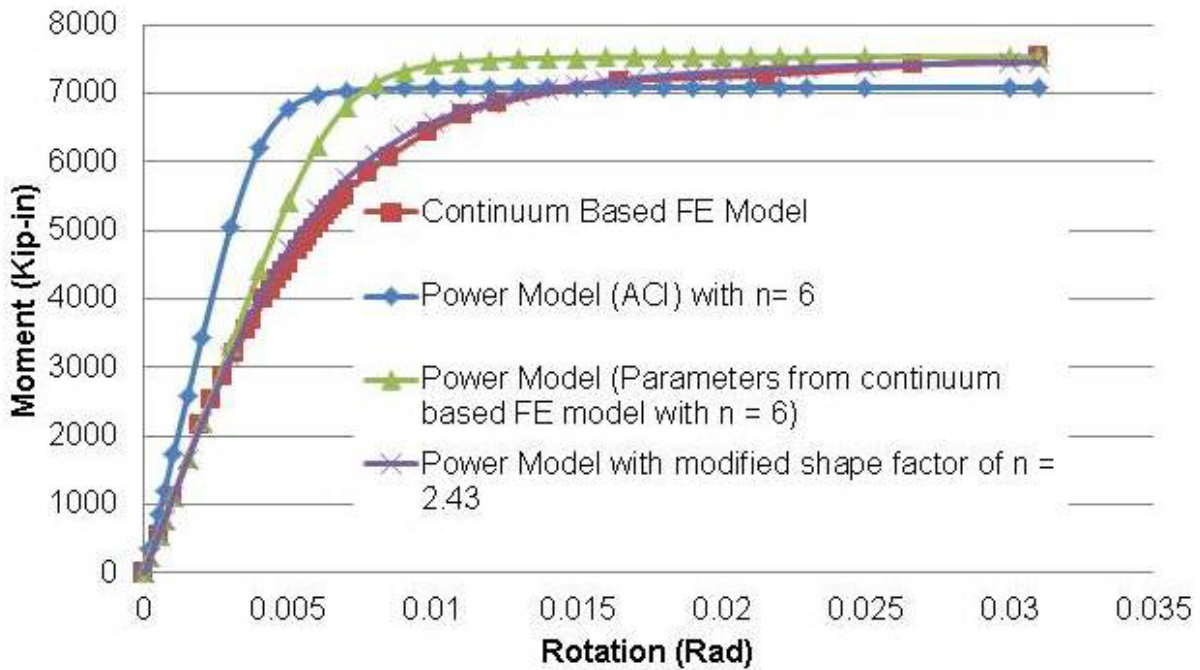


Figure 4-44. Comparison of moment-rotation behaviors from Power Model and the continuum based FE model.

Table 4-1. Parameters of concrete damage plasticity material model.

Description	Symbol	Value
Flow Potential Eccentricity	$\varepsilon$	0.1
Ratio of Initial Equibiaxial Compressive Yield Stress to Initial Uniaxial Compressive Yield Stress	$f_{bo} / f_{co}$	1.16
Ratio of Second Stress Invariant on Tensile Meridian to Compressive Meridian	$K$	0.666
Viscosity Parameter	$\mu$	0.01

Table 4-2. Summarized material models, parameters and method to be used for finite element (FE) modeling from Appendix A.

Description	Suggested Models/Parameters/Methods	Remarks
Material	Concrete	
	Compression Hognestad (1951)	Tension Hsu (1993) $f_{cr} = 3.75 \sqrt{f'_c}$
	Steel	
	Compression Same as tension	Tension Hsu (1993) $C_f = 0.80$ $C_s = 0.50$
Loading Method	Displacement Controlled	
Modelling Technique	Embedded Method	For modelling interaction between concrete and steel

Table 4-3. Changes in dilation angle on the modeled tip load in specimen R4.

Dilation Angle (Degree)	Tip Load (Kips)	% Difference
Experiment R4	28.2	
25	28.06	-0.5
30	28.53	1.2
35	28.97	2.7

Table 4-4. Mesh density variation for specimen R4.

Mesh Density (Inches)	Total No. of Elements	Tip Load (Kips)	% Diff
Experiment R4		28.2	
1	12080	28.06	-0.5
1.25	5591	28.40	0.7
1.5	3547	28.45	0.9

Table 4-5. Moment capacity of the FE models for the interior connection with T-Beam.

	Moment Capacity (Kip-in)			Remarks
	Model	Calculated	% Difference	
Interior Connection (T-Beam – Downward)	12671.1	9874.5	22.1	Calculated from DSAS
Interior Connection (T-Beam – Upward)	8721.7	7264	16.7	Calculated from ACI 318-08 using rectangle stress block

Table 4-6. Comparison of simulation time for FE models.

Model Type	Numbers of Dofs	Simulation Time (mins)
Predominantly Continuum Based FE Model	749208	7620
Structural Element Based Simplified FE Model	83448	18

## CHAPTER 5 CONCLUSION AND DISCUSSION

### **Summary**

The objective of this study was to develop a better understanding of the behavior of an interior connection under monotonic loading. In addition, to develop a simplified structural elements based FE model representing the mechanical resistance function of this interior connection.

In Chapter 2, different types of beam-column connections were introduced and various analytical connection models were described. Furthermore, the effect of the addition of transverse beams and slabs onto the interior connection were discussed, as well. Various materials models for concrete and steel reinforcement were reviewed. The finite element analysis (FEA) approach was briefly introduced as a tool used to solve engineering problems. In addition, the FEA code; Abaqus and its material models were also briefly discussed. Finally, a brief outline of the current design guidelines for progressive collapse was provided.

Chapter 3 outlined the research approach employed to characterize the beam-column-slab interior connection and to simulate its load-rotation relationship when subjected to monotonic loading.

In Chapter 4, additional validation cases for Abaqus/Standard were presented. Results from parametric studies help to identify the various material model and modeling parameters to be used. Predominantly, continuum based FE models were used to derive the load-rotation function for the interior connection in this study. A simplified structural element based FE model for interior connection was also developed as an alternative to the predominantly continuum based FE model.

## **Conclusion**

### **Validations**

Experimental load deformation results of three cases namely a cantilever beam, an exterior beam-column-slab and interior beam-column-slab sub-assemblages were validated using Abaqus/Standard. The validations help to enhance the confidence level in the various material models and parameters which were used to derive the load-rotation function of the interior connection of this study.

### **Characterizations of the Moment-Rotation of Interior Connection**

A predominantly continuum based FE model of the interior connection which includes the effect of the longitudinal, transverse, spandrel beams and slabs was simulated. The load-rotation relationship of this interior connection was successfully derived from the simulation. From the simulation results, it was evident that the effect of the slab plays a significant role in enhancing the load resistance capacity of the interior connection system. In addition, the original assumption that the slab contribution to the flexural strength is only due to the effective flange width as reviewed from seismic research, was not supported by the computed results. From the simulated results, it is evident that the 2D effects of the slab reinforcement needs to be considered, as well. Both the longitudinal and transverse slab reinforcement contributed to load resistance when the interior connection is subjected to loads caused by the removal of the exterior column.

### **Structural Element Based Simplified FE Model**

A structural elements based simplified FE model was developed for this interior connection. The simplified FE model was able to produce a reasonably good estimate of the actual load-rotation, with some discrepancies in the rotational response. Despite

the discrepancies, the simplified FE model was able to drastically cut down on the modeling and computation time. With this substantial saving in time, this simplified FE model could be developed further and be used for progressive collapse prediction for the entire building frame analysis. This could be done by constructing a full scale simplified building frame model of the test structure using the various components as described in the Chapter 4. The simplified building frame model should be subjected to gravity and service load as per the actual test structure. The analysis should be done using Abaqus/ Explicit to account for the dynamics effects from the mass of the structure and from the sudden removal of the column.

### **Limitations**

The interior connection of this study is derived from a test structure, whose results are not available yet. Thus the reliability of the simulation results that was derived from the predominantly continuum based FE model cannot be validated. The simulated results should be used as a pre-test estimate of the actual load carrying capacity of the interior connection system. In addition, in terms of the load-deformation or moment-rotation response of the interior connection, no post-peak behavior was studied on. Only the maximum load capacity and maximum rotation was obtained. Thus, there is not much clarity about the structural response of the connection after failure.

It is evident that the effect of the slab plays an important part in enhancing the load resistance of the interior connection. Majority of the slab in the interior connection system was represented by slab elements with reduced mesh density to reduce computation time. Thus, the accuracy of the simulated results might be compromised as a result in the lower mesh density used.

The simulated results from the predominantly continuum based FE model is greatly dependent on the connection details. Differences in the connection details would require another FE model to be built. Significant resources would thus be needed and the cost associated could be prohibitive.

The simplified structural element based FE model was able to provide a good estimate of the load-rotation response of the interior connection system, however, it is not ideal or complete yet. The current simplified model only account for the bending resistance about the main axis only. Thus, the bending resistance in the weak axis needs to be incorporated for as well. In addition, the interaction effects from the various combinations of force mechanisms are not considered as well, which could affect the overall load-capacity of the whole interior connection system. There exists mathematical models that are used to represent the interaction effects from the various combinations of force mechanism; however, the effects are often done independently. The current simplified FE model also did not considered the spatial variation of stiffness that occurred along the beam length. These issues would need to be addressed in a follow up study.

### **Recommendations for Future Research**

The simulated results from the predominantly continuum based FE model of the interior connection of this study should be validated against the results from the progressive collapse test, when available. This would help in the calibration of the FE model. The calibrated model would thus be able to produce more reliable results. In addition, the post peak behavior response of the interior connection could be further examined. This would allow researcher to better understand the behavior of the connection after failure.

The majority of the slab areas were represented by shell elements to reduce computational time, and thus the accuracy of the simulated result might be affected. A full continuum based FE model for the interior connection, which also models the slab using continuum based elements, could be explored. However, this should only be attempted if there are sufficient computational resources available.

The current simplified FE model could be further improved to account for the following effects:

- Weak axis bending resistance of the RC beam-column connection.
- Interaction effects from the various combinations of force mechanisms.
- Coupling effects to incorporate all the above into one comprehensive model where interactions effects are interdependent of each others.
- Alternative approach to incorporate the spatial variation of the crack stiffness of the beam. Approach such as specifying the behavior of the beam elements via moment-curvature relationship could be explored.

A mathematical model representing the moment-rotation function of the RC connection (rectangle cross-section) could be derived which can be used universally for all kind of connection details. This mathematical model could be used to replace the time consuming continuum based FE model simulations in establishing the resistance function of the RC beam-column connection. Power Model was reviewed to be suitable to represent the mechanical behavior of the RC beam-column connection. However, efforts would be required to develop a physical based analytical approach in estimating the elastic rotation stiffness, the ultimate moment capacity and the applicable shape factor for the RC beam-column connection.

Lastly, progressive collapse analyses of the full building configuration subjected to abnormal loading could be attempted and validated against the actual test structure.

## APPENDIX A PARAMETRIC STUDIES FOR SPECIMEN R4

With reference to Chapter 2, material models for both concrete and steel reinforcement have been presented. This appendix will touched on the parametric studies for the selection of the appropriate material models to be used for the Finite element (FE) modeling of the interior connection of this study. In addition, different loading methods such as displacement controlled and force controlled are discussed. Lastly, two of the techniques used to model the interaction between concrete and steel reinforcement are reviewed. The specimen used for the parametric studies was based on specimen R4 as tested by Ma et al. (1975).

**Concrete Material Models Selection.** The modified Hognestad's stress-strain curve for compression as presented in Figure A-1 and dilation angle (25 degrees) was kept constant throughout the parametric study. Hsu's steel model, as presented in Figure 2-56, was used. The two variables for concrete material models were, as follows:

1) Tension stiffening models where modulus of rupture as provision by America concrete Institute (ACI) Committee 318 (2008) with  $f_{cr} = 7.5 \sqrt{f'_c}$  was used for all three tension stiffening models to allow for a common basis of comparison.

- Vecchio and Collins (1981)
- Mitchell and Collins (1991)
- Hsu (1993)

2) Concrete cracking stress where  $f_{cr}$  was varied to see the effect on the selected tension stiffening model. The selected tension stiffening model was based on the model that give the closer modeled tip load result, as compared to the experimental result.

Figure A-2 presents the results from the variation of the three tension stiffening models while keeping the concrete cracking stress  $f_{cr}$  and dilation angle constant. It appeared that the tension stiffening model proposed by Vecchio and Collins (1981) produced the stiffest structural response with the largest difference (47%) in the tip load when compared to the experimental results. On the other hand, Hsu's tension stiffening model produced the closer results to the experimental tip load. However, the difference is still significantly large at 33%. Thus, it appeared that the choice of the tension stiffening model is not the only parameter that affects the structural response.

From Figure A-2, it was shown that Hsu's tension stiffening model produced the best results out of the three tension stiffening models. With reference to Chapter 2, Hsu proposed that the cracking stress for concrete as  $f_{cr} = 3.75 \sqrt{f'_c}$  instead. This is much reduced from the one proposed by ACI Committee 318 (2008) of  $f_{cr} = 7.5 \sqrt{f'_c}$  used in the preceding parametric study. The reduction of  $f_{cr}$  caused an improvement of the modeled tip load when compared to the measured tip load, as shown in Figure A-3. Nevertheless, the modeled result still differs quite substantially at approximately 18% higher than the experimental results. Other parameters that might have an influence on the modeled results should be considered as well.

**Steel Material Models Selection.** Three variables were studied to see their effects on the structural response. The concrete model will be based on modified Hognestad compression curve and Hsu's tension stiffening model with  $f_{cr} = 3.75 \sqrt{f'_c}$  and dilation angle fixed at 25 degrees. The variables for the steel material model were, as follows:

1) Steel material models, as shown in Figure A-4. The material models were idealized representation derived from the actual steel stress-strain curve presented in Figure 4-6.

- Elastic perfectly plastic
- Idealized linear stress-strain curve
- Modified Hsu steel model with capped maximum stress

2) Equivalent yield stress,  $f'_y$  from Hsu's steel model.

The  $f'_y$  was varied by using a correction factor  $C_f$  to evaluate its effects on the structural response.

3) Reduced initial steel Young's modulus,  $E'_s$ .

Hsu's steel model has a linear stress strain relationship from the start till the equivalent yield stress,  $f'_y$ , as shown in Figure 2-54. It does not take into account the softening effect after the concrete cracked prior to the steel yielding. This softening effect is simulated by using a correction factor  $C_s$  to account for the reduced steel initial stiffness.

$$E'_s = C_s E_s \quad (A-1)$$

As mentioned earlier, three different idealizations of the steel stress-strain curve were studied. The differences in the measured and the modeled tip load are presented in Figure A-5 for each case, as follow:

- Elastic perfect plastic idealization = 4%
- Idealized linear steel stress strain curve = 10.7%
- Hsu steel model = 18%

Although, the elastic perfect plastic stress-strain curve had the least difference between the measured and modeled tip load, the load-deformation curve did not match

the physical observation. It appeared that the best match for the physical behavior of the test specimen was achieved by Hsu's steel model. Nevertheless, it had the highest difference (18%) in the modeled tip load results.

Hsu's steel model is an idealized bilinear stress-strain model, as presented in Figure 2-54, with an empirical equivalent yield stress,  $f'_y$ , obtained from test data. Thus,  $f'_y$  might be subjected to experimental variability. The variability can be due to the limited test samples used to obtain the correlation, error in test setup, testing conditions, or material properties variability. Thus,  $f'_y$  was varied with various correction factors  $C_f$  to study its effects on the structural response, as shown in Figure A-6.

From Figure A-6, it is noted that the Hsu's steel model seems overly strong (for  $C_f = 1.0$ ) with higher yield load as compared to the test results. Correction factors of 0.80 and 0.75 to the equivalent yield stress,  $f'_y$ , produced reasonable good match to the yield load of the specimen R4 and its physical behaviour. The differences in the modeled and measured tip load were 4% and 0.5% for  $C_f$  of 0.8 and 0.75, respectively. However, it was observed that the model behaved too rigidly prior to steel yielding, and this might be due to the inability of the model to represent cracked concrete. To better represent the physical behavior, it was proposed to modify the Hsu's steel model to account for this softening after the concrete had cracked extensively.

Abaqus/Standard does not allow the variation of stiffness in the elastic range of the steel material model. The reduction of stiffness can be achieved via introducing a correction factor  $C_s$  to the initial steel young modulus ( $E_s$ ), which simulated the effect of

cracked concrete prior to steel yielding.  $C_s$  was varied to attempt to match the behavior of the experimental results at the yield load. From Figure A-7, it was observed that the reduction of stiffness had a significant softening effect on the structural response of FE model prior to the yield load. The best result was obtained using  $C_s = 0.5$ , with the difference in the tip load at 0.5%, and the softening effect due to cracked concrete was adequately captured.

**Displacement Controlled Versus Force Controlled Loading.** The previous sections in Appendix A described parametric studies where the displacement controlled loading method was used. Displacement controlled loading is where the loading of the specimens are governed by prescribed displacements at different time intervals with reaction forces measured. In contrast, the force controlled loading is exactly the opposite, forces are specified at different intervals and displacement measured.

It was observed that the structural response of the FE model for specimen R4 depended on the load history. This was evident from the large differences in the load-deformation curve of the displacement controlled FE model versus that of the linearly ramped force controlled FE model, as presented in Figure A-8. At any point beyond the elastic region of the structural response, the load experienced by the structure will not be the same due to the differences in the load history as applied by the two methods.

This was further verified when the reaction forces at the loading point derived from the displacement controlled loading were applied as a force controlled loading. The FE model yielded the same structural response as that of the displacement controlled loading.

**Embedded Versus Tie Nodes Modeling Technique.** Various methods are available to model the reinforced concrete (RC) in Abaqus/Standard. Tan (2010) tried using the embedded technique to model the interaction between the reinforcement and concrete. The embedded reinforcement will lose their translational degree of freedoms (dofs) while maintaining their rotational dofs. This embedded technique assumed perfect bonds occurred between the embedded reinforcement and the concrete and thus no slip can occurred. Another technique is presented here where the concrete and the reinforcement are only tied at nodal locations based on geometry of the reinforcement details. The tied nodes will have the same translational and rotational dofs.

As shown in Figure A-9, both techniques produced similar results and with reasonably close match to the experimental results, both in term of tip load and physical behavior. However, the computation time required for the embedded method was drastically higher than that of the tied nodes method, as presented in Table A-1. The differences in the computation time might be due to the numbers of interaction points generated. As seen from Figure A-10 A, the embedded method created much more interaction points between the concrete and the reinforcement as compared to the tie nodes method in Figure A-10 B. Each interaction point needed to satisfy compatibility and equilibrium requirements, and thus, it required more time for the embedded method to complete a run of the analysis.

Although the tie node method reduced the computational time significantly, it has its drawbacks as well. It took significantly more time to create the model in the graphic user interface (GUI), as compared to the embedded technique. It is recommended that

for large scale FE model, embedded technique should be used instead until a better modeling technique for the tie node method is available. Alternatively, a user subroutine could be programmed to more efficiently tie the nodes between the concrete and the steel together.

**Summary.** In summary, the material models and parameters that produced the best fit with both the physical behavior, and the measured tip load of the specimen R4 are presented in Table A-2. In addition, it was observed that there was no differences in the results between displacement and force controlled loading methods. Displacement controlled loading method was chosen as it closely emulated that of the actual experiments. Both methods (embedded and tie nodes) of modeling the interaction between concrete and reinforcement generated similar and reasonable results. However, the embedded method might be preferred for large scale FE model.

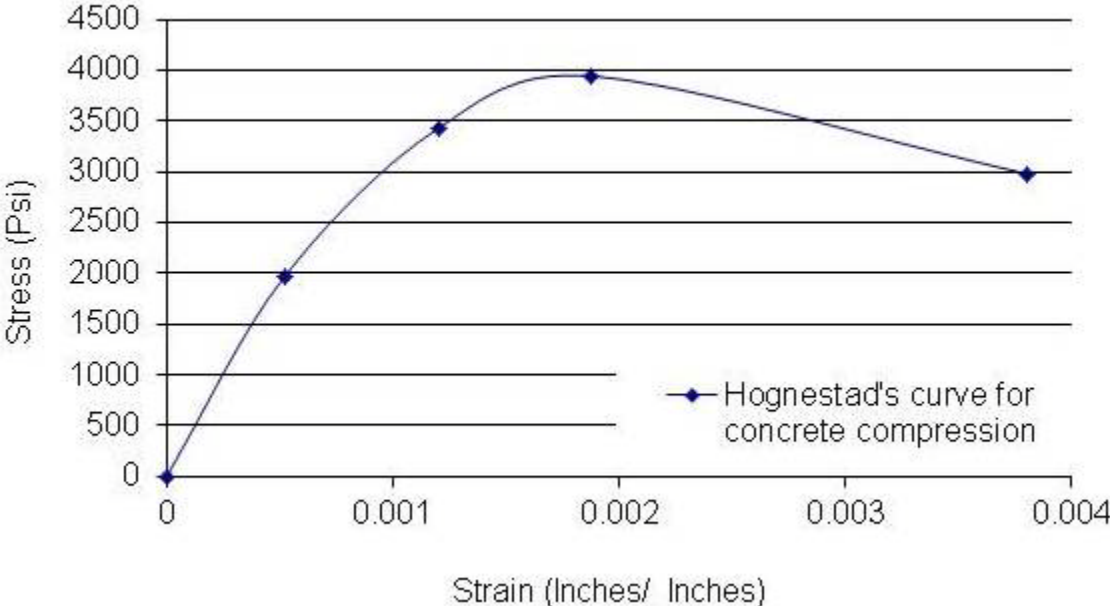


Figure A-1. Modified Hognestad compression stress-strain curve for concrete.

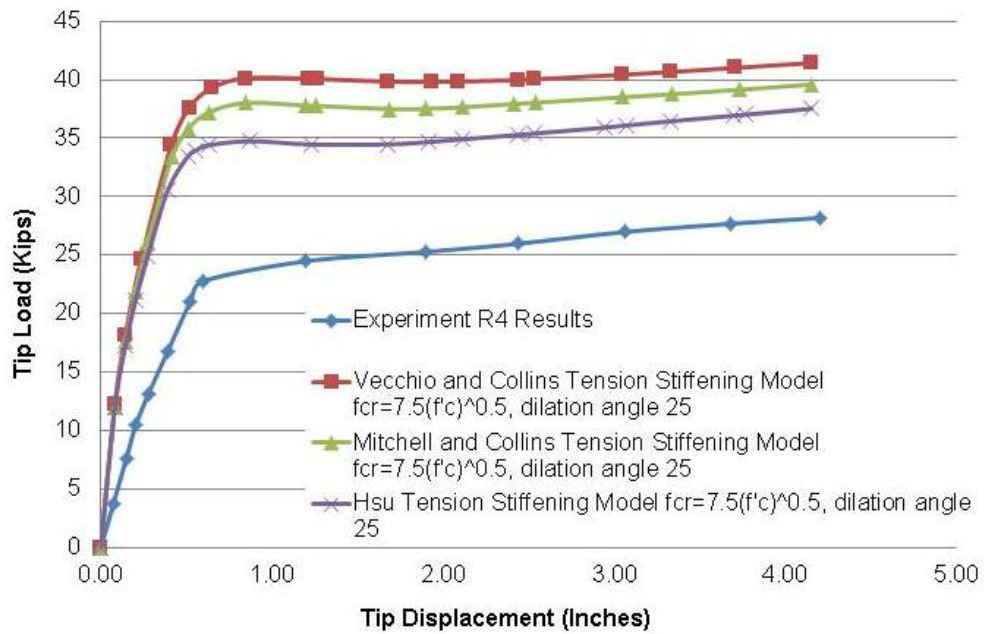


Figure A-2. Comparison plots between various tension stiffening models with constant dilation angle and cracking stress for specimen R4.

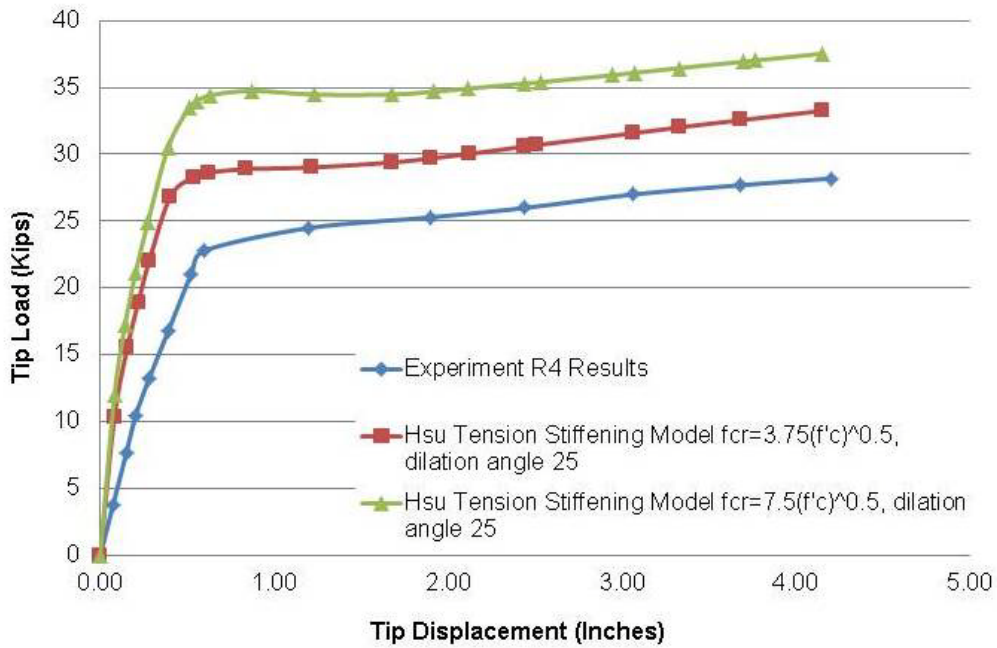


Figure A-3. Comparison plots of different cracking stress  $f_{cr}$  based on Hsu tension stiffening model for specimen R4.

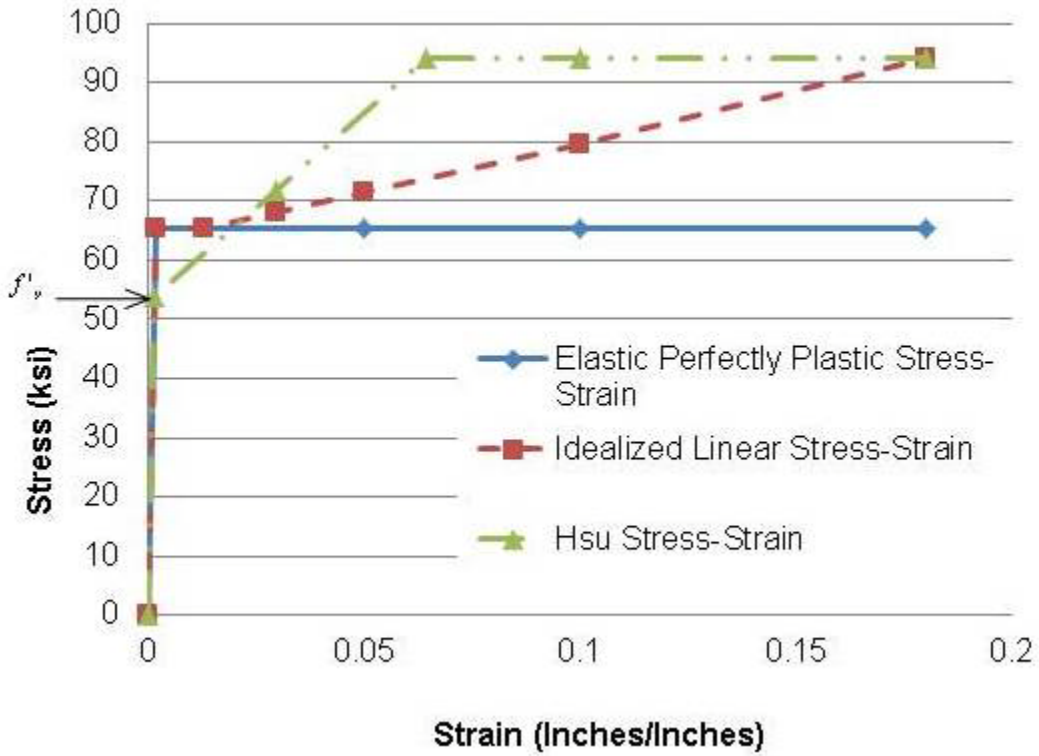


Figure A-4. Different idealization for steel stress-strain curve.

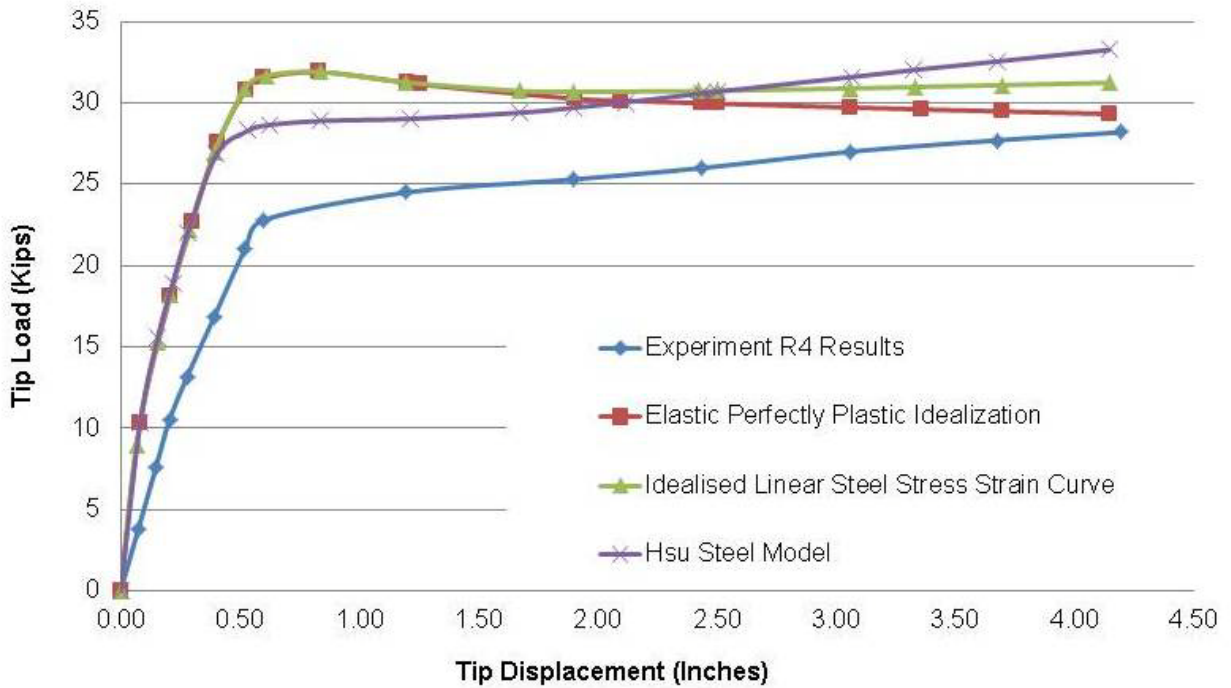


Figure A-5. Comparison plots of different steel stress-strain curve idealization for specimen R4.

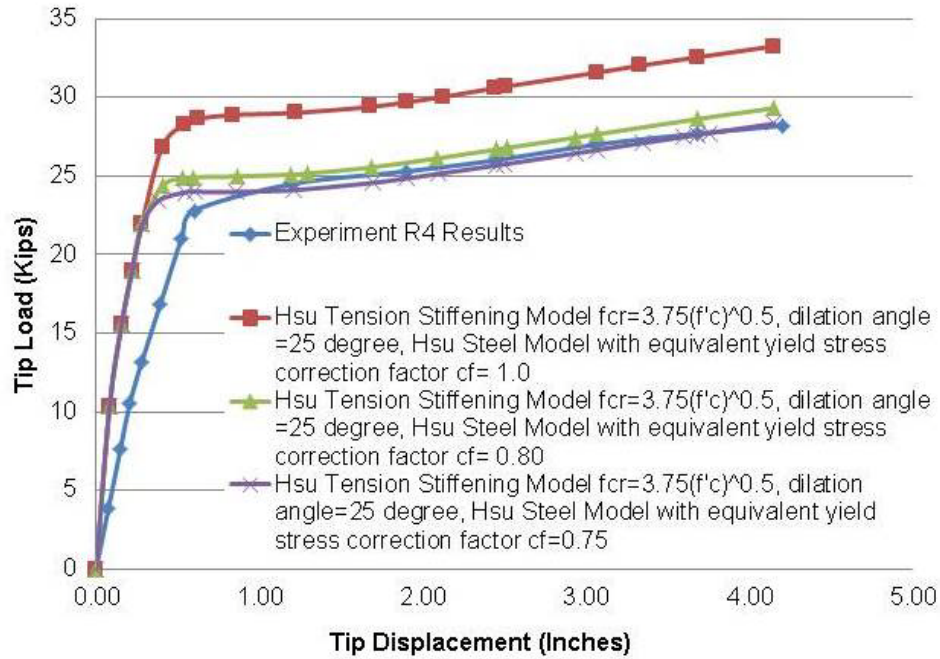


Figure A-6. Comparison plot of load-displacement curve with variation of equivalent yield stress correction factors  $C_f$  for specimen R4.

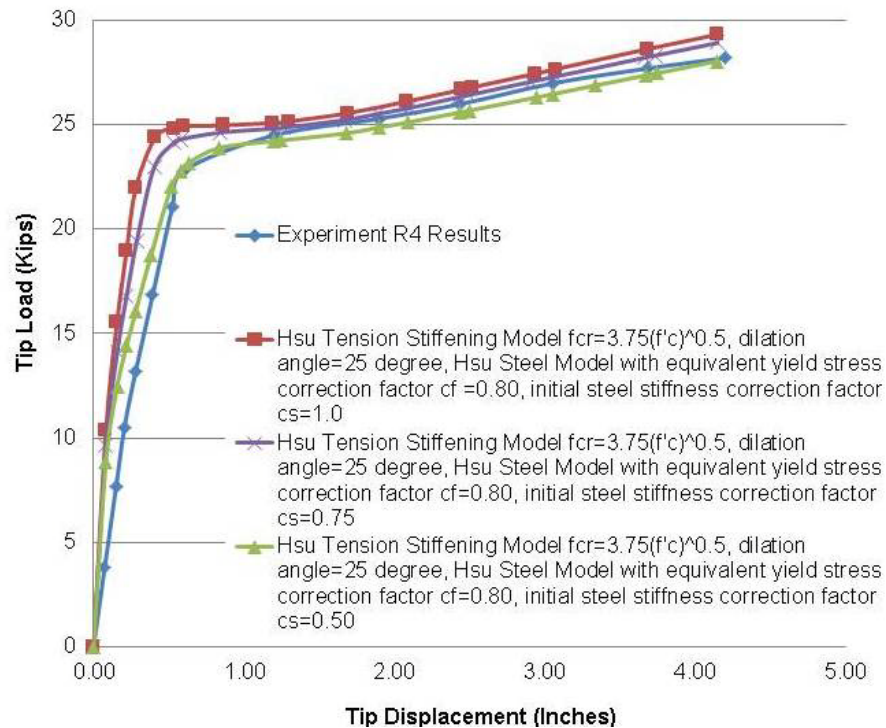


Figure A-7. Comparison plots of load-displacement curve with variation of initial stiffness correction factors  $C_s$  for specimen R4.

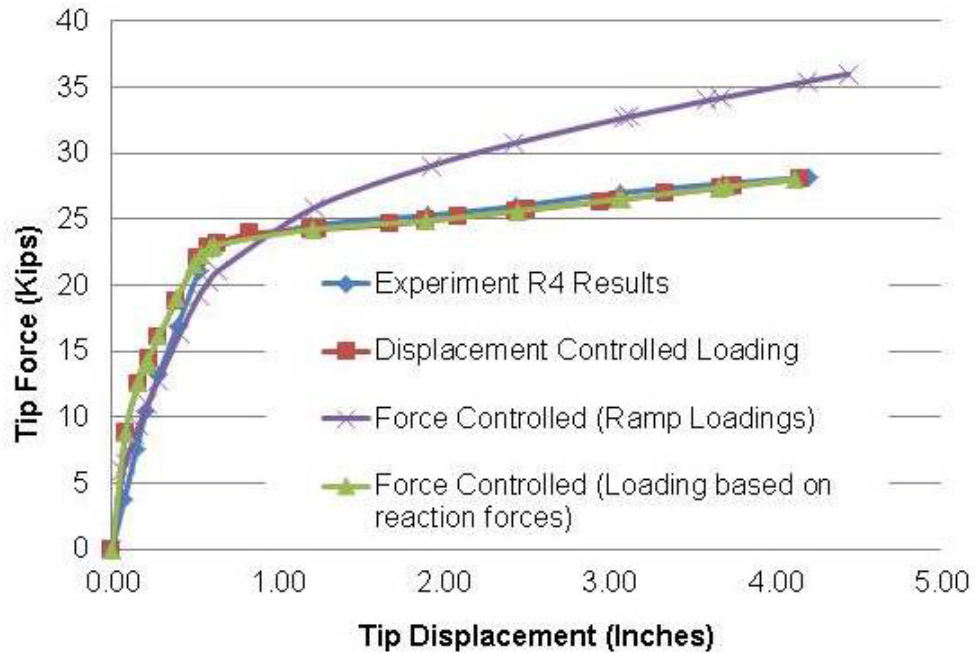


Figure A-8. Comparison plot for displacement and force controlled loading for specimen R4.

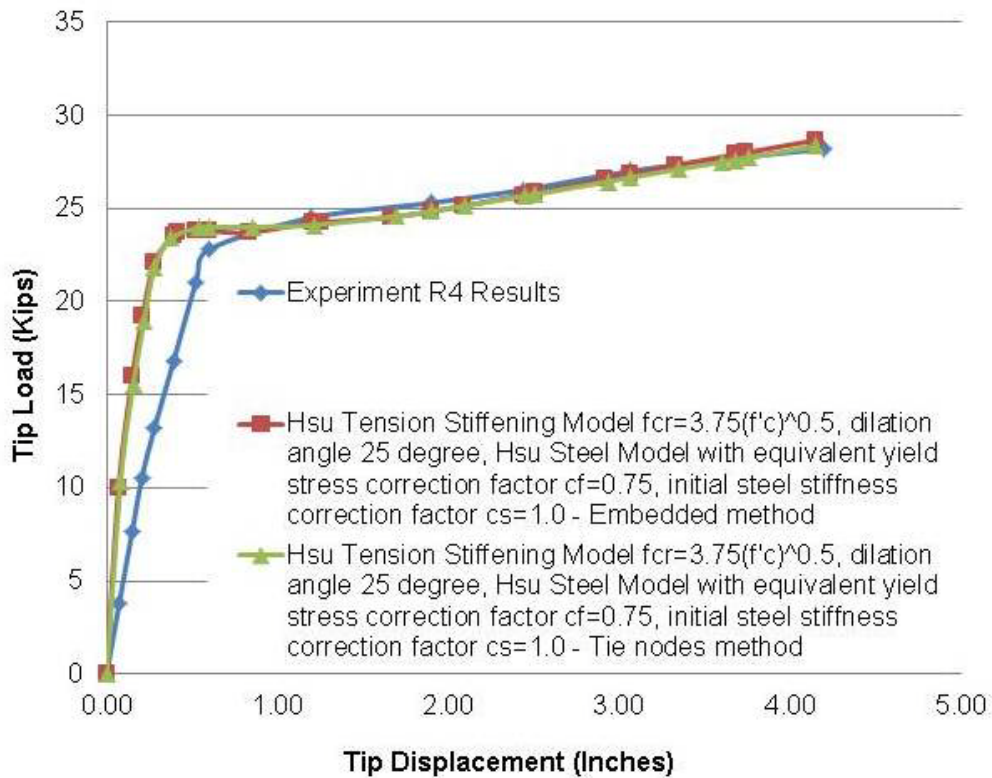


Figure A-9. Comparison of embedded and tie nodes technique for modeling reinforcement for specimen R4.

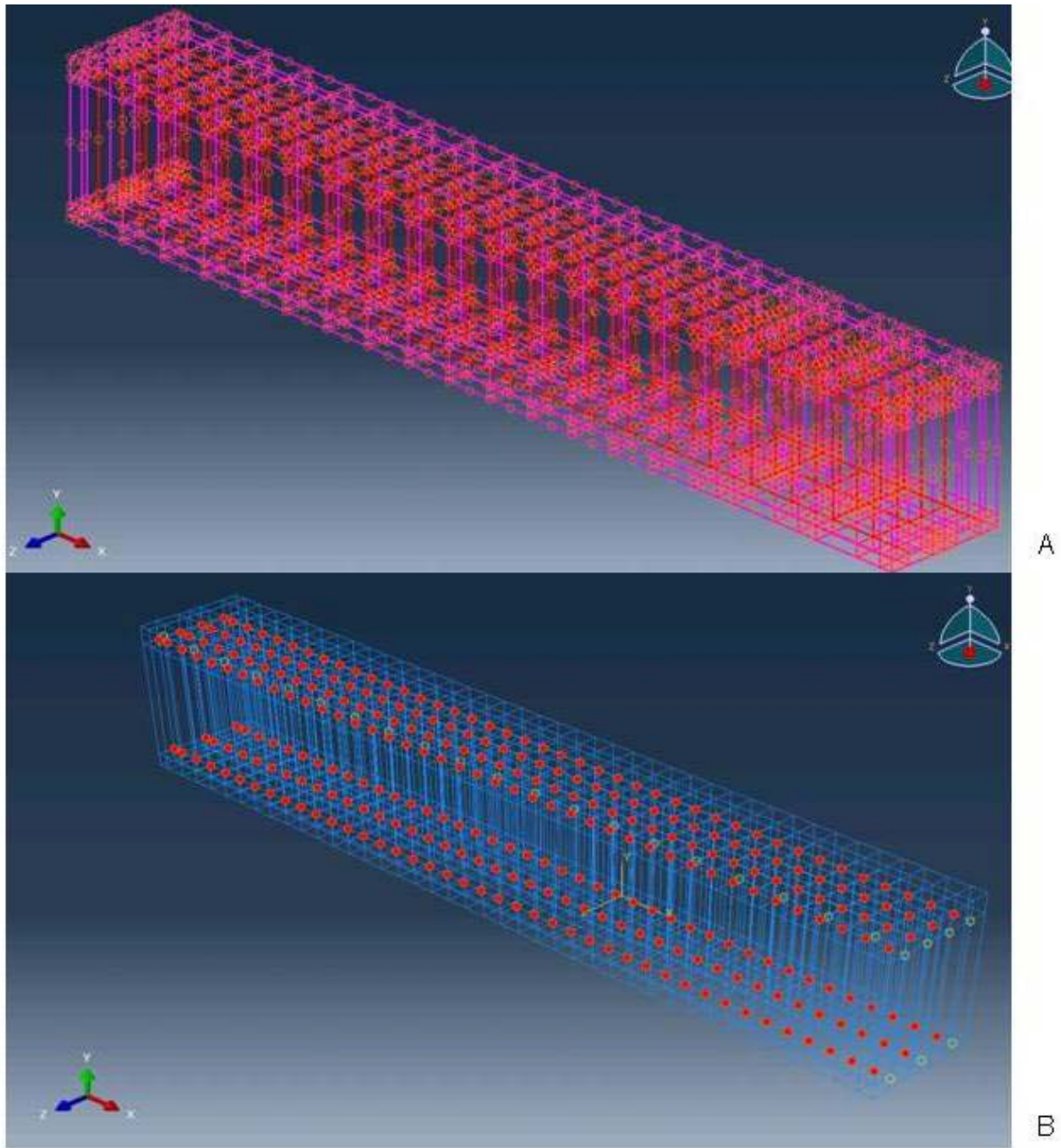


Figure A-10. Comparison of interaction points between reinforcement and concrete. A) embedded method and B) tie nodes method.

Table A-1. Comparison of analysis time between embedded and tie nodes technique for modeling reinforcement for specimen R4.

Technique Descriptions	Tip Loads (Kips)	Difference (%)	Time Taken
Experiment R4	28.2		
Embedded	28.66	1.63	~ 64 hrs
Tie Nodes	28.34	0.50	~ 2 hrs

Table A-2. Summary of material models and parameters.

Material	Compression	Tension	Remarks
Concrete	Hognestad	Hsu	Hsu (1993)
		$f_{cr} = 3.75 \sqrt{f'_c}$	
Steel		Hsu	Hsu (1993)
		$C_f = 0.80$	Equivalent yield stress correction factor
		$C_s = 0.50$	Initial stiffness correction factor

APPENDIX B  
MOMENT CAPACITY CALCULATION OF UPWARD LOADED T-BEAM

The nominal moment capacity of a T-beam with an assumed effective flange width subjected to upward loading (slab in compression) is presented in this appendix. Provisions from ACI Committee 318 (2008) were used for this calculation, which assumed the concrete nominal strain to be 0.003 and a rectangle concrete compression stress block was used. The tensile contribution of concrete was ignored. The geometry, the strain and forces distribution across the cross-section are shown below in Figure B-1.

ORIGIN = 1

**Geometry**

$h := 21.75 \text{ in}$      $b := 185.25 \text{ in}$     Assume Neutral axis lies in the slab

$d_1 := 1.3 \text{ in}$      $d_2 := 2.5 \text{ in}$      $d_3 := 5.5 \text{ in}$      $d_4 := 8.7 \text{ in}$      $d_5 := 19.25 \text{ in}$

$A_{s1} := 34 \cdot (0.11) = 3.74 \text{ in}^2$      $A_{s2} := 4 \cdot (1.27) = 5.08 \text{ in}^2$      $A_{s3} := 2 \cdot (1.27) = 2.54 \text{ in}^2$

$A_{s4} := 34 \cdot (0.11) = 3.74 \text{ in}^2$      $A_{s5} := 3 \cdot (1.27) = 3.81 \text{ in}^2$

**Steel Stress**

$$f_{s1}(c) := \begin{cases} \text{if } \varepsilon_{s1}(c) > 0 \\ \left| \begin{array}{l} (\varepsilon_{s1}(c) \cdot E_s) \text{ if } |\varepsilon_{s1}(c)| \leq \varepsilon_y \\ f_y \text{ otherwise} \end{array} \right. \\ \text{if } \varepsilon_{s1}(c) < 0 \\ \left| \begin{array}{l} (\varepsilon_{s1}(c) \cdot E_s) \text{ if } |\varepsilon_{s1}(c)| \leq \varepsilon_y \\ -f_y \text{ otherwise} \end{array} \right. \end{cases} & f_{s2}(c) := \begin{cases} \text{if } \varepsilon_{s2}(c) > 0 \\ \left| \begin{array}{l} (\varepsilon_{s2}(c) \cdot E_s) \text{ if } |\varepsilon_{s2}(c)| \leq \varepsilon_y \\ f_y \text{ otherwise} \end{array} \right. \\ \text{if } \varepsilon_{s2}(c) < 0 \\ \left| \begin{array}{l} (\varepsilon_{s2}(c) \cdot E_s) \text{ if } |\varepsilon_{s2}(c)| \leq \varepsilon_y \\ -f_y \text{ otherwise} \end{array} \right. \end{cases}$$

$$f_{s3}(c) := \begin{cases} \text{if } \varepsilon_{s3}(c) > 0 \\ \left| \begin{array}{l} (\varepsilon_{s3}(c) \cdot E_s) \text{ if } |\varepsilon_{s3}(c)| \leq \varepsilon_y \\ f_y \text{ otherwise} \end{array} \right. \\ \text{if } \varepsilon_{s3}(c) < 0 \\ \left| \begin{array}{l} (\varepsilon_{s3}(c) \cdot E_s) \text{ if } |\varepsilon_{s3}(c)| \leq \varepsilon_y \\ -f_y \text{ otherwise} \end{array} \right. \end{cases}$$

$$f_{s4}(c) := \begin{cases} \text{if } \varepsilon_{s4}(c) > 0 \\ \left| \begin{array}{l} (\varepsilon_{s4}(c) \cdot E_s) \text{ if } |\varepsilon_{s4}(c)| \leq \varepsilon_y \\ f_y \text{ otherwise} \end{array} \right. \\ \text{if } \varepsilon_{s4}(c) < 0 \\ \left| \begin{array}{l} (\varepsilon_{s4}(c) \cdot E_s) \text{ if } |\varepsilon_{s4}(c)| \leq \varepsilon_y \\ -f_y \text{ otherwise} \end{array} \right. \end{cases}$$

$$f_{s5}(c) := \begin{cases} \text{if } \varepsilon_{s5}(c) > 0 \\ \left| \begin{array}{l} (\varepsilon_{s5}(c) \cdot E_s) \text{ if } |\varepsilon_{s5}(c)| \leq \varepsilon_y \\ f_y \text{ otherwise} \end{array} \right. \\ \text{if } \varepsilon_{s5}(c) < 0 \\ \left| \begin{array}{l} (\varepsilon_{s5}(c) \cdot E_s) \text{ if } |\varepsilon_{s5}(c)| \leq \varepsilon_y \\ -f_y \text{ otherwise} \end{array} \right. \end{cases}$$

### Concrete Stress

$$f_c := 0.85 \cdot f'_c = 3.4 \quad \text{ksi}$$

### Forces

$$a(c) := \beta \cdot c$$

$$F_c(c) := 0.85 \cdot f'_c \cdot a(c) \cdot b \quad F_{s1}(c) := f_{s1}(c) \cdot A_{s1} \quad F_{s2}(c) := f_{s2}(c) \cdot A_{s2} \quad F_{s3}(c) := f_{s3}(c) \cdot A_{s3}$$

$$F_{s4}(c) := f_{s4}(c) \cdot A_{s4} \quad F_{s5}(c) := f_{s5}(c) \cdot A_{s5}$$

### Equate all Forces to Zero to find the Neutral Axis depth, C

$$P(c) := F_c(c) + F_{s1}(c) + F_{s2}(c) + F_{s3}(c) + F_{s4}(c) + F_{s5}(c)$$

$$c := \text{root}(P(c), c, 1, 22)$$

$$c = 1.545 \quad \text{in}$$

## Check

Since  $c$  is less than slab thickness, assumption that Neutral axis lies in the slab is correct.

$$\varepsilon_{s1}(c) = 4.755 \times 10^{-4} \quad \varepsilon_{s2}(c) = -1.855 \times 10^{-3} \quad \varepsilon_{s3}(c) = -7.681 \times 10^{-3}$$

$$\varepsilon_{s4}(c) = -0.014 \quad \varepsilon_{s5}(c) = -0.034$$

## Steel Stress

$$f_{s1}(c) = 13.79 \quad \text{ksi} \quad f_{s2}(c) = -53.789 \quad \text{ksi} \quad f_{s3}(c) = -60 \quad \text{ksi} \quad f_{s4}(c) = -60 \quad \text{ksi}$$

$$f_{s5}(c) = -60 \quad \text{ksi}$$

## Total Compressive Forces

$$F_{CT} := F_c(c) + F_{s1}(c) + F_{s2}(c) = 605.4 \quad \text{Kips}$$

## Total Tension Forces

$$F_{TT} := F_{s3}(c) + F_{s4}(c) + F_{s5}(c) = -605.4 \quad \text{Kips}$$

## Lever arm for various forces

$$l_1 := c - d_1 = 0.245 \quad \text{in} \quad l_2 := c - d_2 = -0.955 \quad \text{in} \quad l_3 := c - d_3 = -3.955 \quad \text{in}$$

$$l_4 := c - d_4 = -7.155 \quad \text{in} \quad l_5 := c - d_5 = -17.705 \quad \text{in} \quad l_c := c - \frac{a(c)}{2} = 0.888 \quad \text{in}$$

## Nominal Moment Capacity about Neutral Axis

$$M := F_{s1}(c) \cdot l_1 + F_{s2}(c) \cdot l_2 + F_{s3}(c) \cdot l_3 + F_{s4}(c) \cdot l_4 + F_{s5}(c) \cdot l_5 + F_c(c) \cdot l_c = 7.264 \times 10^3 \quad \text{Kip} \cdot \text{in}$$

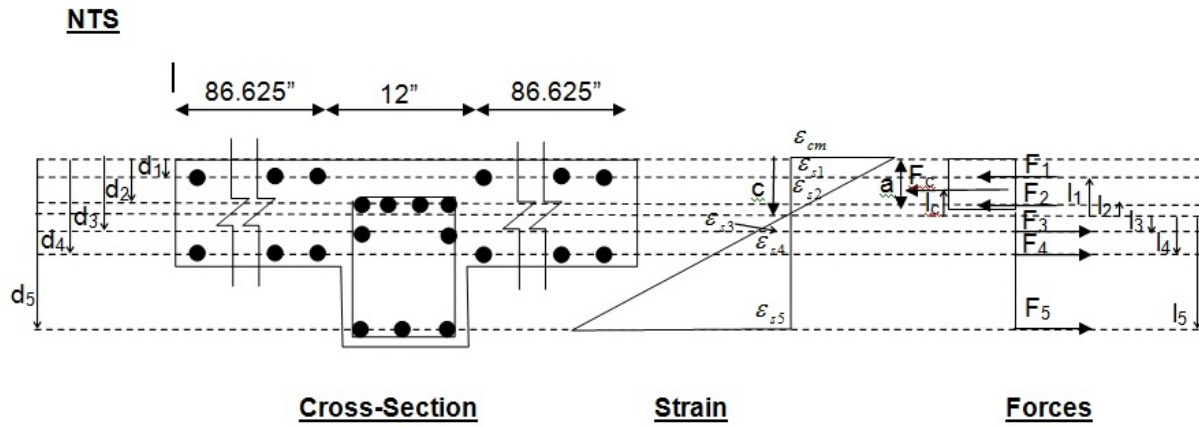


Figure B-1. Cross-section, strain and force distribution of a T-beam loaded upwardly (slab in compression).

## APPENDIX C SIMPLIFIED STRUCTURAL ELEMENTS BASED FINITE ELEMENT MODEL

With reference to Chapter 4, a simplified structural elements based finite element model developed to replace the predominantly continuum based FE model for the interior connection, had been introduced. This appendix described two aspects of the simplified structural elements based FE model in more details. The two aspects are the moment-rotation relationship of the connector elements and the stiffness of the beam elements.

**Connector elements moment- rotation relationship.** The connectors consisted of a combination of JOIN and CARDAN connection types which represent the basic translational and rotational dofs, respectively. The connector elements would be given the moment-rotation relationship of the interior beam-column connection derived from a continuum FE model. The moment-rotation relationship for the continuum FE model for the interior beam-column connection for the main longitudinal beam (See Figure C-1) and spandrel beam at Grid 3-C and 4-D respectively, as shown in Figure 4.23, was obtained and presented in Figure C-2. As the transverse beams have the same geometric and reinforcement details as the longitudinal beams, its moment-rotation relationship would be the same as the longitudinal beams.

**Stiffness of the beam elements.** Beams elements had been used to represent the structural beam components of the predominantly continuum based FE model. The predominantly continuum based FE model for the interior connection was assessed for cracking of its beams. For beams that were cracked, the effective moment of inertia as calculated from the ACI 318-08, Section 9.5.2.3 was used. For beams that suffered no cracking, the transformed moment of inertia that account for the steel reinforcement

stiffness was used instead. Both the moment of inertia in the strong and weak axis bending was considered, while the torsional stiffness was assumed constant. An example of the calculation of the transformed moment of inertia for uncracked beams and effective moment of inertia for cracked beam were presented below for the case of the longitudinal beam cross-section as shown in Figure C-3 and C-4.

**Calculation of the transformed moment of inertia for longitudinal beam, where bottom of the concrete fibre have not reached cracked moment (See Figure C-3)**

Based on ACI 318-08 section 9.5.2.3

Geometry and material properties

$$h := 21.75 \text{ in} \quad b := 12 \text{ in} \quad d_1 := 2.5 \text{ in} \quad d_2 := 5.5 = 5.5 \text{ in} \quad d_3 := 19.25 \text{ in}$$

$$A_{s1} := 4 \cdot 1.27 = 5.08 \text{ in}^2 \quad A_{s2} := 2 \cdot 1.27 = 2.54 \text{ in}^2 \quad A_{s3} := 3 \cdot 1.27 = 3.81 \text{ in}^2$$

$$f_c := 4000 \text{ psi} \quad E_c := 57000 \cdot \sqrt{f_c} = 3.605 \times 10^6 \text{ psi} \quad E_s := 29000 \cdot 1000 = 2.9 \times 10^7 \text{ psi}$$

$$n := \frac{E_s}{E_c} = 8.044$$

Transformed cracked area (Including steel reinforcement)

$$K := (n - 1) \cdot (A_{s1} + A_{s2} + A_{s3}) = 80.517$$

$$A_{tr} := b \cdot h + K = 341.517 \text{ in}^2$$

Compute Neutral Axis, c

$$c = \frac{\frac{b \cdot h^2}{2} + (n - 1) \cdot A_{s1} \cdot (d_1) + (n - 1) \cdot A_{s2} \cdot (d_2) + (n - 1) \cdot A_{s3} \cdot (d_3)}{A_{tr}} = \frac{A + D}{A_{tr}}$$

$$A_{ww} := \frac{b \cdot h^2}{2} = 2.838 \times 10^3$$

$$D := (n - 1) \cdot A_{s1} \cdot (d_1) + (n - 1) \cdot A_{s2} \cdot (d_2) + (n - 1) \cdot A_{s3} \cdot (d_3) = 704.527$$

$$c := \frac{A + D}{A_{tr}} = 10.374 \quad \text{in}$$

$$I_{tr} := \frac{1}{12} \cdot (b) \cdot (h)^3 + b \cdot h \cdot \left(\frac{h}{2} - c\right)^2 + (n - 1) \cdot A_{s1} \cdot (d_1 - c)^2 + (n - 1) \cdot A_{s2} \cdot (d_2 - c)^2 \dots \\ + (n - 1) \cdot A_{s3} \cdot (d_3 - c)^2$$

$$I_{tr} = 1.511 \times 10^4 \quad \text{in}^4$$

### **Calculation of the effective moment of inertia for longitudinal beam (based on cracked section) – See Figure C-4**

Based on ACI 318-08 section 9.5.2.3

#### **Geometry and material properties**

$$h := 21.75 \quad \text{in} \quad b := 12 \quad \text{in} \quad d_1 := h - 2.5 = 19.25 \quad \text{in} \quad d_2 := h - 5.5 = 16.25$$

$$d'_1 := 2.5 \quad \text{in} \quad A_{s1} := 4 \cdot 1.27 = 5.08 \quad \text{in}^2 \quad A_{s2} := 2 \cdot 1.27 = 2.54 \quad \text{in}^2 \quad A_{s3} := 3 \cdot 1.27 = 3.81$$

$$f_c := 4000 \quad \text{psi} \quad E_c := 57000 \cdot \sqrt{f_c} = 3.605 \times 10^6 \quad \text{psi} \quad E_s := 29000 \cdot 1000 = 2.9 \times 10^7$$

$$n := \frac{E_s}{E_c} = 8.044$$

#### **Transformed cracked area (Including steel reinforcement)**

$$K_{ww} := (n - 1) \cdot A_{s3} + n \cdot A_{s1} + n \cdot A_{s2} = 88.137$$

$$A_{cr} = b \cdot c + K = 12 \cdot c + K = 12 \cdot c + 88.137 \quad \text{in}^2$$

#### **Neutral Axis, c**

$$c = \frac{\frac{b \cdot c^2}{2} + (n - 1) \cdot A_{s3} \cdot (d'_1) + n \cdot A_{s1} \cdot d_1 + n \cdot A_{s2} \cdot d_2}{A_{cr}}$$

where

$$D := (n - 1) \cdot A_{s3} \cdot (d'_1) + n \cdot A_{s1} \cdot d_1 + n \cdot A_{s2} \cdot d_2 = 1.186 \times 10^3$$

$$W = 12 \cdot c^2 + 88.137 \cdot c - 6 \cdot c^2 - 1186 = 6 \cdot c^2 + 88.137c - 1186 = c^2 + 14.6895 \cdot c - 197.67$$

$$W(c) := c^2 + 14.6895 \cdot c - 197.67 = 0 \text{ solve, } c \rightarrow \begin{pmatrix} 8.517637984238060491 \\ -23.207137984238060491 \end{pmatrix}$$

$c_c := 8.52$  in  $c$  is lower than  $d_2$ , therefore  $A_{s2}$  is in tension

$$I_{cr} := \frac{1}{12} \cdot (b) \cdot (c)^3 + b \cdot c \cdot \left(\frac{c}{2}\right)^2 + (n - 1) \cdot A_{s3} \cdot (c - d'_1)^2 + n \cdot A_{s1} \cdot (d_1 - c)^2 + n \cdot A_{s2} \cdot (d_2 - c)^2$$

$$I_{cr} = 9.372 \times 10^3 \text{ in}^4$$

Based on ACI 318-08 section 9.5.2.3

$$I_e = \left(\frac{M_{cr}}{M_a}\right)^3 \cdot I_g + \left[1 - \left(\frac{M_{cr}}{M_a}\right)^3\right] \cdot I_{cr}$$

$$I_g := \frac{1}{12} \cdot (b) \cdot (h^3) = 1.029 \times 10^4 \text{ in}^4 \quad M_a := 7537 \cdot 1000 = 7.537 \times 10^6$$

$$M_{cr} = \frac{f_r \cdot I_g}{y_t} \quad f_r = 7.5 \cdot \lambda \cdot \sqrt{f'_c} \quad \lambda := 1 \quad \text{For normal weight concrete, } \lambda \text{ is } 1$$

$$y_t := h - c = 13.23 \text{ in} \quad f_r := 7.5 \cdot \lambda \cdot \sqrt{f'_c} = 474.342 \text{ psi}$$

$$M_{cr} := \frac{f_r \cdot I_g}{y_t} = 3.689 \times 10^5 \text{ lb-in}$$

$$I_e := \left(\frac{M_{cr}}{M_a}\right)^3 \cdot I_g + \left[1 - \left(\frac{M_{cr}}{M_a}\right)^3\right] \cdot I_{cr} = 9.373 \times 10^3 \text{ in}^4$$

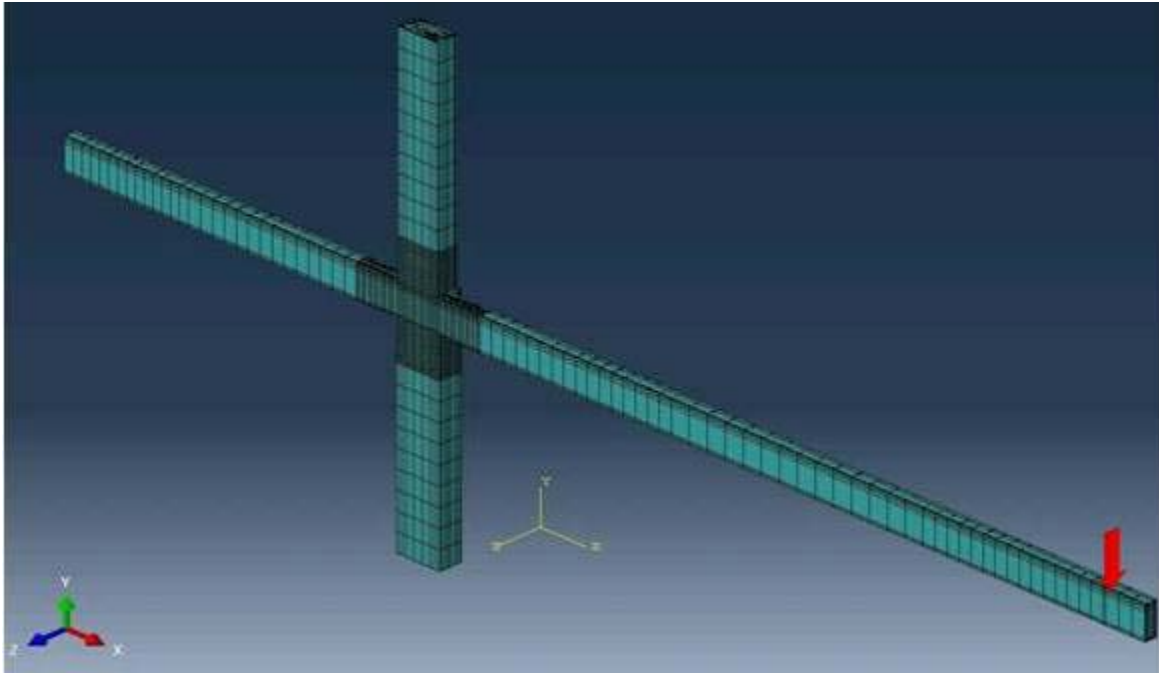


Figure C-1. Continuum FE model for beam-column connection for longitudinal beam (rectangle cross-section only)

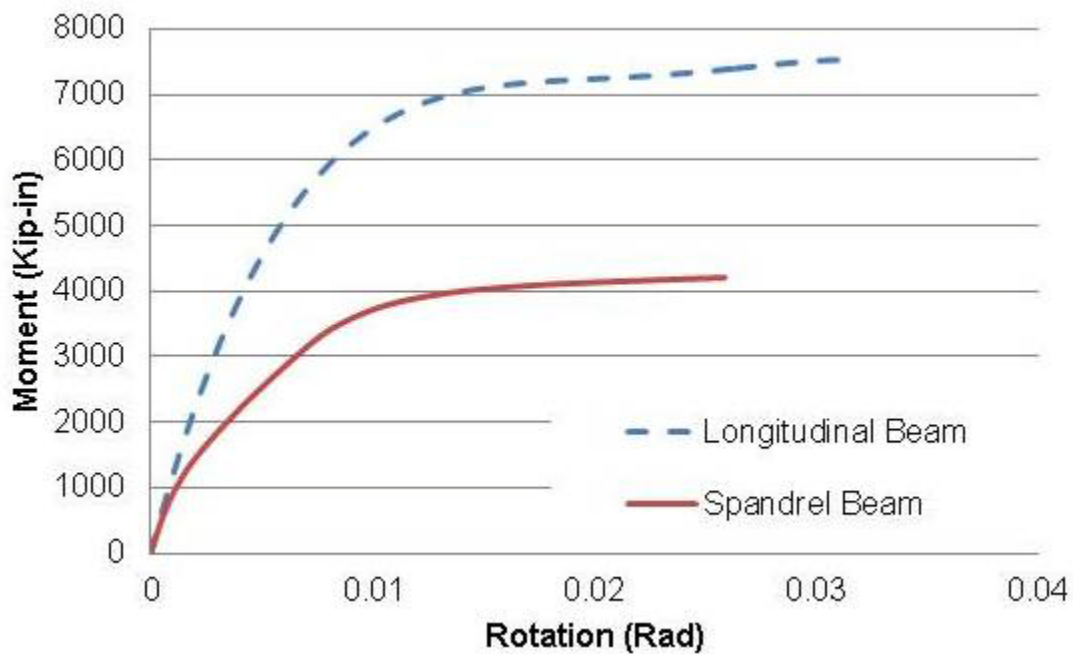


Figure C-2. Moment-rotation relationship of beam-column connection for beams with rectangle cross-sectional subjected to downward loads.

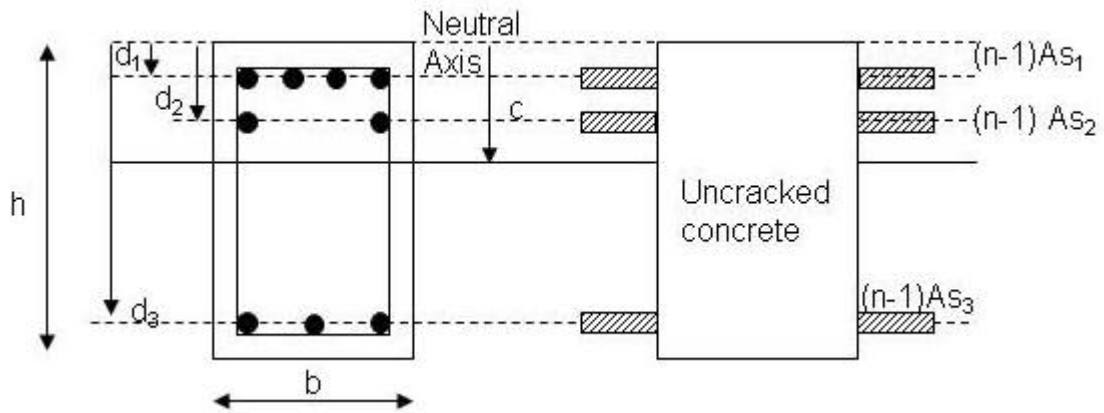


Figure C-3. Geometric for transformed stiffness calculation for uncracked section (Not to scale).

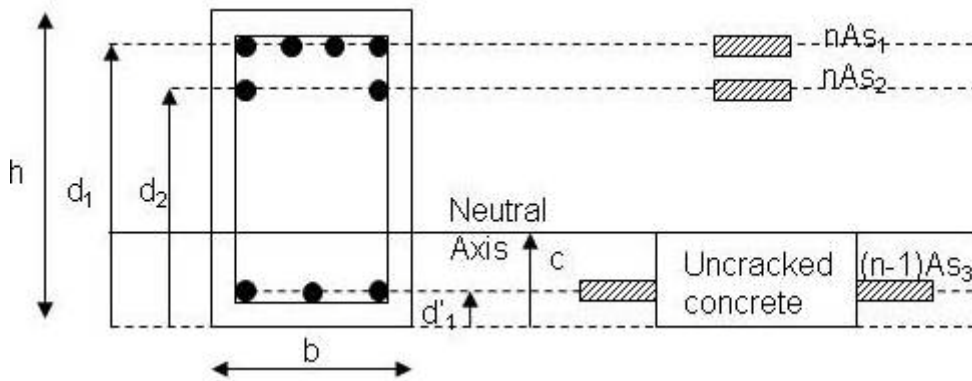


Figure C-4. Geometric for effective moment of inertia calculation for cracked section based on American Concrete Institute (ACI) 318-08 (Not to scale).

## LIST OF REFERENCES

- ACI. (1984). *Earthquake effects on reinforced concrete structure: U.S - Japan Research, SP 84*. Amer. Concr. Inst.
- ACI Committee 318. (2002). *Building code requirements for structural concrete (ACI 318-02) and commentary*. Amer. Concr. Inst.
- ACI Committee 318. (2008). *Building code requirements for structural concrete (ACI 318-08) and commentary*. Amer. Concr. Inst.
- ACI-ASCE Committee 352. (1985). "Recommendations for design of beam-column joints in monolithic reinforced concrete structures." *ACI J.*, ACI-ASCE, 82(3), 266–283.
- ACI-ASCE Committee 352. (2002). *Recommendations for design of beam-column connections in monolithic reinforced concrete structures (ACI 352R-02)*. Amer. Concr. Inst.
- Ammerman, O. V., and French, C. W. (1988). "Reinforced concrete slab-beam-column connections." *Struct. Engrg. Rept. No. 88-03*, Civ. and Mineral Engrg. Dept., Univ. of Minnesota, Minneapolis, Minn.
- Ammerman, O. V., and French, C. W. (1989). "R/C beam-column-slab subassemblages subjected to laterals loads." *J. Struct. Engrg.*, ASCE, 115(6), 1289–1308.
- ASCE 7. (2002). *Minimum design loads for buildings and other structures*. ASCE.
- Astarlioglu, S., and Krauthammer, T. (2009). "Dynamic Structural Analysis Suite (DSAS) User Manual." *Rep. No. CIPPS-TR-003-2009*, Center for Infrastru. Protection and Physical Security (CIPPS), Univ. of Florida, Gainesville, FL.
- Bathe, K. (1996). *Finite element procedures*. Prentice-Hall.
- Chen, W.F. (1982). *Plasticity in reinforced concrete*. McGraw-Hill.
- Cheung, P. C., Paulay, T., and Park, R. (1991). "New Zealand tests on full-scale reinforced concrete beam-column-slab subassemblages designed for earthquake resistance." *Design of Beam-Column Joints for Seismic Resistance*, SP 123-1, Amer. Concr. Inst., Detroit, Mich.
- Cheung, P. C., Paulay, T., and Park, R. (1991). "Mechanisms of slab contributions in beam-column subassemblages." *Design of Beam-Column Joints for Seismic Resistance*, SP 123-10, Amer. Concr. Inst., Detroit, Mich.
- Conrath, E. J., Krauthammer, T., Marchand, K. A., and Mlakar, P.F. (1999). *Structural design for physical security. State of the Practice report*. American Society of Civil Engineers (ASCE).

- Cook, R. D., Malkus, D. S., Plesha, M. E., and Witt, R. J. (2004). *Concepts and applications of finite element analysis*. John Wiley and Sons.
- Cook, W. D., and Mitchell, D. (1988). "Studies of disturbed regions near discontinuities in reinforced concrete members." *ACI Struct. J.*, ACI, 85(2), 206–216.
- Corley, W. G. (1966). "Rotational capacity of reinforced concrete beams." *J. Struct. Div.*, ASCE, 92, ST5, 121–146.
- Durrani, A. J., and Wight, J. K. (1982). "Experimental and analytical study of internal beam to column connections subjected to reversed cyclic loading." *Report UMEE 82R3*, Dept. of Civ. Engrg., Univ. of Michigan, Ann Arbor, Mich.
- Durrani, A. J., and Zerbe, H. E. (1987). "Seismic resistance of R/C exterior connections with floor slab." *J. Struct. Engrg.*, ASCE, 113(8), 1850–1864.
- Dusenberry, D. (2002). "Review of existing guidelines and provisions related to progressive collapse." *Proc., Workshop on Prevention of Progressive Collapse*, Washington, D.C., 1–31.
- Ehsani, M. R., and Wight, J. K. (1985). "Effect of transverse beam and slab on the behavior of reinforced concrete beam-to-column connections." *ACI J.*, ACI, 82(2), 188–195.
- Feldman, A., and Siess, C. P. (1956). "Investigation of resistance and behavior of reinforced concrete members subjected to dynamic loading." *Tech. Rep. to the Office of the Chief of Engineers, Department of the Army*, Dept. of Civ. Engrg., Univ. of Illinois, Champaign, Illin.
- Flanagan, D. P., and Belytschko, T. (1981). "A uniform strain hexahedron and quadrilateral with orthogonal hourglass control." *Int. J. for Numerical Methods in Engrg.*, Wiley, 17(5), 679–706.
- Franco, M. A. D., Mitchell, D., and Paultre, P. (1995). "Role of spandrel beams on response of slab-beam-column connections." *J. Struct. Engrg.*, ASCE, 121(3), 408–419.
- French, C. W., and Boroojerdi, A. (1989). "Contribution of R/C floor slabs in resisting lateral loads." *J. Struct. Engrg.*, ASCE, 115(1), 1–18.
- French, C. W., and Moehle, J. P. (1991). "Effect of floor slab on behavior of slab-beam-column connections." *Design of Beam-Column Joints for Seismic Resistance*, SP 123-9, Amer. Concr. Inst., Detroit, Mich.
- GSA. (2003). *Progressive Collapse Analysis and Design Guidelines for New Federal Buildings and Major Modernization Projects*. U.S. General Services Administration.

- Hassoun, M. N., and Manaseer, A. A. (2005). *Structural concrete – theory and design*. John Wiley & Sons.
- Hognestad, E. (1951). “A study of combined bending and axial load in reinforced concrete members.” *Bulletin 399*, University of Illinois Engrg. Experi. Station, Univ. of Illinois, Champaign, Illin.
- Hsu, T.T. (1993). *Unified theory of reinforced concrete*. CRC Press.
- Jankowiak, T., and Lodygowski, T. (2005). “Identification of parameters of concrete damage plasticity constitutive model.” *Foundations of Civil and Environmental Engrg.*, Poznan Univ. of Technology, 6, 53–69.
- January, L. M., and Krauthammer, T. (2003). “Finite element code validation using precision impact test data on reinforced concrete beams.” *Rep. to U.S. Army Engineering Research and Development Center, Vicksburg, Mississippi*, Protective Technology Center, The Pennsylvania State Univ., State College, Penn.
- Joglekar, M. R. (1984). “Behavior of reinforced concrete floor systems under lateral load.” Thesis submitted to the University of Texas, at Austin, Tex., in partial fulfillment of the requirements for the degree of *Doctor of Philosophy*.
- Kitayama, K., Otani, S., and Aoyama, H. (1991). “Development of design criteria for RC interior beam-column joints.” *Design of Beam-Column Joints for Seismic Resistance*, SP 123-4, Amer. Concr. Inst., Detroit, Mich.
- Krauthammer, T. (2008). *Modern Protective Structures*. CRC Press.
- Kurose, Y., Guimaraes, G. N., Zuhua, L., Kreger, M. E., and Jirsa, J. O. (1991). “Evaluation of slab-beam-column connections subjected to bidirectional loading.” *Design of Beam-Column Joints for Seismic Resistance*, SP 123-2, Amer. Concr. Inst., Detroit, Mich.
- Lee, J., and Fenves, G. L. (1998). “Plastic-damage model for cyclic loading of concrete structures.” *J. Engrg. Mech.*, ASCE, 124(8), 892–900.
- Ma, S. M., Bertero, V. V., and Popov, E. P. (1976). “Experimental and analytical studies on hysteretic behavior of reinforced concrete rectangular and T-beams.” *Rep. No. EERC 76-2*, Earthquake Engrg. Res. Center, Univ. of California, Berkeley, Calif.
- MacGregor, J. G., and Wight, J. K. (2005). *Reinforced Concrete: Mechanics and design*. Pearson Prentice Hall.
- Mohamed, O. A. (2006). “Progressive collapse of structures: Annotated bibliography and comparison of codes and standards.” *J. Performance of Constructed Facilities*, ASCE, 20(4), 418–425.

- Malm, R., James, G., and Sundquist, H. (2006). "Monitoring and evaluation of shear crack initiation and propagation in webs of concrete box-girder sections." *Int. Conference on Bridge Engrg. – Challenges in the 21<sup>st</sup> Century*, Hong Kong, China.
- Malm, R. (2009). "Predicting shear type crack initiation and growth in concrete with non-linear finite element method." *Bulletin 97*, Dept. of Civ. and Arch. Engrg., Royal Institute of Technology, Stockholm, Sweden.
- Mitchell, D., and Collins, M.P. (1991). *Prestressed concrete structures*. Prentice Hall.
- Nielsen, M. P. (1999). *Limit analysis and concrete plasticity*. CRC Press.
- Nilsson, I. H. E. (1973). "Reinforced concrete corners and joints subjected to bending moment." *Document No. D7:1973*, National Swedish Institute for Building Research, Stockholm, Sweden.
- Nilsson, I. H. E., and Losberg, A. (1976). "Reinforced concrete corners and joints subjected to bending moment." *J. Struct. Div.*, ASCE, 102(6), 1229–1254.
- Nilson, A. H., Darwin, D., and Dolan, C. W. (2004). *Design of concrete structures*. McGraw-Hill.
- Oberkampf, W. L., Trucano, T. G., and Hirsch, C. (2004). "Verification, validation and predictive capability in computational engineering and physics." *Appl. Mech. Rev.*, ASME, 57(5), 345–384.
- Park, R., and Paulay, T. (1975). *Reinforced concrete structures*. Wiley.
- Pantazopoulou, S. J., Moehle, J. P., and Shahrooz, B. M. (1988). "Simple analytical model for T-Beam in flexure." *J. Struct. Engrg.*, ASCE, 114(7), 1507–1523.
- Pantazopoulou, S. J., and Moehle, J. P. (1990). "Truss model for 3-D behavior of R.C exterior connections." *J. Struct. Engrg.*, ASCE, 116(2), 298–315.
- Paulay, T., and Priestley, M. J. N. (1992). *Seismic design of reinforced concrete and masonry buildings*. Wiley-Interscience.
- Paultre, P., Castele, D., Rattray, S., and Mitchell, D. (1989). "Seismic response of reinforced concrete frame subassemblages – a Canadian code perspective." *Can. J. Civ. Engrg.*, NRC Research Press, 16, 627–649.
- Qi, X. (1986). "The behavior of R/C slab-column subassemblage under lateral load reservals." *CE299 Report*, Struct. Engrg. and Struct. Mech., Univ. of California, Berkeley, Calif.
- Qi, X., and Pantazopoulou, S. J. (1991). "Response of RC frame under lateral loads." *J. Struct. Engrg.*, ASCE, 117(4), 1167–1188.

- Richard, R. M., and Abbott, B. J. (1975). "Versatile elastic plastic stress-strain formula." *J. Struct. Engrg.*, ASCE, 101(4), 511–515.
- Sasani, M., and Sagioglu, S. (2010). "Gravity load redistribution and progressive collapse resistance of 20-story reinforced concrete structure following loss of interior column." *ACI Struct. J.*, ACI, 107(6), 636–644.
- Sawyer, H. A. (1964). "Design of concrete frames for two failure states." *Proc., International Symposium on the Flexural Mech. of Reinf. Conc.*, Miami, FL., 405–431.
- Shahrooz, B. M., Pantazopoulou, S. J., and Chern, S. P. (1992). "Modeling slab contribution in frame connections." *J. Struct. Engrg.*, ASCE, 118(9), 2475–2494.
- Simulia. (2010). *Abaqus version 6.10 documentation*. Dassault Systèmes Simulia Corp.
- Suzuki, N., Otani, S., and Aoyama, H. (1983). "The effective width of slabs in reinforced concrete structures." *Trans. Japan Concr. Inst.*, JCI, 5, 309–316.
- Tan, L. Y. (2010). "Characterizing a reinforced concrete connection for progressive collapse assessment." Thesis submitted to the University of Florida, at Gainesville, FL., in partial fulfillment of the requirements for the degree of *Master of Science*.
- UFC. (2009). *UFC-4-023-03, Design of buildings to resist progressive collapse*. Unified Facilities Criteria.
- Uma, S. R., and Prasad, A. M. (2006). "Seismic behavior of beam-column joints in RC moment resisting frames: A review." *The Indian Concrete J.*, ACC Limited, 80(1), 33–42.
- Vecchio, F.J., and Collins, M.P. (1981). "Stress-strain characteristic of reinforced concrete in pure shear." *Advanced Mech. of Reinforced Concrete*, IABSE, 221–225.
- Wang, C. K., Salmon, C. G., and Pincheira, J. A. (2007). *Reinforced concrete design*. John Wiley & Sons.
- Watson, A. J., and Inkester, J. E. (1982). "Impact loading of a reinforced concrete beam-to-column joint." *Special Publications ACI J.*, ACI, 73, 143–164.
- Yim, H. C. (2007). "A study of steel moment connections for structures under blast and progressive collapse loading rates." Thesis submitted to the Pennsylvania State University, at State College, Penn., in partial fulfillment of the requirements for the degree of *Doctor of Philosophy*.
- Yoshimura, M., and Kurose, Y. (1985). "Inelastic behavior of the building." *Earthquake Effects on RC Structures: U.S. Japan Research*, SP 84-7, Amer. Concr. Inst., Detroit, Mich.

Zerbe, H. E., and Durrani, A. J. (1985). "Effect of a slab on the behavior of exterior beam to column connections." *Report No. 30*, Dept. of Civ. Engrg., Rice Univ., Houston, Tex.

## BIOGRAPHICAL SKETCH

Yong Hong Koh was born in Singapore in 1977. He attended secondary school and junior college in Singapore. He was drafted into the army for his national service from 1995 to 1998. He began his undergraduate studies at Nanyang Technological University, Singapore, in July 1998 and obtained his Bachelor of Engineering degree in civil and environmental engineering on June 2002. In July 2002, he joined the Defence Science and Technology Agency (DSTA), Singapore, as a project engineer. He was involved in the master planning, design, construction and project management of airbase facilities in Singapore. He continued with his part-time graduate studies in Building Science at the National University of Singapore in July 2004 and obtained his Master of Science degree in July 2006. In 2009, he was awarded a postgraduate scholarship from DSTA to pursue a master's degree in civil engineering at the University of Florida, specializing in the field of protective structures.